Experiments with tunable quantum gases in optical lattices

Dissertation
zur Erlangung des akademischen Grades
Doktor der Naturwissenschaften

eingereicht an der
Fakultät für Mathematik, Informatik und Physik
der Universität Innsbruck

von

Ing. Mag. rer. nat. Manfred Johann Mark

Betreuer der Dissertation:
Univ.-Prof. Dr. Hanns-Christoph Nägerl,
Institut für Experimentalphysik

Innsbruck, Jänner 2012

Abstract

The investigation of dilute gases of ultracold atoms is currently a fast growing field, both in experimental and theoretical physics. Major research directions include the simulation of condensed matter systems, the investigation of superfluidity and the realization of controlled quantum chemistry. In this thesis we present our contributions in form of several experiments covering four different topics, sharing the usage of optical lattice potentials and the tunability of interatomic interactions.

In a three-dimensional optical lattice, we investigate the properties of ultracold atoms for various interatomic interaction strengths. Such a system can be described by the Bose-Hubbard model, which originates from solid state physics. For large repulsive values of the interaction strength, we create a strongly interacting system and show the breakdown of the basic assumptions of the Bose Hubbard model by precisely measuring the excitation spectrum. When preparing a Mott insulating state and subsequently changing to attractive interactions, we observe a surprising stability and find indications that the system stabilizes itself via inhibited three-body loss, grounded on the quantum zeno effect.

We examine the dynamics of matter waves along a lattice potential by analyzing Bloch oscillations, which occur when a force is applied along the lattice direction. The effect of interactions and of external force gradients is investigated in detail, and we can demonstrate the analog between this system and the Talbot effect known from classical optics. When modulating the applied force, we observe large oscillations in position space, so called super Bloch oscillations, which can be used to induce transport along the lattice direction without dissipation.

In a set of experiments, we achieved the production of ultracold rovibronic groundstate molecules, a prerequisite for many fundamental studies in quantum chemistry. We associate ultracold atoms to weakly bound dimers employing a Feshbach resonance, and use an optical lattice to shield the molecules against inelastic collisions. Subsequently we transfer them into the rovibronic ground state using the STIRAP technique, removing a binding energy corresponding to a temperature of $\sim 5200\,\mathrm{K}$ without additional heading. This allows full control over all internal and external degrees of freedom.

Elongated tubes created by an optical lattice potential realize an effective one-dimensional geometry, which we use to study the physical models describing such systems. For strong repulsive interactions we enter deeply into the regime of the Tonks-Girardeau gas, a gas of impenetrable pointlike particles. Employing a confinement induced resonance, we can switch the interactions to strong attractive values and thereby prepare a novel, highly excited quantum phase, the Super-Tonks-Girardeau gas. By adding a weak lattice along the tubes, we observe the so-called pinning quantum phase transition from a Luttinger liquid to a Mott insulator.

Zusammenfassung

Die Untersuchung ultrakalter Quantengase ist ein schnell wachsendes Teilgebiet der experimentellen und theoretischen Physik. Die derzeitigen Forschungsrichtungen beinhalten unter anderem die Simulation von Festkörpersystemen, die Erforschung von Suprafluidität und die Realisierung kontrollierter Quantenchemie. In dieser Doktorarbeit stellen wir unseren Beitrag in Form mehrerer durchgeführter Experimente, gruppiert in vier Themengebiete, vor.

In einem dreidimensionalen optischen Gitter untersuchen wir die Eigenschaften ultrakalter Atome in Abhängigkeit von der Wechselwirkungsstärke. Dieses System kann mit dem aus der Festkörperphysik stammenden Bose-Hubbard Modell beschrieben werden. Für ein stark wechselwirkendes System können wir das Versagen einiger grundlegenden Annahmen des Bose-Hubbard Modells durch präzise Messung des Anregungsspektrums zeigen. Bei Präparation eines Mott-Isolators und anschließendem Umschalten zu attraktiven Wechselwirkungen beobachten wir eine überraschende Stabilität und finden Hinweise darauf, dass sich das System durch Unterdrückung von Dreikörperverlusten aufgrund einer hohen Dreikörperverlustrate in Verbindung mit dem Quanten Zeno-Effekt selbst stabilisiert.

Wir untersuchen die Dynamik von Materiewellen entlang eines Gitterpotentials durch Analyse von Bloch-Oszillationen, welche durch eine auf die Atome wirkende Kraft auftreten. Wir testen die Auswirkungen von Wechselwirkung und externen Kraftgradienten auf diese Oszillationen und können die Analogie zwischen unserem System und dem Talbot-Effekt aus der klassischen Optik demonstrieren. Bei Modulation der Kraft beobachten wir Super-Bloch-Oszillationen, die wir zum Teilchentransport durch das Gitter ausnutzen.

In einer weiteren Reihe von Experimenten erzeugen wir ultrakalte Moleküle im absoluten Rotations-Schwingungs-Grundzustand nahe der Quantenentartung, eine Grundvoraussetzung für viele grundlegende Quantenchemieexperimente. Wir erzeugen zuerst schwach gebundene Moleküle durch Nutzung einer Feshbach-Resonanz und schützen die Moleküle mithilfe eines optischen Gitters vor inelastischen Stößen. Anschließend transferieren wir die Moleküle mit Hilfe der STIRAP-Technik in den absoluten Grundzustand, wobei wir eine Bindungsenergie entsprechend einer Temperatur von $\sim 5200\,\mathrm{K}$ ohne Erwärmung der Moleküle abführen können. Damit behalten wir nahezu die volle Kontrolle über alle internen und externen Freiheitsgrade der Moleküle.

Durch ein optisches Gitterpotential erzeugte Röhren realisieren eine effektiv eindimensionale Geometrie, welche wir zur Untersuchung entsprechender physikalischer Modelle nutzen. Für stark repulsive Wechselwirkung gelangen wir in den Bereich des Tonks-Girardeau Gases, das einem idealen Gas harter Kugeln entspricht und sich durch starke Teilchenkorrelationen auszeichnet. Mithilfe einer Einschlussresonanz können wir die Wechselwirkung auf große attraktive Werte umschalten, wodurch wir das hochangeregte Super-Tonks-Girardeau Gas erzeugen können. Durch Hinzunahme eines schwachen Gitters entlang der Röhren können wir den sogenannten 'Pinning'-Quantenphasenübergang beobachten.

CONTENTS

CHAPTER 1

INTRODUCTION

Cooling of atoms down to temperatures in the ultracold regime was first demonstrated by successful laser cooling of ions in 1978 [Win78, Neu78]. Shortly afterwards laser cooling of a beam of neutral atoms was realized [And81, Phi82], enabling the trapping of atomic vapors by magnetic fields [Mig85] and the three-dimensional cooling in an optical molasses [Chu85]. The temperature of such laser cooled clouds reaches down to values of μK, and with further cooling by evaporation the preparation of a new state of matter was realized, the Bose-Einstein condensate [And95, Dav95]. The Bose-Einstein condensate (BEC) brings fascinating phenomena of quantum mechanics into the macroscopic world as it is a giant matter wave, built up by all the atoms in the ensemble in the groundstate of the trap that holds the BEC. Since the first experimental realization many other elements have been condensed successfully, first the other alkaline atoms [Bra95, Fri98, Mod01, Web03a], more recently two alkaline earth metals [Kra09, Ste09] and two rare earth metals [Tak03, Lu11], and the transition metal chromium [Gri05] as well as the noble gas helium [Rob01]. The phenomenon of Bose-Einstein condensation has been observed also in more exotic systems like exciton polaritons [Kas06] in semiconductors and with photons [Kla10] in a optical resonator. Also a BEC of weakly bound molecules composed of two fermionic atoms has been demonstrated [Joc03a, Gre03, Zwi03].

The creation of the BEC triggered an enormous amount of activities in the research field of ultracold gases. As the BEC represents a coherent matter wave, basic quantum mechanic phenomena like the interference of two overlapping matter waves [And97] or the effect of quantum statistics leading to bosonic bunching [Bur97] were directly observable. The superfluidity of a BEC was shown in exciting experiments by the realization of vortices [Mat99, Mad00] and vortex lattices [AS01]. A crucial step forward was the observation of Feshbach resonances [Ino98, Cou98, Chi10], as they provide tunability of interparticle interactions over a wide range. For example, they enabled the preparation of a BEC with attractive interactions, leading to the observation of an collapsing BEC, a so-called Bosenova [Ger00]. Feshbach resonances also allowed the

creation of bright solitons [Kha02, Str02], dispersion-free matter-wave packets with attractive interactions, in contrast to the previously observed dark solitons [Bur99, Den00] which are shape-preserved density-kinks in a BEC.

The tunability of interactions provided by Feshbach resonances is also a key ingredient for the preparation and investigation of ultracold gases composed of fermionic atoms. The great interest in ultracold fermionic samples arises from the superfluid phase at attractive interactions, predicted by Bardeen, Cooper and Schrieffer (BCS) [Bar57] to explain superconductivity in metals. This phase arises from a pairing mechanism between two fermions, forming Cooper pairs in momentum space. The possibility to cool fermionic gases deep into the quantum degenerate regime, for example by preparing a two component mixture with different spins to facilitate thermalizing collisions [DeM99], enables the ongoing intense investigation of the BCS phase and the crossover to the BEC side at repulsive interactions [Bar04a, Bar04b, Chi04a], where two fermions form a bosonic molecule, thus allowing the formation of a BEC [Joc03a, Gre03, Zwi03]. These weakly bound molecules are stable under collisions due to their fermionic compounds [Reg03, Cub03, Str03, Joc03b]. The regime in between these two phases, the strongly interacting Fermi gas in the unitarity limit, currently attracts a lot of interest [Rie08, Sch09a, Gae10].

Another central element of many experiments in the field of ultracold atoms are optical lattices [Blo08]. They are heavily used to create three-dimensional lattice structures [Gre02a] or to reduce the dimensionality of the system to create one-dimensional [Gre01, Mor03a] or two-dimensional [Had06] systems, optionally with an overlaid lattice along the non-confined directions [Stö04, Spi07]. Some key experiments were for example the observation of the quantum phase transition between the superfluid and insulating phase for bosons [Gre02a] and fermions [Sch08, Jör08] in three-dimensional systems and the realization of the strongly correlated Tonks-Girardeau gas [Kin04, Par04] in a one-dimensional geometry. One of the major challenges in the near future lies in the simulation and implementation of quantum magnetism models with dipolar gases [Bar06].

This thesis is built up of 14 publications, grouped thematically together in four chapters. This lead-in chapter intends to be a broad introduction into the four different topics, giving an overview over the past and current status of the appropriate research fields. The main result of this thesis is presented in chapter 2, where we investigate a strongly interacting many-body system in a 3D optical lattice and show the breakdown of the approximations used in the standard Bose-Hubbard model [Mar11b]. We prepare a metastable Mott-insulating state using strong attractive interactions and find evidence that the metastability is supported by inhibited three-body recombination loss [Mar11c]. In chapter 3 we investigate the effect of interactions [Gus10], force gradients [Mar11a] and a modulation of the applied force [Hal10b] onto Bloch oscillations. In a series of measurements presented in chapter 4 we produce deeply bound [Dan08, Dan09a] and subsequently rovibronic groundstate molecules [Dan10b], supplemented by prerequisite precision spectroscopy data on various molecular levels [Dan09b, Mar09]. Our investigations of tunable quantum gases confined to

an one-dimensional geometry are summarized in chapter 5. We see clear evidence for the existence of the Super Tonks-Girardeau gas [Hal09], a metastable excited many-body system with attractive interactions, by employing a confinement induced resonance, which is investigated in more detail [Hal10d]. Additionally we were able to observe a novel type of quantum phase transition in this geometry [Hal10c], and by measuring three-body recombination loss we determined the local three-body correlation function for 1D gases over a large region of interaction strengths [Hal11].

1.1. Matter wave dynamics along an optical lattice

Optical lattice potentials build up by standing light waves greatly extend the research field of ultracold gases. They serve as a defect free crystal structure, enabling the investigation of condensed matter phenomena and the implementation of novel many-body phases not possible in bulk matter [Blo08]. A paradigm example are Bloch oscillations (BO) [Blo28, Zen34], an oscillation in momentum space of the particle inside a lattice structure, when a constant force is acting on it. In condensed matter systems BO are typically interrupted within one oscillation period by scattering events due to defects in the crystal structure. By artificially increasing their oscillation frequency using semiconductor superlattice structures, coherent submillimeter-wave emission arising from BO has been successfully measured [Was93].

By using ultracold atoms in an optical lattice, a direct observation of BO in momentum space [BD96, And98] is possible. Unlike defects in solid state systems, atomic interactions lead to a coherent dephasing of BO, which can be controlled and reversed by external fields and dynamical tuning of interactions [Gus10]. Avoiding this dephasing by using noninteracting fermions [Roa04], non-condensed bosons with a low background interaction strength [Fer06], or by switching interactions to zero by means of a feshbach resonance in bosonic BECs [Fat08a, Gus08b], it is possible to detect several thousand oscillations over the course of seconds. Figure 1.1 shows BO as series of absorption pictures after some expansion time to map the quasimomentum onto real space [Kas95], where we vary the hold time during which the force accelerates the atoms. Currently BO are used in new types of precision atom interferometers to measure the fine structure constant, gravity or atom-surface interactions [Cad08, Cla09, Sor09, Bou11].

The dynamical modulation of one parameter in such a system brings a new degree of freedom into play. A shaking of the lattice can introduce photon-assisted tunneling between lattice sites [Sia08]. The same effect can be observed when modulating the applied force, in this case it is even possible to induce huge oscillations in real space or directed transport through the lattice, depending on the phase and frequency difference between the force modulation and the Bloch cycle [Hal10b]. Lattice shaking or a modulated force can be also viewed in terms of an effective tunneling matrix element J_{eff} between lattice sites [Lig07], which can be tuned to zero or even negative depending on the modulation strength

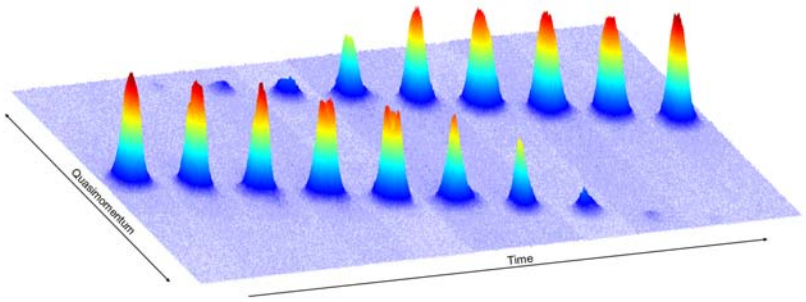

Fig. 1.1.: Time resolved imaging of Bloch oscillations of a non-interacting atomic BEC. The atoms are accelerated and Bragg-reflected when they reach the edge of the Brillouin-zone. Due to the finite momentum width of the atomic ensemble the reflection appears gradually. Here one Bloch cycle lasts $\sim 575\,\mu$s.

and frequency. This leads to the introduction of a complex tunneling matrix element and has drawn a lot of attention in the past few years, as corresponding models predict the possibility to drive phase transitions [Eck05b, Str11] and the creation of artificial gauge fields [Dal11].

1.2. Many-body physics in three-dimensional optical lattices

The BEC as macroscopic matter wave can be described by a single particle wave function, where the many-body aspect is reduced to a mean-field interaction term [Gro61, Pit61]. In contrast, ultracold atoms in optical lattices exhibit strong correlations due to the spatial confinement [Blo08]. In a pioneering experiment, Greiner *et al.* observed the quantum phase transition from a superfluid phase to a Mott insulator phase for bosons, where strong on-site interactions inhibit tunneling processes and therefore transport through the lattice [Gre02a]. Such a phase transition is predicted by the Hubbard model originating from solid state physics [Mot37, Hub63, Fis89]. For fermionic systems the appearance of a band insulator [Köh05] and more recently the phase transition between a metallic phase and the Mott insulating phase in three-dimensional lattices was observed [Sch08, Jör08]. Also mixtures of bosonic and fermionic atoms loaded into optical lattices have been realized [Gün06, Osp06c, Bes09], enabling the study of new exotic phases, for example boson-fermion pairing [Lew04].

The Hubbard model also governs the physics of particles in lower-dimensional lattice structures, and the phase transition between the superfluid and the Mott insulator has also been observed in one-dimensional [Stö04] and two-dimensional [Spi07] geometries. In the context of ultracold atoms, the Hubbard model can be

derived from microscopical considerations [Jak98] and can include the statistical properties of either bosons or fermions. The superfluid phase in the lattice is characterized by the existence of global phase coherence of the wavefunction, poissonian number fluctuations of the occupation number at a single lattice site and a continuous excitation spectrum. In the Mott insulator, the atoms are localized to the individual lattice sites, corresponding to local Fock states. No phase coherence between the lattice sites is present in this state, and the excitation spectrum is gapped, as the minimum excitation energy is given by the on-site interaction energy between two atoms.

The superfluid to Mott insulator phase transition for bosonic systems was detected by measurements of the reversal loss and recovery of coherence between the atoms across the sample [Gre02a], the appearance (and disappearance) of the excitation gap by applying a force gradient [Gre02a] and by amplitude modulation of the lattice depth [Stö04], and the direct imaging of the on-site number fluctuations in both regimes [Bak10, She10]. For fermionic systems, the suppression of doubly occupied sites and the incompressibility of the Mott insulator region [Sch08, Jör08] and again the gap in the excitation spectrum [Jör08] was observed. As an example, the loss and recovery of coherence between the atoms across the sample is directly observable with the standard time of flight technique as disappearance respectively reappearance of the interference pattern in momentum space for bosons as shown in figure 1.2.

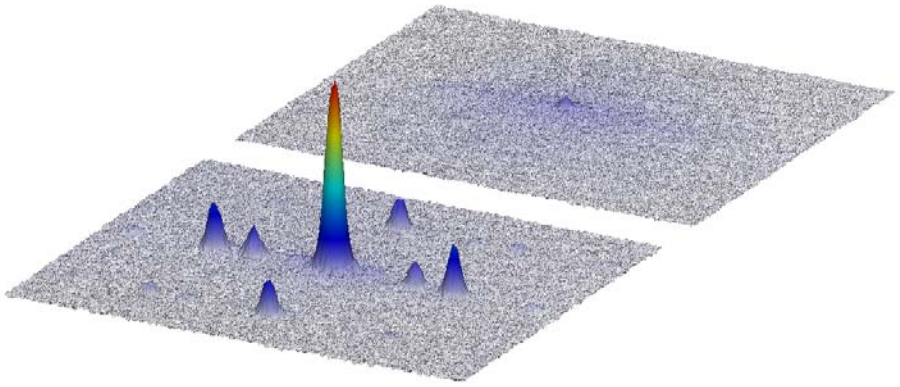

Fig. 1.2.: Quantum phase transition from a superfluid to a Mott insulator. Interference pattern in momentum space created by bosonic ultracold atoms in a three-dimensional lattice in the superfluid state (bottom left) and in the Mott insulator state (top right) imaged using the time of flight technique.

The importance of interactions in such systems was demonstrated with the preparation of long-lived repulsively bound pairs [Win06], which are 'bound' by repulsive interactions due to the fact that the pair cannot decay due to energy and momentum conservation. Especially for strong interactions or high lattice site occupancies the approximations of the Bose-Hubbard model break down, leading to important modifications in the energy gaps and the tunneling rates depending on the on-site particle number [Bus98, Sch09b, Joh09, Büc10]. First

indications of this modifications where observed by microwave spectroscopy of the Mott insulator shell structure [Cam06] and collapse and revival frequency measurements [Wil10], although these measurements were limited to the lattice occupancy as main variable parameter. A precise spectroscopy of the interaction modifications over a broad range of interaction strengths [Mar11b, Mar11c] verifies the exact numerical [Büc10] and renormalized analytical calculations [Sch09b].

Up to now, the experimental and most of the theoretical work concerning the Hubbard model for bosons was focused to the case of repulsive interactions, since for attractive interactions the ground state reduces to the situation where all atoms move on the same lattice site to minimize their energy, and three-body recombination processes would lead to a fast loss of atoms. Recent theoretical investigations in the regime of attractive interactions suggested that for large on-site three-body loss rates the effective loss from the system gets inhibited [Dal09]. This leads to an effective Bose-Hubbard model description with a local three-body hard-core constraint. Latest experimental progress [Mar11c] demonstrates the successful preparation of a metastable bosonic system with attractive interactions, and by spectroscopy of the three-body state indications of a suppression of three-body occupancy are observed. Such a state opens up new possibilities to create unusual and exciting quantum phases like a dimer superfluid [Die10], Pfaffian-like states in one-dimensional systems [Par07] or a stable superfluid condensate with negative temperature [Rap10].

The possibility to change practically all relevant parameters in such systems as a function of time enables the study of dynamical processes additionally to the groundstate properties. Paradigm examples are the collapse and revival of the coherent matter wave field when the system is quenched suddenly from the superfluid phase into the Mott insulator phase [Gre02b] or the other way around [Tuc06]. Also the transport of atoms happening across the phase transition was observed experimentally [Hun10]. Another fascinating idea is the realization of lattice geometries different to the standard simple cubic structure. Using a superlattice structure by means of an additional sublattice with half the lattice spacing of the original one along one direction, it is possible to realize double well structures in a massive parallel way. This enabled the direct observation of second order tunneling [Föl07], exchange [And07] and superexchange interactions [Tro08]. Recently hexagonal [SP11b] and triangular [Bec10] lattice structures were realized experimentally and used for the observation of twisted superfluid phases [SP11a] and frustrated classical magnetism [Str11].

Recently the realization of a quantum gas microscope [Bak09] opened the door to a new class of experiments. Through carefully designed optics it allows an in-situ detection of single atoms at their respective lattice sites and the same optics can be used to manipulate them on a single site level with optical fields [Wei11]. Using this technique it is possible to directly image the spatial structure across the superfluid to Mott insulator phase transition [Bak10, She10] and enabled the observation of correlated particle-hole pairs [End11] and antiferromagnetic spin chains [Sim11] in low-dimensional Mott insulators.

1.3. Ultracold molecules

Preparing and controlling ultracold molecules enables or improves a variety of fundamental studies in physics and chemistry [Doy04, Dul06, Fer09c, Sch09c], for example collisional studies and the investigation and control of chemical reactions [Wei99, Kre08, Dul09], precision measurements of fundamental constants [Chi09] and the measurement of the hypothetical electron electric dipole moment [Hud02]. For many of those studies the control of internal and external degrees of freedom at a single quantum level is necessary, which can be achieved by trapping a high phase-space density sample of the molecules of interest. Direct laser cooling, which was so successful in the case of atoms and ions, seems challenging in the case of molecules, as the internal vibrational and rotational level structure normally does not provide a closed optical cycling transition [Bah96]. Recent progress on this topic [Shu10] showed that for a certain class of molecules, which feature nearly closed transitions, this problem can be technically solved.

At present the preparation of molecules via association of ultracold atoms is the main path for the creation of high phase space density samples of ultracold molecules. This approach starts with ultracold atoms, which can be associated to molecules either by direct photoassociation [Wyn00, Jon06] or via magnetic field ramps using a Feshbach resonance [Don02, Köh06]. This methods preserve the already high phase space density of ultracold atoms, although it limits the variety of available molecules. Direct cooling and slowing of molecules [van08, Nar08, Mee09, Sch09c, Car09] would have the advantage of being applicable to a broad range of molecules, including some of high importance to life sciences and chemistry. The drawback of this method lies in the phase space density they are currently able to reach, which is far below usable values for quantum gas studies [Car09].

Pure samples of weakly bound ultracold molecules created via Feshbach association [Her03] allowed the detailed investigation of the molecular structure near threshold [Mar07a, Mar07b, Lan08a]. These molecules are typically created in highly excited rovibronic states, which, for a high density sample, leads to fast trap loss due to the high relaxation probability during collisions. This loss is highly suppressed if the molecule is build up of fermions as already mentioned, for many of the other configurations collisional stability can be assured when transferring the molecules into the rovibronic ground state in a controlled way [Żuc10]. Especially heteronuclear molecules [Osp06a] in the rovibronic ground-state are of high interest, as they exhibit a permanent electric dipole moment [Ni08] which introduces long range anisotropic dipole-dipole interactions.

The transfer from weakly bound molecules to deeply bound dimers is done using the Stimulated Rapid Adiabatic Passage (STIRAP) technique, which has been demonstrated between two adjacent vibrational levels with high efficiency using ultracold atoms [Win07]. For this measurement the molecules were prepared inside an optical lattice, where the association efficiency of doubly occupied sites using a magnetic field ramp over a Feshbach resonance can nearly reach unity [Tha06, Vol06] and the molecules reside in their motional state in

the lattice. The successful preparation of high phase-space density samples of deeply bound molecules [Dan08, Osp08] showed that the STIRAP technique is capable to perform a coherent transfer bridging energy differences of several tens of $h\times$ THz without significantly heating the sample.

Finally molecules in the rovibronic groundstate of the singlet and triplet potential of KRb [Ni08] in a dipole trap, of Rb_2 in the triplet potential [Lan08b] and the singlet potential of Cs_2 [Dan10b] in an optical lattice have been successfully produced. The demonstration of complete control of all internal and external degrees of freedom by preparing a BEC of rovibronic groundstate molecules [Jak02] is now within reach. Heteronuclear molecules in a lattice structure are supposed to give rise to novel quantum phases [Gór02], to allow the realization of quantum computation schemes [DeM02] and enable the simulation of quantum magnetism models [Bar06]. A promising candidate for this schemes, which is stable under binary collisions [Żuc10], is RbCs, where the creation of heteronuclear groundstate molecules is within reach [Deb11].

1.4. Physics of low-dimensional systems

Many physical properties are affected by the dimensionality of the system. For example, the well-known behavior of simple graphite changes drastically when it is reduced to a single atomic layer called graphene [Nov04, CN09] or to carbon nanotubes [Iij91, Cha07]. Effects due to reduced dimensionality provided by surfaces or crystalline layers inside bulk materials are believed to hold the key for the understanding of high temperature superconductivity [Leg06]. Also the effect of correlations and quantum fluctuations gets enhanced in such geometries. The direct investigation of these effects is rather challenging, as bulk materials offer in general little tunability, and the verification of simple theoretical models normally gets disturbed by lattice defects, phonons and other side effects. Ultracold atoms within optical lattices [Gre01] or high aspect ratio magnetic traps [Det01, Hof07] provide an ideal testing ground to implement those theoretical models, as they offer an almost perfect control over all relevant parameters.

A textbook example for such systems is the Tonks-Girardeau gas in one dimension, where bosons, for sufficiently strong repulsive interactions, build up strong correlations and their density distribution becomes, in the limit of infinite repulsive interactions, identical to the one of non-interacting fermions [Gir60]. Such a system has been prepared successfully in one-dimensional tubes created with optical lattices [Kin04, Par04, Hal09]. The correlation functions reflect the non-classical nature of such states and the local two-body and three-body correlation function in such a gas have been measured using photoassociation rates [Kin05] and three-body recombination processes [O'H04, Hal11]. Recently the direct observation of atom number fluctuations, which are heavily depending on the two-body correlation function, was realized [Jac11]. The time evolution in this regime can be described analytically and is therefore integrable, which has been demonstrated in a Newton's cradle experiment [Kin06].

Recently it was suggested to use the Tonks-Girardeau gas as starting point

to create a highly excited metastable state, the so-called super-Tonks-Girardeau gas [Bat05]. This state is characterized by attractive interactions and its density distribution is analog to fermions with repulsive long-range interactions, showing a power-law decay in the correlation function [Ast05]. The observation of this state [Hal09] was enabled by employing a confinement induced resonance [Ols98] to switch from strong repulsive to strong attractive interactions. Such scattering resonances are a direct consequence of the confinement used in the experimental realizations of one-dimensional systems and have been observed for various geometries [Hal10d, Lam10].

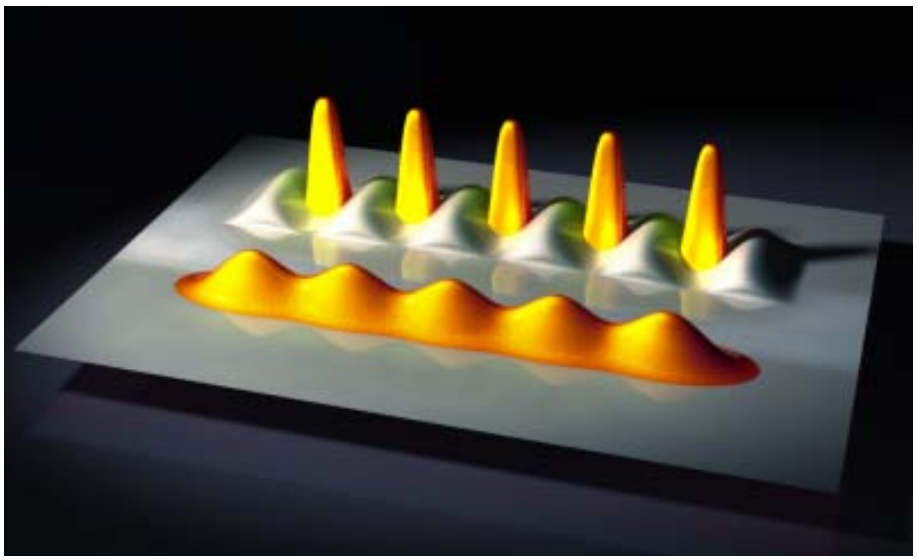

Fig. 1.3.: Sketch of the pinning quantum phase transition in a one-dimensional geometry. A weak lattice structure is enough to pin the already correlated atoms onto the lattice sites.

For the description of a one-dimensional system with a sufficiently deep lattice the standard Bose Hubbard model can be used, and the quantum phase transition between the superfluid and the Mott insulator state has been observed [Stö04]. For weak lattice structures the system has to be described by the sine-Gordon model [Gia03]. In such a system, for commensurate densities and strong interactions, an arbitrary weak lattice is sufficient to be in the Mott insulating state [Büc03]. This gives rise to a novel quantum phase transition, the so-called pinning transition, schematically shown in Figure 1.3. Here an arbitrary weak lattice induces the transition from the superfluid to the Mott insulating state. Evidence for this phase transition has been observed recently [Hal10c].

1.5. Overview

This thesis is built up of 14 publications, grouped thematically together in chapters. Each chapter includes another short introduction to the respective topic. A detailed description about the experimental setup in general is given in the

PhD thesis of Mattias Gustavsson [Gus08a] and the diploma thesis of Peter Unterwaditzer [Unt05], Anton Flir [Fli06] and Gabriel Rojas Kopeinig [Roj07].

Chapter 2 contains two publications with the main topic of this thesis, our results on the experimental investigation of a tunable quantum gas in a 3D optical lattice. We show that the standard Bose-Hubbard model fails for large interaction strength and we precisely measure the corresponding interaction shifts for two- and three-body states. By tuning interactions to strong attractive values, we prepare a metastable Mott-insulating state and find evidence that the metastability is supported by inhibited three-body recombination loss. Counterintuitively this reduced three-body recombination loss is a result of a highly increased three-body loss rate, which can be explained in terms of the quantum zeno effect.

Chapter 3 discusses our measurements of matter-wave dynamics in an one-dimensional optical lattice within three publications. We investigate the effect of interactions, force gradients and a modulation of the applied force onto Bloch oscillations, a phenomenon which occurs when a constant force acts on the atoms in the presence of a lattice structure.

Chapter 4 covers five publications about the creation and investigation of ultracold rovibronic groundstate molecules. These publications are also part of the PhD thesis of Johann Danzl [Dan10a]. We show our ability to transfer weakly bound dimers produced on a Feshbach resonance efficiently to the rovibronic groundstate within an optical lattice.

Chapter 5 shows our investigation of the behavior of a tunable quantum gas when confined to an one-dimensional geometry in the context of four publications. These publications are also part of the PhD thesis of Elmar Haller [Hal10a]. We see clear evidence for the existence of the Super Tonks-Girardeau gas, a metastable excited many-body system with attractive interactions, by employing a confinement induced resonance, which is investigated in more detail. Additionally we were able to observe a novel type of quantum phase transition in this geometry, and by measuring three-body recombination loss we determined the local three-body correlation function for strongly correlated 1D gases.

Chapter 6 gives a short outlook to the near future of the experiment, which will experience some major changes. Work on the extension to a mixture of potassium-cesium has already started, which will open up new possibilities and enable exciting experiments.

The following publications, here chronologically ordered, are included in this thesis:

1. Manfred J. Mark, Elmar Haller, Katharina Lauber, Johann G. Danzl, Alexander Janisch, Hans Peter Büchler, Andrew J. Daley, and Hanns-Christoph Nägerl *Preparation and spectroscopy of a metastable Mott insulator state with attractive interactions*, submitted for publication in Physical Review Letters (2012)

2. Elmar Haller, M. Rabie, Manfred J. Mark, Johann G. Danzl, Russell Hart, Katharina Lauber, Guido Pupillo, and Hanns-Christoph Nägerl, *Three-*

body correlation functions and recombination rates for bosons in three and one dimensions, Physical Review Letters **107**, 230404 (2011).

3. Manfred J. Mark, Elmar Haller, Katharina Lauber, Johann G. Danzl, Andrew J. Daley, and Hanns-Christoph Nägerl *Precision Measurements on a Tunable Mott Insulator of Ultracold Atoms*, Physical Review Letters **107**, 175301 (2011).

4. Manfred J. Mark, Elmar Haller, Johann G. Danzl, Katharina Lauber, Mattias Gustavsson, and Hanns-Christoph Nägerl, *Demonstration of the temporal matter-wave Talbot effect for trapped matter waves*, New Journal of Physics **13**, 085008 (2011).

5. Elmar Haller, Russell Hart, Manfred J. Mark, Johann G. Danzl, Lukas Reichsöllner, Mattias Gustavsson, Marcello Dalmonte, Guido Pupillo, and Hanns-Christoph Nägerl, *Pinning quantum phase transition for a Luttinger liquid of strongly interacting bosons*, Nature **466**, 597 (2010).

6. Mattias Gustavsson, Elmar Haller, Manfred J. Mark, Johann G. Danzl, Russell Hart, Andrew J. Daley, and Hanns-Christoph Nägerl, *Interference of interacting matter waves*, New Journal of Physics **12** 065029 (2010).

7. Elmar Haller, Russell Hart, Manfred J. Mark, Johann G. Danzl, Lukas Reichsöllner, and Hanns-Christoph Nägerl *Inducing Transport in a Dissipation-Free Lattice with Super Bloch Oscillations*, Physical Review Letters **104**, 200403 (2010).

8. Elmar Haller, Manfred J. Mark, Russell Hart, Johann G. Danzl, Lukas Reichsöllner, Vladimir Melezhik, Peter Schmelcher, and Hanns-Christoph Nägerl, *Confinement-induced resonances in low-dimensional quantum systems*, Physical Review Letters **104**, 153203 (2010).

9. Johann G. Danzl, Manfred J. Mark, Elmar Haller, Mattias Gustavsson, Russell Hart, Jesus Aldegunde, Jeremy M. Hutson, and Hanns-Christoph Nägerl *An ultracold, high-density sample of rovibronic ground-state molecules in an optical lattice*, Nature Physics **6**, 265 (2010).

10. Elmar Haller, Mattias Gustavsson, Manfred. J. Mark, Johann G. Danzl, Russell Hart, Guido Pupillo, and Hanns-Christoph Nägerl, *Realization of an Excited, Strongly-Correlated Quantum Gas Phase*, Science **325**, 1224 (2009).

11. Johann G. Danzl, Manfred J. Mark, Elmar Haller, Mattias Gustavsson, Russell Hart, Andreas Liem, Holger Zellmer, and Hanns-Christoph Nägerl, *Deeply bound ultracold molecules in an optical lattice*, New Journal of Physics **11**, 055036 (2010).

12. Johann G. Danzl, Manfred J. Mark, Elmar Haller, Mattias Gustavsson, Nadia Bouloufa, Olivier Dulieu, Helmut Ritsch, Russell Hart, and Hanns-Christoph Nägerl *Precision molecular spectroscopy for ground state transfer of molecular quantum gases*, Faraday Discussions **142**, 283 (2009).

13. Manfred J. Mark, Johann G. Danzl, Elmar Haller, Mattias Gustavsson, Nadia Bouloufa, Olivier Dulieu, Houssam Salami, Tom Bergeman, Helmut Ritsch, Russell Hart, and Hanns-Christoph Nägerl, *Dark resonances for ground-state transfer of molecular quantum gases*, Applied Physics B **95** 219 (2009).

14. Johann G. Danzl, Elmar Haller, Mattias Gustavsson, Manfred J. Mark, Russell Hart, Nadia Bouloufa, Olivier Dulieu, Helmut Ritsch, and Hanns-Christoph Nägerl *Quantum gas of deeply bound ground state molecules*, Science **321**, 1062 (2008).

1.6. Basic scattering properties of ultracold cesium

The description of elastic scattering processes between two particles in quantum mechanics is typically done via partial wave expansion. For very low scattering energies all partial waves except the s-wave can be neglected. Therefore, in the ultracold regime, it is possible to describe the scattering process with one single number: the s-wave scattering length a_{S}, which is defined through the phase shift $\delta(k_{\mathrm{dB}})$ between incoming and outgoing wave through $a_{\mathrm{S}} = \lim_{k_{\mathrm{dB}}\to 0} \tan\delta(k_{\mathrm{dB}})/k_{\mathrm{dB}}$. Here, $k_{\mathrm{dB}} = 2\pi/\lambda_{\mathrm{dB}}$ is the wavenumber and λ_{dB} the de Broglie wavelength of the particle. The scattering length concentrates all the short range details of the interatomic interactions into one single value and has a very simple interpretation: The magnitude gives the strength of the interaction and the sign defines the type of interaction, either repulsive (plus) or attractive (minus). It can also be viewed as length scale such that the scattering of particles with a_{S} gives the same scattering cross section as hard spheres with radius a_{S} [Lan77].

The scattering length depends on the short range details of the scattering potential, especially on molecular states near the scattering threshold energy, if the scattering state can couple to these molecular states. The molecular states can have different magnetic moments compared to the free atoms, which means that the energy of these states can be shifted relative to the scattering state by changing the magnitude of an applied magnetic field B. When the energy of a molecular state crosses the energy of the scattering state, a so-called Feshbach resonance appears and the scattering length diverges at this point. The width of such resonances in terms of magnetic field depends on the coupling strength between the molecular state and the scattering state, and the behavior of the scattering length around a resonance can be modeled analytically with

$$a_{\mathrm{S}}(B) = a_{\mathrm{bg}}\left(1 - \frac{\Delta}{B - B_0}\right) \tag{1.1}$$

where a_{bg} is the background scattering length far away from the Feshbach resonance, B_0 is the magnetic field position and Δ is the width of the resonance. A detailed review of Feshbach resonances in the context of ultracold gases is given in Ref. [Chi10].

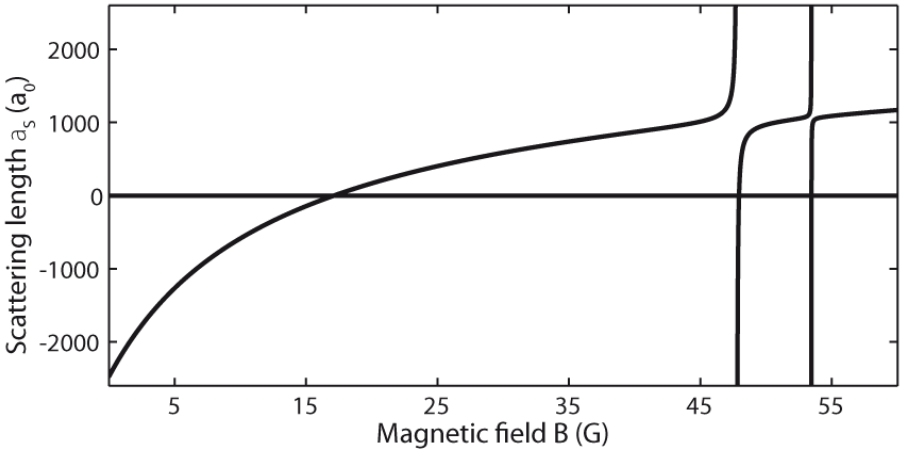

Fig. 1.4.: Tunability of ultracold cesium. Scattering length a_{S} of cesium in the lowest hyperfine state as a function of the magnetic field. The main curvature is caused by a broad Feshbach resonance located at $\sim -12\,\mathrm{G}$. Also visible are two medium Feshbach resonances at $\sim 48\,\mathrm{G}$ and $\sim 53\,\mathrm{G}$, where the 48 G resonance can be used to increase a_{S} up to $1500\,\mathrm{a_0}$ given our magnetic field stability. Not shown are several narrow Feshbach resonances at 19.9 G, 15 G, 14.3 G and 11 G. A detailed description about the calculation can be found in [Mar11a].

The details of the molecular state structure and of the coupling strengths depend on the atomic species, for example in the widely used rubidium 87 no Feshbach resonance occurs in the magnetically trappable state below 1000 G, therefore the scattering length in this region is constant with a value of $a_{\mathrm{S}} = 102\,\mathrm{a_0}$ [Wil10], where $\mathrm{a_0}$ is Bohr's radius. In contrast, cesium has a rich molecular structure near threshold, and due to the strong relativistic couplings several Feshbach resonances with different widths are accessible in the low-field region between 0 G and 60 G. Figure 1.4 shows the calculated scattering length as a function of the magnetic field for cesium in the lowest hyperfine state $|F = 3, m_F = 3>$. Within this region, a_{S} can be tuned continuously from $-2500\,\mathrm{a_0}$ up to $+1500\,\mathrm{a_0}$ with a precision of better than $1\,\mathrm{a_0}$ given by the typical magnetic field stability. Additional broad Feshbach resonances are available at higher magnetic fields and are currently used for a detailed investigation of the Efimov effect [Ber11]. Other bosonic species like potassium 39 [Roa07], lithium 7 [Kha02], sodium 23 [Ino98] or the other isotope of rubidium [Cor00] also have at least one Feshbach resonance at magnetic fields lower than 1000 G, but in comparison to cesium their continuous tuning range is more limited. A very important feature in figure 1.4 is the zero crossing of a_{S} at about 17 G, where the atoms are essentially non-interacting. At such a point effects arising from small magnetic dipole-dipole interactions [Fat08b] become accessible within experiments . Preparing a non-

interacting sample is particular interesting for atom interferometers [Gup02] or for the controlled investigation of interaction effects as we will show in chapter 3 in more detail.

Beside elastic scattering processes described in terms of the scattering length, inelastic scattering processes, which change the internal state of the atoms like the already mentioned spin-changing collisions, play an important role in experiments with ultracold atoms. Typically, the released energy in such inelastic scattering processes is magnitudes higher than the trapping potential and therefore they lead to immediate loss of the involved atoms. In our experiments, inelastic scattering of two atoms can be neglected since we prepare the atoms in the lowest hyperfine state and endothermic processes are highly suppressed in the ultracold regime. A scattering event involving three atoms is the next higher order process which has to be taken into account. This three-body scattering can lead to a three-body recombination process, where two atoms form a weakly bound molecule during the scattering event and the third atom leads to a decay of the molecule into a more deeply bound state. The released energy gets converted into kinetic energy of the molecule and the atom, ensuring energy and momentum conservation, and is sufficiently high that both particles are lost from the trap.

The three-body loss rate γ_3 can be described using the three-body loss rate coefficient L_3 and, in the universal regime where the scattering length is much larger than the van-der-Waals length $a_\mathrm{S} \gg l_\mathrm{vdW}$ [Köh06], is given by

$$\gamma_3 = \dot{N} = L_3 n^3 \quad , \quad L_3 = n_l C(a_\mathrm{S}) \frac{\hbar}{m} a_\mathrm{S}^4 \tag{1.2}$$

where m is the atomic mass, n the density, $\hbar$ Plank's constant, n_l the number of atoms lost in one three-body recombination process and C a dimensionless factor, which can be in principle a function of a_S [Web03b]. It has been shown that $C(a_\mathrm{S})$ and therefore also L_3 can exhibit a periodic resonant behavior when taking weakly bound Efimov three-body states [Efi70] into account, which has been verified experimentally by three-body loss measurements [Kra06, Zac09, Ber11]. In a simple picture, such an Efimov resonance occurs when the energy of the three-body state crosses the threshold energy of the three atoms scattering state, opening up an additional loss channel. There is also evidence for the existence of four-body states affecting the overall loss rate in terms of additional four-body resonances [von09, Fer09b]. A more detailed review about Efimov physics in ultracold atoms can be found in Ref. [Bra07, Fer11].

CHAPTER 2

MOTT INSULATOR WITH TUNABLE INTERACTIONS

2.1. Introduction

The description of atoms in optical lattices using delocalized Bloch states [Blo28] is most convenient in shallow lattices and when the atoms do not interact with each other. For deep lattices or non-negligible interactions, an alternative description using the tight binding approximation is more instructive. The Hubbard model [Hub63] describes the properties and dynamics of interacting particles in deep lattices using so-called Wannier functions, which are wavefunctions localized to individual lattice sites. These Wannier functions can be calculated by summing up all Bloch states of a specific band in a well defined manner [Koh59], equivalent to a basis transformation from Bloch states to Wannier states. Depending on the type of species, either the Bose-Hubbard or the Fermi-Hubbard model is used. Here, we restrict ourself to the bosonic case.

The Hamiltonian of the standard Bose-Hubbard (BH) model is surprisingly clear and concise, and an elementary derivation in the context of ultracold atoms can be found for example in Ref. [Jak05]. In brief, it is given by

$$\widehat{H} = -J \sum_{<i,j>} \widehat{a}_i^\dagger \widehat{a}_j + \sum_i \frac{U}{2} \widehat{n}_i \left(\widehat{n}_i - 1\right) + \sum_i \epsilon_i \widehat{n}_i, \tag{2.1}$$

where J denotes the tunneling rate between nearest neighboring lattice sites, U represents the interaction energy of two particles located at the same lattice site and ϵ_i is an energy offset at lattice site i due to an external potential. $\widehat{a}_i^\dagger$ and $\widehat{a}_i$ are the bosonic creation and annihilation operators for an atom at the lattice site i, and $\widehat{n}_i$ is the corresponding number operator. J and U can be calculated using overlap integrals of the corresponding Wannier functions. In the case of the standard BH model only the Wannier functions of the lowest Bloch band are taken into account. The properties of the groundstate of the system at zero temperature depend on the ratio between J and U. For $J/U \to \infty$ the atoms

tend to delocalize and form a superfluid, whereas for $J/U \to 0$ the atoms localize and create an insulating state, the so-called Mott insulator [Mot49]. In between, for a finite critical ratio $(J/U)_C$, a quantum phase transition between these two states occurs.

Figure 2.3 shows the calculated phase diagram of the BH model as a function of J/U and μ/U, where μ is the chemical potential. The height shows the mean atom number N per lattice site and the color indicates the amount of superfluidity, going from a complete superfluid state (bright green) to a fully localized state (dark blue). For large values of J/U the system is always in the superfluid state, which is characterized by phase coherence between different lattice sites and a superposition of number states at each lattice site given by the poissonian distribution of the mean density. For small values of J/U, insulating regions with constant integer density and without phase coherence between the lattice sites, so-called Mott lobes or Mott shells, appear. This calculation assumes a homogeneous system, the effect of an external harmonic confinement can be included by allowing for a spatial variance of the chemical potential, as indicated by the solid line at fixed J/U. The starting point is the local chemical potential in the trap center, and following the line gives the density when moving outwards from the trap center until the density reaches 0. This means that for finite J/U the system will have Mott insulating shells separated by superfluid regions.

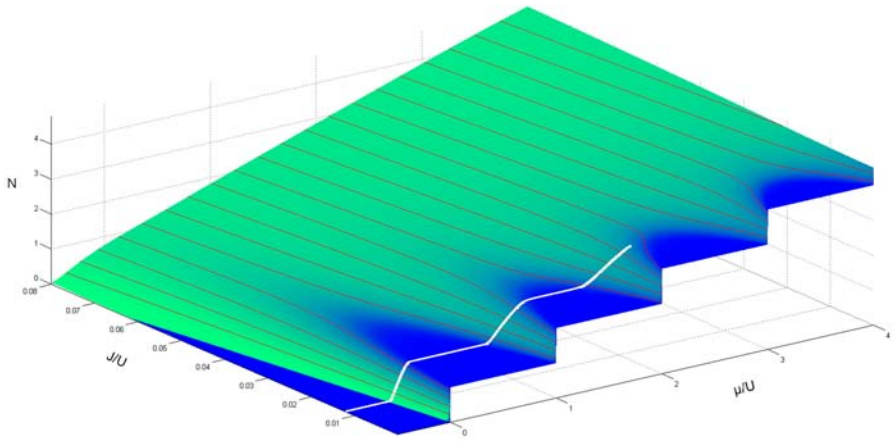

Fig. 2.1.: Calculated phase diagram of the Bose-Hubbard model in three dimensions with the mean particle density per lattice site as a function of J/U and μ/U. The color coding indicates the amount of superfluidity in the system, going from a superfluid state (bright green) to a fully localized state (dark blue). The solid line at constant J/U indicates the spatial density profile for a system in an external harmonic trap. The calculation is done via the Gutzwiller mean field approach [Kra92].

The experimental observation of the quantum phase transition between the superfluid phase and the Mott insulator phase by changing J/U in optical lattices for bosons [Gre02a] and fermions [Jör08, Sch08] triggered a tremendous amount of activities, both in theory and experiments. A recent highlight was

the realization of a quantum gas microscope, being able to image single atoms on individual lattice sites [Bak09], and the observation of this phase transition and the shell structure on a microscopic level [Bak10, She10].

The BH model gives a fairly accurate description of such systems as long as the on-site interaction energies are weak compared to the separation between the lowest and the first excited Bloch band. But what happens for a strongly interacting system, where these energies are comparable? In this context one has to be aware of the fact that the standard BH model relies on several approximations, which, for strong interactions, have to be reviewed in terms of validity. Some approximations like the neglection of nearest-neighbors interactions and next-nearest-neighbor tunneling are still valid. The restriction to the lowest Bloch band has to be omitted since the interaction can lead to a coupling between the different bands. In a simple picture the interaction between atoms on the same lattice site will modify the on-site wavefunction, for example repulsive interactions will lead to a broadening compared to the single particle Wannier function of the lowest Bloch band. This broadening can be expressed in terms of an admixture of higher band population. In the limit of infinite strong repulsive interactions two atoms will tend to avoid each other, and the wavefunction will evolve into the Wannier function of the first excited band. Also the treatment of interactions via a zero-range pseudopotential is in general not valid, instead it is necessary to use the fully regularized zero-range potential [Bus98]. To include these effects, one would have to expand the BH model to include higher bands, which would increase the complexity of the model drastically. To keep the simplicity of the standard BH model, it is possible to incorporate these effects by introducing a number-dependent interaction energy $U(\widehat{n}_i)$.

A similar problem, the calculation of the energy spectrum of two interacting atoms in a harmonic oscillator for all interaction strengths using the fully regularized zero-range potential, has been solved analytically [Bus98]. Using this solution, one is able to rescale it properly to derive the interaction energy $U(2)$ in a lattice, taking into account the anharmonicity at a lattice site [Sch09b]. Also the direct numerical calculation of $U(2)$ in the lattice by including higher bands and the fully regularized zero-range potential has been achieved [Büc10]. The interaction energy for three atoms at the same lattice site $U(3)$, specifically the correction to $U(2)$ as a function of the scattering length can be calculated in the framework of perturbation theory [Joh09] using effective three-body interactions, but the validity of this corrections only holds for weak interactions. In principle, also the tunneling rate J would have to be modified accordingly [Lüh11, Bis11]. Indications of this number-dependent change of the on-site interaction energy already have been observed [Cam06, Wil10], although these investigations were limited in scope since it was not possible to tune the interactions.

Up to now, the experimental and most of the theoretical work on the BH model was focused to the case of repulsive interactions, meaning a positive sign for the onsite interaction energy U. The BH model with attractive interactions did not draw that much attention, since the ground state in this case reduces to the situation where all atoms move on the same lattice site to minimize their

energy, and the three-body recombination loss in real systems would destroy the sample rather quickly. Counterintuitively, the situation changes drastically when the three-body loss rate γ_3 is much larger than all the other energy scales. It can be shown that the effective loss rate scales with J^2/γ_3 [Dal09], which means that for the limit where the three-body loss rate goes to infinity the actual loss from the system will be inhibited. This behavior can be connected to the quantum mechanical analogue of the Zeno effect[Win61, Mis77], where the continuous measurement of a state prevents its time evolution. Such a state would be stable against collapse and opens up possibilities to create unusual and exciting new quantum phases like a dimer superfluid [Die10], Pfaffian-like states in one-dimensional systems [Par07] or a stable superfluid condensate at finite momentum with negative temperature [Rap10].

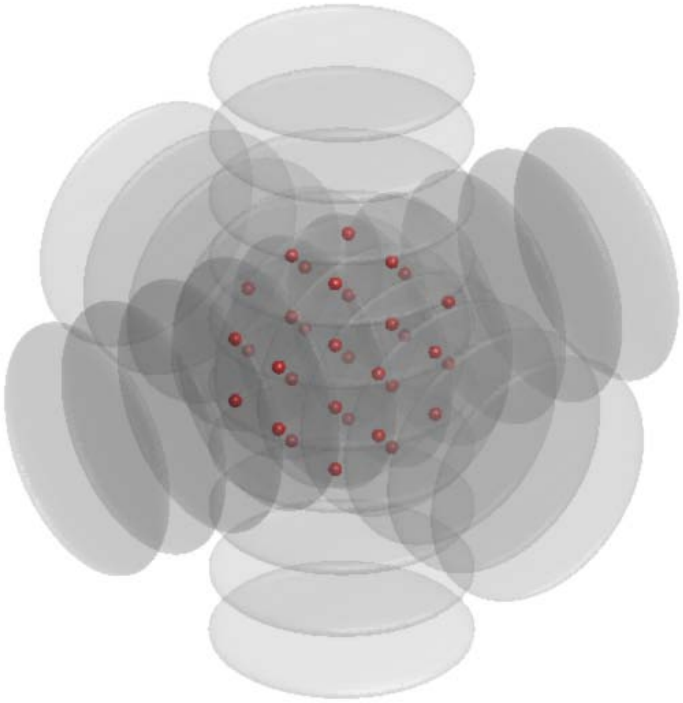

Fig. 2.2.: Experimental setup. Three retroreflected laser beams form a cubic lattice structure for the atoms, indicated by the red dots. The overall confinement is given by the Gaussian shape of the lattice beams and additionally by the initial dipole trap which can be independently tuned of the lattice depth.

In this chapter we investigate the properties of our sample of ultracold cesium atoms in a Mott insulating state. With our ability to tune interaction, we can reach the regime of strong repulsive interactions and, by ramping over the zero crossing of the scattering length, switch the sign of interactions and probe its behavior with attractive interactions. The experimental setup is illustrated in Figure 2.2. It consists of three retro-reflected laser beams, forming a 3D cubic optical lattice. The external confinement is given by the initial dipole trap

combined with the confinement caused by the lattice beams themselves. For our simulation of the BH model as given in equation 2.1, we can independently tune the tunneling rate J via the lattice depth, the onsite interaction energy U by changing the scattering length with the magnetic field and the distribution of the local energy offset ϵ_i with the strength of the external confinement.

Chapter 2.2 presents our investigation of the BH model for weak and strong repulsive interactions. First we characterize the superfluid to Mott insulator phase transition point as a function of the tunneling rate and interaction strength by measuring the coherence of the system through rapid release out of the lattice and imaging the interference pattern visible in momentum space using the time of flight technique. When changing the lattice depth while holding the interaction strength constant, a sudden drop of coherence at a critical lattice depth can be identified, indicating the phase transition. We map out the critical lattice depth as a function of the scattering length and see reasonably good agreement with the calculated values for the transition point from Quantum Monte Carlo simulations [CS07] and mean field calculations [Fis89].

A second signature for the Mott insulator phase beside the loss of coherence between lattice sites is the appearance of an excitation gap in contrast to the continuous excitation spectrum of a superfluid. A simple picture of the excitation mechanisms in a Mott insulator is given in figure 2.3. Localized atoms can only be excited by inducing tunneling events, for example within the singly occupied shell as illustrated in figure 2.3(b). The energy needed for the tunneling atom to hop onto the already singly occupied lattice site is given by the onsite interaction energy U. For the excitation process in figure 2.3(c) the energy difference is again U, whereas for the process in figure 2.3(d) $2U$ is needed. Since we choose the parameters of our preparation procedure such that we initially create only singly and doubly occupied sites, excitations at higher lattice site fillings are omitted.

A measurement of the excitation spectrum and thereby of the interaction energy U can be realized by monitoring the energy deposited into the system by amplitude modulation of the lattice depth for a given time. This amplitude modulation creates sidebands on the lattice light and enables two-photon Bragg transitions [Stö04] when the modulation frequency hits the corresponding energy needed for the tunneling process. We perform such modulation spectroscopy and map out the interaction energy U as a function of interaction strength from the weakly into the strongly interacting regime. As already discussed, one would expect that the interaction energy U gets number-dependent for strong interactions, which lifts the energetic degeneracy between excitations within the single occupied shell and excitations in the doubly occupied shell.

We observe this effect as splitting of the excitation resonance into two separate resonances for increasing interaction strengths. By additionally monitoring atom loss and the amount of doubly occupied sites, we are able to assign our resonances to the different excitation processes. Comparing our data to different theoretical models we can show that only the full calculation incorporating higher bands and the fully regularized pseudopotential [Sch09b, Büc10] is compatible with our data, whereas an approach that only includes higher bands [Lüh09] fails.

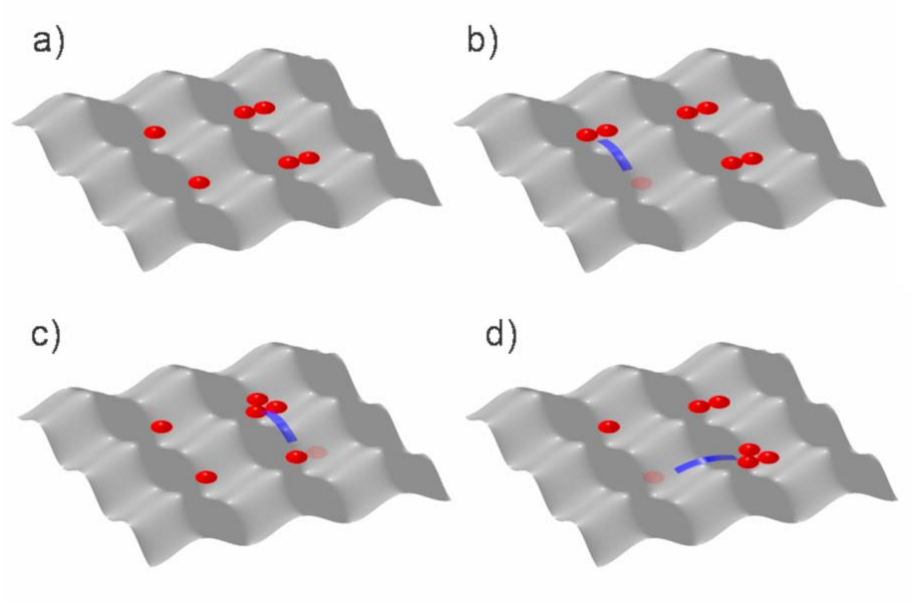

Fig. 2.3.: Excitation mechanisms in a Mott insulator. a) Schematic ground state of the system. The two lattice sites with a single atom illustrate the singly occupied shell, the others indicate the doubly occupied shell. b) Excitation through a tunneling event within the singly occupied shell. c) Excitation through a tunneling event within the doubly occupied shell. d) Excitation through a tunneling event from the singly occupied shell to the doubly occupied shell.

Chapter 2.3 extends these measurements to the attractive interaction region. For this we prepare a Mott insulator state with weak repulsive interactions and subsequently change the interactions to the desired attractive value on a timescale that is fast compared to the tunneling time, which ensures that no significant additional heating effects occur during the transfer. We observe that the system at attractive interactions remains stable on the order of seconds in both the total atom number and in terms of temperature, whereas for vanishing interactions the system shows significant heating and loss already after 50 ms. This clearly shows that the system is stabilized by attractive interactions and allows us to investigate the excitation spectrum in the same way as for repulsive interactions by modulation of the lattice depth.

We observe several excitation resonances and are able to connect them to excitations within the singly occupied shell and excitations in the doubly occupied shell, corresponding to the formation of two-body bound states and three-body bound states in the lowest Bloch band. Mapping out the dependence of the excitation resonances on the interaction strength, we see good agreement with the theoretical expectations for the two-body bound state. The three-body bound state excitation energies are deviating from both, the standard BH model prediction and the perturbation theory expectations [Joh09]. We are also able to identify a resonance showing an inverted behavior to the lowest Bloch band states, decreasing its frequency when increasing the attractive interaction strength. We

believe that the underlying excitation process creates atom pairs in the first excited two-body bound state, and the numerical calculations of the energy of this state [Büc10] show reasonable agreement for weak attractive interactions, whereas for strong attractive interactions a significant deviation is visible.

The resonance corresponding to excitations into three-body bound states shows another important feature, it rapidly decreases in strength and increases in width as we increase the interaction strength until it finally cannot be resolved anymore for the used experimental parameters. We interpret this behavior as signature of the inhibition of three-body loss [Dal09] caused by a rapidly increasing three-body recombination rate of three atoms at the same lattice site, which scales like a_S^4 [Kra06]. Such a system represents a BH model with a three-body constraint and can be used as starting state to realize exciting new quantum phases [Die10, Par07, Rap10]. Also a detailed investigation of the energy dependence of the three-body bound states with attractive interactions in a lattice seems worthwhile, as it could be that Efimov-related physics heavily influences these bound states, possibly allowing for example the observation of Efimov states or universal four-body states in the lattice.

2.2. Publication: Precision Measurements on a Tunable Mott Insulator of Ultracold Atoms

Physical Review Letters **107**, 175301 (2011)[†]

Manfred J. Mark[1], Elmar Haller[1], Katharina Lauber[1], Johann G. Danzl[1], Andrew J. Daley[2] and Hanns-Christoph Nägerl[1]

[1] *Institut für Experimentalphysik und Zentrum für Quantenphysik, Universität Innsbruck, Technikerstraße 25, A–6020 Innsbruck, Austria*

[2] *Department of Physics and Astronomy, University of Pittsburgh, Pittsburgh, PA 15260, USA*

We perform precision measurements on a Mott-insulator quantum state of ultracold atoms with tunable interactions. We probe the dependence of the superfluid-to-Mott-insulator transition on the interaction strength and explore the limits of the standard Bose-Hubbard model description. By tuning the on-site interaction energies to values comparable to the interband separation, we are able to quantitatively measure number-dependent shifts in the excitation spectrum caused by effective multi-body interactions.

[†]The author of the present thesis developed the experimental procedure, performed the measurements and made the data analysis for this publication with support from KL. The paper was written by MJM and HCN. All authors contributed to the paper writing and by general experimental and theoretical support.

2.2.1. Introduction

The observation of the superfluid-to-Mott-insulator transition in the context of ultracold atoms [Jak98, Gre02a] has triggered numerous activities both in theory and in experimental physics [Blo08]. It has become clear that ultracold gaseous systems confined to optical lattice potentials are capable of serving as bottom-up models for condensed matter phenomena [Jak05, Lew07, Blo08]. In addition, in view of unprecedented control and read-out capabilities [Bak10, She10, Wei11], there is justified hope that ultracold atomic and molecular systems will allow the implementation of quantum simulation schemes [Jan03, Bul09]. While there is tremendous progress for fermionic systems confined to optical lattices [Jör08, Sch08], most experiments have so far addressed the case of bosonic quantum gases and in particular the quantum phase transition from a superfluid to an insulating Mott state [Gre02a, Stö04, Cam06, Gem09, Cle09, Fuk09, Hal10c, Bak10, She10]. In this case, as long as the interaction can be treated as a weak perturbation, the system is described by the Bose-Hubbard (BH) model [Fis89]. One of the merits of ultracold atomic systems is the fact that all parameters of the BH model can be derived in a microscopic way [Jak98]. Nevertheless, recent theoretical [Lüh09, Joh09, Sch09b, Büc10] and experimental [Wil10] investigations have shown that already for comparatively weak interactions corrections to the standard BH model are needed.

In this Letter we use our capability to tune interaction energies to values comparable to the interband spacing and thereby leave the range of validity for the approximations of the standard BH model description - specifically, the restriction that only the lowest Bloch band in the lattice is occupied, and the treatment of interactions via the zero-range pseudopotential applied in the Born approximation. Using a Bose-Einstein condensate (BEC) of Cs atoms loaded into a 3D optical lattice potential we first investigate the superfluid-to-Mott-insulator transition and its dependence on the interaction strength. We precisely determine the on-site interaction energies including effective multi-body interaction shifts, demonstrating the breakdown of the standard approximations. Our results show good agreement with treatments beyond the BH model incorporating both higher bands and regularization of the pseudopotential.

2.2.2. The Bose Hubbard model

The standard BH model introduces two parameters to describe the dynamics of ultracold atoms in an optical lattice: the rate $J/\hbar$, which describes tunneling between neighboring lattice sites, and the energy U, which quantifies the interaction of atoms at the same lattice site. In the presence of weak external harmonic confinement the Hamiltonian reads

$$\widehat{H} = -J \sum_{<i,j>} \widehat{a}_i^\dagger \widehat{a}_j + \sum_i \frac{U}{2} \widehat{n}_i \left(\widehat{n}_i - 1\right) + \sum_i \epsilon_i \widehat{n}_i, \tag{2.2}$$

where $\widehat{a}_i^\dagger$ ($\widehat{a}_i$) are the bosonic creation (annihilation) operators at the i-th lattice site, $\widehat{n}_i = \widehat{a}_i^\dagger \widehat{a}_i$ is the number operator, and ϵ_i denotes the on-site energy shift due

to an external confinement. For small U/J the ground state at zero temperature is a superfluid (SF), whereas for large U/J and commensurate filling on-site interactions inhibit tunneling and the ground state is the Mott insulator (MI) of exponentially localized atoms. These limits are connected by a quantum phase transition. The transition point for a homogeneous system at unity filling can be calculated in a mean-field approach, giving $(U/J)_\mathrm{c} = 34.8$ in a 3D cubic lattice [Fis89], close to the quantum Monte-Carlo result $(U/J)_c \approx 29.3$ [CS07].

In the standard BH model, U and J are usually calculated from lowest-band Wannier functions [Jak98]. Two-body interactions can be described via a regularized zero-range pseudopotential, as the system is dilute, and relative momenta between atoms are small compared with scales determined by the range of the interaction potential [Tie00, Cas01]. For small values of the s-wave scattering length a_S, this pseudopotential is then replaced by a δ-function in the integrals that determine U (giving the Born approximation result). Under these approximations, the standard BH model was successfully used to describe a range of experiments with ultracold atoms in optical lattices [Gre02a, Blo08]. However, for sufficiently strong interactions the approximations break down. In a simple picture, two or more particles localized at a single lattice site with strong interactions tend to avoid each other and the on-site wave function increases in width to minimize the energy, resulting in coupling to higher Bloch bands. This admixture of higher bands results in number-dependent shifts for the on-site interaction energy, and the standard BH model may be modified to reproduce the new bound state energies [Büc10] by replacing U by a number-dependent term $U(n_i)$ [1][Lüh09, Joh09, Wil10]. However, care must be taken, as the replacement of the pseudopotential with a δ-function is in general not valid when including higher bands, and instead it is necessary to use the full regularized zero-range potential [Bus98]. Note that small modifications for U as a function of n_i are already visible for weak interactions but reasonably deep lattices [Cam06, Wil10].

The starting point for our experiment is a BEC without detectable non-condensed fraction of typically 1.0×10^5 Cs atoms in the energetically lowest hyperfine ground state confined by a crossed dipole trap. Atom cooling and trapping follow the procedures described in Ref. [Web03a, Kra04]. The cubic lattice is generated by three retro-reflected laser beams at a wavelength of $\lambda = 1064.5\,\mathrm{nm}$. With the given laser power the maximum lattice depth V_0 is $30\,E_\mathrm{R}$, where $E_\mathrm{R} = h^2/(2m\lambda^2)$ is the atomic recoil energy with the mass m of the Cs atom. The strength of interactions can be widely tuned as a_S depends strongly on magnetic field B (see 2.2.6 for suppl. material) due to multiple Feshbach resonances as illustrated in Fig. 2.4(a).

2.2.3. Superfluid to Mott insulator transition

We first probe the transition from the SF to the MI state as we vary the strength of interactions, using the standard interference-contrast technique [Gre02a]. We

[1]Note that the admixture of higher bands can also change tunneling rates.

gently load the BEC within 400 ms into the lattice (see 2.2.6 for suppl. material), hold the atoms for 10 ms, and then instantly switch off both the lattice and the external trap to determine the momentum distribution in a 50 ms time-of-flight (TOF). We determine the FWHM d of the central peak of the resulting interference pattern [Wes04] as shown in Fig. 2.4(b). As expected, d shows a strong dependence on V_0 (see Fig. 2.4(c)). We relate the onset of the MI phase to the abrupt kink in the data, corresponding to a critical depth V_C [2]. Fig. 2.4(d) shows V_C as a function of a_S. We find good agreement with the values for the calculated MI-transition points [CS07] for the case of a homogeneous system with integer density of one atom per lattice site. We note that in general our data on the set of transition points exhibits some dependence on the initial density. Therefore, we choose the density for this measurement such that for a given interaction strength the mean atom number per lattice site in the central region of the trap is near unity at the transition point.

2.2.4. Excitation spectrum

A second signature for the MI phase is the opening up of a gap and hence the appearance of distinct resonances in the excitation spectrum [Gre02a, Stö04, Cla06b, Kol06]. Here, we will find that the experiment deviates significantly from the results of the standard BH model and the associated approximations. Fig. 2.5(a) shows a typical spectrum when the system is deeply in the MI phase. Here the external confinement is chosen such that we create a $n = 2$ Mott shell in the central region of the lattice. We plot the BEC fraction [Nar98] after 150 ms of amplitude modulation (AM) at 20 % of V_0 and back-transfer into the initial dipole trap as a function of the AM frequency f_M. The BEC fraction is a sensitive indicator for temperature changes and hence for the amount of energy deposited into the system. The spectrum in Fig. 2.5(a), taken for comparatively weak interactions and low atom density, shows three characteristic peaks around the energies $U/2$, U and $2\,U$. The $U/2$ peak relates to a two-phonon transition, while the $2\,U$ peak corresponds to an excitation at the edge between the singly and doubly occupied shells [Cla06b, Kol06]. We have checked that defects in the singly occupied shell caused by residual thermal excitations make up a minor contribution to the $2U$ peak. Interestingly, when we take spectra like the one in Fig. 2.5(a), the peaks, in particular the one at U, are typically not well fit by symmetric gaussian functions. The reason for this will become evident below. Fig. 2.5 (b) plots the positions of the U and $2\,U$ resonances as a function of V_0 for $a_S = 212\,a_0$ and compares them to the results of the standard BH model. In general, the agreement is not satisfactory. For comparatively deep lattices (above $18\,E_R$) we measure a significant downshift for both the U and the $2\,U$ resonance. Near the transition point (here at $V_0 = 12\,E_R$) the $2\,U$ resonance is clearly upshifted. The latter can be understood when taking the spatially separated coexistence of the SF and MI phase into account, as for the SF part

[2] The critical depth V_C is identified as the intersection point of two linear functions that we add quadratically and fit to the data.

the maximal excitation probability lies energetically above the expected value for U and hence also for $2\,U$ [Cla06b, Kol06]. In the following, we will find an explanation for the downshift.

Fig. 2.5(c) shows an excitation spectrum as we increase the effect of interactions ($a_S = 320\,a_0$). Evidently, the resonance corresponding to U splits into two clearly visible but not yet fully resolved components. The resonance at $U/2$ develops a shoulder on the high-frequency side. The splitting becomes more pronounced for even higher values of a_S. A detailed excitation spectrum around U is shown in Fig. 2.6(a) for three different values for the initial density ($a_S = 427\,a_0$). The two components are now well separated from each other. Their strength depends in opposite ways on the initial density: The resonance at lower frequency (R_1) decreases in strength when the initial density is reduced and nearly disappears at low densities, whereas the resonance at higher frequency (R_2) increases in strength. We interpret this behavior in the following way: R_1 is caused by excitations in the doubly occupied Mott shell, whereas for R_2 singly occupied sites are excited. We also detect an increased atom loss in conjunction with R_1 as shown in Fig. 2.6(b). Evidently, this resonance corresponds to excitations of doubly into triply occupied sites, thereby leading to three-body atom loss [Web03b]. In Fig. 2.6(c) we plot the number of atoms at doubly occupied sites measured directly by associating them to molecules via a Feshbach resonance, removing the unpaired atoms, and detecting the remaining fraction of molecules n_M [Dan09a, Dan10b]. We observe a decrease of n_M at R_1 and an increase at R_2, in agreement with our interpretation for the origin of the two resonances. The width of resonance R_2 matches roughly the expected broadening caused by the external confinement, whereas for R_1 an additional broadening mechanism, probably related to fast three-body atom loss, has to be taken into account.

We map out the dependence of the resonances on the interaction strength by varying the magnetic field B from the point at about $B = 21\,\mathrm{G}$, where the two resonances start to split, to $B = 40\,\mathrm{G}$, spanning the range from $a_S \approx 200\,a_0$ to $a_S \approx 900\,a_0$ (see 2.2.6 for suppl. material). As the loading of the lattice at high values for a_S leads to considerable heating and loss, we ramp into the MI phase at $a_S = 400\,a_0$, set $V_0 = 20\,E_R$, and subsequently increase a_S to the desired value with a ramp speed of $5\,\mathrm{G/ms}$. Fig. 2.7(a) shows the frequencies for R_1 and R_2 and for the resonance at $2\,U$ as a function of a_S. Computing the number dependent energies $U(2)$ and $U(3)$ is non-trivial because of the anharmonicity of the lattice potential and the need to regularize the δ-function pseudopotential for the interactions. Values for $U(2)$ were calculated in Ref. [Büc10], and for our parameters are also well approximated by rescaling the exact result for two atoms in a harmonic trap [Bus98] to correct for anharmonicity, using the ratio of the Born approximation results for the lowest oscillator levels in our lattice and the harmonic trap [Sch09b, Men09, Gri09]. We plot the rescaled result from Ref. [Bus98] in Fig. 2.7(a) as the solid black line and see that it agrees well with our data for R_2. Note that an approach incorporating higher bands but not renormalizing the pseudopotential fails within our range of a_S values (see 2.2.6 for suppl. material). $U(3)$ can be estimated using the renormalized

perturbation theory of Ref. [Joh09]. This result is plotted as a dashed line in Fig. 2.7(a), and agrees well for small values of a_S. In order to reach larger values of a_S we would need to properly resum the perturbation expansion, which up to now is an open problem. Interestingly, we find that the function $3U(3)-2U(2) \approx U(2)/\left(1+1.34U(2)/(\hbar\omega)\right)$, with $\hbar\omega$ the band gap, equivalent at second order in $U(2)/(\hbar\omega)$ to the perturbation result, agrees well with our experimental data for R_1, as shown by the solid red line in Fig. 2.7(a). The same measurements and calculations for a lattice depth of $25\,E_R$ are shown in Fig. 2.7(b), and we see again good agreement between the calculations and our experimental data. For comparison we plot also the interaction energies calculated with the standard BH model as dotted lines. Remarkably, this basic calculation fits our data for $U(2)$ even at intermediate interaction strengths, due to opposing corrections that arise from including higher bands and regularizing the pseudopotential (see 2.2.6 for suppl. material).

2.2.5. Conclusion

We have investigated the SF-to-MI quantum phase transition and the MI phase over a large region of interaction strengths. For strong interactions, beyond single-band BH effects appear, leading to a splitting of the excitation resonances in the MI phase. Our precise measurements amount to a careful calibration of system parameters, including the scattering length over a wide range. The splitting of the excitation resonances can be used to manipulate the Mott shells independently, for example increasing the number of doubly occupied sites without loss due to excitation to triply occupied sites.

We are indebted to R. Grimm for generous support. We thank D. Boyanovsky, H. Büchler, P. Johnson, W. Niedenzu, and E. Tiesinga for fruitful discussions. We gratefully acknowledge funding by the Austrian Science Fund (FWF) within project I153-N16 and within the framework of the European Science Foundation (ESF) EuroQUASAR collective research project QuDeGPM.

2.2.6. Supplementary material

Corrections to the standard BH model

The standard application of the BH model to cold gas experiments involves calculating the two-particle onsite interaction energy using $U = 4\pi\hbar a_S/m \int w_0^4(\mathbf{r}) d^3r$, where $w_0(\mathbf{r})$ is the maximally localized Wannier function of the lowest Bloch band. This energy depends linearly on the scattering length a_S and is shown as a dotted line in Fig. 2.8. As the scattering length becomes larger, this energy can become comparable to the energy gap between Bloch Bands, and admixtures of higher bands must be taken into account. At the same time, the Born approximation which is implicit in this formula for U (which is equivalent to replacing a fully regularized zero-range pseudopotential with a δ-function) becomes invalid.

If we correct the value of U for the admixture of higher bands while using a δ-function potential, we obtain the dashed line in Fig. 2.8 as a function of a_S. To

compute these energies, we diagonalize the full Hamiltonian with a predefined number of higher bands included (four, in this case) and find the lowest energy eigenvalues. This correction decreases the onsite interaction energy significantly when compared to the standard BH model result. An exact result was found for two atoms in a harmonic potential interacting via the full regularized zero-range potential by Busch et al. [Bus98], and two-body bound state energies on a lattice were computed by Büchler [Büc10]. In the parameter regime in which we work, we can correct the Busch result for anharmonicity, rescaling it by the ratio of the Born approximation results for the lowest oscillator levels in the lattice and the harmonic trap [Sch09b]. The resulting energies agree with the bound state energies of Büchler [Büc10], and are plotted as the solid line in Fig. 2.8 as a function of a_S. These results remarkably coincide with the standard BH model calculation of U up to $\approx 700 a_0$, leading to the observation that the correction caused by using the full regularized zero-range potential almost cancels the correction caused by the admixture of higher bands in this parameter regime.

Loading the optical lattice

After evaporation the BEC is confined in a crossed optical dipole trap with typical trap frequencies of $\omega_{x,y,z} = 2\pi \times (15.0(2), 21.6(3), 15.5(2))$ Hz. The loading into the cubic lattice, consisting of three retro-reflected beams with a $1/e^2$ beam waist of $\approx 300\,\mu$m, is realized by exponentially ramping up the intensity of the lattice beams over the course of 400 ms with a time constant of 67 ms. Depending on the final lattice depth, the lattice beams themselves create an additional harmonic confinement of $2\pi \times 20$ Hz at our maximum lattice depth of $30\,E_R$. During lattice loading we can independently adjust the harmonic confinement of the crossed optical dipole trap to values up to $\omega_{x,y,z} = 2\pi \times (47.7(2), 68.4(3), 49.1(2))$ Hz using an exponential ramp for the power in each beam. For the shown experimental data we set the overall harmonic confinement to values between $\omega_{x,y,z} = 2\pi \times (22.1(2), 27.0(3), 22.5(2))$ Hz and $\omega_{x,y,z} = 2\pi \times (34.2(2), 46.3(3), 35.0(2))$ Hz, depending on the number of doubly occupied sites we want to create.

Conversion between magnetic field and scattering length

In Ref. [Lan09] the scattering length a_S was calculated from measurements of the binding energy of weakly bound dimers near the Feshbach resonances around 48 G and 53 G. For overlapping Feshbach resonances a_S can be parameterized via

$$\frac{a_S}{a_{bg}} = \prod_{i=1}^{N} \frac{B - B_i^*}{B - B_{0,i}},$$

where a_{bg} is the background scattering length, $B_{0,i}$ is the pole, and B_i^* is the zero crossing for the i-th Feshbach resonance. With a fit to the dimer data the

poles and zero crossings of three Feshbach resonances were determined, namely the narrow d-wave and g-wave resonances at 48 G and 53 G and the broad s-wave resonance at -11 G [Lan09]. In order to fit the result of the newest global multi-channel calculations for a_S in a range between 0 and 60 G [3], we somewhat modified the parameters of the s-wave Feshbach resonance, adapted a_{bg}, and added an auxiliary resonance to ensure a residual error of less then 1 a_0 over the whole region. The parameters that we use for the magnetic-field to scattering-length conversion are summarized in Table 2.1. We use $a_{bg} = 2476\, a_0$.

Table 2.1.: Parameters for the calculation of $a_S(B)$

Resonance	$B_i^*(G)$	$B_{0,i}(G)$
s-wave	17.148	-12.357
d-wave	47.944	47.780
g-wave	53.457	53.449
auxiliary	-90.68	-126.23

[3] The conversion between B and a_S is based on new data provided by P.S. Julienne and J.M. Hutson (private communication).

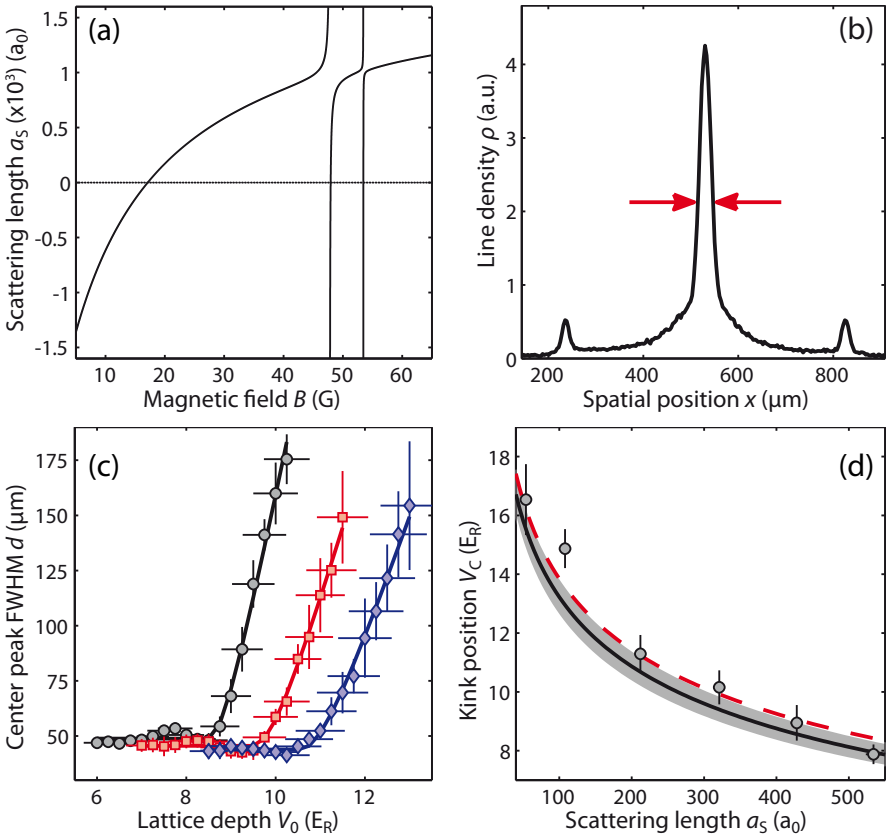

Fig. 2.4.: (color online) a) Scattering length a_S for Cs atoms in the lowest hyperfine ground state as a function of the magnetic field B (see 2.2.6 for suppl. material). b) Example of an integrated density profile of the BEC for 50 ms TOF. The arrows indicate the FWHM d. c) Center peak FWHM d as a function of lattice depth V_0 for $427\,a_0$ (circles), $320\,a_0$ (squares), and $212\,a_0$ (diamonds). The solid lines are fits from which the critical lattice depth V_C is determined. d) Critical depth V_C as a function of a_S. The solid (dashed) line corresponds to the transition points for the SF-to-MI transition given by the QMC (mean field) calculation $(U/J)_c = 29.3(34.8)$ [CS07] ([Fis89]), the shaded area indicates our uncertainty for V_0 for the QMC calculation.

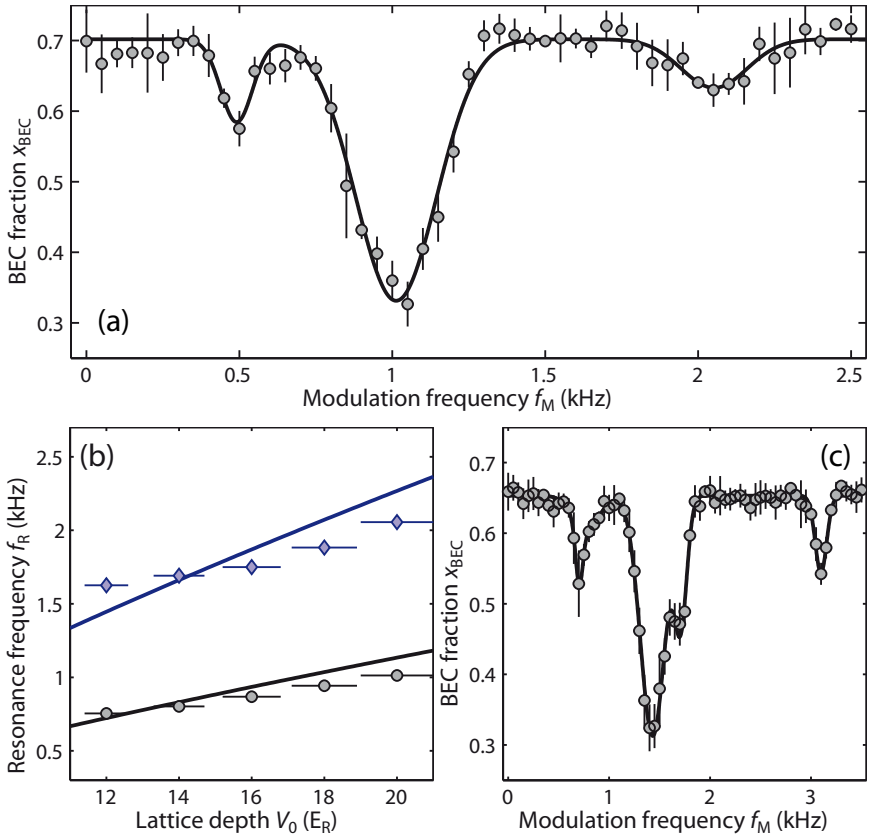

Fig. 2.5.: (color online) a) Excitation spectrum in the MI phase at $V_0 = 20\,E_\mathrm{R}$ and $a_\mathrm{S} = 212\,a_0$. The solid line is a triple gaussian fit. We take the resonance positions as the centers of the gaussian peaks. b) Frequency of the U resonance (circles) and the $2U$ resonance (diamonds) for various values of V_0 for $a_\mathrm{S} = 212\,a_0$. The solid lines are the calculated frequencies corresponding to $U(1)$ and $2\,U(1)$. At this value for a_S the transition point occurs at $\approx 12\,E_\mathrm{R}$. c) Excitation spectrum in the MI regime at $20\,E_\mathrm{R}$ and $a_\mathrm{S} = 320\,a_0$. The solid line is a five-peak gaussian fit.

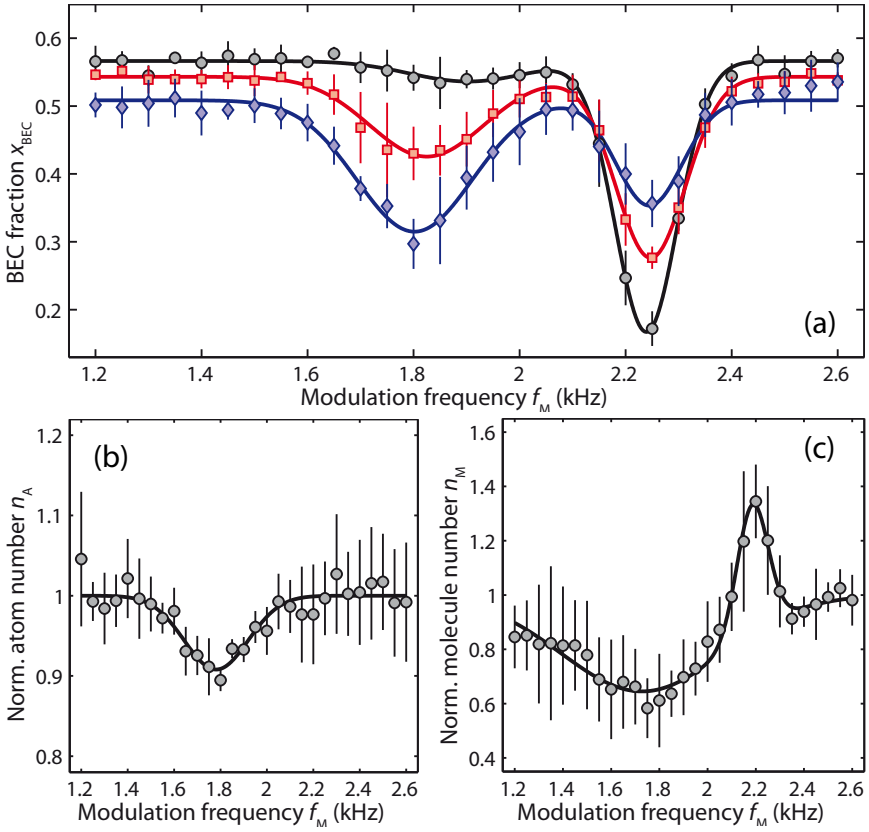

Fig. 2.6.: (color online) a) Detailed structure of the resonance near U for different values of the initial atom density at $a_S = 427\,a_0$ (low density, no double occupancy (circles), intermediate density, some double occupancy (squares), high density, high double occupancy (diamonds), for details see text). Every data point is the statistical average of five measurements, the error bars are the standard deviation. b) Remaining atom number n_A after AM at the same interaction strength as in a), normalized to n_A without AM. The solid line is a gaussian fit. c) Remaining molecule number n_M after AM at the same interaction strength as in a), normalized to n_M without AM. The solid line is a double gaussian fit.

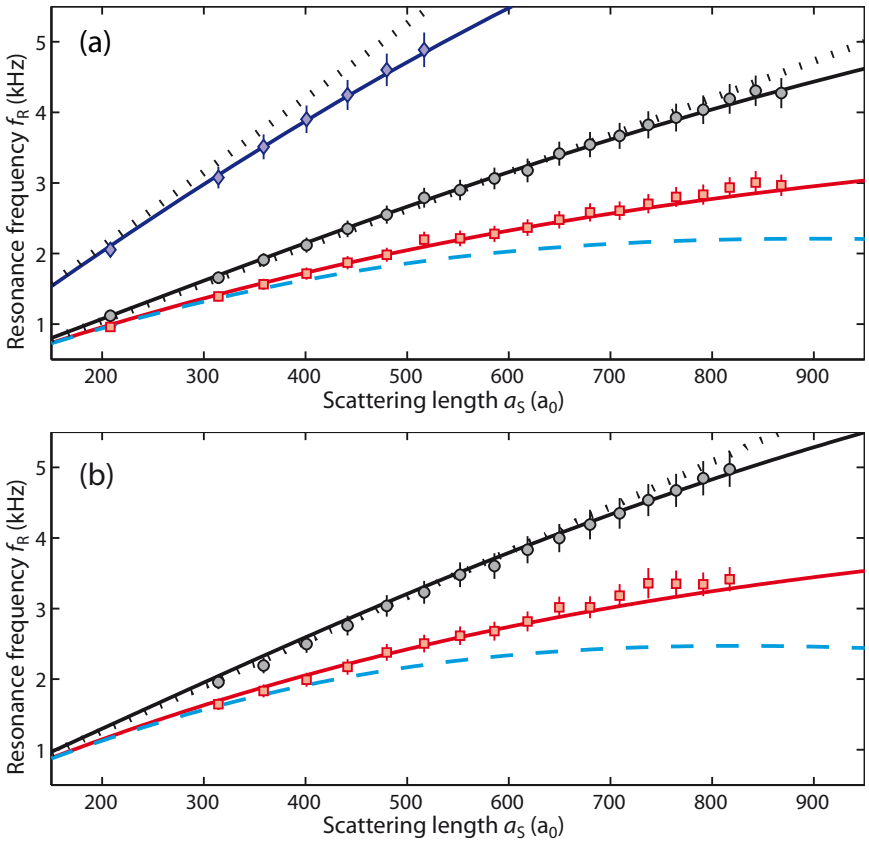

Fig. 2.7.: (color online) a) Frequency of the upper (R_2, circles) and lower (R_1, squares) resonance around U and of the resonance around $2U$ (diamonds) as a function of a_S for a lattice depth $V_0 = 20\,E_R$. The dotted lines are the calculated $U(1)/h$ and $2\,U(1)/h$ values from the standard BH model. The solid lines are the result of the more elaborate calculations for $U(2)/h$ and $3\,U(3)/h - 2\,U(2)/h$ (see text). The dashed line is the calculated $3\,U(3)/h - 2\,U(2)/h$ using the renormalized perturbation theory [Joh09]. b) Same as in a), but for $V_0 = 25\,E_R$.

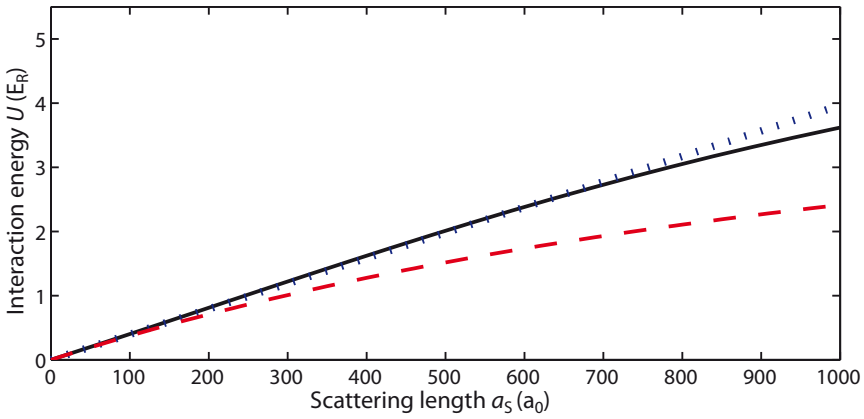

Fig. 2.8.: (color online) Calculated onsite interaction energy using different models. The dotted line shows the standard BH model result, and the dashed line shows the energy corrected by an admixture of higher bands. The solid line shows the exact result using the full regularized zero-range potential for two particles in a Harmonic trap, rescaled to correct for anharmonicity (see text).

2.3. Publication: Preparation and spectroscopy of a metastable Mott insulator state with attractive interactions

submitted for publication in Physical Review Letters (2012)†

Manfred J. Mark[1], Elmar Haller[1,2], Katharina Lauber[1], Johann G. Danzl[1], Alexander Janisch[3], Hans Peter Büchler[3], Andrew J. Daley[4], and Hanns-Christoph Nägerl[1]

[1]*Institut für Experimentalphysik und Zentrum für Quantenphysik, Universität Innsbruck, Technikerstraße 25, A–6020 Innsbruck, Austria*
[2]*Institut für Quantenoptik und Quanteninformation, Österreichische Akademie der Wissenschaften, 6020 Innsbruck, Austria*
[3]*Institut für Theoretische Physik III, Universität Stuttgart, Germany*
[4]*Department of Physics and Astronomy, University of Pittsburgh, Pittsburgh, PA 15260, USA*

We prepare and study a metastable attractive Mott insulator state formed with bosonic atoms in a three-dimensional optical lattice. Starting from a Mott insulator with Cs atoms at weak repulsive interactions, we use a magnetic Feshbach resonance to tune the interactions to large attractive values and produce a metastable state pinned by attractive interactions with a lifetime on the order of 10 seconds. We probe the (de-)excitation spectrum via lattice modulation spectroscopy, measuring the interaction dependence of two- and three-body bound state energies. As a result of increased on-site three-body loss we observe resonance broadening and suppression of tunneling processes that produce three-body occupation.

†The author of the present thesis developed the experimental procedure, performed the measurements and made the data analysis for this publication with support from KL. The paper was written by MJM and HCN. All authors contributed to the paper writing and by general experimental and theoretical support.

2.3.1. Introduction

Ultracold atomic gases in optical lattices provide a platform for investigating novel many-body dynamics in a highly controllable environment [Blo08]. Recent studies of the quantum phase transition between a superfluid and an insulating Mott state for bosons [Gre02a, Gem09, Fuk09, Bak10, She10] and the metal to insulator transition for fermions [Jör08, Sch08] exemplify the control available over these systems by tailoring the lattice potential, or tuning interparticle interactions using magnetic Feshbach resonances [Chi10]. This opens the door towards quantitative studies of phenomena that are not well understood in condensed matter physics, and also novel dynamics beyond what is normally realizable in solid state systems. Key examples of the latter include non-equilibrium dynamics such as transport processes [Hac10, Tro11], quenches across phase transitions [Che11b, Che11a, Kol07], and the potential to realize metastable many-body states that are long-lived on experimental timescales. For example, repulsively bound atom pairs can be formed in experiments [Win06, Str10] and are stable in optical lattice systems because of the lack of strong dissipative mechanisms such as lattice phonons that could remove energy on short timescales.

Here we prepare and study a novel metastable many-body state, specifically a metastable Mott insulator, in which particles are exponentially localized at individual sites through attractive two-body interactions. This state can be prepared via a sudden change in interparticle interactions, starting from a Mott insulator state with repulsive interactions, and then switching to attractive interactions abruptly on the tunneling timescale in the lattice. This is made possible by a broad Feshbach resonance for Cs atoms in the lowest hyperfine state [Chi04b]. We demonstrate that the resulting highly excited many-body state is long-lived, allowing for detailed studies of its properties. Using amplitude modulation (AM) of the optical lattice corresponding to two-photon Bragg transitions [Stö04], we measure the (de-)excitation spectrum. By identifying specific excitation resonances, we map out two-body bound state energies over a wide range of scattering lengths and make a quantitative comparison with the corresponding theoretical prediction [Büc10]. We also observe shifted resonances connected to three-body bound states [Joh09], which feature a fast broadening and strength reduction for increasing attractive interactions due to increasing three-body loss [Kra06]. This reduction in strength corresponds to an inhibition of tunneling events that create three-body occupation due to on-site loss processes, which promises interesting effects on the many-body physics of the system [Dal09].

The standard Bose-Hubbard (BH) model describes the dynamics of bosons in an optical lattice using the two-body on-site interaction energy U and the nearest neighbor tunneling rate J. There are two groundstates for zero temperature, the superfluid state for $U \ll J$ and the Mott insulator for $U \gg J$. Here we prepare a metastable Mott insulator state with attractive interactions ($U < 0$). This state is analogous to a standard bosonic Mott insulator with repulsive interactions, in that particles are exponentially localized at different lattice sites, and the state exhibits an energy gap due to inter-particle interactions. However, for $U < 0$

in a uniform system at unit filling, it is the most highly excited Hamiltonian eigenstate of the BH model in the limit $|U| \gg J$. The state is metastable on long timescales because of an energy gap of order U to lower lying eigenstates, and there are no fast dissipative mechanisms to remove this energy from the system. This is analogous to metastability in a gas of repulsively bound pairs [Win06, Str10] and the super-Tonks-Girardeau gas [Hal09]. The preparation of this highly excited system is realized by starting in a standard Mott insulator with $U > 0$, $U \gg J$, and then rapidly switching U to a large attractive value, on a timescale that is faster than h/J, but sufficiently slow to avoid population of higher Bloch bands.

2.3.2. Experimental procedure

We start with the production of an essentially pure Bose-Einstein condensate (BEC) of 1.0×10^5 Cs atoms in an optical dipole trap in the lowest hyperfine state following mainly the procedures detailed in Ref. [Kra04]. We load the BEC over the course of 500 ms into a cubic optical lattice created by three retro-reflected laser beams with a wavelength of $\lambda = 1064.5\,\mathrm{nm}$. The lattice depth V_0 for the measurements that follow is typically set to $V_0 = 20\,E_\mathrm{R}$, where $E_\mathrm{R} = h^2/(2m\lambda^2)$ is the atomic recoil energy with the mass m of the Cs atom. The scattering length a_S can be tuned in a range between $\approx -2500\,\mathrm{a_0}$ and $\approx 1500\,\mathrm{a_0}$ by applying a magnetic field B between 0 G and 48 G, employing a broad Feshbach resonance with pole at $\sim -12\,\mathrm{G}$ and a narrow resonance at $\sim 48\,\mathrm{G}$ [Lan09]. Here, $\mathrm{a_0}$ is Bohr's radius. The zero crossing for a_S is at 17.119 G. During loading of the lattice the interaction strength is set to $a_\mathrm{S} = +220\,\mathrm{a_0}$ to prepare an atomic Mott insulator state as the starting point for all subsequent measurements. The number of doubly occupied lattice sites can be controlled via the external confinement, which is primarily set by the dipole trap laser beams used for the initial BEC preparation.

2.3.3. Stability of the attractive Mott insulator state

To first investigate the stability of the many-body system with attractive interactions, we ramp B and therefore the interaction strength to the desired value with a ramp speed of 2.5 G/ms, wait for a variable hold time t_H and return to the initial interaction strength. Subsequently we ramp down the optical lattice and recapture the cloud of particles in the dipole trap. Using the time-of-flight technique, we deduce the number of remaining atoms N_A and the BEC fraction x_BEC. In the course of the ramps, we have to cross several narrow Feshbach resonances [Chi04b]. To avoid heating through interaction-induced band-transfer [Köh05], we cross the resonances using fast ramps with a speed of $2 \times 10^4\,\mathrm{G/ms}$ [Dan09a]. Figure 2.9(a) and (b) show x_BEC and N_A as a function of a_S for $t_\mathrm{H} = 50\,\mathrm{ms}$. Sharp dips for both observables occur near the expected locations of the narrow resonances. Also, around the zero crossing of a_S the system becomes unstable. An approximately 20% (10%) decrease for x_BEC (N_A) is observed for

$a_S < 0$ compared to the values at $a_S > 0$, probably caused by the crossing of the zero interaction region within a finite time. Figure 2.9(c) and (d) show x_{BEC} and N_A as a function of t_H for different values of a_S. As one would expect, x_{BEC} decays somewhat faster than N_A at given a_S. Exponential fits to the data yield lifetimes. These are reduced for more attractive interactions, but stay in the range of 10 to 20 seconds, more than 30 times larger than the bare tunneling time h/J at this lattice depth. This clearly shows that the system is stabilized by attractive interactions and allows us to investigate its properties in more detail.

2.3.4. Deexcitation spectrum

In this work we focus on the (de-)excitation spectrum [Gre02a, Stö04], which we measure by AM at frequency f_M of one of the lattice beams at typically 20 % of V_0 for a duration of $t_H = 300\,\text{ms}$. Tunneling processes at $U < 0$ to sites with non-zero occupation lower the overall energy and lead to a deexcitation of the system. The deexcitations - through the spatial configuration - are mapped onto excitations when returning subsequently to repulsive interactions, leading to an increased overall energy of the system, which we detect again by measuring x_{BEC} as a sensitive indicator for the energy deposited into the system. Figure 2.10(a) shows the measured excitation spectrum for $a_S = -306\,a_0$ in the vicinity of $|U|/h \approx 1.6\,\text{kHz}$ as calculated from the standard BH model. A double resonance structure can clearly be identified, similar to our previous work in the regime of strong repulsive interactions [Mar11b]. At comparatively low initial densities, with a small number of doubly occupied sites, the lower resonance is dominant, whereas for higher initial densities, giving a larger fraction of doubly occupied sites, the upper resonance becomes more pronounced at the expense of the lower resonance. As in the repulsive case, this splitting is caused by the energy difference for excitations in the different Mott shells through effective multibody interactions for three particles at the same lattice site [Joh09]. We associate the lower resonance with excitations in the singly occupied shell, creating doubly occupied sites, i. e. two-body bound states in the presence of the lattice, and the upper resonance with excitations in the doubly occupied shell, creating triply occupied sites, i. e. three-body bound states in the presence of the lattice. In contrast to the repulsive case [Mar11b] the three-body resonance is now at higher energies. Our interpretation is confirmed by a measurement of the number of doubly occupied sites through molecule formation [Dan09a]. Figure 2.10(b) shows the molecule number N_M as a function of f_M. For the lower resonance we find a greatly increased probability for dimer formation, which we attribute to an increase in the number of sites with double occupancy, while for the upper resonance we observe a strongly reduced probability for dimer formation, in agreement with the fact that doubly occupied sites are resonantly emptied upon modulation and that particles at triply occupied sites are lost due to fast three-body recombination at negative a_S [Kra06].

Figure 2.10(c) shows excitation spectra taken over a comparatively large fre-

quency range as a_S is varied from $-112\,a_0$ to $-2334\,a_0$. The resonance discussed above corresponding to the excitation into the two-body bound state is clearly visible and it is shifted to higher frequencies as $|a_S|$ is increased, as one would expect. The three-body resonance is only visible for weak interaction strengths. It also shifts to higher frequencies, as expected. We will discuss the behavior of this resonance below. Interestingly, we observe another resonance with an inverse behavior compared to the two-body and three-body resonances, with decreasing frequency as $|a_S|$ increases. We observe an additional resonance at twice the frequency with the same behavior, visible in the spectra taken for strong interactions. These resonances do not disappear when we prepare a purely singly-occupied Mott insulator. We therefore suspect that they are related to excitations into the first excited two-body bound state of the lattice [Büc10]. The strong visibility of the half-frequency resonance most likely is a result of the presence of the first harmonic in the frequency spectrum of J, which for our parameters reaches a strength of up to 20 % of the main frequency component (see 2.3.8 for suppl. material).

2.3.5. Comparison to theory

Figure 2.11 provides an overview over the measured excitation energies ΔE as a_S is varied and compares our data to the prediction by theory [Büc10, Mar11b]. The three relevant excitation processes are illustrated in the inset to this figure. We determine $\Delta E = h f_{M,c}$ by fitting simple gaussians to the loss features as shown in Figure 2.10(a) and taking the peak positions $f_{M,c}$. The data for repulsive interactions ($a_S > 0$) is taken from Ref. [Mar11b], augmented by new measurements at strong repulsive interactions ($a_S > 1000\,a_0$). In general, we find good agreement between our measurements and the calculated energies for the excitations to the lowest-band two-body bound state using the exact numerical results [Büc10] (see 2.3.8 for suppl. material), and the fitting function described in Ref. [Mar11b], which extrapolates the result for the three-body resonance from Ref. [Büc10]. Only for comparatively strongly attractive interactions do we find a significant deviation for the energy of the three-body bound state, which is expected due to more complex three-body physics arising at negative values for the scattering length [4]. The excitation energies into the first excited two-body bound states, derived by doubling the measured frequency values, show the same qualitative behavior as the exact numerical calculations [Büc10] (see 2.3.8 for suppl. material), though with a significant offset for strong attractive interactions. Note that the exact numerical analysis is only valid for two particles or a very dilute system, and does not include the influence of a Mott insulating background. Its contribution will increase for stronger particle interactions and might account for the offset observed. Also, we are not able to completely exclude the possibility of a systematic deviation in the calculation of a_S in this magnetic field region.

[4] J. von Stecher, private communication

2.3.6. Supression of three-body occupation

Detailed spectra with the three-body bound state excitation resonance for attractive interactions are shown in Fig. 2.12(a). Compared to the two-body bound-state resonance at lower frequencies, we clearly observe a broadening of the three-body resonance as a_S is increased. In fact, the resonance broadens so much that it finally disappears. Given our finite signal-to-noise ratio, we are not able to detect the resonance for $|a_S| > 500\,a_0$. Fig. 2.12(b) shows the width (FWHM) as a function of a_S. We note that, as there is currently no theory on the lineshapes of three-body resonances, the FWHM is obtained from simple gaussian fits as used above. The broadening leads to a decrease in the height of the resonance, i.e., a decrease in the formation rate of triply-occupied sites, and thus to a decrease in the overall loss rate. We interpret this behavior in terms of the process discussed in Ref. [Dal09]: Fast three-body loss can suppress the formation of triply occupied sites, analogous to the suppression of inelastic two-body processes as reported in Ref. [Sya08] for the case of weakly-bound molecules. As the three-body recombination rate scales like $\dot{N} \sim a_S^4 n^3$ with the density n, one would expect a strong increase of the three-body loss rate. We note that for repulsive interactions a similar broadening of the three-body bound-state excitation resonance can be observed. This is shown in Figure 2.12(c). In this case the increase of the FWHM as a function of a_S is far less drastic. Further experimental and theoretical investigations will be needed for a quantitative analysis of the broadening, including a calculation of the modified on-site density of three-body bound states and the corresponding tunneling rates at attractive and repulsive interactions and the role of Efimov physics in confined dimensions [Por11].

2.3.7. Conclusion

In summary we have investigated a metastable Mott insulating state with attractive interactions and have shown that this state exhibits a very long lifetime on the order of 10 seconds. By measuring excitation spectra we were able to determine the energies of two-body and three-body bound states. The broadening of the excitation resonance corresponding to the three-body bound state gives a strong indication that very high three-body recombination rates suppress the creation of triply occupied sites, thereby reducing the effective loss rate of the system, which also can be interpreted in terms of the quantum Zeno effect [Mis77] with the three-body recombination rate playing the role of the measurement. This effect can be used to realize a Bose-Hubbard model with a three-body hard-core constraint [Dal09], leading to interesting many-body physics, including a dimer superfluid phase and a continuous supersolid phase for attractive bosons [Die10, Bon11], the realization of Pfaffian-like states in one-dimensional geometries [Par07], and the stabilization of an atomic color superfluid for fermions [Kan09]. The Mott insulating state with attractive interactions can also serve as starting point for the preparation of stable superfluid condensates at finite momentum with negative temperature [Rap10].

We are indebted to R. Grimm for generous support. We thank J. von Stecher, P. Johnson, and E. Tiesinga for fruitful discussions. We gratefully acknowledge funding by the Austrian Science Fund (FWF) within project I153-N16 and within the framework of the European Science Foundation (ESF) EuroQUASAR collective research project QuDeGPM.

2.3.8. Supplementary material

Modifications and frequency components of U and J during amplitude modulation

A sinusoidal modulation of the lattice depth leads to a modulation in both U and J. Excitations are driven mainly by the modulation of J [Cla06b]. To characterize this process in a first approximation, we write the lattice depth modulation as $V(t) = V_0(1 + M\sin(\omega_\mathrm{M}\, t))$ with $\omega_\mathrm{M} = 2\pi f_\mathrm{M}$ and numerically calculate $U(t)$ and $J(t)$ for each time step using tunneling rates and Wannier functions for the lowest Bloch band. Here, we do not include the modification of U and J arising for stronger interactions. To derive the frequency components of $J(t)$, we Fourier transform $J(t)$, omit the DC part and normalize the strength of the frequency components to the peak strength at the main frequency ω_M. Due to the nonlinear dependence of J on V_0, higher harmonics at $2\omega_\mathrm{M}$ and $3\omega_\mathrm{M}$ are visible, and their strength as a function of the modulation depth M is shown in figure 2.13(a) for three different values of the lattice depth V_0. For our experimental parameters ($V_0 = 20\,\mathrm{E_R}$, $M = 20\,\%$) the $2\omega_\mathrm{M}$ component reaches 20 % peak strength of the main frequency peak, whereas the $3\omega_\mathrm{M}$ component stays below 3 %. This explains the good visibility of the half-frequency resonance into the first excited two-body bound state. Note that a half-frequency resonance is also present for the lowest two-body bound state as shown in Ref. [Mar11b]. The weak $3\omega_\mathrm{M}$ component would give rise to a further resonance, which, however, is not observable given the finite signal-to-noise ratio for our experiment.

Due to the nonlinearity of J and U as a function of V_0 the corresponding time averaged values during the modulation are different from the values that one obtains assuming no modulation. Figure 2.13(b) shows the relative change of the time averaged $\langle U\rangle$ and $\langle J\rangle$ as a function of M for three different values of V_0. The shift of U by less than 0.5 % is nearly independent of V_0 and can be neglected in view of the uncertainties in our experiment. The shift of J is more pronounced, but it does not affect the experimental results on the measurement of interaction energies. Nonetheless, this effect has to be taken into account for a future investigation of modulation-assisted tunneling rates, additionally to the changes due to modifications in the on-site wave functions arising from interactions [Lüh11].

Numerical analysis of the two-particle bound states

The numerically efficient and precise determination of the attractive and repulsive bound state energies for two particles in a three-dimensional optical lattice

has been presented in Ref. [Büc10]. Here, we use this method for the comparison with the experimental data; the notation is in analogy to Ref. [Büc10]. Within the two channel description of the short range pseudo-potential, the s-wave scattering length a_S is related to the detuning ν of the molecular channel, and the coupling g via $4\pi\hbar^2 a_S/m = -g^2/\nu$. The influence of the optical lattice is a shift $\chi(E)$ in the detuning and is associated with a change of the free particle properties due to the formation of Bloch bands. The relation between the bound state energies E_{bs} and the shift $\chi(E)$ in the detuning takes the form $\chi(E_{bs}) = -\pi a/(8E_R a_S)$ with a the lattice spacing. The numerical determination of $\chi(E)$ involves the precise determination of Bloch wave functions and band energies, as well as a summation over a high number of Bloch bands. In addition, it requires a regularization of the coupling between the open and closed channel. Here, we choose the regularization $\alpha(\mathbf{r}) = \int_{v(\Lambda)} d\mathbf{k} \exp(i\mathbf{kr})/(2\pi)^3$, where the volume $v(\Lambda) = \Lambda^3 v_0$ is centered around $\mathbf{k} = 0$ with $v_0 = (2\pi)^3/a^3$ the volume of the first Brillouin zone. For fixed cut-off Λ, the summation over Bloch bands converges very quickly for $S > \Lambda$, see inset to Fig. 2.14; the shell parameter S denotes the number of Bloch bands for each spatial direction included in the summation. Finally, we can remove the cut-off Λ via the asymptotic scaling relation $\chi_\Lambda(E) = c/\Lambda + \chi(E)$ [5], see Fig. 2.14. The convergence of the numerical data is checked by varying the shell parameter S, cut-off Λ, and the precision for the determination of the Bloch wave functions and Bloch bands.

Using the above procedure, the repulsive and attractive bound states are determined for the experimentally relevant parameters with $V_0 = 20E_R$. The lowest bound state for weak interactions is dominated by the contributions of two particles in the lowest Bloch band, and for increasing interactions smoothly connects to the state with a single bound molecule of mass $2m$ within the lowest Bloch band of an optical lattice with strength $2V_0$. In turn, the first excited bound state corresponds for weak interactions to a state with one particle in the lowest Bloch band and the second particle in the first excited Bloch band. Again for increasing interactions, this state smoothly connects to a single molecule in the first excited Bloch band.

[5] Note that the numerical data in the original manuscript was based on an incorrect assumption on the cut-off function, and an Erratum is in preparation.

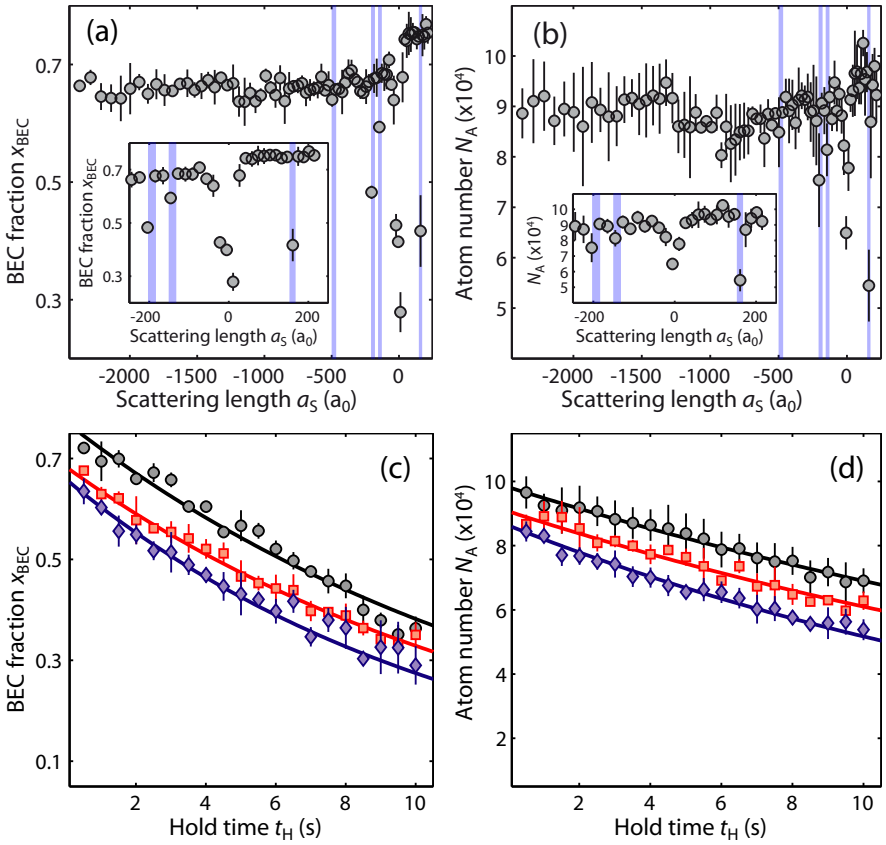

Fig. 2.9.: (color online) Stability of the many-body system for attractive interactions a) BEC fraction x_{BEC} as a function of a_{S} with $t_{\mathrm{H}} = 50\,\mathrm{ms}$. The narrow shaded areas indicate the locations of Feshbach resonances. The inset shows the region around $a_{\mathrm{S}} = 0\,\mathrm{a_0}$. b) Number of remaining atoms N_{A} as a function of a_{S} with the same settings as in a). c) x_{BEC} as a function of t_{H} for $a_{\mathrm{S}} = +220\,\mathrm{a_0}$ (circles), $a_{\mathrm{S}} = -240\,\mathrm{a_0}$ (squares) and $a_{\mathrm{S}} = -2000\,\mathrm{a_0}$ (diamonds). The solid lines are exponential fits giving $1/e$-decay times of $14.2 \pm 0.6\,\mathrm{s}$ ($+220\,\mathrm{a_0}$), $13.7 \pm 0.6\,\mathrm{s}$ ($-240\,\mathrm{a_0}$) and $11.4 \pm 0.4\,\mathrm{s}$ ($-2000\,\mathrm{a_0}$). d) N_{A} as a function of t_{H} for the same settings as in c). The solid lines are exponential fits giving decay times of $28.3 \pm 0.9\,\mathrm{s}$ ($+220\,\mathrm{a_0}$), $25.2 \pm 1.8\,\mathrm{s}$ ($-240\,\mathrm{a_0}$) and $19.5 \pm 0.5\,\mathrm{s}$ ($-2000\,\mathrm{a_0}$). The vertical error bars reflect the one-sigma statistical error.

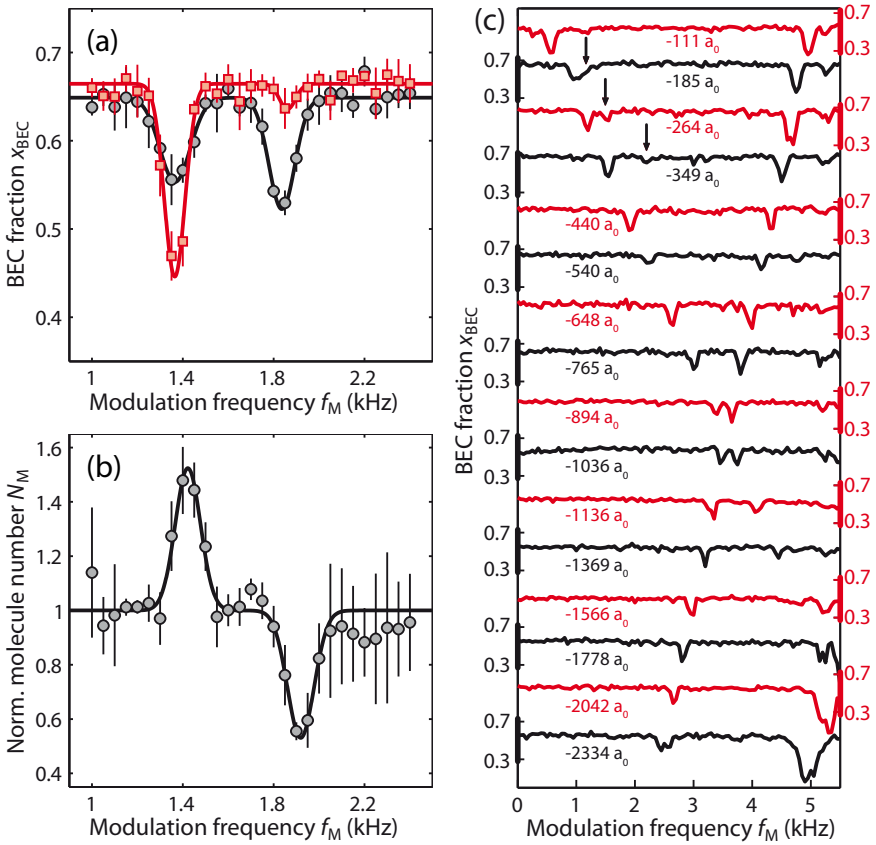

Fig. 2.10.: (color online) Excitation spectrum for a Mott insulating state with attractive interactions a) BEC fraction x_{BEC} as a function of f_{M} for high (low) initial density shown as circles (squares) at $a_{\mathrm{S}} = -306\,\mathrm{a}_0$. The solid lines are double Gaussian fits. b) Normalized molecule number N_{M} as a function of f_{M} at $a_{\mathrm{S}} = -306\,\mathrm{a}_0$. The vertical error bars reflect the one-sigma statistical error. c) Set of excitation spectra with x_{BEC} as a function of f_{M} as a_{S} is varied: $a_{\mathrm{S}} = -111\,\mathrm{a}_0$ (top) to $a_{\mathrm{S}} = -2334\,\mathrm{a}_0$ (bottom). The three-body resonance is indicated by an arrow.

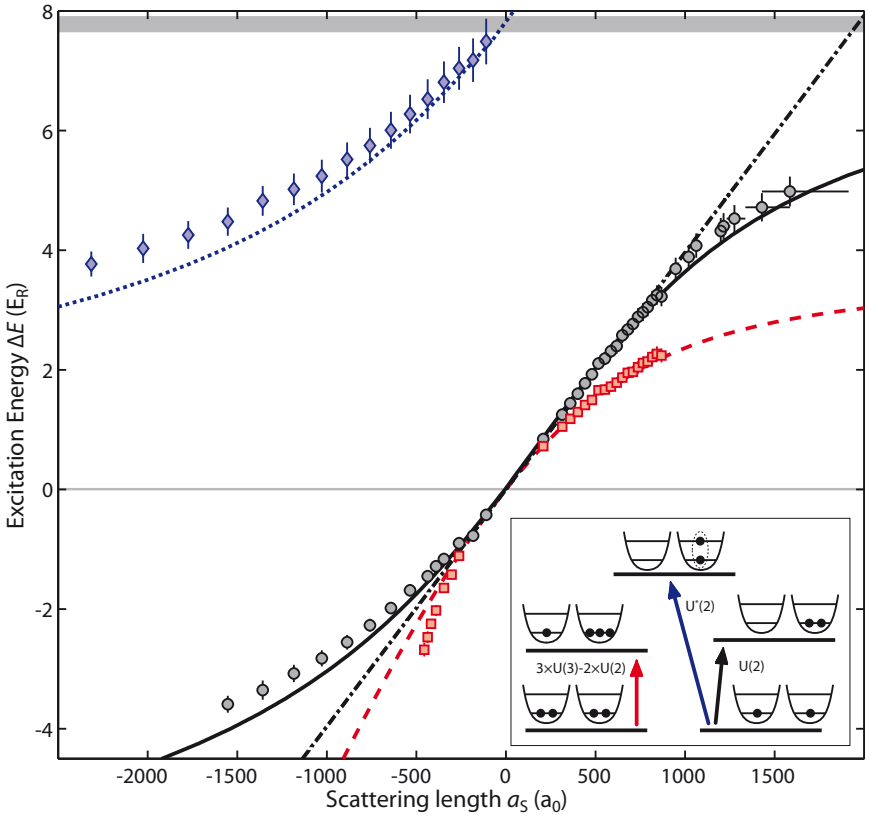

Fig. 2.11.: (color online) Excitation energies ΔE into two- and three-body bound states. Two-body bound state excitation energy (circles), three-body bound state excitation energy (squares), and first excited two-body bound state excitation energy (diamonds, obtained by doubling the measured values) are shown as a function of a_S. We have added to the plot the data for $a_S > 0$ from Ref. [Mar11b], augmented by new measurements for $a_S > 1000\,a_0$. The shaded areas at the top indicate the first two single-particle bands. The solid (dashed) line is the calculated excitation energies for the two-body (three-body) bound state and the dotted line is the calculated excitation energy for the first excited two-body bound state. The dashed-dotted line is the standard BH model calculation. The vertical error bars reflect the one-sigma statistical error as derived from the gaussian fit. The horizontal error bars indicate the variation of a_S over the cloud due to the gradient in B. The inset illustrates the main excitation processes.

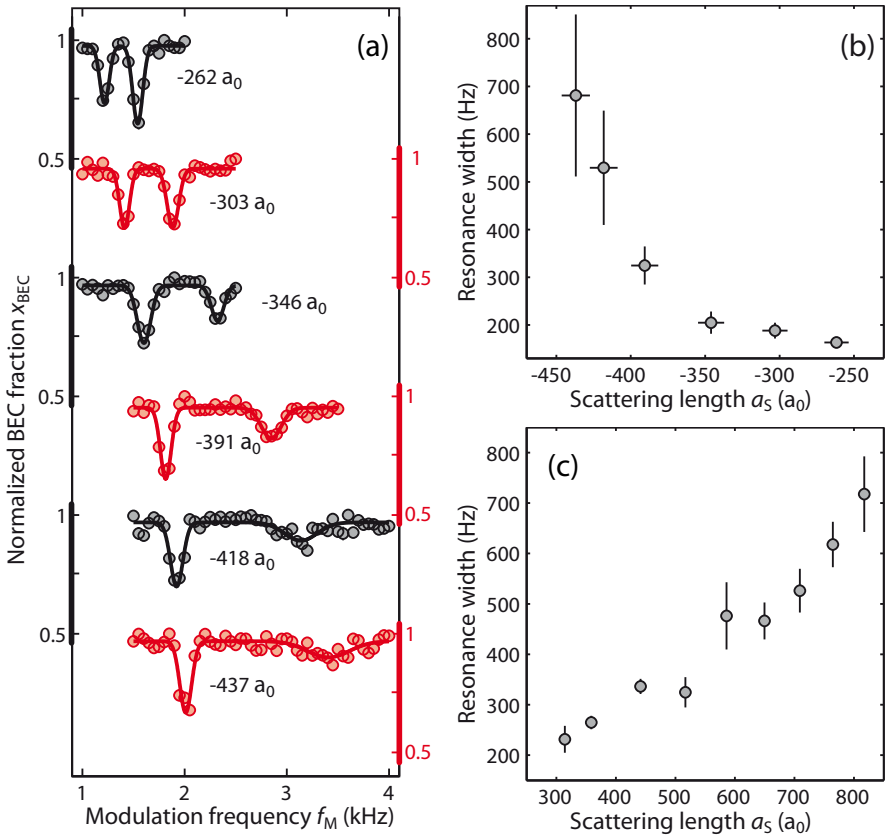

Fig. 2.12.: (color online) Broadening of the three-body excitation resonance. a) Set of excitation spectra showing the normalized BEC fraction x_{BEC} as a function of f_{M} for various values of a_{S} as indicated. The resonance peak connected to the two-body (three-body) bound state is located at lower (higher) frequency. The solid lines are double-peaked Gaussian fits, from which the width (FWHM) of the resonances is deduced. b) FWHM of the three-body excitation resonance as a function of a_{S} for attractive interactions. c) For comparison, we show the FWHM of the three-body excitation resonance as a function of a_{S} for repulsive interactions [Mar11b].

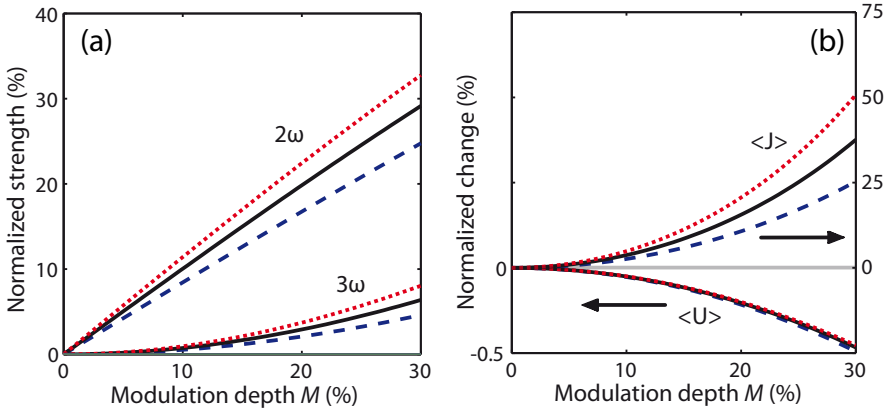

Fig. 2.13.: (color online) a) Normalized strength of the 2ω and 3ω frequency components of $J(t)$ as a function of the modulation depth M for $V_0 = 20\,\mathrm{E_R}$ (solid line), $V_0 = 15\,\mathrm{E_R}$ (dashed line), and $V_0 = 25\,\mathrm{E_R}$ (dotted line). b) Normalized change for the time averaged values $\langle U \rangle$ and $\langle J \rangle$ for U and J as a function of M for different values of V_0 as in a).

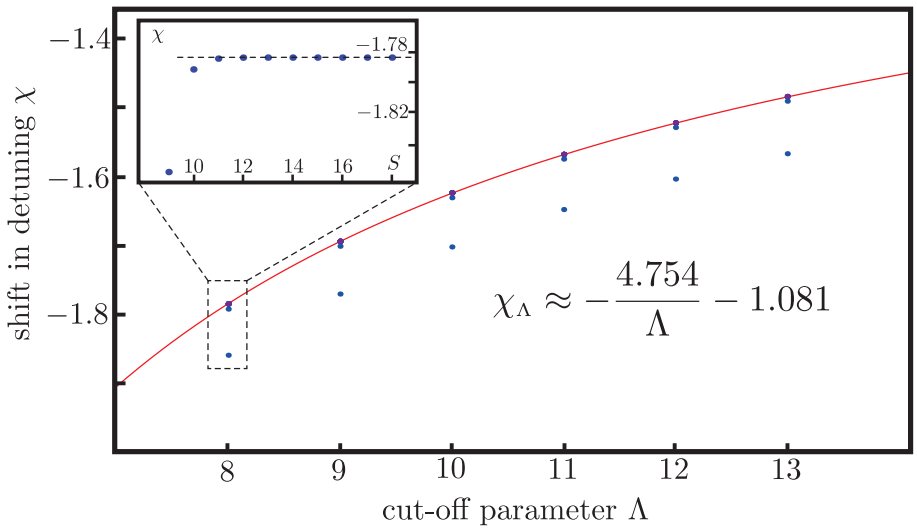

Fig. 2.14.: (color online) Convergence of the numerical analysis for increasing cut-off parameter and number of Bloch bands: Regularized shift of the detuning $\chi_\Lambda(E)$ at energy $E = 5.5E_\mathrm{R}$ and for an optical lattice with $V_0 = 16E_\mathrm{R}$. The dots are the values for different shell parameters S. The shift satisfies the asymptotic behavior $\chi_\lambda = c/\Lambda + \chi$ (solid line). The inset shows the fast convergence for fixed Λ by increasing the shell parameter S, i.e., the involved number of Bloch bands.

CHAPTER 3

MATTER-WAVE DYNAMICS ALONG ONE DIMENSION

3.1. Introduction

In this chapter we investigate the single particle matter-wave dynamics along one dimension within an optical lattice potential. Excitations and motion perpendicular to the lattice direction are neglected. The system behavior, for example scattering properties, are the same as for the three-dimensional case, in contrast to a one-dimensional system as discussed later in chapter 5, where the confinement strength perpendicular to the lattice has to fulfill a special requirement.

When applying a constant force along the optical lattice axis, the atoms get accelerated until the Bragg-condition between the atoms and the lattice light is fulfilled and the atoms are Bragg-reflected. In the Bloch-band picture, the atoms reach the edge of the first Brillouin-zone and, due to the periodicity of the quasimomentum, reappear on the opposite side with an inverted quasimomentum. The system undergoes so-called Bloch oscillations [Blo28, Zen34].

For electrons in a conductor with an applied electric field, Bloch oscillations typically are interrupted within one oscillation period by scattering events due to defects in the crystal structure, which inhibits their observation in standard bulk materials. Using semiconductor superlattice structures it was possible to observe coherent submillimeter-wave emission arising from Bloch oscillations [Was93]. An optical lattice provides an ideal crystal structure without defects, allowing the direct observation of these oscillations [BD96, And98]. In this case interactions between atoms were supposed to destroy and wash out Bloch oscillations, allowing long observation times only in the case of dilute thermal samples with a low background interaction strength [Fer06] or noninteracting fermions [Roa04]. Using our ability to tune interactions and in particular to minimize them by turning the scattering length to a zero crossing, we were able to observe more than 20.000 Bloch oscillations with a BEC, allowing us to measure the Bloch period with an accuracy of the order of 10^{-6} [Gus08b].

By adding interactions in a controlled way to the Bloch oscillations we were able to verify theoretical predictions that the momentum width broadens due to interactions [Wit05] until it fills the complete first Brillouin-zone and the oscillations are not visible anymore.

Figure 3.1 illustrates our experimental configuration. A standing wave creates a vertically oriented lattice potential, intersected by a horizontal dipole trap beam which provides the confinement along the lattice. An additional vertical dipole trap beam superimposed with the standing wave can be used to control the confinement perpendicular to the lattice independent of the lattice depth. Thus we create a series of pancake-shaped microtraps, and a BEC loaded into this configuration fills typically between 10 and 30 lattice sites, where the atom number per lattice site is given by the density distribution of the BEC during the loading process. To study matter-wave dynamics along the lattice direction, we suspend the atoms to a force directed along the lattice, which in our case is realized by gravity and the levitation force provided by a magnetic field gradient. During the sample preparation, the two forces are balanced so that the atoms feel no overall acceleration.

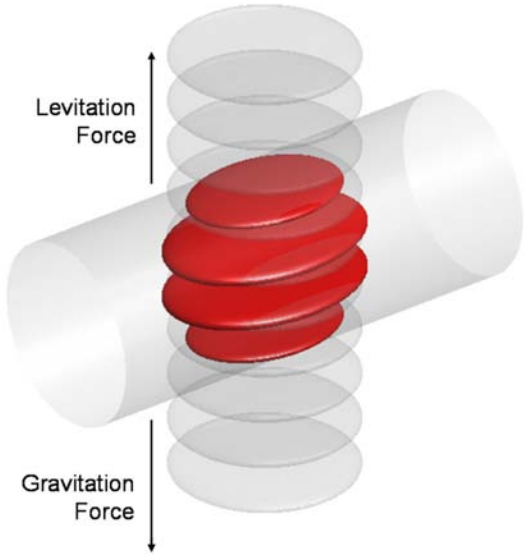

Fig. 3.1.: Schematic experimental setup. A vertically oriented standing wave and an intersecting horizontal dipole trap beam create a series of pancake shaped microtraps. The force along the lattice direction can be controlled via the balance between gravity and the levitation force.

In contrast to the crystal defects in solid state systems, interactions do not destroy the Bloch oscillations, as we show in section 3.2. Experimentally, we observe that after the first broadening of the momentum width a high-contrast interference pattern appears in the completely filled first Brillouin-zone as shown in Figure 3.2. In a mean-field picture, the interactions cause an additional phase shift between different lattice sites, leading to a coherent dephasing. We are able to probe this coherence with a spin-echo type experiment, where we reverse

the time evolution by switching off interactions and applying an external force gradient, effectively switching the sign of the phase shift, and show a refocusing to Bloch oscillations.

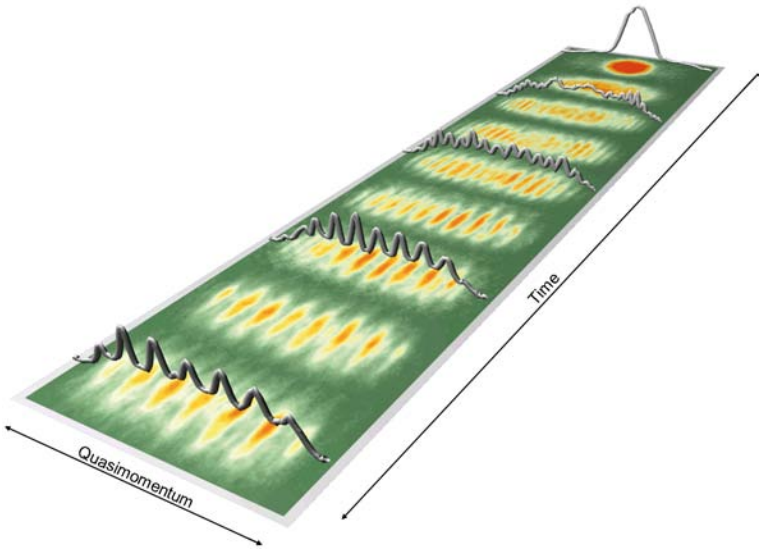

Fig. 3.2.: High-contrast time series of interference patterns in fully dephased Bloch oscillations. After a first rapid broadening an interference pattern appears, which evolve in time according to mean-field calculations.

It is also possible to describe the time evolution of our setup in terms of the Talbot effect, the self-imaging of an illuminated grating in near field diffraction [Tal36]. We show in section 3.3 that the time evolution of the microtrap phases are identical to the spatial phase evolution of coherent light behind a grating, when we switch interactions to zero and add an external quadratic potential. The self-image of the grating in optics, which occurs after the so-called Talbot length, is equivalent to the refocusing of the momentum distribution of the atoms to the initial one after a corresponding Talbot time. Higher-order interference patterns similar to those shown in Figure 3.2, which appear at fractional multiples of the Talbot time, are analogous to the fractional Talbot effect [Now97].

All the measurements above were performed applying a constant force to the atoms. In section 3.4 we investigate the properties of the system with a periodically modulated force. For fractional ratios n/m between the driving frequency and the Bloch oscillation frequency we observe modulation-enhanced tunneling resonances [Sia08, Iva08], where tunneling between lattice sites n lattice units apart via a m-phonon process [Eck05a] gets enabled. For a small detuning of the modulation frequency from such a resonance we observe huge oscillations in real space. This so-called super-Bloch oscillations spread over hundreds of lattice sites, compared to only a few sites for normal Bloch oscillations. We investigate these super-Bloch oscillations in detail and show that by changing the sign of the detuning at the appropriate point in time this mechanism can be used to induce transport along the lattice, which normally would be prevented through Bloch oscillations.

3.2. Publication: Interference of interacting matter waves

New J. Phys. **12** 065029 (2010)†

Mattias Gustavsson[1], Elmar Haller[1], Manfred J. Mark[1], Johann G. Danzl[1], Russell Hart[1], Andrew J. Daley[2,3], and Hanns-Christoph Nägerl[1]

[1] *Institut für Experimentalphysik und Zentrum für Quantenphysik, Universität Innsbruck, Technikerstraße 25, A–6020 Innsbruck, Austria*
[2] *Institut für Theoretische Physik und Zentrum für Quantenphysik, Universität Innsbruck, Technikerstraße 25, A–6020 Innsbruck, Austria*
[3] *Institut für Quantenoptik und Quanteninformation der Österreichischen Akademie der Wissenschaften, Technikerstraße 21a, A–6020 Innsbruck, Austria*

The phenomenon of matter wave interference lies at the heart of quantum physics. It has been observed in various contexts in the limit of non-interacting particles as a single particle effect. Here we observe and control matter wave interference whose evolution is driven by interparticle interactions. In a multi-path matter wave interferometer, the macroscopic many-body wave function of an interacting atomic Bose-Einstein condensate develops a regular interference pattern, allowing us to detect and directly visualize the effect of interaction-induced phase shifts. We demonstrate control over the phase evolution by inhibiting interaction-induced dephasing and by refocusing a dephased macroscopic matter wave in a spin-echo type experiment. Our results show that interactions in a many-body system lead to a surprisingly coherent evolution, possibly enabling narrow-band and high-brightness matter wave interferometers based on atom lasers.

†The author of the present thesis contributed to this work by assisting the experimental measurements and performing parts of the theoretical calculations. He also maintained and improved the experimental setup and contributed to the paper writing.

3.2.1. Introduction

Matter wave interference has been observed as a single particle effect for electrons [Dav27], neutrons [Hal36], atoms and molecules [Est30]. Macroscopic matter wave interference was first directly observed in the case of two independent atomic Bose-Einstein condensates (BEC) that were brought to overlap [And97]. This experiment validated the notion of the BEC as a macroscopic matter wave and coined the expression of the atom laser in analogy to the laser for the case of photons. Matter wave interferometers [Ber97, Cro09, Har07], in particular for applications to precision measurements, are typically operated in the dilute single particle limit [Wic02, Cla06a, Fix07] to avoid particle-particle interactions. Atom interferometers based on Bose-Einstein condensates (BEC) are expected to benefit from the extremely low momentum spread, the exceptional brightness, and the low spatial extent of the BEC [Gup02], but they readily enter the nonlinear matter wave regime as a result of the interaction-induced mean field potential. A possible solution is to operate BEC-based interferometers in the non-interacting limit [Gus08b, Fat08a] by exploiting the cancellation of the scattering phase shift near a scattering resonance. This condition, however, is difficult or impossible to fulfill for most atomic species. In the present work we demonstrate a BEC-based multipath atom interferometer where the dynamics is dominated by interaction-induced phase shifts, and we show that full control and also cancellation of these phase shifts is possible. We realize the multipath interferometer by loading an interacting BEC into an optical lattice potential along one dimension, coherently splitting the BEC into several parts that are then each subject to different linear and nonlinear phase shifts. The linear phase shifts due to the gravitational force lead to the the well-known phenomenon of Bloch oscillations [BD96, And98], whereas the interaction-induced nonlinear phase shifts cause the macroscopic wave function to first spread in momentum space as a function of time and then, surprisingly, to exhibit high-contrast interference. We demonstrate a high degree of coherence by reversing the nonlinear phase evolution, thereby refocusing the BEC momentum wave function. By application of an external potential we cancel the dominant mean-field contribution to the phase evolution and become sensitive to beyond-mean-field effects. A crucial ingredient of our experiments is the capability to tune a, the atomic scattering length which determines the strength of the interaction, by means of a Feshbach resonance [Web03a]. In particular, a can be switched to zero to stop the interaction driven part of the evolution in the interferometer or to perform high resolution wave function imaging in momentum space.

3.2.2. Phase evolution

Our interferometer consists of a BEC adiabatically loaded into a 1D optical lattice potential with a superimposed harmonic trap, as illustrated in figure 3.3a. In the tight-binding regime, it is convenient to write the macroscopic wave function of the condensate, Ψ, in a basis [Sme03] of wave functions $\Psi_j(z, r_\perp)$ centered at the position $z_j = jd$ of the individual lattice sites j, $\Psi(z, r_\perp, t) =$

$\sum_j c_j(t)\Psi_j(z, r_\perp)$. Here, z is the coordinate along the (vertical) lattice direction, $r_\perp$ is the transverse coordinate, d is the distance between adjacent lattice sites and $c_j(t)$ are time-dependent complex amplitudes.

After the BEC is loaded into the lattice, we tilt the lattice potential by applying a strong force F along the lattice direction. In the limit $Fd \gg J$, where J is the tunnelling matrix element, tunnelling between lattice sites is inhibited. The on-site occupation numbers $|c_j|^2$ are then fixed, and we can write $c_j(t) = c_j(0)e^{i\phi_j(t)}$, where the phase $\phi_j(t)$ evolves in time according to the local potential at each specific lattice site [Wit05],

$$\begin{aligned} \hbar\frac{\partial\phi_j}{\partial t} &= Fdj + V_j^{\mathrm{trap}} + \mu_j^{\mathrm{loc}} \\ &= Fdj + \beta_{\mathrm{tr}} j^2 - \alpha_{\mathrm{int}} j^2. \end{aligned} \tag{3.1}$$

Here, the total potential at each lattice site j consists of three terms. The applied force leads to a term linear in j and causes Bloch oscillations [BD96, And98] with angular frequency $Fd/\hbar$. The second term comes from an optional harmonic confinement, where $\beta_{\mathrm{tr}} = m\omega_{\mathrm{tr}}^2 d^2/2$ characterizes the strength of the confining potential and ω_{tr} is the trap frequency. Atom-atom interactions give rise to a third term, the local chemical potential μ_j^{loc}, which depends on the scattering length a and the site occupation number as [Sme03] $\mu_j^{\mathrm{loc}} \propto \sqrt{a|c_j|^2}$. When the BEC is loaded in the Thomas-Fermi regime, as is done here, its initial value can be calculated in a simple way. The density distribution will be such that the local chemical potential mirrors the trapping potential that is present during loading into the lattice, $\mu_{\mathrm{loc}}^j = \mu - V_j^{\mathrm{trap}}$, with μ being the (global) chemical potential of the BEC. We then initially have $\mu_j^{\mathrm{loc}} = \alpha_{\mathrm{int}} j^2$, where $\alpha_{\mathrm{int}} = m\omega_{\mathrm{lo}}^2 d^2/2$ and ω_{lo} is the trap frequency during loading. Note that although the initial value of α_{int} is independent of the scattering length used at loading, a later change in scattering length will also change the value of α_{int}.

The phase terms proportional to j^2 lead to a nonlinear relative phase evolution between lattice sites, i.e., dephasing. This results in a time-varying interference pattern of the macroscopic matter wave, as we will demonstrate below. The key in our experiments is that we have full control over these nonlinear terms, not only over β_{tr} via the external trapping potential, but also over the interaction term characterized by α_{int}, both via the initial density distribution, and, more importantly, via the scattering length a. By tuning the scattering length [Web03a] from its initial value a to a', we can ramp α_{int} to a new value α'_{int}, which can in particular be set to zero for $a = 0$. Nonlinear phase terms for matter waves are well known in single particle quantum mechanics. They play an important role for matter wave Talbot interferences [Ber97, Den99] and can be visualized in terms of so-called matter wave quantum carpets [Kap00]. In these contexts, the phase terms arise from propagation. In our case, the nonlinear phase terms for $\alpha_{\mathrm{int}} \neq 0$ arise from interactions and thus lead to a density dependent many-body effect in the multipath atom interferometer.

In the preceding discussion, we have assumed that the minimum of the trapping potential is centered directly over one of the lattice minima. If this is

not the case, the trapping potential term in equation (1) has to be modified to $\beta_{\mathrm{tr}}(j-\delta)^2 = \beta_{\mathrm{tr}} j^2 - 2\beta_{\mathrm{tr}}\delta j + const.$, where $\delta \in [0,1]$ describes the offset of the trap center in the z-direction with respect to the lattice minima, and an analogous modification has to be done to the interaction term. This adds a small term linear in j and therefore leads to a slight modification of the Bloch oscillation frequency. In our experiments, δ is the only parameter that we do not fully control. It is constant on the timescale of a single experimental run, but it drifts over the course of minutes as the beam pointing of the horizontally propagating laser beam generating the trapping potential is not actively stabilized.

3.2.3. Interaction-induced matter wave interference

The starting point for our experiments is a BEC trapped in a crossed optical dipole trap and adiabatically loaded into an optical lattice, as illustrated in figure 3.3a. The sample preparation is described in appendix A. The gravitational force acting on the BEC is initially compensated using magnetic levitation [Web03a]. We effectively start the multipath atom interferometer and hence the evolution of the interacting macroscopic wave function by turning off magnetic levitation and ramping down the vertical confinement created by laser beam L_2 within 0.3 ms, inducing Bloch oscillations in the lowest band of the lattice. With $Fd/\hbar \approx 2\pi \times 1740$ Hz and $J/\hbar \approx 2\pi \times 40$ Hz the on-site occupation numbers $|c_j|^2$ are fixed to their initial values. After an evolution time τ, we close the interferometer by ramping down the lattice in 1 ms and directly image the (vertical) quasi-momentum distribution in the first Brillouin zone (BZ). The ramp is adiabatic with respect to the bandgap and maps quasi-momentum onto real momentum [Kas95], which is measured by taking an absorption image after a period of free expansion. Figure 3.3b shows absorption images of the first Bloch oscillation [BD96]. The Bloch period is about 0.58 ms and the peaks have a root mean square (rms) width of $0.2\hbar k$, where $k = \pi/d$ is the lattice wave vector, thus being well separated.

We study the evolution of the wave function at high resolution in momentum space by taking snapshots after extended time-of-flight. As illustrated in figure 3.4a, the BEC wave function spreads out in the BZ in about $N = 18$ Bloch cycles. Then, surprisingly, an interference pattern gradually develops at the edge of the BZ and later also becomes visible at the center of the BZ, while the number of interference maxima and minima changes as time progresses. Images are taken after an integer number of Bloch cycles for cycle phase $\phi = 0$, corresponding to the first image in figure 3.3b. The data is acquired with an interacting BEC with the scattering length set to 190 a_0, where a_0 is the Bohr radius, at an initial peak density of $n = 4 \times 10^{13}$ atoms/cm^3, occupying about 35 lattice sites after loading. We can follow the evolution of the interference pattern for more than $N = 100$ Bloch cycles, corresponding to times beyond 60 ms. This is about a factor 10 longer than the timescale for the initial broadening. We find that the number of maxima and minima in the interference pattern as measured after a fixed evolution time τ depends on the number of occupied lattice sites and on

the trap frequency of the external harmonic confinement employed when loading the lattice. We also find that the measured quasi-momentum distribution for a given τ is reproducible from one experimental realization to the next, except that the pattern appears slightly shifted within the BZ after several experimental realizations. We attribute this to a drift of δ, the offset of the lattice minima from the dipole trap center, which leads to a small change of the Bloch frequency as noted before. We do not actively stabilize the vertical position of L_2 with respect to the lattice, and hence temperature variations in the laboratory slowly change δ.

We combine two techniques to achieve a high resolution in momentum space and to visualize the interference pattern. First, we minimize broadening of the distribution as a result of interactions by setting a to zero during the release from the lattice and the subsequent free expansion [Gus08b]. In addition, we use long expansion times, employing magnetic levitation to prevent the BEC being accelerated by gravity and falling out of the field of view. Figure 3.5 shows how the contrast emerges during the expansion for a BEC after $N = 40$ Bloch cycles. It takes more than 100 ms of expansion for the interference pattern to acquire full contrast. In general, we find that the contrast is improved when the horizontally confining beam L_1 is not switched off abruptly but is ramped down slowly within the first 55 ms of time-of-flight, reducing the horizontal expansion rate. However, this happens at the cost of some additional momentum broadening along the vertical direction. Our imaging techniques allow us to resolve structure in momentum space on a scale below $0.1\hbar k$ in a single shot absorption image.

To understand the interference structure and its evolution in time, we compute the total BEC wave function in quasi-momentum space for the case where the phase at each lattice site evolves according to equation (1) (details can be found in appendix B). Figure 3.4b shows the interference pattern for our experimental parameters according to this simple model. The experimental results are qualitatively very well reproduced by the model when we reduce α_{int} by 10 % compared to the value deduced from our experimental parameters. This scale factor accounts primarily for the fact that our simple model does not take into account any horizontal dynamics. In particular, switching off L_2 when starting the evolution leads to an excitation of a radial breathing mode in the horizontal plane, reducing the density at each site and modulating it in time. To a first approximation, rescaling of α_{int} accounts for this. Nevertheless, the agreement between the experiment and the analytical model indicates that the dominant driving mechanism for the wave function spreading and interference is the nonlinear phase evolution. In particular, phase coherence is not lost, in contrast to previous experiments [Mor03b]. We test this coherence and demonstrate control over the phase evolution in two experiments.

3.2.4. Cancellation of the dephasing

Equation (1) suggests that the effect of interactions can be cancelled by the application of an external potential [Zha08]. Indeed, choosing this potential to be equal to the initial loading potential, i.e. choosing $\alpha_{int} \approx \beta_{tr}$, allows us to observe persistent Bloch oscillations for an interacting BEC. This demonstrates that the detrimental effects of the mean field phase shift in a BEC matter wave interferometer can be compensated for. The BEC quasi-momentum distribution after $N = 40$ Bloch cycles is shown in figures 3.6a and 3.6b as a function of the strength of the external compensating potential, given by the power in laser L_2. When the external potential does not compensate for interactions, the condensate wave function is dephased and spreads over the whole BZ within less than $N = 20$ Bloch cycles. In contrast, when the external potential balances the effect of interactions, the BEC wave function does not spread out and Bloch oscillations are clearly visible. The time during which Bloch oscillations can be observed is now greatly extended compared to the case when the compensating potential is absent. The transition from a dephased to a non-dephased wave function as a function of confinement strength is quantified in figure 3.6c, where the rms-width Δp of the singly-peaked quasi-momentum distribution after $N = 40$ Bloch cycles is plotted as a function of the laser power in L_2. Figures 3.6d and 3.6e show the time evolution of the quasi-momentum distribution without and with the compensating potential while all other parameters are kept the same. Figure 3.6d essentially shows the broadening of the distribution as described before. Interestingly, the condensate wave function in the presence of a compensating potential shown in figure 3.6e dephases in a completely different way. Initially, the central peak shows no broadening. However, it is slowly depopulated, while a much broader background distribution is increasingly populated. After about 100 oscillations, the shape of the central peak starts to develop side lobes or splits in two, with the exact shape varying from one experimental run to the next. The timescale for the loss of interference is a factor 10 larger than the timescale on which the dephasing and hence the initial broadening takes place in the uncompensated case.

3.2.5. Rephasing of a dephased condensate

Second, we perform a matter wave spin-echo-type experiment. We initially proceed as shown in figure 3.4, letting the wave function evolve for a time corresponding to about $N = 40$ Bloch cycles until it is fully dephased and shows, upon measurement, a regular interference structure. We then essentially remove the effect of interactions by ramping to $a = 10$ a_0 within 10 ms. By not switching the interaction entirely off and by ramping comparatively slowly we avoid excessive excitation of the radial breathing mode as a result of the change in the mean field potential at each site. At the same time, we gradually turn on the harmonic potential as given by the horizontal dipole trapping laser beam L_2 within 4 ms to approximately the same depth as during the initial BEC loading phase. From equation (1) we expect that the wave function now experiences a

phase shift with a quadratic spatial dependence with opposite sign, allowing us to reverse the evolution and to recover the initial condition. Figure 3.7 shows the resulting quasi-momentum distributions. As time progresses, the wave function indeed refocuses while it continues to perform Bloch oscillations. As we do not control the value of δ for a particular run, we record about 10 distributions for each evolution time and select those that are symmetrical, corresponding to Bloch cycle phase $\phi = 0$ or $\phi = \pi$. For the chosen strength of the potential, refocusing happens after about 24 Bloch cycles after the ramp of a. This confirms that the initial broadening and dephasing mechanism must have been coherent. We note that we cannot avoid some excitation of the radial breathing mode as seen in the absorption images given in figure 3.7.

3.2.6. Discussion

Our results raise several important questions: To what extent can matter wave interferometry be performed in the presence of interactions? What sets the timescale for the eventual loss of interference contrast? Certainly, our simple analytic model does not predict any loss of contrast. In particular, it should be possible to completely eliminate the effect of interactions with the compensating external potential. However, there are several effects not included in the model that could cause the residual dephasing we observe. Motion in the radial direction, which causes the density and therefore the interaction energy to change over time, could lead to mixing of the different degrees of freedom and hence to additional dephasing. This might apply to our matter wave spin-echo experiment shown in figure 3.7, but in the experiment in figure 3.6 where we compensate interactions by means of the external potential there is hardly any radial excitation and this effect should not play a role. The appearance of dynamical instabilities [Zhe04, Cri04, Fal04] can be ruled out, as the force applied along the lattice is about 2.5 times stronger than the force needed for the instability to disappear [Zhe04]. Going beyond the mean-field treatment, a variety of factors can lead to dephasing. For example, at each lattice site there exists a superposition of number states, accumulating different phases corresponding to their respective interaction energies [Li07, Ima97]. This leads to an effective dephasing, as the phase on a particular lattice site becomes ill-defined. Basic estimates [Li07, Ima97] indicate a dephasing time of about 20 ms for our system, on the same order as we observe.

These experiments constitute a clear demonstration of coherent dynamics in an interacting macroscopic quantum system. This coherence affords a large degree of control over the system, as demonstrated by the possibility to rephase the wave function using an external potential in order to reverse dephasing due to interactions. The control demonstrated here has potential application in matter-wave interferometry, and such a degree of control over the mean-field evolution also opens the possibility to probe beyond-mean-field effects in atom interferometers.

We note that coherent phase shifts due to interparticle interactions have also been observed recently in Ramsey interferometry experiments in a two-component BEC [And09].

We thank E. Arimondo, O. Morsch, W. Schleich, A. Smerzi, D. Witthaut and A. Buchleitner and his group for helpful discussions. We are indebted to R. Grimm for generous support and gratefully acknowledge funding by the Austrian Ministry of Science and Research (Bundesministerium für Wissenschaft und Forschung) and the Austrian Science Fund (Fonds zur Förderung der wissenschaftlichen Forschung) in form of a START prize grant and through SFB 15. R.H. is supported by a Marie Curie International Incoming Fellowship within the 7th European Community Framework Programme.

3.2.7. Appendix

Sample preparation

Our experimental approach initially follows the procedure described in [Gus08b]. In brief, within 10 s we produce an essentially pure BEC with tunable interactions [Web03a] in the Thomas-Fermi limit with up to 1.5×10^5 Cs atoms. The BEC is trapped in a crossed-beam dipole trap generated by a vertically (L_1) and a more tightly focused horizontally (L_2) propagating laser beam. The BEC is cigar-shaped with the long axis oriented along the direction of L_2. The trap frequencies are $(\omega_x,\omega_y,\omega_z)=2\pi\times(39,5,39)$ Hz, where x denotes the horizontal direction perpendicular to L_2, y is the axial direction along L_2, and z is the vertical direction. We magnetically control the scattering length a in the range between $0\,a_0$ and $300\,a_0$ with a resolution of about $0.1\,a_0$. For BEC production, we work at $a = 210$ a_0, where three-body losses are minimized [Kra06]. Initially, we support the optical trapping by magnetic levitation against gravity [Web03a]. As shown in figure 3.3a we superimpose an optical lattice with $d=\lambda/2$ along the vertical direction, where $\lambda = 1064.5$ nm is the wavelength of the lattice light. To load the BEC into the lattice, we stiffen the horizontal confinement within 1 s, leading to trap frequencies of $2\pi\times(41,13,39)$ Hz, and at the same time turn on the lattice potential exponentially to a depth of $8E_R$. Here, $E_R=h^2/(2m\lambda^2)=k_B\times64\,\mathrm{nK}$ is the photon recoil energy and m the mass of the Cs atom. The BEC is thus gently loaded into the lattice, occupying about 25 to 35 lattice sites, with up to 7000 atoms at the central site.

Derivation of the BEC wave function in momentum space

Here, we outline the method used to calculate the images in figure 3.4b. Due to the comparatively small interaction energies in our system, the atoms are restricted to move in the lowest Bloch band and we can write the local wavefunction at lattice site j as $\Psi_j(r_\perp,z)=w_0^{(j)}(z)\Phi_\perp(\rho_j,r_\perp)$, where $w_0^{(j)}(z)$ is the lowest-band Wannier function localized at the j-th site and $\Phi_\perp(n_j,r_\perp)$ is a radial wave function depending on the occupation number $n_j=|c_j|^2$ at each site

[Sme03]. We can then write the total time-dependent wave function in momentum space as

$$\begin{aligned}\Psi(p_z, p_\perp, t) &= \sum_j c_j(t) w_0^{(j)}(p_z) \Phi_\perp(n_j, p_\perp) \\ &= w_0^{(0)}(p_z) \sum_j c_j(t) e^{-ip_z jd} \Phi_\perp(n_j, p_\perp). \end{aligned} \tag{3.2}$$

Transforming to quasi-momentum space and assuming that the phase at each lattice site evolves according to equation (1), we can write [Wit05]

$$\Psi(q_z, p_\perp, t) = \sum_j c_j(0) e^{-i(q+\frac{Ft}{\hbar})jd} \, e^{-i(\beta_{\rm tr} j^2 - \alpha_{\rm int} j^2)t/\hbar} \Phi_\perp(n_j, p_\perp), \tag{3.3}$$

where q_z denotes the quasimomentum. The images in figure 3.4b show the BEC density distribution $|\Psi(q_z, p_\perp, t)|^2$ integrated along one radial direction, using a Thomas-Fermi wave function as radial wave function $\Phi_\perp(n_j, p_\perp)$.

We have compared the result in figure 3.4b with a numerical integration of the discrete nonlinear Schrödinger equation [Sme03], which includes tunnelling between lattice sites, and find essentially identical results, confirming that tunnelling is inhibited.

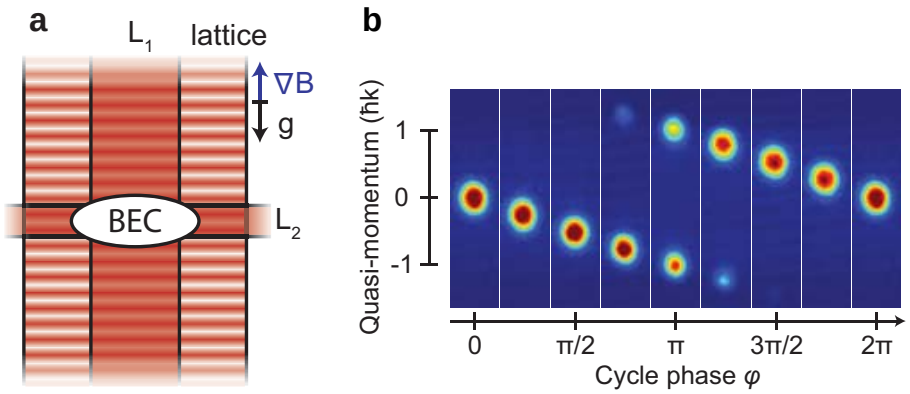

Fig. 3.3.: BEC-based atom interferometer. a, Experimental configuration: The tunable BEC is formed at the intersection of the vertical guide laser beam L_1 and a horizontal trapping beam L_2. The lattice is oriented along the vertical direction. Gravity, g, is initially compensated by a force due to a magnetic field gradient, ∇B. **b,** Imaging the first Brillouin zone (BZ): One cycle of Bloch oscillations for a non-interacting BEC as seen in time-of-flight absorption imaging, showing narrow peaks cycling through quasi-momentum space for cycle phases $\phi = 0$, $\pi/4$, $\pi/2$, ..., to 2π.

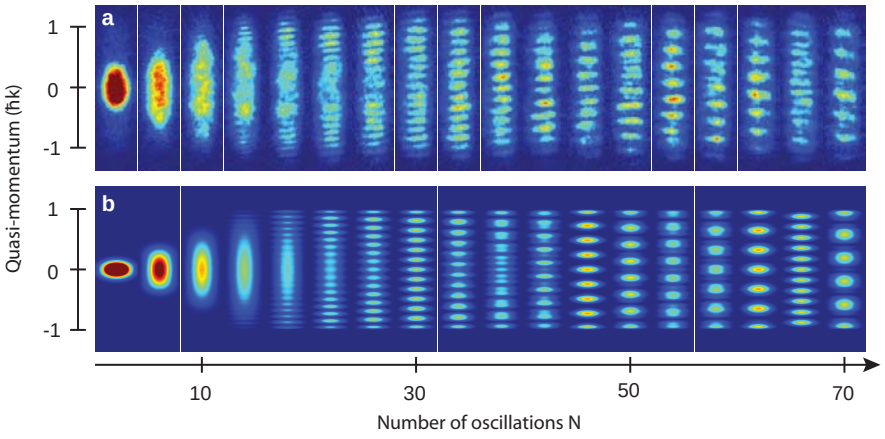

Fig. 3.4.: Interaction induced macroscopic matter wave interference. a, Experimental results showing the quasi-momentum distribution as a function of evolution time τ given in units of the Bloch period. The absorption images are taken in steps of 4 Bloch cycles for a BEC with an initial peak density of $n = 4 \times 10^{13}$ atoms/cm^3 loaded into about 35 lattice sites with $a = 190$ a$_0$. Each image corresponds to a single realization of the experiment. **b,** Evolution of the wave function in quasi-momentum space when the phase at the individual lattice sites evolves according to equation (1) with $\beta_{\mathrm{tr}} = 0$ (no external trap) for $n = 4 \times 10^{13}$ atoms/cm^3 loaded into 35 lattice sites with $a = 190$ a$_0$. α_{int} is slightly rescaled to account for the reduction in density due to transversal dynamics, see text. In **a**, some additional broadening, largely due to the presence of the horizontal trapping potential during expansion, can be seen.

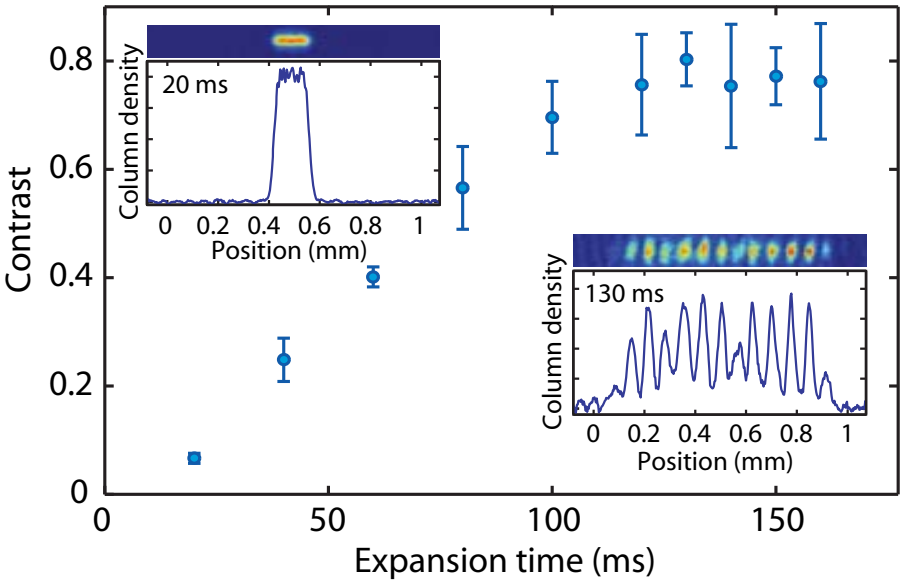

Fig. 3.5.: Contrast of interference fringes. Contrast of matter wave interference emerging during time-of-flight expansion for a BEC after $N = 40$ Bloch cycles, where the wave function completely fills the BZ. We define the contrast as $(I_{max} - I_{min})/(I_{max} + I_{min})$, where I_{max} (I_{min}) is the average value of the maxima (minima) of the central peak structure. Each data point is the average contrast of 10 experimental runs and the error bars indicate the 1σ statistical error. The insets show measured quasi-momentum distributions integrated along the transverse direction at two expansion times as indicated.

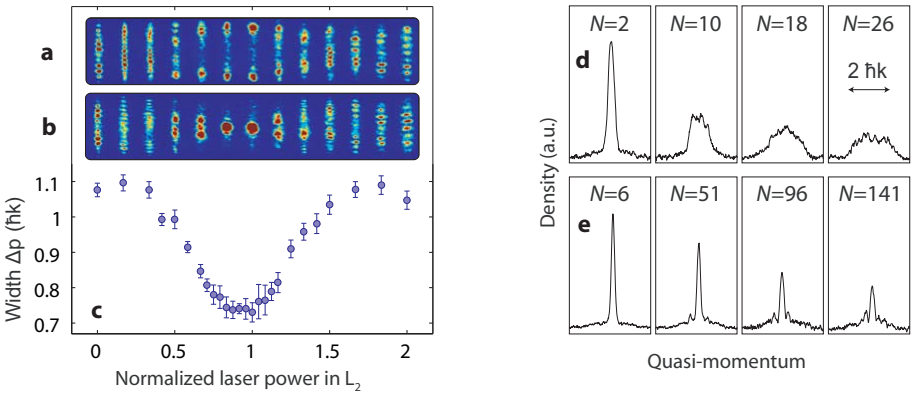

Fig. 3.6.: Cancellation of interaction induced dephasing and observation of persistent Bloch oscillations. a-c, Absorption images showing the quasi-momentum distribution for cycle phase $\phi = \pi$ (**a**) and $\phi = 0$ (**b**) after $N = 40$ Bloch cycles and (**c**) momentum width Δp for $\phi = 0$ as a function of confinement strength, normalized to the confinement strength at loading. **d** Momentum distribution for $\phi = 0$ as a function of the number N of Bloch cycles when no compensating potential is present, showing fast broadening. **e** The evolution of the momentum distribution for the case of optimum cancellation of interactions.

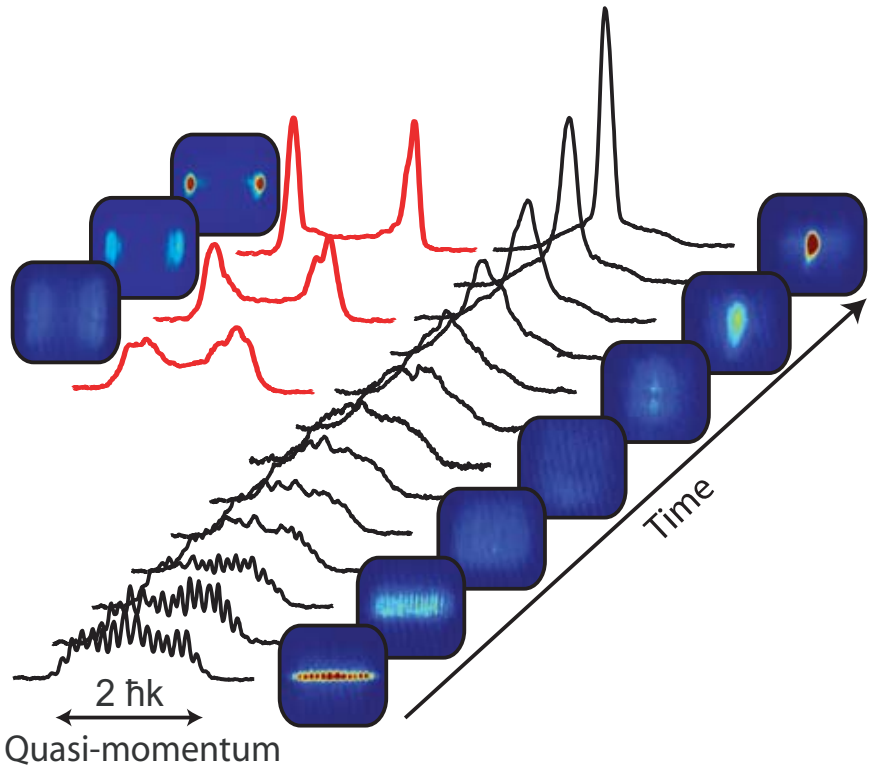

Fig. 3.7.: Matter wave spin-echo-type experiment. Rephasing of the BEC from a fully dephased wave function back into a narrow distribution after switching interactions to near zero and turning on an external potential. Time progresses from front to back. The black solid lines correspond to selected quasi-momentum distributions that refocus into the characteristic singly-peaked distribution (cycle phase $\phi = 0$), see text. They are separated in time by 1.15 ms or two Bloch cycles, and they are offset for clarity. The red solid lines correspond to selected distributions that refocus into the characteristic double-peaked distribution (cycle phase $\phi = \pi$). The images are absorption images corresponding to the adjacent quasi-momentum distributions. Some radial excitation is also present.

3.3. Publication: Demonstration of the temporal matter-wave Talbot effect for trapped matter waves

New J. Phys. **13**, 085008 (2011)†

Manfred J. Mark[1], Elmar Haller[1], Johann G. Danzl[1], Katharina Lauber[1], Mattias Gustavsson[2], and Hanns-Christoph Nägerl[1]

[1] *Institut für Experimentalphysik und Zentrum für Quantenphysik, Universität Innsbruck, Technikerstraße 25, A–6020 Innsbruck, Austria*
[2] *Department of Physics, Yale University, P.O. Box 208120, New Haven, Connecticut 06520, USA*

We demonstrate the temporal Talbot effect for trapped matter waves using ultracold atoms in an optical lattice. We investigate the phase evolution of an array of essentially non-interacting matter waves and observe matter-wave collapse and revival in the form of a Talbot interference pattern. By using long expansion times, we image momentum space with sub-recoil resolution, allowing us to observe fractional Talbot fringes up to 10^{th} order.

†The author of the present thesis performed the measurements and made the data analysis for this publication with support from KL. The experimental procedure was developed originally by MG and was refined by MJM. The paper was written by MJM and HCN. All authors contributed to the paper writing and by general experimental support.

3.3.1. Introduction

Interference of matter waves is one of the basic ingredients of modern quantum physics. It has proven to be a very rich phenomenon and has found many applications in fundamental physics as well as in metrology [Cro09] since the first electron diffraction experiments by Davisson and Germer [Dav27]. Matter-wave optics has now developed into a thriving subfield of quantum physics. Many key experiments from classical optics have found their counterpart with matter waves, for example the realization of Young's double slit experiment with electrons [Jön61], the implementation of a Mach-Zehnder-type interferometer with neutrons [Rau74], or, more recently, the observation of Poisson's spot with molecules [Rei09]. The creation of Bose-Einstein condensates (BEC) in 1995 [And95, Dav95] opened the door to many more exciting experiments with matter waves, to a large extent in the same way as the laser did in the case of classical light waves.

One remarkable phenomenon in classical optics is the Talbot effect, the self-imaging of a periodic structure in near field diffraction [Ber01]. The effect was first observed by Talbot in 1836 [Tal36] and was later explained in the context of wave optics by Rayleigh in 1881 [Ray81]. When light with a wavelength λ illuminates a material grating with period d, the intensity pattern of the light passing through the grating reproduces the structure of the grating at distances behind the grating equal to odd multiples of the so-called Talbot length $L_{\mathrm{Talbot}} = d^2/\lambda$. At even multiples of the Talbot length the intensity pattern again reproduces the structure of the grating, but shifted laterally in space by half of the grating period. In between these recurrences, at rational fractions n/m of L_{Talbot} (with n, m coprime), patterns with smaller period d/m are formed. This effect is known as the fractional Talbot effect. A necessary requirement for the appearance of the Talbot effect and its fractional variation is the validity of the paraxial approximation [Krz89]. Crucial to the Talbot effect is the fact that the accumulated phase differences of the propagating waves behind the grating show a quadratic dependence on lateral distance or grating slit index.

The first observations of the atomic matter-wave Talbot effect [Sch93, Cha95] were based on setups comprising an atomic beam and two material gratings, where the second grating acted as a mask used for detection purposes. The demonstration of the fractional Talbot effect with atomic matter waves used the fact that the interference fringes could be recorded directly by using a spatially resolving detector [Now97]. The Talbot effect can also be demonstrated with spatially incoherent wave sources by using an additional first grating to create spatial coherence according to Lau [Lau48]. In this way, an interferometer is formed that is made of two or even three gratings. Such Talbot-Lau interferometers [Cla94] are now an important tool in atomic and molecular interferometry [Cro09, Bre02, Ger07]. In the context of macroscopic matter waves, i.e. atomic BECs, the Talbot effect has been observed in the time domain by using pulsed phase gratings formed by standing laser waves [Den99]. During expansion after release from the trap the BEC was exposed to two short grating pulses separated by a variable time delay and the momentum distribution was measured. At a

specific delay, this distribution was observed to rephase to the initial one. In essence, the quadratic dispersion relation of freely propagating, non-interacting matter waves resulted in a quadratic phase evolution for the diffracted momentum states and hence to a temporal version of the Talbot effect. Intriguingly, the Talbot effect is also present for interacting matter waves, as we could show in our previous work [Gus10]. The momentum distribution of a trapped array of decoupled two-dimensional BECs proved to exhibit a regular, time-varying interference pattern. In this case, the quadratic phase evolution was driven by the local mean-field interaction that had a quadratic spatial dependence reflecting the parabolic shape of the initial density distribution.

In the present work, we report on the demonstration of the temporal Talbot effect using trapped, non-interacting matter waves. Here, the Talbot effect is not driven by interactions but by the (weak) external harmonic dipole-trap confinement, leading to a characteristic quadratic phase evolution. Unlike in our earlier work [Gus10], the contrast of the Talbot pattern is not degraded by interaction-driven on-site phase diffusion [Li07], allowing us to follow the phase evolution for long times and hence allowing us to observe matter-wave revivals. For our measurements we use as before an array of pancake-shaped, two-dimensional BECs in a one-dimensional optical lattice [Gus10]. The optical lattice takes on the role of the grating. Cancelling the effect of interactions in the vicinity of a Feshbach resonance and decoupling the individual BECs by means of a gravitational tilt initiates long-lived Bloch oscillations (BO) in momentum space [Gus08b]. These are quickly superimposed by a Talbot-type interference pattern in the presence of the external confinement. The pattern can be directly connected to the (fractional) Talbot effect. In particular, after specific hold times that are multiples of the Talbot time, the time-analogue to the Talbot length, a rephasing of the momentum distribution can be observed.

3.3.2. Preparation of the initial sample

We first produce an essentially pure BEC of Cs atoms (no detectable non-condensed fraction) by largely following the procedure detailed in Ref. [Web03a, Kra04]. The atoms are in the lowest hyperfine sublevel $F = 3$, $m_F = 3$ trapped in a crossed optical dipole trap and initially levitated against gravity by a magnetic gradient field. As usual, F is the atomic angular momentum quantum number, and m_F its projection on the magnetic field axis. For the present experiments, the atom number is set to typically 6×10^4 atoms. The trap frequencies in the crossed dipole trap are chosen to be $\omega_x = 2\pi \times 21.7(3)\,\mathrm{Hz}$, $\omega_y = 2\pi \times 26.7(3)\,\mathrm{Hz}$, and $\omega_z = 2\pi \times 26.9(3)\,\mathrm{Hz}$. The confinement along the vertical axis (z) and the two horizontal axes (x, y) is controlled by two horizontally propagating dipole trap beams with beam waists of $46\,\mu\mathrm{m}$ and $144\,\mu\mathrm{m}$ and one vertically propagating dipole trap beam with a beam waist of $123\,\mu\mathrm{m}$. The atomic scattering length a_s and therefore the strength of interactions in the BEC can be tuned via a magnetic offset field B in a range between $a_\mathrm{s} = 0\,\mathrm{a}_0$ and $a_\mathrm{s} = 1000\,\mathrm{a}_0$ by setting B to values between approximately 17 and 46 G using a magnetically

induced Feshbach resonance [Chi04b] as illustrated in figure 3.8(a). Here, a_0 is Bohr's radius. For the initial preparation of the sample, we set a_s to positive values, typically between $100\,a_0$ and $210\,a_0$. Later, a_s is set to zero as discussed below. We gently load the condensed atomic sample into a vertical standing wave as illustrated in figure 3.8(b) by exponentially ramping up the power in the standing wave over the course of about 1000 ms. The standing wave is generated by a retro-reflected laser beam at a wavelength of $\lambda = 1064.48(5)$ nm with a $1/e$-waist of about $350\,\mu$m. We are able to achieve well depths of up to $40\,E_R$, where $E_R = \hbar^2k^2/(2m) = h^2/(2m\lambda^2) = k_B \times 64\,\mathrm{nK}$ is the atomic photon recoil energy. Here $k = 2\pi/\lambda$, m denotes the mass of the Cs atom, h is Planck's constant, and k_B is Boltzmann's constant. The lattice light as well as the light for the dipole trap beams is derived from a single-frequency, narrow-band, highly-stable Nd:YAG laser that seeds a home-built fibre amplifier [Lie03]. The maximum output power is up to 20 W without spectral degradation. The powers in all light beams are controlled by acousto-optical intensity modulators and intensity stabilization servos.

3.3.3. Phase evolution and the Talbot effect

Our system, the BEC loaded into a 1D optical lattice with spacing $d = \lambda/2$, can be modelled by a discrete nonlinear equation (DNLE) in one dimension [Sme03], as discussed in our earlier work [Gus10]. In brief, this equation can be obtained by expanding the condensate wave function from the Gross-Pitaevskii equation, Ψ, in a basis of wave functions $\Psi_j(z, r_\perp)$ centred at individual lattice sites with index j, $\Psi(z, r_\perp, t) = \sum_j c_j(t)\Psi_j(z, r_\perp)$. Here, z is the coordinate along the (vertical) lattice direction, $r_\perp$ is the transverse coordinate, and $c_j(t)$ are time-dependent complex amplitudes. The atoms are restricted to move in the lowest Bloch band and we can write $\Psi_j(r_\perp, z) = w_0^{(j)}(z)\Phi_\perp(\rho_j, r_\perp)$, where $w_0^{(j)}(z)$ are the lowest-band Wannier functions localized at the j-th site and $\Phi_\perp\rho_j, r_\perp)$ is a radial wave function depending on the peak density ρ_j at each site [Sme03]. By inserting this form into the Gross-Pitaevskii equation and integrating out the radial direction, the DNLE is obtained,

$$i\hbar\frac{\partial c_j}{\partial t} = J(c_{j-1} + c_{j+1}) + E_j^{\mathrm{int}}(c_j)c_j + V_j c_j. \tag{3.4}$$

Here, J/h is the tunnelling rate between neighbouring lattice sites, $V_j = \mathfrak{F}d\ j + V_j^{\mathrm{trap}}$ describes the combination of a linear potential with force $\mathfrak{F}$ and an external, possibly time-varying trapping potential V_j^{trap}, and $E_j^{\mathrm{int}}(c_j)$ is the nonlinear term due to interactions.

We first load the BEC into the vertical lattice and then allow the gravitational force to tilt the lattice potential. We thus enter the limit $\mathfrak{F}d \gg J$, in which tunnelling between sites is inhibited and the on-site occupation numbers $|c_j|^2$ are constant, determined by the initial density distribution. The time evolution of the system is then given by the time-dependent phases of all c_j, and the 1D wave function $\tilde{\Psi}(q, t)$ in quasi-momentum space q acquires a particularly simple form [Wit05]:

$$\begin{aligned}\tilde{\Psi}(q,t) &= \sum_j c_j(t)e^{-iqjd} = \sum_j c_j(0)e^{-i(\mathfrak{F}dj+V_j^{\mathrm{trap}}+E_j^{\mathrm{int}})t/\hbar}e^{-iqjd} \\ &= \sum_j c_j(0)\, e^{-i(q+\frac{\mathfrak{F}t}{\hbar})jd}\, e^{-i(\beta_{\mathrm{tr}}(j-\delta)^2-\alpha_{\mathrm{int}}(j-\delta)^2)t/\hbar} \qquad (3.5)\end{aligned}$$

Here, we have assumed that our external potential is harmonic, given by $V_j^{\mathrm{trap}} = \beta_{\mathrm{tr}}(j-\delta)^2$, where $\beta_{\mathrm{tr}} = m\omega_{\mathrm{z}}^2 d^2/2$ characterizes the strength of the potential with trapping frequency ω_{z} along z for a particle with mass m. The parameter δ in the interval $[-1/2, 1/2]$ describes a possible offset of the potential centre with respect to the nearest lattice well minimum along the z-direction. For the interaction term α_{int}, the spatial dependence is also parabolic, reflecting the fact that we initially load a (parabolically shaped) BEC in the Thomas-Fermi regime. In our experiments, the offset δ is not well controlled. It is nearly constant on the timescale of a single experimental run (duration of up to 20 s), but its value changes over the course of minutes as the positions of the horizontally propagating laser beams generating the trapping potential and the position of the retro-reflecting mirror generating the vertical standing wave drift due to changes of the ambient conditions.

The phase evolution in equation 3.5 has a simple interpretation. The term in the exponent linear in j results in Bloch oscillations [Gus08b, BD96, And98] with a Bloch period $T_{\mathrm{Bloch}} = 2\pi\hbar/(\mathfrak{F}d)$. In figure 3.8(c) a full cycle of one BO, corresponding to a Bloch phase from 0 to 2π, is shown. When restricting ourselves to times that are integer multiples of T_{Bloch} this term can be omitted. The nonlinear exponents proportional to j^2 lead to a dephasing between lattice sites, resulting in a time-varying interference pattern for the quasimomentum distribution [Gus10]. In our experiments we have full control over these nonlinear terms, not only over β_{tr} via the external trapping potential, but also over the interaction term characterized by α_{int} via the scattering length a_{s}. Our previous work [Gus10] has focused on the role of interactions, whereas in this work we focus on the (nonlinear) term caused by the external potential. For this we tune a_{s} in such a way that the term with α_{int} is minimized. Now the phase evolution depends only on the term with β_{tr}. The offset δ slightly modifies the Bloch period, resulting in a global shift of the interference pattern in quasimomentum space when imaged at integer multiples of the original T_{Bloch}. However, as it is irrelevant for the Talbot effect, we set δ to zero here. By including the simplifications and introducing the Talbot time $T_{\mathrm{Talbot}} = h/(m\omega_{\mathrm{z}}^2 d^2)$, equation 3.5 reduces to

$$\tilde{\Psi}(q,t) = \sum_j c_j(0,q)\, e^{-i\pi j^2 t/(2T_{\mathrm{Talbot}})} \qquad (3.6)$$

with $c_j(0,q) = c_j(0)\exp(-iqjd)$. Now the Talbot effect is evident. For times that are even multiples of T_{Talbot} the original wave function is recovered, whereas

for odd multiples the original wave function appears with a shift of $\hbar k$ in quasimomentum space. This realisation of the Talbot effect is nearly ideal, since no paraxial approximation is needed and since there is no limitation in time due to decreasing wave packet overlap [Den99]. For fractions n/m of T_{Talbot}, m copies of the original wave function with a spacing $2\hbar k/m$ appear, corresponding to the fractional Talbot effect. The evolution of the quasimomentum distribution as a function of time can be visualized in terms of so-called matter-wave quantum carpets [Kap00, Ruo01]. Such a quantum carpet, calculated by solving equation 3.4 numerically with the parameters typical to our experiment, is shown in figure 3.9. Note that in this case the more simple calculation based on equation 3.6 leads to the same result. However, equation 3.4 gives us more flexibility in relaxing the requirements of harmonic confinement or negligible tunnelling. We plot the distribution as a line density plot with white areas indicating high densities. Only times that are integer multiples of T_{Bloch} are shown. After a fast spreading of the quasimomentum distribution a regular pattern appears at times for which one expects fractional Talbot interferences. The number of peaks in the momentum distributions directly represents the fraction t/T_{Talbot}. At T_{Talbot} a refocusing to the initial distribution occurs, shifted by $\hbar k$ in quasimomentum space. The evolution is then repeated until at $2T_{\mathrm{Talbot}}$ the original wave function is recovered.

3.3.4. Experimental realisation

For the present experiments we choose a lattice depth of $8\,\mathrm{E}_R$. For lattice loading the interaction strength is set to $a_{\mathrm{s}} = 100\,\mathrm{a}_0$ and the external trap frequencies are changed adiabatically to populate about 40 lattice sites. After loading, we change ω_z to the final value. This change is done sufficiently quickly (within 3 ms) to avoid a change in the initial distribution due to tunnelling, but sufficiently slowly to avoid motional excitations along the z-direction. Then, within 0.1 ms, we switch off the levitating magnetic field gradient to decouple the individual lattice sites and set the scattering length to the value near $a_{\mathrm{s}} = 0\,\mathrm{a}_0$ that gives minimal dephasing [Gus08b]. Note that the point of minimal dephasing does not correspond exactly to $0\,\mathrm{a}_0$ as residual magnetic dipole-dipole interactions have to be taken into account [Fat08b]. The shift is calculated to be about $-0.7\,\mathrm{a}_0$. After a variable hold time t_{hold}, which typically corresponds to hundreds of Bloch cycles with $T_{\mathrm{Bloch}} = 0.575$ ms, we switch the levitation field back on in 0.1 ms and ramp down the optical lattice and the dipole trap responsible for trapping in the vertical direction in 0.3 ms. The ramp is adiabatic with respect to the trap frequency of the individual lattice sites, ensuring that the atoms stay in the lowest Bloch band and thus mapping quasimomentum onto real momentum [Kas95]. Before taking an absorption picture we let the sample expand for 80 ms while it remains levitated and thus map momentum to real space. The dipole trap responsible for horizontal trapping is not turned off immediately, but instead it is ramped down slowly over the course of 50 ms to reduce spreading of the sample in the horizontal direction. At the same time,

a_s is kept at the value that gives minimal interactions to avoid broadening of the sample in the vertical direction. From the absorption pictures we calculate the momentum width Δp as two times the second moment of the momentum distribution along the vertical direction. Note that the presence of the horizontal trap during expansion leads to additional broadening in vertical direction. This broadening plus some residual incoherent background limits the observable values of Δp. Nevertheless, with our ability to image the quasimomentum with high resolution [Gus10] we are able to compare not only the momentum width but also the substructure in the momentum distribution to theory.

Figure 3.10 shows the measured momentum distribution of the atom cloud at specific hold times t_{hold} that are fractions of the calculated Talbot time T_{Talbot}. For this measurement we choose a vertical trap frequency of $\omega_z = 2\pi \times 22.0(2)\,\mathrm{Hz}$, which gives $T_{\mathrm{Talbot}} = 555(10)\,\mathrm{ms}$. Figure 3.10(a) shows the absorption images as density plots (white areas indicate regions with high density), while figure 3.10(b) plots the horizontally integrated densities from the corresponding images of figure 3.10(a). Initially, the momentum distribution is singly peaked, as expected for a non-dephased BEC. After a rapid coherent dephasing (corresponding to a rapid broadening of the momentum distribution, not shown here) regularly structured patterns appear. The number of peaks within the first Brillouin zone $[-\hbar k, +\hbar k]$ corresponds exactly to the fraction $t_{\mathrm{hold}}/T_{\mathrm{Talbot}}$, as expected from the theoretical considerations. A small fraction of the atoms is detected outside the first Brillouin zone, likely caused by imperfections in the mapping of quasimomentum onto real momentum. Finally, at the Talbot time, the momentum distribution rephases again to the initial distribution. In general, apart from an overall shift of each individual distribution in quasimomentum space due to variations in δ as discussed below, we find very good qualitative agreement with the results of the calculation shown in figure 3.9.

Figure 3.11 illustrates the effect of δ on the observed patterns in quasimomentum space. For two different hold times $t_{\mathrm{hold}} = T_{\mathrm{Talbot}}$ and $t_{\mathrm{hold}} = T_{\mathrm{Talbot}}/2$, absorption images for several individual experimental realisations and the corresponding horizontally integrated densities are shown. The expected single- and double-peaked momentum patterns are reproduced from one experimental realisation to the next, but they experience a varying shift in quasimomentum space. As a consequence of the periodic structure of quasimomentum space, a peak that is located near one edge of the Brillouin zone also reappears at the opposite edge. The maximum possible shift of the pattern in quasimomentum space due to δ increases with hold time and is calculated to be $\pm\hbar k \times t_{\mathrm{hold}}/T_{\mathrm{Talbot}}$. This is why the patterns shown in figure 3.10, e. g. at $t_{\mathrm{hold}} = T_{\mathrm{Talbot}}$ or at $t_{\mathrm{hold}} = T_{\mathrm{Talbot}}/2$, agree with the calculated patterns only modulo the shift in quasimomentum space. Note that, alternatively, we could have chosen to present in figure 3.10 selected patterns from a sufficiently large sample of measurements, e.g. the one from experimental run 4 for $t_{\mathrm{hold}} = T_{\mathrm{Talbot}}$ or the one from experimental run 1 for $t_{\mathrm{hold}} = T_{\mathrm{Talbot}}/2$ shown in figure 3.11.

A simple quantitative comparison between experiment and calculations can be done by considering the time evolution of the momentum width Δp. The

distribution of this quantity across several experimental realisations is evidently sensitive to the de- and rephasing of the matter wave. In fact, we can relax the choice of the Bloch phase and allow its value to be random. For example, for a non-dephased BEC the momentum width Δp is measured to range from $(\Delta p)_{\min} \approx 0.6\,\hbar k$, corresponding to the singly peaked momentum distribution, to $(\Delta p)_{\max} \approx 1.7\,\hbar k$ when the momentum distribution is evenly peaked at both edges of the Brillouin zone (e. g. at half the first Bloch period, see figure 3.8(c)). For a completely dephased sample corresponding to a uniform distribution over the first Brillouin zone we measure a value of $\Delta p \approx 1.25\,\hbar k$. Accordingly, the range for the momentum width Δp at a given hold time t_{hold} shows a distinct behaviour as a function of t_{hold}, in particular indicating the revival at T_{Talbot} by maximizing the difference $D_{\Delta\text{p}} = (\Delta p)_{\max} - (\Delta p)_{\min}$ between the extrema of Δp. Figure 3.12(a) shows $(\Delta p)_{\max}$ and $(\Delta p)_{\min}$ as a function of t_{hold} as calculated from equation 3.4. Initially and at T_{Talbot} the extrema lie far apart (at these times the calculation gives values for $(\Delta p)_{\min}$ that are close to zero in accordance with the fact that the momentum width is determined only by the spread in position space, which is large), whereas at intermediate times the difference is drastically reduced, only increasing slightly at rational fractions of $t_{\text{hold}}/T_{\text{Talbot}}$. In figure 3.12(b) we plot the measured momentum width extrema. These are determined from samples of 10 single measurements at each chosen value for t_{hold}. The initial rapid collapse agrees well with the fact that the sample dephases. Then, near the calculated value for T_{Talbot}, a clear increase in $D_{\Delta\text{p}}$ can be seen. The difference recovers almost completely to the initial value. We attribute the slight reduction to additional dephasing mechanisms not included in our simple model as discussed below.

The behaviour of $D_{\Delta\text{p}}$ offers a simple method to test the dependence of the Talbot time T_{Talbot} on the vertical trap frequency ω_z. Evidently, $D_{\Delta\text{p}}$ has a maximum at T_{Talbot}. Figure 3.13(a) shows the momentum width Δp in the vicinity of the calculated T_{Talbot}, here for a specific trap frequency of $\omega_z = 2\pi \times 26.9(2)$ Hz. Again we evaluate 10 experimental realisations for each hold time and select $(\Delta p)_{\max}$ and $(\Delta p)_{\min}$ to calculate $D_{\Delta\text{p}}$. We locate the position of its maximum by a simple gaussian fit, as shown in figure 3.13(b). We then vary ω_z and determine T_{Talbot} accordingly. In Figure 3.13(c) T_{Talbot} is plotted as a function of ω_z. The experimental values are in excellent agreement with the calculated values for the Talbot time according to $T_{\text{Talbot}} = h/(m\omega_{\text{z}}^2 d^2)$.

We finally discuss the main limitations for our experiment. We believe that the total number of subsequent revivals that we can observe (we detect up to 4 revivals) is mainly limited by three-body loss and by the anharmonicity of the trapping potential. Three-body loss heats the two-dimensional BECs residing at each lattice site. This leads to a loss of phase coherence and thus decreases the visibility of the revivals. Perhaps more interestingly, the anharmonicity of the trapping potential along the vertical direction causes deviations from the quadratic phase evolution required for the Talbot effect. In order to test this effect we generate the vertical trapping potential with a more tightly focused dipole trap beam, which enhances the effect of anharmonicity. We then

observe non-perfect Talbot revivals followed by subrevivals as can be seen in figure 3.14(a). This is in qualitative agreement with calculations shown in figure 3.14(b), for which the real gaussian shape of the trapping potential instead of a simple harmonic one has been used. The full calculated time evolution of the momentum distribution is shown in figure 3.14(c). The distortion of the matter-wave quantum carpet can clearly be seen.

3.3.5. Conclusion

We have demonstrated the temporal Talbot effect with trapped, non-interacting matter waves. High resolution imaging in quasimomentum space allows us to resolve Talbot fringes up to the 10th order. We have tested the dependence of the Talbot time on the strength of the confinement and have found very good agreement with the calculated value. We find that the interference pattern is sensitive to the anharmonicity of the trapping potential. In principle, the detailed structure of the interference pattern and the precise revival times are sensitive probes for force gradients and interactions between atoms. The weak magnetic dipole-dipole interaction, for example, has recently been investigated in the context of matter-wave interferometry [Fat08b]. Matter-wave interferometry in the Talbot regime could potentially be used to examine in detail the effect of the long-range nature of such an interaction. Similarly, a spatially dependent force like the Casimir-Polder force [Cas48, Har05, Chw10] near a surface could be investigated through its influence on the Talbot interference pattern.

We are indebted to R. Grimm for generous support and we thank A. Daley for valuable discussions. We gratefully acknowledge funding by the Austrian Science Fund (FWF) within project I153-N16 and within the framework of the European Science Foundation (ESF) EuroQUASAR collective research project QuDeGPM.

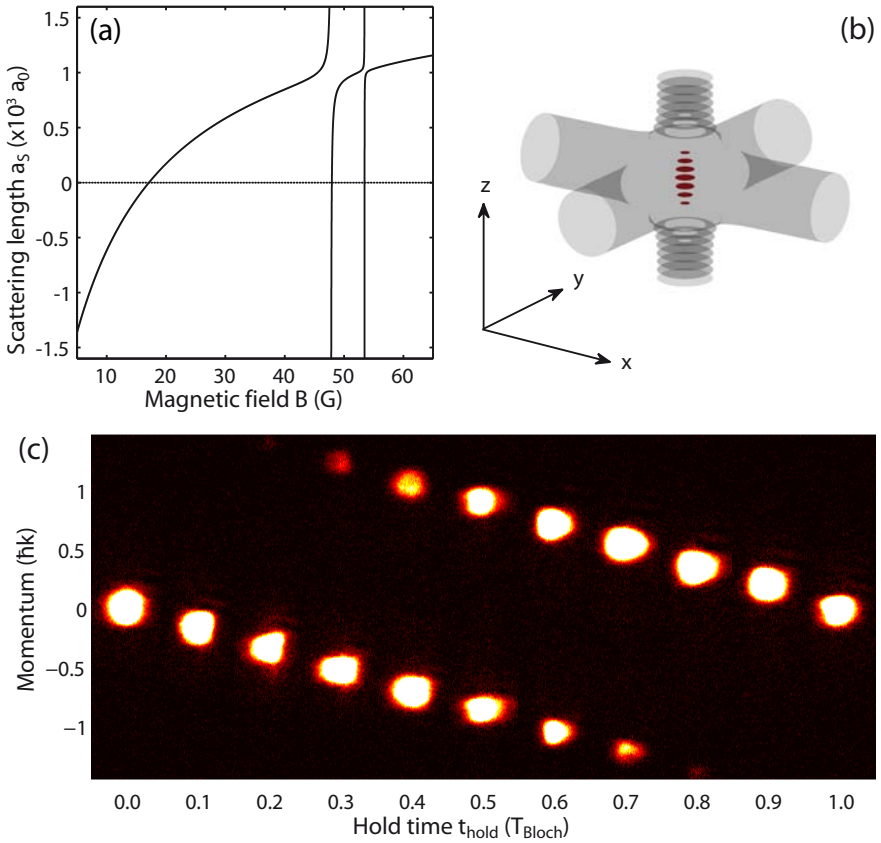

Fig. 3.8.: (a) Magnetic-field dependence of the scattering length a_s for Cs atoms in $F = 3$, $m_F = 3$: Wide tunability is given by a broad magnetic Feshbach resonance with a pole near -11 G (not shown), leading to a region with attractive interaction, a zero crossing at about 17 G, and a repulsive region above [Chi04b]. Two narrow Feshbach resonances can be seen in the vicinity of 50 G. (b) Experimental configuration: A vertically-oriented standing laser wave creating a stack of pancake-shaped traps is intersected by two horizontal laser beams. (c) Bloch oscillations: Time series in steps of about 57 μs showing the quasimomentum distribution over the course of one Bloch cycle.

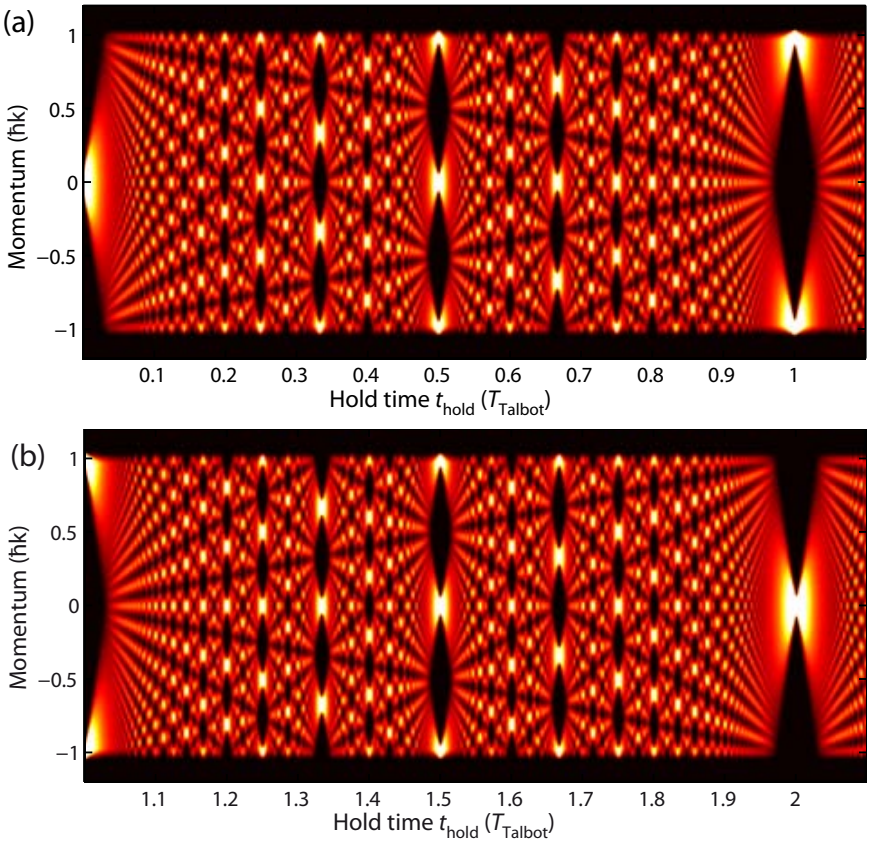

Fig. 3.9.: Calculated BEC-based temporal Talbot effect. (a) Momentum distribution as a function of the hold time t_{hold} starting from the initial BEC to the first revival at T_{Talbot} for a pure harmonic potential. White areas indicate a high occupation of the respective momentum state. (b) Same as in (a) from $t_{\mathrm{hold}} = T_{\mathrm{Talbot}}$ to $t_{\mathrm{hold}} = 2T_{\mathrm{Talbot}}$.

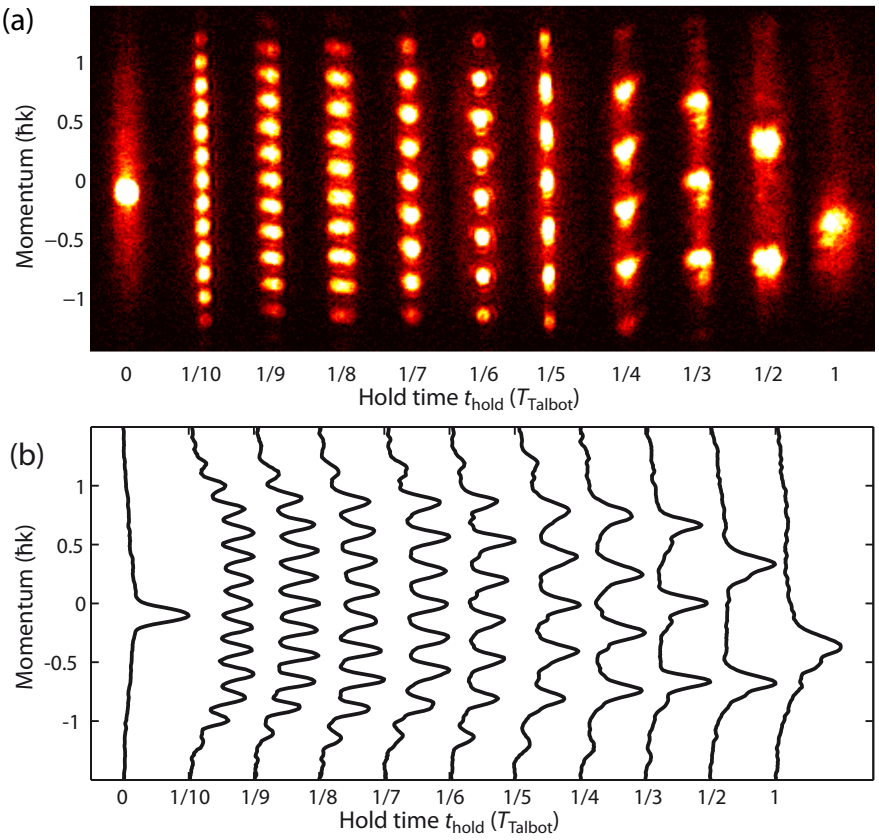

Fig. 3.10.: BEC-based temporal Talbot effect - experiment. (a) Series of absorption images after 80 ms of expansion, showing fractional Talbot fringes of different order in momentum space, starting from the initial momentum distribution of the BEC after two BOs (left), followed by the 10^{th} order at $T_{\text{Talbot}}/10$, 9^{th} order at $T_{\text{Talbot}}/9$, etc., down to the 0^{th} order at the Talbot time (right). Note that the time axis is not linear. White areas indicate higher density. (b) Horizontally integrated density profiles obtained from the absorption images shown in (a). Note that, e.g. for $T_{\text{Talbot}}/10$, the outermost momentum component appears twice, i.e. at both edges of the Brillouin zone.

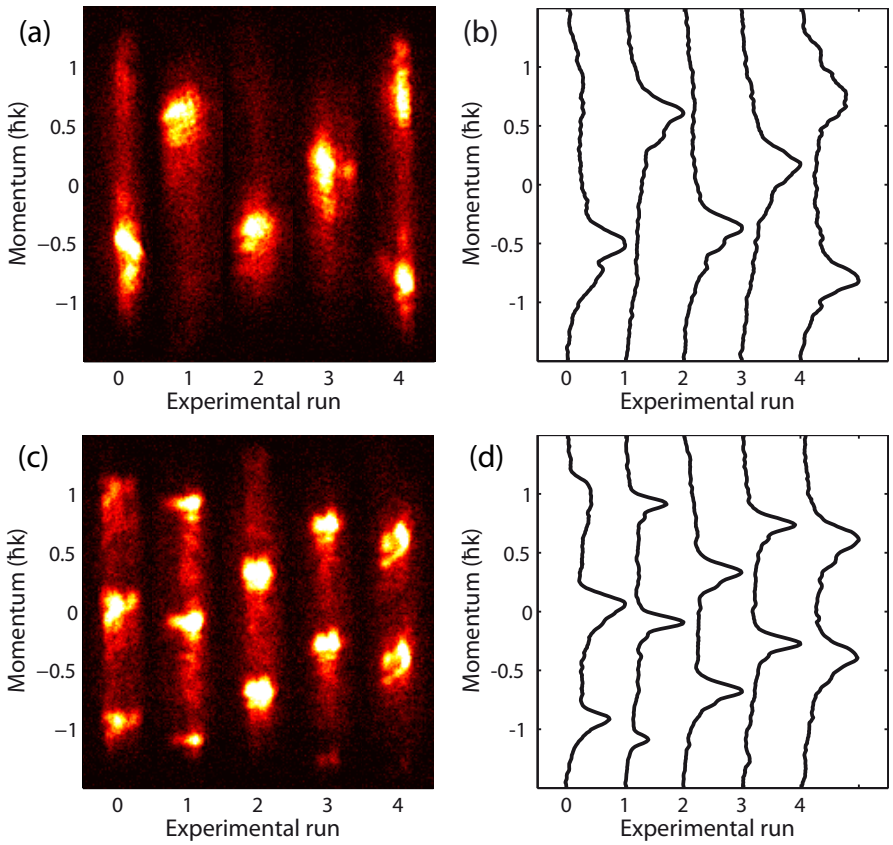

Fig. 3.11.: Variations in the momentum distribution between successive experimental realisations for long hold times. (a) Absorption images of five individual experimental realisations with $t_{\mathrm{hold}} = T_{\mathrm{Talbot}}$. White areas indicate higher density. (b) Horizontally integrated density profiles obtained from the absorption images shown in (a). (c) Absorption images of five individual experimental realisations with $t_{\mathrm{hold}} = T_{\mathrm{Talbot}}/2$. (d) Horizontally integrated density profiles obtained from the absorption images shown in (c). Note that, in addition to the random shift in quasimomentum space caused by δ, effects of horizontal dynamics, especially fragmentation and density variations along the horizontal axis, can be observed.

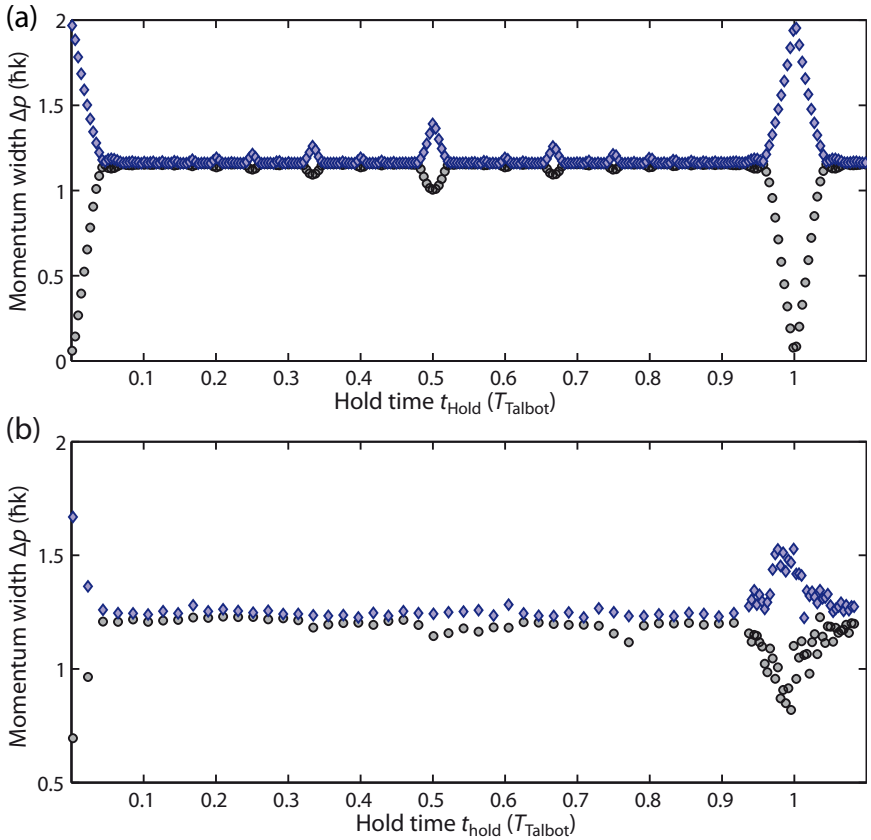

Fig. 3.12.: Talbot revival as evidenced by the spread of the momentum width Δp. (a) Calculated $(\Delta p)_{\max}$ (blue diamonds) and $(\Delta p)_{\min}$ (black circles) as a function of t_{hold} in units of T_{Talbot}. (b) Measurement of $(\Delta p)_{\max}$ (blue diamonds) and $(\Delta p)_{\min}$ (black circles) as a function of t_{hold} in units of T_{Talbot} for a vertical trap frequency of $\omega_z = 2\pi \times 22.0(2)\,\text{Hz}$. The extrema are determined from a sample of 10 single experimental realisations for each value of t_{hold}.

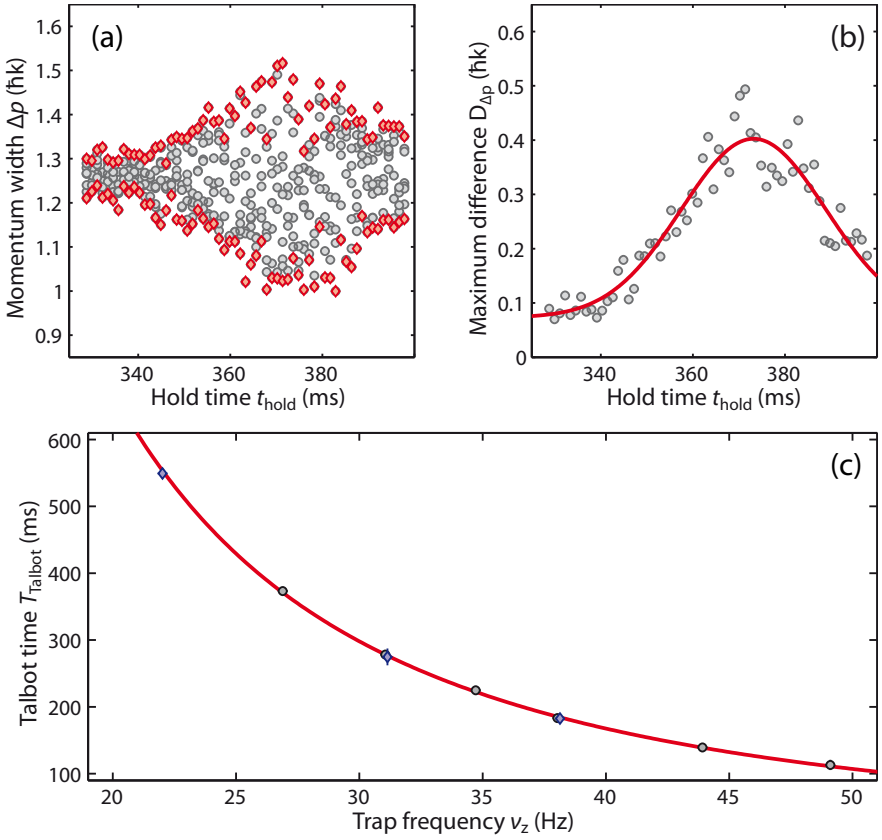

Fig. 3.13.: Talbot time T_{Talbot} as a function of the external confinement strength. (a) Momentum width Δp in the vicinity of the expected T_{Talbot} for a dipole trap frequency of $\omega_z = 2\pi \times 26.9(2)$ Hz for 10 single experimental realisations (black circles). The extrema $(\Delta p)_{\mathrm{max}}$ and $(\Delta p)_{\mathrm{min}}$ are indicated as red diamonds. (b) Calculated $D_{\Delta \mathrm{p}}$ for the measured extrema in (a). The solid line represents a gaussian fit, from which T_{Talbot} is derived. (c) Dependence of T_{Talbot} on the trap frequency $\nu_z = \omega_z/(2\pi)$. The black (blue) circles (diamonds) represent measurements for which the external harmonic trap is generated by the dipole trap beam with 46 μm (144 μm) beam waist. The solid line gives the calculated values for T_{Talbot}. The vertical error bars are the 1σ uncertainty of the maximum position of the gaussian fit as shown in (b). The horizontal error bars are equal or smaller than the symbol size.

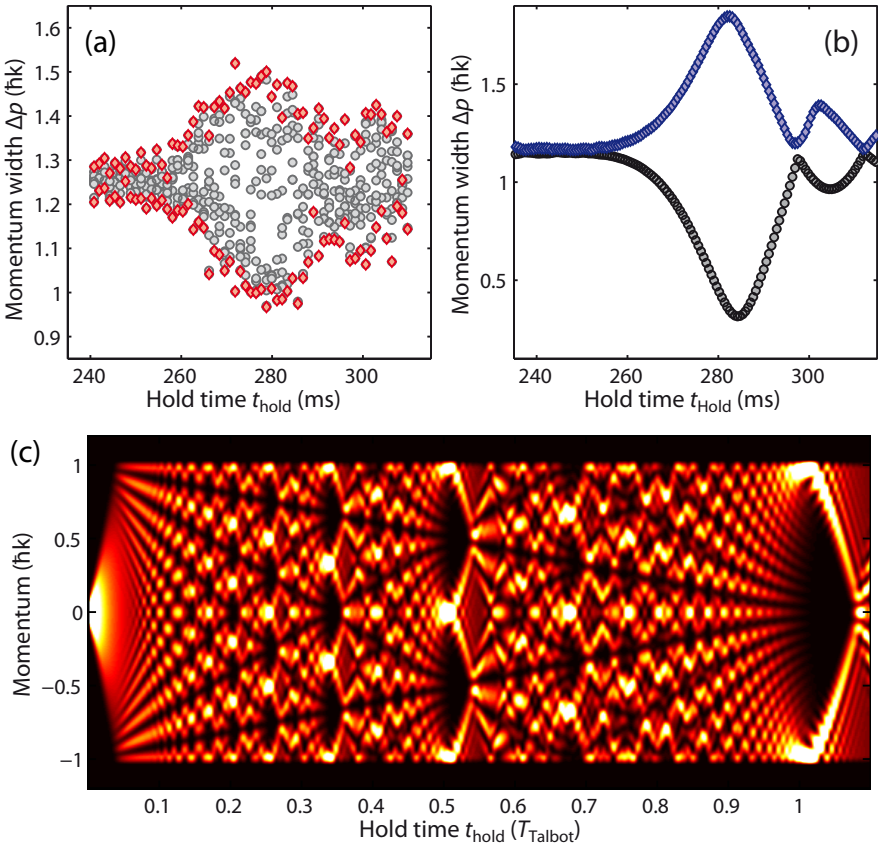

Fig. 3.14.: Effect of the anharmonic trapping potential on the momentum distribution. (a) Momentum width Δp in the vicinity of the expected T_{Talbot} for a dipole trap frequency of $2\pi \times 31.1(2)\,\mathrm{Hz}$ for 10 single experimental realisations (black circles). The vertical dipole trap is created by the more tightly focused dipole trap beam with a beam waist of $46\,\mu\mathrm{m}$. The extrema $(\Delta p)_{\mathrm{max}}$ and $(\Delta p)_{\mathrm{min}}$ are indicated as red diamonds. (b) Calculated $(\Delta p)_{\mathrm{max}}$ and $(\Delta p)_{\mathrm{min}}$ in the vicinity of the expected T_{Talbot} for the same experimental parameters as in (a). For the trapping potential the real gaussian shape of the dipole trap is used. (c) Full calculation of the momentum distribution as a function of the hold time t_{hold} using the same parameters as in (b).

3.4. Publication: Inducing Transport in a Dissipation-Free Lattice with Super Bloch Oscillations

Phys. Rev. Lett. **104**, 200403 (2010)[†]

Elmar Haller, Russell Hart, Manfred J. Mark, Johann G. Danzl, Lukas Reichsöllner, and Hanns-Christoph Nägerl

Institut für Experimentalphysik und Zentrum für Quantenphysik, Universität Innsbruck, Technikerstraße 25, A–6020 Innsbruck, Austria

Particles in a perfect lattice potential perform Bloch oscillations when subject to a constant force, leading to localization and preventing conductivity. For a weakly-interacting Bose-Einstein condensate (BEC) of Cs atoms, we observe giant center-of-mass oscillations in position space with a displacement across hundreds of lattice sites when we add a periodic modulation to the force near the Bloch frequency. We study the dependence of these "super" Bloch oscillations on lattice depth, modulation amplitude, and modulation frequency and show that they provide a means to induce linear transport in a dissipation-free lattice.

[†]The author of the present thesis contributed to this work by maintaining and improving the experimental setup and paper writing.

3.4.1. Introduction

Understanding the conduction of electrons through solids is of fundamental concern within the physical sciences. The simplified situation of an electron under a constant force F within a perfect, non-dissipative, periodic lattice was originally studied by Bloch and Zener [Blo28, Zen34] over 70 years ago. Their and subsequent studies revealed that the particle would undergo so-called Bloch oscillations (BOs), a periodic oscillation in position and momentum space, thereby quenching transport and hence resulting in zero conductivity. BOs can be viewed as periodic motion through the first Brillouin zone, resulting in a Bloch period $T_B = 2\hbar k/F$, where $k = \pi/d$ is the lattice wave vector for a lattice spacing d. They result from the interference of the particle's matter wave in the presence of the periodic lattice structure, requiring a coherent evolution of the wave during the time T_B. Generally, it is believed that conductance is restored via dissipative effects such as scattering from lattice defects or lattice phonons [Kan95, Ash76]. In bulk crystals, relaxation processes destroy the coherence of the system even before a single Bloch cycle is completed. These systems thus exhibit conductivity but prevent the observation of BOs. To observe BOs, the BO frequency $\nu_B = 1/T_B$ must be large compared to the rate of decoherence. In semiconductor superlattices, where the Bloch frequency is enhanced, a few cycles have been observed [Leo92].

A recent approach to observe and study BOs is to use systems of ultracold atoms in optical lattice potentials with a force that is provided by gravity or by acceleration of the lattice potential. In these engineered potentials, generated by interfering laser waves, dissipation is essentially absent, and decoherence can be well-controlled [Gus10]. Essentially all relevant system parameters are tunable, e.g. lattice depth and spacing, particle interaction strength, and external force, i.e. lattice tilt. For sufficiently low temperatures, a well-defined narrow momentum distribution can initially be prepared. BOs have been observed for thermal samples [BD96, Bat04, Fer06], for atoms in weakly-interacting Bose-Einstein condensates (BECs) [And98, Mor01, Gus08b], and for ensembles of non-interacting quantum-degenerate fermions [Roa04]. Non-interacting BECs [Gus08b, Fat08a] are ideally suited to study BOs as interaction-induced dephasing effects are absent, allowing for the observation of more than 20000 Bloch cycles [Gus08b].

As for any oscillator, classical or quantum, it is natural that one investigates the properties of the oscillator under forced harmonic driving. The dynamics of a harmonically driven Bloch oscillator has recently been the subject of several theoretical [Kor03, Har04, Tho02, Kol09] and experimental studies [Wil96, Sia08, Iva08, Alb09]. For example, modulation-enhanced tunneling between lattice sites [Sia08, Iva08] and spatial breathing of incoherent atomic samples [Alb09] have been observed. Here, for a weakly-interacting atomic BEC in a tilted lattice potential, we demonstrate that harmonic driving can lead to directed center-of-mass motion and hence to transport. More strikingly, for slightly off-resonant driving, we observe giant matter-wave oscillations that extend over hundreds of lattice sites. These "super Bloch oscillations" result from

a beat between the usual BOs and the drive. They are rescaled BOs in position space and can also be used, by appropriate switching of the detuning or the phase, to engineer transport.

3.4.2. Super Bloch oscillations

The experimental starting point is a tunable BEC of 1.2×10^5 Cs atoms in a crossed beam dipole trap [Kra04] adiabatically loaded within 400 ms into a vertically oriented 1D optical lattice [Gus08b] as illustrated in Fig. 3.15(a). The lattice spacing is $d = \lambda/2$, where $\lambda = 1064.49(1)$ nm is the wavelength of the light. Unless stated otherwise, we work with a shallow lattice with depth $V = 3.0(3)\ E_R$, where $E_R = h^2/(2m\lambda^2)$ is the photon recoil energy for particles with mass m. The atoms are initially levitated against gravity by means of a magnetic field gradient and spread across approximately 50 lattice sites with an average density near 5×10^{13} cm^{-3} in the central region of the sample. We control the strength of the interaction as measured by the s-wave scattering length a near a Feshbach resonance [Kra04]. Throughout this work, unless stated otherwise, we work at $a = 11(1)\ a_0$, where a_0 is Bohr's radius. We initiate BOs by removing, the dipole trap confinement in the vertical direction and by reducing the levitation in 1 ms to cause a force that is a small fraction of the gravitational force mg, for which ν_B is near 100 Hz. An additional harmonic modulation of the levitation gradient then results in an oscillating driving force $F(t) = F_0 + \Delta F \sin(2\pi\nu t + \phi)$, where F_0 is the constant force offset, ΔF is the amplitude of the modulation, ν is the modulation frequency, and ϕ is a phase difference between the BOs and the drive. After a given hold time τ we switch off all optical beams and magnetic fields and take in-situ absorption images after a short delay time of 800μs.

We first determine the excitation spectrum. Fig. 3.15(b) shows the $1/\sqrt{e}$-width W of the matter wave after $\tau = 2$ s as a function of ν. A series of narrow resonances at rational multiples of ν_B can clearly be identified. In agreement with recent experiments [Sia08, Iva08], we attribute these resonances to modulation-enhanced tunneling between lattice sites, leading to dramatic spreading of the atomic wave packet. Tunneling between nearest neighbor lattice sites is enhanced when ν_B is an integer multiple j of ν via a j-phonon process [Eck05a], while tunneling between lattice sites i lattice units apart is enhanced when ν is an integer multiple i of ν_B. Even combinations thereof, e.g. $i/j = 2/3$ or $2/5$, are detectable.

We now investigate the dynamics of the wave packet in more detail. For this, we use the resonance with $i = j = 1$ and choose $\nu = \nu_B + \Delta\nu$, where $\Delta\nu$ is the detuning. In Fig. 3.16(a)-(d) we present absorption images and spatial profiles for the weakly-interacting BEC. The time evolution for the width, shape, and center position of the BEC is dramatic. On resonance ($\Delta\nu = 0$), (c) and (d), the atomic ensemble spreads as it develops pronounced edges. Also, as we will see below, the center-of-mass motion depends crucially on the phase ϕ. Off resonance, (a) and (b), for small detuning $\Delta\nu = -1$ Hz, the wave packet

exhibits giant oscillatory motion across hundreds of lattice sites that we denote as "super Bloch oscillations" (sBO). Note that, for the parameters used here, the amplitude for ordinary BOs corresponds to about $4d = 2.1$ μm. Also the width and higher moments of the distribution show oscillatory behavior. In Fig. 3.16(e) we plot the center-of-mass position as a function of time for $\Delta\nu = -1$ Hz. At $a = 11(1)$ a_0 we typically observe sBOs over the course of several seconds. The dynamics of sBOs strongly depends upon the site-to-site phase evolution of the matter-wave. In fact, stronger interactions, e.g. $a = 90(1)$ a_0, distort the density profile of the driven BEC and alter the BEC's oscillation frequency and amplitude. For sufficiently strong interactions, no sBOs are observed. We also attribute the wave-packet spreading as seen after one cycle in Fig. 3.16(b) mostly to interactions. For the measurements above, we intentionally use a large modulation amplitude ΔF to enhance the amplitude of sBOs. However, all effects equally exist for $\Delta F \ll F_0$, as we will also demonstrate below in Fig. 3.18(b).

3.4.3. Models and data analysis

It is useful to develop a simple semi-classical model to obtain a qualitative understanding of the origin of sBOs. The only elements of this model are that the wave packet is accelerated by the applied force and that, once the wave packet reaches the edge of the first Brillouin zone, it is Bragg reflected. This model does not include an effective mass and cannot be used to predict quantitative results. Fig. 3.17(a)-(d) shows the result of a numerical integration of the time-dependent acceleration $a(t) = F_0/m + \Delta F/m \sin(2\pi(\nu_B + \Delta\nu)t + \phi)$ with periodic Bragg reflection. For a constant acceleration $\Delta F = 0$, the wave packet's velocity shows the well-known saw-tooth-like time evolution that corresponds to BOs. The curve in (a) is symmetric, hence, there is no net movement, as indicated by the shaded regions of equal area. If, however, there is additional harmonic modulation at $\nu = \nu_B$, the velocity excursions will not be symmetric about zero, (b), and result in a net movement for each period, leading to linear motion, (c). Only for $\phi = \pi/2$ or $\phi = 3\pi/2$ symmetry is restored and no net movement will occur. Note that, in general, the velocity of the linear motion depends non-trivially on ϕ. Off-resonant modulation with $\Delta\nu \ll \nu_B$ induces a slowly-varying phase mismatch between the drive and the original Bloch period. This results in a slow oscillation of the net movement for each Bloch cycle, which finally sums up to a giant oscillation in position space, (d). Evidently, this oscillation is the result of a beat between the drive and the original BO. The initial direction of the motion depends on ϕ and $\Delta\nu$. In particular, a change in the sign of $\Delta\nu$ at a given ϕ can lead to opposite motion in position space, as verified experimentally in Fig. 3.17(e) for $\Delta\nu = \pm 1$ Hz.

A quantitative understanding of sBOs [Kol09] can be obtained from an approach based on Wannier-Stark states [Tho02]. In essence, the harmonic drive is expected to lead to a rescaling of the tunneling rate $J \to J_{\text{eff}} = JB_1(\Delta F/F_0)$ and the force $F_0 \to F_{\text{eff}} = h\Delta\nu/d$ for a stationary lattice with tilt. Here, B_1

is the first Bessel function of the first kind. The amplitude of sBOs is thus given by a new Wannier-Stark localization length $L_{\text{eff}} \approx J_{\text{eff}}/(dF_{\text{eff}})$ [Kol09]. In this sense, sBOs are rescaled BOs. We quantitatively study the dependence of amplitude and period of sBOs on $\Delta\nu$, $\Delta F/F_0$, and V. The results are shown in Fig. 3.18. As expected, the period T is given by $1/\Delta\nu$. Also, the oscillation amplitude scales as $1/\Delta\nu$, and its Bessel-function dependence on $\Delta F/F_0$ is well reproduced. Given our spatial resolution, we can observe sBOs down to $\Delta F/F_0 = 0.08$ (Fig. 3.18(b)). Note that sBOs can only be observed with sufficient wave function coherence and for well-defined initial conditions, i.e. for sufficient wave packet localization in the first Brillouin zone of the lattice. Nevertheless, incoherent atomic samples exhibit a breathing of the spatial distribution [Alb09] as the oscillation period is insensitive to the initial conditions. In the work of Ref.[Alb09], the breathing can be understood in terms of an incoherent sum over localized Wannier-Stark states that individually show a breathing motion with period T [Tho02].

3.4.4. Inducing transport

The results above provide two mechanisms to circumvent the localization inherent in BOs and to induce coherent transport in an otherwise insulating context. As shown in Fig. 3.19(a), resonant modulation ($\Delta\nu = 0$) causes directed motion of the wave packet's center-of-mass. For longer times, we find that the motion is approximately linear. The mean velocity depends on the relative phase ϕ of the Bloch oscillator and the drive. In the experiment, we varied ϕ via $\phi = \phi_0 + \Delta\phi$, where ϕ_0 is a constant phase offset, which depends on the details how BOs are initiated. For off-resonant modulation, transport can be induced by switching the sign of $\Delta\nu$ before a half-cycle of a sBO is completed. The wave packet then continues to move in the original direction. This motion is shown in Fig. 3.19(b), where we switch the sign after 400 ms. For comparison, Fig. 3.19(c) shows a sBO with $T = 1$ s without switching.

3.4.5. Conclusion

In summary, we have studied the coherent evolution of matter waves in tilted periodic potentials under forced driving and have observed giant sBOs, which result from a beat of BOs with the drive when a small detuning $\Delta\nu$ from the Bloch frequency is introduced. Localization as a result of BOs is broken, allowing us to engineer matter wave transport over macroscopic distances in lattice potentials with high relevance to atom interferometry [Cro09]. We are now in a position to investigate the effect of interactions on driven transport, for which subdiffusive and chaotic dynamics have been proposed [Kol09].

During the final preparation of the manuscript we became aware of related work on non-dissipative transport in a quantum ratchet [Sal09]. We thank A. R. Kolovsky, A. Zenesini, and A. Wacker for discussions and R. Grimm for generous support. We acknowledge funding by the Austrian Ministry of Science

and Research and the Austrian Science Fund and by the European Union within the framework of the EuroQUASAR collective research project QuDeGPM. R.H. is supported by a Marie Curie Fellowship within FP7.

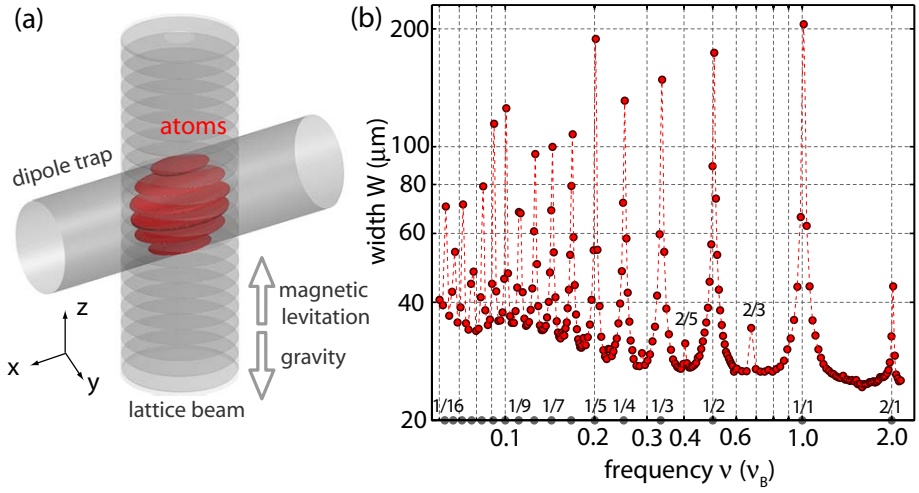

Fig. 3.15.: (color online) Experimental setup (a) and excitation spectrum (b) for atoms in a tilted periodic potential. The width W is plotted as a function of the drive frequency ν. The resonances correspond to a drastic spreading of the atomic wave packet as a result of modulation-assisted tunneling [Sia08] when $\nu \approx i/j \times \nu_B$, where i, j are integers. The parameters are $F_0 = 0.096(1)mg$, $\Delta F = 0.090(4)mg$, $V = 3.0(3)\ E_R$, and $\tau = 2$ s. The dashed line is a guide to the eye.

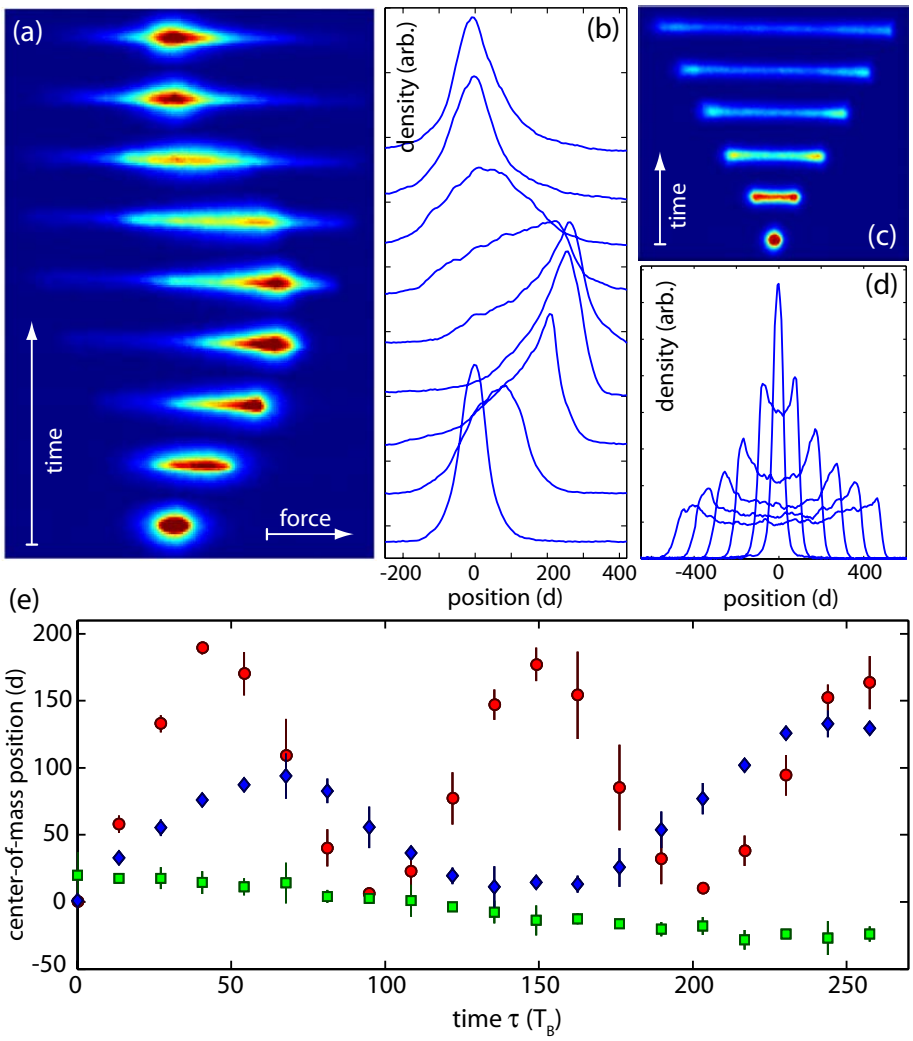

Fig. 3.16.: (color online) Observation of super Bloch oscillations and modulation-driven wave packet spreading. (a) and (b) In-situ absorption images and density profiles for off-resonant modulation ($\Delta\nu = -1$ Hz), showing giant oscillatory motion across more that 200 sites. (time steps of 120 ms, average of 4 images).(c) and (d) In-situ absorption images and density profiles for resonant modulation ($\Delta\nu = 0$ Hz), showing a wave packet that spreads symmetrically (time steps of 100 ms, average of 4 images). The phase ϕ was adjusted to allow for a symmetric spreading, corresponding to a calculated value of $\phi = \pi/2$. For (a)-(d), the parameters are $F_0 = 0.062(1)mg$, $\Delta F = 0.092(4)mg$, $V = 3.0(3)E_R$, $a = 11(1)$ a_0. (e) Center-of-mass motion for $a = 11(1)a_0$ (circles), $a = 90(1)a_0$ (diamonds), $a = 336(4)a_0$ (squares).

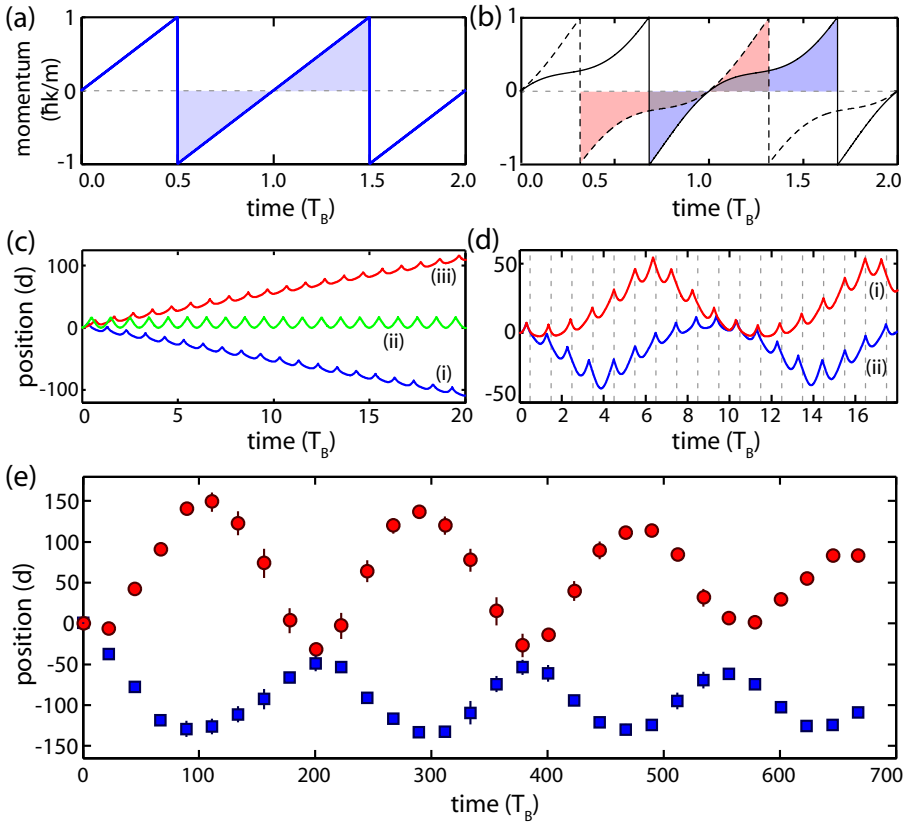

Fig. 3.17.: (color online) Results from a semi-classical model for sBOs. (a) For a constant force, here $F_0 = 0.06mg$, the velocity (in units of $\hbar k/m$) exhibits a symmetric, saw-tooth-like time evolution, typical for BOs. (b) Resonant modulation, here with $\Delta F = 0.8F_0$, alters the symmetric periodic velocity excursions of normal BOs ($\phi = 0$, solid line, $\phi = \pi$, dashed line), leading to a net-movement, (c), with $\phi = 0$ (i), $\phi = \pi/2$ (ii), and $\phi = \pi$ (iii). An additional detuning $\Delta\nu = \pm 0.1\nu_B$ results in a periodically changing phase difference and hence in giant oscillations in position space, (i) and (ii) in (d). On top of the motion, normal BOs can clearly be seen. The phase of sBOs depends on the sign of $\Delta\nu$, as shown by experimental data in (e), where $F_0 = 0.096(1)mg$, $\Delta F = 0.090(4)mg$, $\Delta\nu = 1$ Hz (circles), -1 Hz (squares).

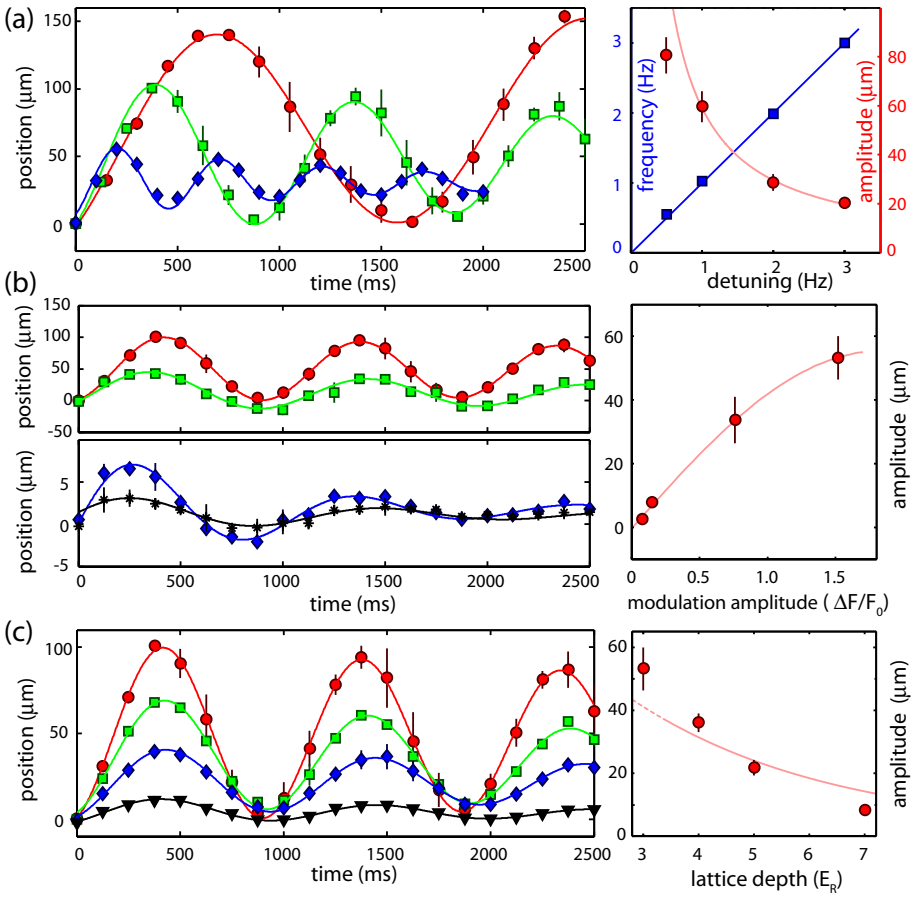

Fig. 3.18.: (color online) Quantitative analysis of sBOs. (a) The effect of the detuning $\Delta\nu$ on the oscillation frequency and the amplitude of sBOs, with $\Delta\nu = 0.5$ Hz (circles), 1 Hz (squares), 2 Hz (diamonds). Right: The solid lines are fits with linear and $\Delta\nu^{-1}$-dependence, respectively. (b) Dependence of the amplitude of sBOs on $\Delta F/F_0$. The data sets correspond to $\Delta F/F_0 = 1.52$ (circles), 0.76 (squares), 0.15 (diamonds), 0.08 (stars). Right: The solid line is a fit proportional to $B_1(\Delta F/F_0)$. (c) Amplitude of sBOs as a function of lattice depth, V= 3 E_R (circles), 4 E_R (squares), 5 E_R (diamonds), 7 E_R (triangles). Right: The solid line is a fit proportional to J, for which we omit the first data point for the shallow lattice. If not stated otherwise, the parameters for all measurements shown here are $F_0 = 0.062(1)mg$, $\Delta F = 0.092(4)mg$, $\Delta\nu = -1$ Hz.

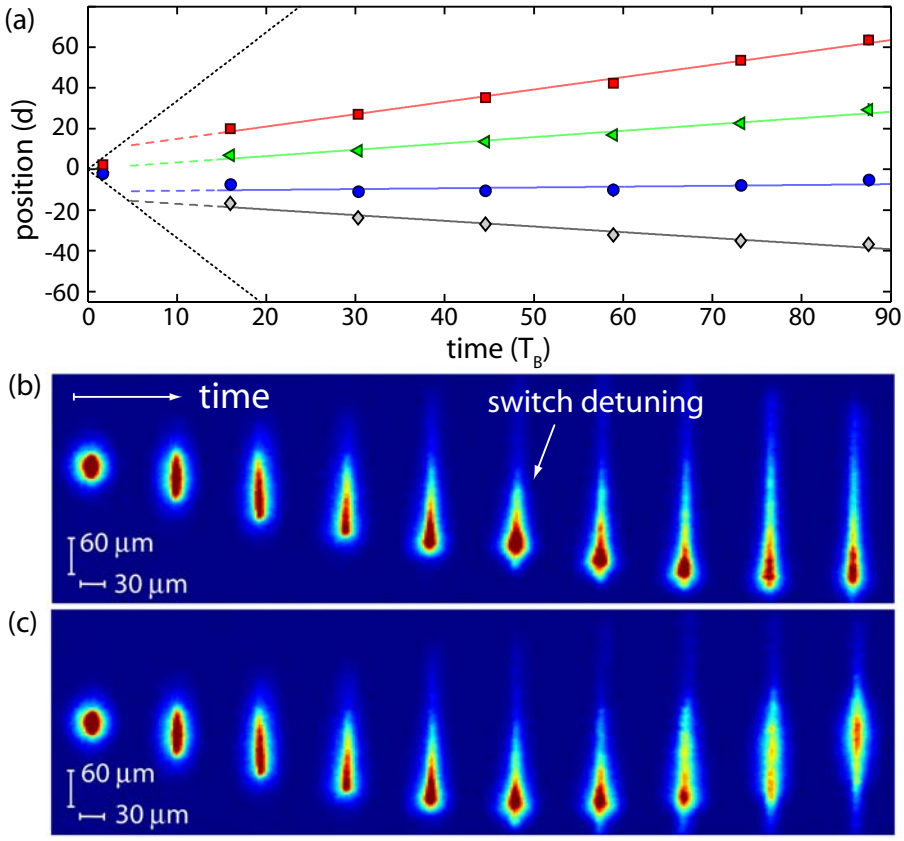

Fig. 3.19.: (color online) Inducing transport and suppressing interaction-induced dephasing. (a) Linear motion for resonant modulation. $\Delta\phi = 0°$ diamonds, 65° circles, 120° triangles, 190° squares. $\Delta\phi = 0°$ and $\Delta\phi = 190°$ were chosen to maximize the speed in opposite directions. The solid lines are linear fits to the data points excluding the first data point. For comparison we plot the linear motion that corresponds to a tunneling rate of J_{eff}, dotted lines. (b) Directed motion for off-resonant modulation. $\Delta\nu$ was switched from -1 Hz to 1 Hz after 400 ms. For comparison, (c) shows the oscillatory motion without switching (time steps of 80 ms). The parameters are $F_0 = 0.096(1)mg$, $\Delta F = 0.090(4)mg$.

CHAPTER 4

ULTRACOLD ROVIBRONIC GROUNDSTATE MOLECULES

4.1. Introduction

In this chapter, we report on our results of the creation of ultracold rovibronic groundstate molecules via association of cesium atoms to weakly bound dimers and subsequent transfer into deeply bound molecular states with the Stimulated Raman Adiabatic Passage (STIRAP) technique [Ber98]. Especially ultracold molecules in the rovibronic groundstate are of high interest, since collision-induced relaxations are absent and reactive collisions are energetically forbidden for most alkaline dimers [Żuc10]. They would allow collisional studies and the investigation and control of chemical reactions [Wei99, Kre08, Dul09], and in the case of heteronuclear dimers [Osp06a] enable the realization of dipolar quantum gases, as they exhibit a permanent electric dipole moment [Ni08] introducing long range anisotropic dipole-dipole interactions. A more detailed introduction and description of the experiments discussed in this chapter is given in the PhD thesis of Johann Danzl [Dan10a].

Several possible ways can lead to the creation of a trapped, high phase-space density sample of the rovibronic groundstate molecules. Direct laser cooling of molecules, recently demonstrated by Shuman *et al.* [Shu10], holds a great potential for the future, but is currently not able to cool molecules into the quantum degenerate regime. The same holds for methods directly cooling and slowing molecules [van08, Nar08, Mee09], as the temperatures they are currently able to reach are on the order of mK. Direct photoassociation [Wyn00, Jon06] in laser cooled atomic clouds produces molecules with very low temperatures, but does not reach high densities. The most successful method at the moment is the association of already ultracold atoms via magnetic field ramps using a Feshbach resonance [Köh06] and the subsequent transfer to the rovibronic ground state using STIRAP. This methods preserve the already high phase space density of ultracold atoms, and all created molecules populate one defined molecular state.

A trivial requirement for the creation of ultracold molecules via Feshbach association is the existence of such magnetically tunable resonances. As discussed already in section 1.6 they appear when the energy of a molecular state crosses the energy threshold of free atoms. Cesium in the lowest hyperfine state offers a rich molecular structure at low magnetic fields. Figure 4.1 shows the energy of the most relevant molecular states relative to the threshold of free atoms for cesium in the low magnetic field region.

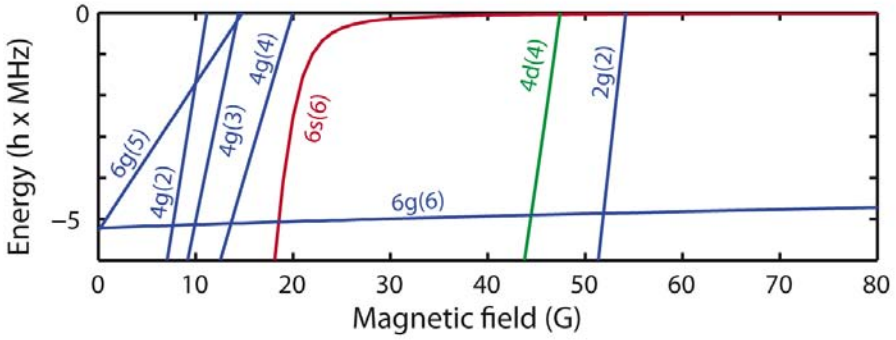

Fig. 4.1.: Molecular structure of Cs_2 near threshold. The molecular states are labeled according to $f, l, (m_f)$, with $\vec{f} = \vec{F_1} + \vec{F_2}$ the sum of the total atomic spins $\vec{F_1}, 2$ and m_f its projection, and the rotation $l = 0, 2, 4$ labeled as s, d, g-states [Chi04b]. Each crossing of a molecular state with the threshold gives rise to a Feshbach resonance with a width depending on the strength of the coupling between the states. The curvature of the $6s(6)$ state is the result of a huge avoided crossing with a molecular state from the uppermost hyperfine channel. The figure is taken from [Dan10a].

Especially the Feshbach resonances connected to the $4d(4)$ and $4g(4)$ molecular states are typically used for the production of weakly bound dimers. For the subsequent transfer to deeply bound states the $6s(6)$ state is of special interest, since its character changes below the curvature at $\sim 20\,\mathrm{G}$ into a molecular state from the uppermost hyperfine channel, leading to an effective binding energy of more than $2 \times h\nu_{\mathrm{Cs}}$ with $\nu_{\mathrm{Cs}} \approx 9.19\,\mathrm{GHz}$ the hyperfine splitting in cesium. Thus the wavefunction overlap and therefore the coupling strengths to deeply bound states of the electronically excited state potential improves substantially.

The general scheme of our experiments is shown in Figure 4.2. After the production of a cesium BEC, we adiabatically load the BEC into our three-dimensional cubic lattice and drive the phase transition from the superfluid phase to the Mott insulator as already discussed in chapter 2. During this loading, we adapt the external confinement given by the additional dipole trap beams such that we maximize the number of doubly occupied sites [Vol06]. Using a Mott insulator as starting state for the transfer, losses due to inelastic molecule-molecule or atom-molecule collisions are greatly reduced. By ramping the magnetic field over a Feshbach resonance, we associate the atoms at doubly occupied sites to weakly bound molecules [Vol06] in the corresponding molec-

ular state. The remaining atoms are removed from the system by a combined microwave- and light-pulse [Tha06], and the molecules are transferred to the $6s(6)$ state, passing several avoided crossings, where we either ramp over adiabatic to change the molecular state or jump across fast enough to stay in the same state. The pure molecular sample is then transfered into an intermediate deeply bound state with a STIRAP sequence using lasers 1 and 2. Another STIRAP sequence using lasers 3 and 4 brings the molecules into the rovibronic ground state. An alternative transfer scheme employs a direct 4-photon STIRAP sequence, where lasers 1 and 4 perform the STIRAP sequence and laser 2 and 3 are kept on during the whole transfer, effectively coupling all the intermediate states together. To measure the amount of successfully transferred molecules, we reverse the whole procedure and count the number of reappearing atoms.

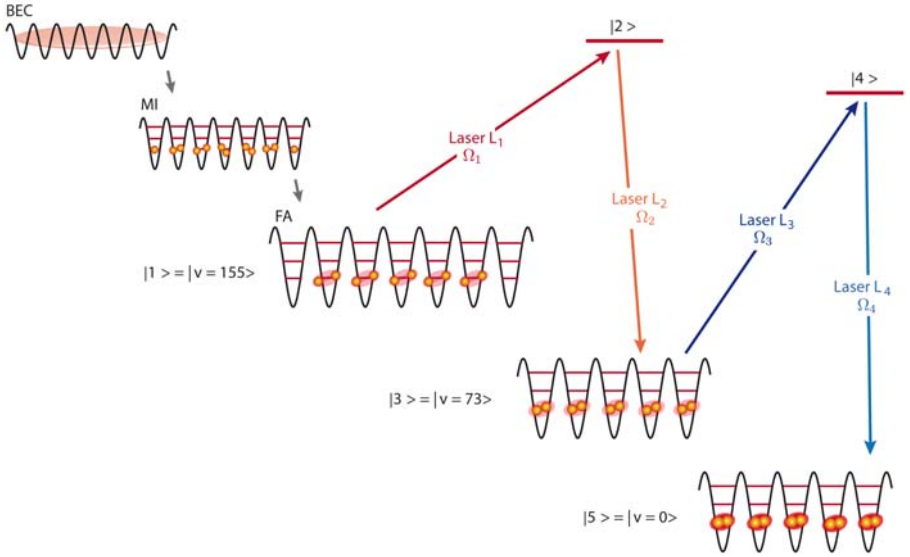

Fig. 4.2.: Production and transfer scheme of Cs_2 groundstate molecules. After loading a BEC into a 3D optical lattice and preparing a Mott insulator state, doubly occupied sites are transfered to weakly bound molecules via a adiabatic ramp over a magnetic feshbach resonance. In the first STIRAP step the molecules are transfered from the feshbach state |1> with lasers 1 and 2 over the excited state |2> into the deeply bound intermediate state |3> with a binding energy of $\sim$ 30 THz. The second STIRAP step transfers the molecules from state |3> into the rovibronic groundstate |5> via excited state |4> using lasers 3 and 4. The figure is adapted from [Dan10b]

The first step towards implementation of this scheme was the realization of the STIRAP transfer to the intermediate molecular state described in section 4.2. We showed that such a transfer between a weakly bound dimer and an chemically bound molecule with an binding energy of $\sim h \times 30$ THz can be realized with a high efficiency of over 80 %. The coherent character of the transfer was probed via a Ramsey-type experiment, showing interference between the weakly and deeply bound molecular state. Without employing the optical lattice for this

measurement, we were able to show that the molecular sample was not heated due to the transfer process. In Section 4.3 we repeated the measurement of this transfer step including the preparation of the molecular sample in an optical lattice. We were able to show that the transfer efficiency is not affected by the presence of the optical lattice, yet the rather short lifetime of the deeply bound molecules in the optical lattice of 20 ms indicated that near-resonant scattering from the lattice light has to be taken into account.

In section 4.4 we realized the second STIRAP transfer step into the rovibronic ground state reaching an overall transfer efficiency of $\sim 60\,\%$. By probing the lattice band structure with modulation spectroscopy we were able to calculate the polarizibility of the groundstate molecules, showing that our lattice fulfills the magic wavelength condition between the ground state molecules and the weakly bound dimers [Vex11]. This means that we have prepared rovibronic groundstate molecules in the lowest motional state on each lattice site, enabling us to perform fully state-selective experiments. The lifetime of the molecules in the lattice of more than 8 s proves that the lattice light is far off-resonant for excitations of the rovibronic groundstate, allowing long hold times for future experiments in the lattice and dipole traps. After improving the overall transfer efficiency, the dynamical melting of the lattice should enable us to create a stable BEC of rovibronic groundstate molecules [Jak02].

In Section 4.5 and 4.6 we show detailed spectroscopy data on the molecular levels needed for the first and second STIRAP transfer step. These measurements were necessary prerequisites for performing the transfers between the molecular states and contributed to theoretical improvements on the excited state calculations [Bai11].

4.2. Publication: Quantum gas of deeply bound ground state molecules

Science **321**, 1062 (2008)†

Johann G. Danzl[1], Elmar Haller[1], Mattias Gustavsson[1], Manfred J. Mark[1], Russell Hart[1], Nadia Bouloufa[2], Olivier Dulieu[2], Helmut Ritsch[3], and Hanns-Christoph Nägerl[1]

[1]*Institut für Experimentalphysik und Zentrum für Quantenphysik, Universität Innsbruck, Technikerstraße 25, 6020 Innsbruck, Austria*
[2]*Laboratoire Aimé Cotton, Université Paris-Sud Bât. 505, 91405 Orsay Cedex, France*
[3]*Institut für Theoretische Physik und Zentrum für Quantenphysik, Universität Innsbruck, Technikerstraße 25, 6020 Innsbruck, Austria*

Molecular cooling techniques face the hurdle of dissipating translational as well as internal energy in the presence of a rich electronic, vibrational, and rotational energy spectrum. Here, we create a translationally ultracold, dense quantum gas of molecules bound by more than 1000 wavenumbers in the electronic ground state. Specifically, we stimulate with 80% efficiency a two-photon transfer of molecules associated on a Feshbach resonance from a Bose-Einstein condensate of cesium atoms. In the process, the initial loose, long-range electrostatic bond of the Feshbach molecule is coherently transformed into a tight chemical bond. We demonstrate coherence of the transfer in a Ramsey-type experiment and show that the molecular sample is not heated during the transfer. Our results show that the preparation of a quantum gas of molecules in specific rovibrational states is possible and that the creation of a Bose-Einstein condensate of molecules in their rovibronic ground state is within reach.

†The author of the present thesis contributed to this work by assisting the experimental measurements. He also maintained and improved the experimental setup and contributed to the paper writing.

4.2.1. Introduction

Ultracold samples of molecules are ideally suited for fundamental studies in physics and chemistry, ranging from few-body collisional physics [Chi05, Kra06, Sta06, Zah06], ultracold chemistry [Kre05], and high resolution spectroscopy [Zel08, DeM08], to quantum gas preparation, molecular Bose-Einstein condensation [Ing08], and quantum processing [DeM02]. For many of the proposed experiments full control over the molecular wave function in specific deeply bound rovibrational states is needed. High densities are required for molecular quantum gas studies. Only in the rovibronic ground state, i.e. the lowest vibrational and rotational energy level of the electronic ground state, is collisional stability assured. However, direct molecular cooling towards high phase space densities seems yet out of reach [Doy04], whereas techniques like Feshbach association [Köh06] and photoassociation [Jon06] either produce molecules exclusively in weakly bound rovibrational levels, or suffer from low production rates and low state selectivity.

In order to produce a quantum gas of molecules in their absolute ground state, Jaksch *et al.* [Jak02] proposed a scheme for homonuclear alkali molecules in which the technique of stimulated two-photon transfer is repeatedly applied to molecules associated from a high-density sample of ultracold atoms. The initially very loosely bound molecules are transferred in successive steps to the rovibrational ground state of the singlet $X^1\Sigma_g^+$ molecular potential. The advantage of this scheme is that it is fully coherent, not relying on spontaneous processes, and that it involves only a very small number of intermediate levels. It promises that a ground state binding energy of typically 0.5 eV can be carried away without heating the molecular sample. It essentially preserves phase space density, allowing the molecular sample to inherit the high initial phase space density from the atomic sample. However, to realize this scheme, several challenges have to be met. First, there is a large difference in internuclear separation that has to be bridged: the overlap between the radial wave function of the least bound molecules with the radial wave functions of deeply bound molecular levels is extremely low, potentially leading to prohibitively low transition rates for the two-photon transitions. Second, the scheme requires the identification of suitable intermediate molecular levels while strictly avoiding parasitic excitations. Third, a large difference in binding energy has to be overcome. On a more technical side, the lasers driving the two-photon transitions at widely different wavelengths need to have extremely low relative short term phase jitter and high long term frequency stability to allow for coherence and reproducibility. In important experiments, Winkler *et al.* [Win07] and recently Ospelkaus *et al.* [Osp08] demonstrated highly efficient two-photon transfer into lower lying molecular levels starting from weakly bound dimer molecules, which were associated from ultracold atoms on a Feshbach resonance [Köh06]. However, the transferred molecules are still weakly bound. Their binding energy, on the order of the atomic hyperfine splitting, is less than 10^{-4} of the binding energy of the rovibrational ground state, and wave function overlap with this state is still negligible.

Here we demonstrate the crucial step towards full control of the molecular wave function and towards the formation of a Bose-Einstein condensate (BEC) of molecules in their rovibronic ground state by linking weakly bound molecular states with deeply bound rovibrational states. We coherently transfer an ultracold quantum gas of weakly bound cesium Feshbach molecules to the rovibrational level $|\nu = 73, J = 2>$ of the singlet $X^1\Sigma_g^+$ potential, bound by 1061 cm^{-1} (or $h\times$31.81 THz), corresponding to more than one fourth of the binding energy of the rovibrational ground state. To achieve this result, we overcome low wave function overlap by using a suitable intermediate excited molecular state while avoiding excitation into loss channels, and we reference the transfer lasers to a frequency comb, allowing us to flexibly bridge binding energy differences of more than 1000 cm^{-1}.

4.2.2. Preparation of Feshbach molecules

Figure 4.3 shows the energy of the relevant molecular and atomic states. Our experiment starts with a cigar-shaped BEC of cesium atoms in the lowest hyperfine sublevel $F = 3, m_F = 3$ in an optical dipole trap. For BEC production, we essentially follow the procedure detailed in [Web03a]. For Feshbach molecule production out of the BEC, we ramp up the offset magnetic field from the initial value of 2.1 mT to about 5.0 mT in 10 ms. We then ramp down, sweeping across a d-wave Feshbach resonance at 4.8 mT after about 1 ms as shown in Figure 4.3B [Her03, Mar07a]. Our procedure [Her03] gives an ultracold and dense sample of up to 11000 molecules every 10 s at densities above 1×10^{11} cm^{-3}. For the state transfer experiments discussed here, we do not separate the molecules from the original BEC. Upon lowering the magnetic field, the molecules are transferred from the initial state $|d>$ to a still weakly bound s-wave molecular state $|s>$ of the lowest hyperfine channel ($F_1 = 3, F_2 = 3$) via an avoided crossing [Mar07a]. The index $i = 1, 2$ denotes the i-th atom.

Upon further lowering the magnetic field to about 2.2 mT, the molecules enter into a closed channel s-wave molecular state $|a>$ via a second, broad avoided crossing [Mar07a]. This state belongs to the uppermost hyperfine channel ($F_1 = 4, F_2 = 4$) and thus has an effective binding energy of more than $2 \times h\nu_{\mathrm{Cs}}$. Here h is Planck's constant and $\nu_{\mathrm{Cs}} \approx 9.19$ GHz is the Cs clock frequency. Similar to $|s>$ this state is a mixture of the $X^1\Sigma_g^+$ ground state and the lowest triplet $a^3\Sigma_u^+$ state, coupled by hyperfine interaction, and it has zero rotational angular momentum. At a field of 1.9 mT, it has a binding energy of 5 MHz$\times h$ with respect to the $F = 3, m_F = 3$ two-atom asymptote [Mar07a]. As one might expect, we find that optical transition rates as measured below are improved when using this effectively more deeply bound state as the initial state for two-photon transfer instead of state $|s>$. We shut off the trap and perform all subsequent experiments in free flight. This does not affect the particle density immediately, but reduces it during the later detection procedure, which takes about 6ms, in order to avoid collisions between atoms and weakly bound dimers and hence loss. We detect molecules in $|a>$ via states $|s>$ and $|d>$ by first

applying a magnetic field gradient for atom-molecule Stern-Gerlach separation, then reversing the magnetic field ramp, and finally dissociating them on the Feshbach resonance at 4.8 mT, and imaging the resulting atoms [Her03].

4.2.3. Molecular spectroscopy

Efficient two-photon transfer via the stimulated Raman adiabatic passage (STIRAP) technique [Ber98, Win07] relies on a suitable choice for the excited state $|e\rangle$. In our case this state must have singlet character so that it can be used as a transfer state to deeply bound levels of the $X^1\Sigma_g^+$ potential. In general, it must be well separated from other states, which otherwise could be off-resonantly excited. It should thus be situated far to the red of the excited $S_{\frac{1}{2}}+P_{\frac{1}{2}}$ potential asymptote to avoid the high density of excited molecular states near that asymptote. We have performed optical loss spectroscopy starting from state $|a\rangle$ in the wavelength range from 1120 to 1130 nm, about 2300 cm^{-1} to the red of the cesium D_1 line. For this measurement we recorded the number of remaining molecules in $|a\rangle$ as a function of excitation wavelength and found two progressions of lines, which we assign to the potential curves of the mixed $(A^1\Sigma_u^+ - b^3\Pi_u)\ 0_u^+$ excited states and to the $(1)^3\Sigma_g^+$ excited state, respectively. For the present experiments, we choose for $|e\rangle$ a level of the 0_u^+ progression which is 8879.63(1) cm^{-1} above the $F=3, m_F=3$ two-atom asymptote, corresponding to a transition wavelength of 1126.173(1) nm (Figure 4.3A). We measure all wavelengths on a home-built wavemeter. We identify this previously unknown level as the 225th one of the 0_u^+ system, with an uncertainty of two in the absolute numbering.

The ground state level $|g\rangle$ with vibrational quantum number $\nu = 73$ is well known from conventional molecular spectroscopy [Wei85, Ami02]. However, its binding energy, as well as the binding energy of all deeply bound vibrational levels, has only been known with an uncertainty of about ± 0.45 cm^{-1} prior to the present experiments [Ami02]. We search for $|g\rangle$ by exciting the transitions from $|a\rangle$ to $|e\rangle$ with laser L_1 and from $|e\rangle$ to $|g\rangle$ with laser L_2 simultaneously. The two light fields create a molecule-molecule dark state. The molecules initially in $|a\rangle$ are lost unless the second laser L_2 is on two-photon resonance, provided that the Rabi frequency Ω_2 on the second transition is equal to or greater than Ω_1, the Rabi frequency on the first transition. For coherence, stability, and reproducibility, we lock both lasers to independent narrow-band optical resonators, which we reference to an optical frequency comb [1]. The comb is not calibrated,

[1] Laser L_1 near 1126 nm and laser L_2 near 1006 nm are continuous-wave grating-stabilized tunable diode lasers with up to 26 mW and 5 mW of power at the sample position, respectively, both focused to a $1/e^2$-waist of about 25 μm for sufficiently high Rabi frequencies. We estimate the laser linewidth for both lasers to be on the order of 1 kHz. The laser beams propagate horizontally at an angle of 80° with the long axis of the BEC with vertical linear polarization. Copropagation assures that the imparted photon recoil during STIRAP is minimal, corresponding to an energy of $k_B \times 0.4$ nK, with Boltzmann's constant k_B. The beam intensity is controlled by acousto-optical modulators, allowing pulse lengths down to 1 μs.

but it allows precise differential frequency measurements and provides long-term stability needed for systematic line searches [2]. We find the resonance condition with vibrational level $\nu=73$ at 1005.976(1) and 1005.982(1) nm, corresponding to rotational quantum numbers $J=0$ and 2. Identification of J is possible since the rotational energy splitting is well known. Figures 4.4 A and B show typical molecular dark resonances when we set L_2 on resonance and step the detuning Δ_1 of L_1 near 1126.173 nm. Figure 4.4C shows a dark resonance involving $\nu=73, J=2$ using a different excited molecular state $|e'>$, which is excited with L_1 near 1123.104 nm.

Figures 4.4 D-F show dark resonances involving the neighboring vibrational levels $\nu=71$ and $\nu=72$. These $X^1\Sigma_g^+$-levels were easily found based on previously acquired Cs_2 spectra [Ami02]. We determine the binding energy of these levels with respect to the atomic $F_1=3, F_2=3$ asymptote at zero magnetic field to be $1060.9694(10), 1088.3101(10), 1115.9148(10)$ cm^{-1} for $\nu=73, 72, 71$ with $J=0$, respectively. The binding energy of the rovibrational ground state $\nu=0$ is thus 3628.7053(14) cm^{-1}, which represents an improvement in precision of more than two orders of magnitude compared to the previous determination [Ami02]. Fitting the data for the dark resonances with a three-level model taking into account off-resonant excitations and laser line widths, we determine the molecular transition strengths as given by the normalized Rabi frequencies for the transitions $|a>$ to $|e>$ and $|e>$ to $|\nu=73, J=2>$ to be $\Omega_1=2\pi\times 2$ kHz $\sqrt{I/(\mathrm{mW/cm^2})}$ and $\Omega_2=2\pi\times 11$ kHz $\sqrt{I/(\mathrm{mW/cm^2})}$, respectively. A comparison with a typical atomic transition strength of $\Omega_a=2\pi\times 5$ MHz $\sqrt{I/(\mathrm{mW/cm^2})}$ giving $|\Omega_1/\Omega_a|^2 < 10^{-6}$ reflects the minuteness of the wave function overlap.

4.2.4. STIRAP transfer

We are now in a position to carry out coherent transfer using the STIRAP technique. For $|g>$ we choose the vibrational level with $\nu=73, J=2$. This level will allow us to reach the rovibrational ground state $\nu=0, J=0$ with a second STIRAP step in view of the selection rule $\Delta J=0,\pm 2$. STIRAP uses a counterintuitive overlapping pulse sequence in which L_2 is pulsed on prior to L_1. As is well known [Ber98], STIRAP relies on the existence of a dark state of the form $|D>=\alpha(t)|a>+\beta(t)|g>$. With sufficient adiabaticity, the function $|\alpha(t)|^2$ decreases smoothly from 1 to 0, while the function $|\beta(t)|^2$ increases smoothly from 0 to 1. The initial state $|a>$ is thus rotated via $|D>$ into the final state $|g>$. The criterion for adiabaticity is $\tau_p\Omega^2 \gg (2\pi)^2\Gamma$, where τ_p is the pulse overlap time, $\Omega \approx \Omega_1 \approx \Omega_2$ is the peak Rabi frequency during the pulse, and $\Gamma \approx 2\pi \times 4$ MHz is the (spontaneous) decay rate from the upper state $|e>$ as determined from our loss measurements. This criterion is quite stringent, in particular in view of the low wave function overlap that enters into Ω. An upper (experimental) limit for τ_p is given by the relative laser coherence time for L_1

[2] The wavemeter calibration is currently not sufficient to allow absolute numbering of the frequency comb teeth.

and L_2. We choose τ_p to be approximately 10 μs. For detection, we apply the reverse STIRAP sequence after a waiting time $\tau_w \approx 10$ μs to transfer the molecules back into $|a>$. During this time we leave laser L_1 on to assure that all possible residual population in state $|a>$ is removed.

We perform double STIRAP about 3 ms after the production of the Feshbach molecules and 1 ms after shutting off the trap. Figure 4.5A shows the molecular population in $|a>$ as a function of the STIRAP time τ, and Figure 4.5B shows the timing sequence for the double transfer scheme. For recording the time evolution of the population we interrupt the transfer process after time τ and measure the remaining population in $|a>$. The molecules in $|a>$ initially disappear during the first STIRAP sequence. They are now in level $|\nu=73, J=2>$ of the singlet $X^1\Sigma_g^+$ potential. Then a large fraction of them returns in the course of the reverse STIRAP sequence. For this particular measurement both lasers are on resonance. The peak Rabi frequencies are $\Omega_1 \approx 2\pi \times 3$ MHz and $\Omega_2 \approx 2\pi \times 6$ MHz. We typically obtain an overall efficiency of more than 65% for the double transfer process, corresponding to single pass efficiencies of more than 80%, assuming equal efficiencies for both passes. Figure 4.5C shows the double pass efficiency as a function of detuning Δ_2 of laser L_2. Simulations for the three-level system show that the ~ 800 kHz full width at half maximum of the efficiency curve is compatible with a combination of laser power broadening and Fourier broadening. Our simulations also show that higher transfer efficiencies can be expected for an optimized STIRAP pulse sequence in which both peak Rabi frequencies are equal. Molecules not transferred by STIRAP are resonantly excited to $|e>$ and then lost from our three-level system by spontaneous emission into a multitude of ground state levels.

4.2.5. Coherence and temperature

We demonstrate coherence of the transfer process in a Ramsey-type experiment [Win07], halting the transfer process by simultaneously shutting off both lasers 12 μs into the first STIRAP sequence when a balanced superposition of $|a>$ and $|g>$ has been created with $|\alpha(\tau)|^2 \approx \frac{1}{2} \approx |\beta(\tau)|^2$. After a hold time τ_h we resume the STIRAP transfer, with the roles of lasers L_1 and L_2 reversed. Thus, for $\tau_h = 0$ the population will simply be rotated back into the initial state. A three-level calculation shows that the population in the initial state $|a>$ is expected to oscillate at the rate of the two-photon detuning $|\Delta_2 - \Delta_1|/(2\pi)$. Figure 4.6A shows the initial state population for $\Delta_1 \approx 0$ and $\Delta_2 \approx 2\pi \times 113$ kHz as a function of τ_h. Indeed, the population oscillates with a frequency at $|\Delta_2 - \Delta_1|/(2\pi)$, however with marked increase in phase jitter on the time scale of 30 μs. We attribute this apparent loss of phase coherence to a slow relative frequency drift of lasers L_1 and L_2, leading to a slightly different two-photon detuning from one experimental run to the next. In Figure 4.6A, we have added a region indicating a frequency jitter of ± 6 kHz. This value is compatible with the present long-term stability of our lasers. Note that the frequency drift does not affect an individual STIRAP process as the transfer efficiency is very robust

against laser detuning as shown in Figure 4.5C.

We now show that the molecular sample is not heated during the transfer process and is indeed in the quantum gas regime. Specifically, we measure and compare the rate of expansion of the molecular sample in state $|a>$ without and with the double transfer process. In our regime the energy scale for expansion is usually set by the mean field of the BEC, resulting in typical expansion energies for the atoms in the range from $k_B \times 2$ nK to $k_B \times 10$ nK, where k_B is Boltzmann's constant, depending on the strength of the atomic interaction [Kra04]. We find that the initial magnetic field ramping excites collective motion of the BEC in the form of a breathing mode as a result of a change in the mean field potential due to a change in atomic interaction strength [Web03a]. The breathing is transformed into expansion of the sample when the trap is shut off. We follow the expansion by monitoring the change of the Thomas-Fermi radius r of the sample. Figure 4.6B shows this radius along the horizontal direction as a function of expansion time without and with STIRAP. Without STIRAP, we obtain from a linear fit an expansion rate of $dr/dt = 1.0(1)$ mm/s, corresponding to an energy of $k_B \times 14(4)$ nK. With STIRAP, the rate is $dr/dt = 0.7(1)$ mm/s, corresponding to an energy of $k_B \times 7(2)$ nK. Both values are compatible with a separate measurement of the expansion of the atomic BEC for the same magnetic field ramp. Interestingly, the rate for the case with STIRAP is lower. We speculate that STIRAP with the tightly focused laser beams L_1 and L_2 preferentially transfers molecules in the center of the sample and is hence responsible for some selection in velocity space.

It should now be possible to add a second STIRAP step for transfer into the rovibrational ground state $\nu = 0, J = 0$. A suitable two-photon transition at readily available laser wavelengths is via the 68th excited state level of the 0_u^+ potential near 1329 nm (up) and 991 nm (down) with comparatively good wave function overlap at the level of $|\Omega/\Omega_a|^2 \approx 10^{-4}$. We expect that searching for dark resonances will be straightforward as now all two-photon transition energies are known to 10^{-3} cm^{-1}. Molecules in $\nu = 0, J = 0$ cannot further decay into a lower state upon a two-body collision, and they are thus expected to allow the formation of an intrinsically stable molecular BEC. The high speed of our STIRAP transfer will allow us to perform in-situ as well as time-of-flight imaging for direct characterization of the spatial and momentum distribution of the molecular ensemble.

4.2.6. Conclusion

With our technique any low-lying vibrational state can be coherently populated in a controlled fashion with full control over the rotational quantum number, allowing, e.g., state-specific collisional studies and high-precision molecular spectroscopy with possible implications for fundamental physics [Zel08, DeM08]. Our procedure can be adapted to other species, in particular to heteronuclear alkali dimers such as RbCs [Sag05] and KRb [Osp08] for the creation of dipolar quantum gases [Gór02]. For heteronuclear alkali dimers a single two-photon transfer

step might suffice as a result of favorable wave function overlap [Stw04]. We expect that the combination of our technique with Feshbach molecule production out of a Mott-insulator state in a three-dimensional lattice [Vol06] will increase the initial Feshbach molecule production efficiency, avoiding collective excitations as a result of magnetic field ramping and inhibiting collisional loss, and will provide full control over all internal and external quantum degrees of freedom of the ground state molecules.

We thank the team of J. Hecker Denschlag, the LevT team in our group, and T. Bergeman for very helpful discussions and M. Prevedelli for technical assistance. We are indebted to R. Grimm for generous support and gratefully acknowledge funding by the Austrian Ministry of Science and Research (BMWF) and the Austrian Science Fund (FWF) in form of a START prize grant and by the European Science Foundation (ESF) in the framework of the EuroQUAM collective research project QuDipMol.

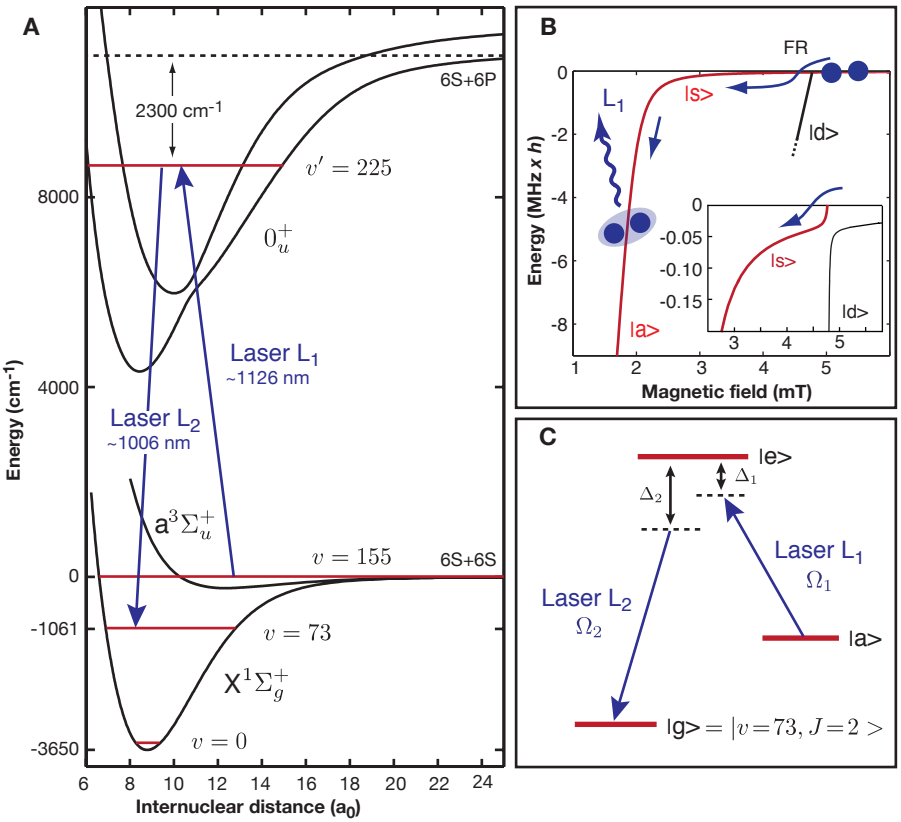

Fig. 4.3.: **A** Molecular level scheme for Cs_2. Molecules in a weakly bound Feshbach level are transferred to rovibrational level $|\nu=73, J=2>$ of the singlet $X^1\Sigma_g^+$ potential with a binding energy of 1061 cm^{-1} in a two-photon STIRAP process with wavelengths near 1126 nm and 1006 nm via the 225th level of the electronically excited $(A^1\Sigma_u^+ - b^3\Pi_u)$ 0_u^+ potentials. The $X^1\Sigma_g^+$ potential has about 155 vibrational levels. **B** Zeeman diagram showing the energy of all relevant weakly bound molecular levels for initial Feshbach molecular state preparation [Mar07a]. The binding energy is given with respect to the $F=3, m_F=3$ two-atom asymptote. The molecules are produced on a d-wave Feshbach resonance at 4.8 mT (see inset) and then transferred to the weakly bound s-wave state $|s>$ on an avoided state crossing. Further lowering of the magnetic offset field to 1.9 mT transfers the molecules from $|s>$ to state $|a>$, the starting state for the STIRAP transfer. **C** STIRAP transfer scheme [Ber98]. The molecules are transferred from the initial state $|a>$ to the final state $|g>=|\nu=73, J=2>$ by means of two overlapping laser pulses for which laser L_2 is pulsed on prior to L_1. The detunings and Rabi frequencies of L_i are Δ_i and Ω_i, $i=1,2$.

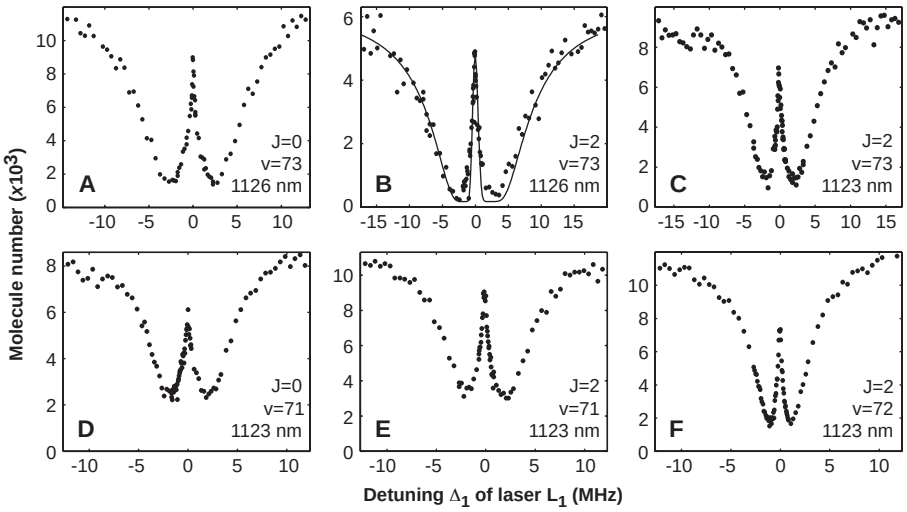

Fig. 4.4.: Dark resonances for vibrational levels $\nu = 71$, 72, and 73. Laser L_2 is held on resonance, while the detuning Δ_1 of L_1 is scanned. We record the number of molecules in $|a>$ while both lasers are pulsed on simultaneously. **A**, **B**, and **C** show dark resonances involving $\nu = 73$ for excitation with L_1 near 1126 nm into $J = 0$ and 2 and for excitation with L_1 near 1123 nm into $J = 2$, respectively. **D**, **E**, and **F** show the neighboring levels $\nu = 71$ and 72 for excitation near 1123 nm. The solid line in B is the result of a three-level model calculation matched to the data giving $\Omega_1 = 2\pi \times 2$ kHz $\sqrt{I_1/(\mathrm{mW/cm^2})}$ and $\Omega_2 = 2\pi \times 11$ kHz $\sqrt{I_2/(\mathrm{mW/cm^2})}$ for a pulse time of 5 μs at intensities of $I_1 = 4 \times 10^5$ mW/cm^2 for L_1 and $I_2 = 2 \times 10^5$ mW/cm^2 for L_2 assuming a laser linewidth of 2 kHz.

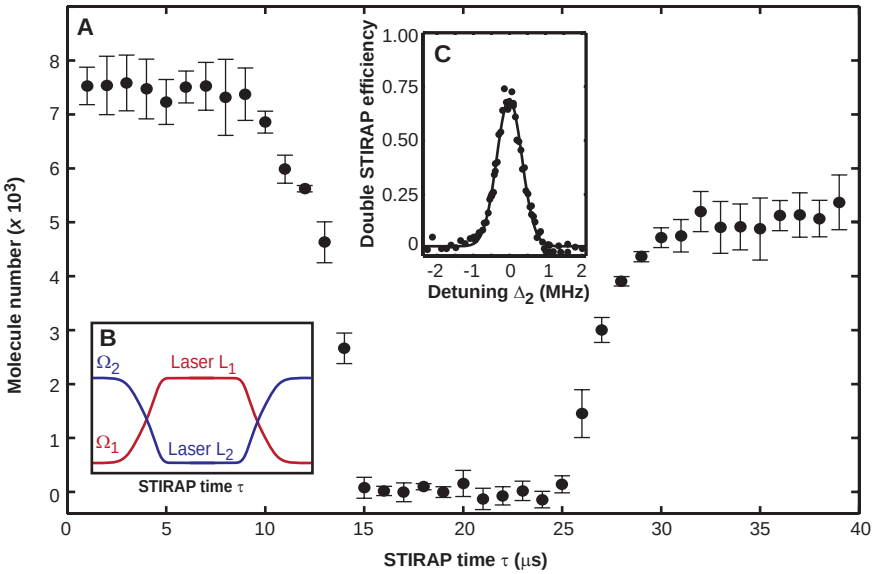

Fig. 4.5.: STIRAP transfer from the weakly bound state $|a>$ to the deeply bound state $|g>=|\nu=73, J=2>$ and back to $|a>$. **A** shows the number of molecules in state $|a>$ as a function of STIRAP time τ for $\Delta_1 \approx 0 \approx \Delta_2$. The measured pulse overlap begins at 5 μs and ends at about 15 μs. The second pulse overlap starts at 25 μs and ends at about 33 μs. **B** schematically shows the timing for the Rabi frequencies Ω_i, $i = 1, 2$, during the double STIRAP sequence. Laser L_1 is left on after the first STIRAP sequence to clear out any remaining population in $|a>$. **C** Double STIRAP efficiency as a function of the detuning Δ_2 of laser L_2 for $\Delta_1 \approx 0$. The solid line is a gaussian fit with a FWHM of 811 kHz. The peak Rabi frequencies are $\Omega_1 \approx 2\pi \times 3$ MHz and $\Omega_2 \approx 2\pi \times 6$ MHz. The error bars refer to the 1-sigma error in determining the particle number.

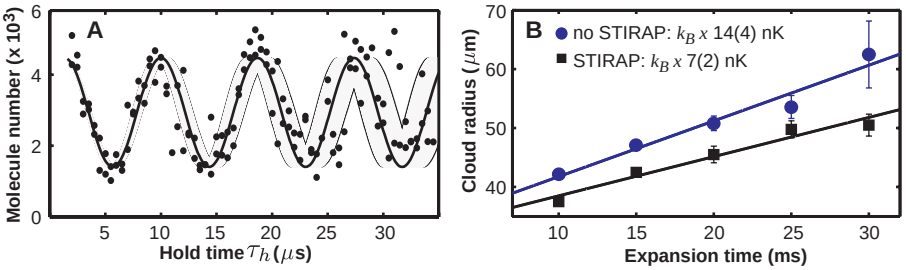

Fig. 4.6.: A Ramsey-type experiment. The population in the initial state $|a>$ oscillates as the hold time τ_h during which both transfer lasers are off is increased. The solid line is a sinussoidal fit to the data up to $\tau_h = 20$ μs. Its frequency f is 115(2) kHz, in good agreement with the expected value of 113 kHz. The thin lines are borders to a region that is given by varying f by ± 6 kHz, illustrating the estimated jitter in the two-photon detuning $|\Delta_2 - \Delta_1|$. **B** Comparison of the rate of expansion in the horizontal direction for the molecular sample without and with STIRAP transfer. The top curve (circles) shows the Thomas-Fermi radius r of the molecular sample as a function of expansion time without STIRAP. The linear fit gives a rate of expansion of $dr/dt = 1.0(1)$ mm/s, corresponding to an energy of $k_B \times 14(4)$ nK. The bottom curve (squares) shows the expansion after double STIRAP with $dr/dt = 0.7(1)$ mm/s, corresponding to $k_B \times 7(2)$ nK.

4.3. Publication: Deeply bound ultracold molecules in an optical lattice

New J. Phys. **11**, 055036 (2010)†

Johann G. Danzl[a], Manfred J. Mark[a], Elmar Haller[a], Mattias Gustavsson[a], Russell Hart[a], Andreas Liem[b], Holger Zellmer[c], and Hanns-Christoph Nägerl[a]

[a] *Institut für Experimentalphysik und Zentrum für Quantenphysik, Universität Innsbruck, Technikerstraße 25, A–6020 Innsbruck, Austria*
[b] *JT Optical Engine GmbH + Co. KG, Prüssingstraße 41, D–07745 Jena, Germany*
[c] *Hochschule für Technik, Wirtschaft und Kultur Leipzig, Gutenbergplatz 2-4, D–04103 Leipzig, Germany*

We demonstrate efficient transfer of ultracold molecules into a deeply bound rovibrational level of the singlet ground state potential in the presence of an optical lattice. The overall molecule creation efficiency is 25%, and the transfer efficiency to the rovibrational level $|v = 73, J = 2>$ is above 80%. We find that the molecules in $|v = 73, J = 2>$ are trapped in the optical lattice, and that the lifetime in the lattice is limited by optical excitation by the lattice light. The molecule trapping time for a lattice depth of 15 atomic recoil energies is about 20 ms. We determine the trapping frequency by the lattice phase and amplitude modulation technique. It will now be possible to transfer the molecules to the rovibrational ground state $|v=0, J=0>$ in the presence of the optical lattice.

†The author of the present thesis contributed to this work by assisting the experimental measurements and optimizing the molecule production and cleaning in the lattice. He also maintained and improved the experimental setup and contributed to the paper writing.

4.3.1. Introduction

The generation of molecular quantum gases and molecular Bose-Einstein condensates (BEC) has been a major goal for the field of atomic and molecular physics. It has been achieved for the case of two fermionic atoms that pair up to form a bosonic dimer molecule in the limit of vanishing binding energy [Joc03a, Gre03] at ultralow temperatures. In this limit, collisional stability is assured, and this has allowed the investigation of the BEC-BCS crossover [Ing08]. Here, we are interested in the opposite limit of deeply bound molecules. Collisional stability is expected only for the rovibronic ground state, and most likely it will be necessary that one prepares the lowest molecular hyperfine sublevel [Ald09] to avoid hyperfine changing collisions. Our approach to producing a quantum gas of ground state molecules is based on laser cooling of atoms to the point of quantum degeneracy, followed by molecule association on a Feshbach resonance and subsequent coherent two-photon molecule transfer [Dan08, Mar09, Dan09b, Win07, Ni08, Lan08b]. In principle, this approach combines high molecular densities and ultralow temperatures with full state selectivity. For optimization of both the initial molecule creation process and the transfer process, the use of a three-dimensional optical lattice has been proposed, as illustrated in Figure 4.7 C. In a superfluid-to-Mott-insulator phase transition doubly occupied lattice sites can be favored [Vol06, Dür08], and collisional relaxation during the transfer can, at least in principle, be fully avoided. It should be possible that one finally creates a molecular BEC by dynamical melting of the lattice after the two-photon transfer [Jak02].

In the present work, we report on two-photon transfer into a deeply bound rovibrational level by means of the stimulated Raman adiabatic passage (STIRAP) technique [Ber98, Win07] in the presence of a three-dimensional optical lattice. We extend our previous work of transfering Cs_2 molecules to rovibrational level $|v=73, J=2>$ of the $^1\Sigma_g^+$ electronic ground state in the quantum gas regime [Dan08] by first using the superfluid-to-Mott-insulator phase transition to efficiently produce pairs of atoms at the wells of the lattice. The pairs are then associated to weakly bound molecules on a Feshbach resonance. Subsequently, the molecules are transferred by magnetic field ramping to the starting state for optical transfer. From there, they are efficiently transferred to the deeply bound rovibrational level $|v=73, J=2>$ by means of STIRAP. Note that in our previous work [Dan08] all experiments were performed in free flight. Figure 4.7 A shows the relevant molecular states for the Cs dimer molecule and the transitions involved. We find that the molecules in $|v=73, J=2>$ are trapped in the lattice with a $1/e$-trapping time of about 20 ms, limited by scattering of lattice light. We measure the trapping frequency of the molecules in the lattice and find that the polarizability in $|v=73, J=2>$ is about 30% of that of the Feshbach molecules. It will now be possible that one adds a second STIRAP transfer step to reach the rovibronic ground state $|v=0, J=0>$, giving full quantum control over the external and internal degrees of freedom for the molecules.

4.3.2. Preparation of Feshbach molecules in the optical lattice

To produce an ultracold sample of Feshbach molecules trapped at the individual sites of an optical lattice we first produce an atomic BEC with typically 1×10^5 Cs atoms in the lowest hyperfine sublevel $F=3,\ m_F=3$ in a crossed optical dipole trap. As usual, F is the atomic angular momentum quantum number, and m_F its projection on the magnetic field axis. For BEC production, we essentially follow the procedure detailed in Ref.[Web03a]. We set the atomic scattering length to a value of 210 a_0, where a_0 is Bohr's radius, by tuning the magnetic offset field to 2.1 mT. At this value, three-body losses are minimal [Kra06]. We then drive the superfluid-to-Mott-insulator phase transition [Gre02a] by exponentially ramping up the power in a three-dimensional optical lattice within about 400 ms while simultaneously ramping up the harmonic confinement in the dipole trap. The lattice is generated by three mutually orthogonal, retro-reflected laser beams at a wavelength of $\lambda = 1064.5$ nm, each with a $1/e$-waist of about 350 μm. For the atoms, we achieve a well depth of up to 40 E_R, where $E_R = h^2/(2m\lambda^2) = k_B\times64\,\mathrm{nK}$ is the atomic photon recoil energy with the mass m of the Cs atom. h is Planck's constant, and k_B is Boltzmann's constant. Throughout the paper we give lattice depths in units of the atomic recoil energy. The lattice light as well as the light for the dipole trap beams is derived from a single-frequency, narrow-band, highly-stable Nd:YAG laser that is amplified to up to 20 W without spectral degradation in a home-built fiber amplifier [Lie03]. The power in each lattice beam is controlled by an acousto-optical intensity modulator and an intensity stabilization servo. While ramping up the lattice potential, the power in the two dipole trap beams is increased to assure that the central density in the trap is sufficiently high to allow the preferential formation of atom pairs at the central wells of the lattice, but not too high in order to avoid triply occupied sites. We typically ramp the lattice to a depth of 15 to 25 E_R. Typically about 30% of the atoms reside at doubly occupied lattice sites. We estimate this number from the molecule production efficiency. This value is not optimal yet, as loading from a parabolic potential should give a maximum of 53% [Dür08, Han06].

We now produce Feshbach molecules on a Feshbach resonance [Reg03, Her03, Köh06] near a magnetic field value of $B = 1.98$ mT [Mar07a] in the presence of the optical lattice [Tha06, Vol06]. Figure 4.7 B shows the relevant weakly bound Feshbach levels. The resonance at 1.98 mT is quite narrow, but it lies at a conveniently low value of the magnetic field, allowing us to simply lower the magnetic offset field from the BEC production value and ramp over the resonance with a rate of about 0.006 T/s. The molecules produced are then in level $|g>$. These molecules have g-wave character, i.e. $\ell=4$, where ℓ is the quantum number associated with the mechanical rotation of the nuclei [Chi04b]. After association, atoms remaining at singly occupied lattice sites are removed by microwave transfer to $F = 4$ and a resonant light pulse. Starting from level $|g>$ we have recently identified transitions to deeply bound excited rovibrational levels of the Cs_2 mixed $(A^1\Sigma_u^+ - b^3\Pi_u)\ 0_u^+$ excited states [Dan09b]. These transitions should allow STIRAP transfer to the target rovibrational level $|v=73, J=2>$ of the electronic ground state, but for the present work we have decided to use

Feshbach level $|s>$ as the starting state as in our previous work [Dan08] so that the transfer performances with and without the presence of the lattice can be compared. To reach level $|s>$ from level $|g>$, we have implemented Feshbach state transfer as realized in Ref.[Mar07a] using a combination of slow and fast magnetic field ramps. In brief, we first transfer the molecules from $|g>$ to level $|g_2>$ by lowering the magnetic field B sufficiently slowly to a value of 1.22 mT, thereby following the upper branch of an avoided crossing near 1.33 mT as shown in Figure 4.7 B. We then increase B abruptly to a value of 1.67 mT, thereby jumping the two crossings with levels $|g>$ and $|l>$. The maximum magnetic field rate of change is $\sim$ 2000 T/s. We finally follow slowly on the upper branch of the avoided crossing with $|s>$ at 1.85 mT, stopping at $B = 1.9$ mT. Our procedure allows us to essentially transfer all molecules from $|g>$ to $|s>$. For molecule detection, we reverse the magnetic field ramps to level $|g>$, dissociate the molecules at the Feshbach resonance at $B = 1.98$ mT and detect the resulting atoms by standard absorption imaging [Her03].

For comparison with our data obtained below we first measure the lifetime of the weakly-bound Feshbach molecules in the optical lattice. Typical lifetime measurements for these molecules are shown in Figure 4.8 A-C. In such measurements, we record the number of remaining molecules as a function of hold time in the lattice. The lifetime of the molecules depends strongly on which Feshbach level is used and on the value of the magnetic field B. For example, for molecules in level $|g>$ at $B = 1.82$ mT the lifetime is 1.8 s at a lattice depth of 15 E_R, while in level $|s>$ the lifetime is 0.09 s at $B = 1.9$ mT and 10 s at $B = 2.9$ mT for the same lattice depth. We attribute this strong dependence of the lifetime of molecules in $|s>$ to the fact that the molecular character changes strongly from being predominantly closed channel dominated to being open channel dominated as the magnetic field is increased [Köh06], reducing wave function overlap with excited molecular levels. We always determine the lifetime for two values of the lattice depth, 15 E_R and 25 E_R. In all cases, the lifetime is reduced for higher lattice depth, indicating residual optical excitation by the lattice light. Nevertheless, the long lifetimes reflect the fact that the lattice perfectly shields the molecules from inelastic molecule-molecule collisions, which would otherwise limit the lifetime to a few ms at the given molecular densities [Tha06].

4.3.3. Lattice-based STIRAP transfer

We implement two-photon STIRAP transfer to the deeply bound rovibrational level $|3>= |v = 73, J = 2>$ of the $^1\Sigma_g^+$ electronic ground state potential in a similar way as in our previous work [Dan08], except that now the molecules are trapped at the individual wells of the optical lattice. In brief, laser L_1 near a wavelength of 1126 nm, driving the transition from $|1>= |s>$ to $|2>$, where $|2>$ is a deeply bound level of the mixed $(A^1\Sigma_u^+ - b^3\Pi_u)$ 0_u^+ excited states, is pulsed on after laser L_2, which drives the transition from $|3>$ to $|2>$ at 1006 nm, see Figure 4.7 A. The pulse (or pulse overlap) time τ_p is typically $\tau_p = 10$ μs for the present experiments. A schematic time course for the transition Rabi

frequencies is shown in Figure 4.9 C. We estimate the peak Rabi frequencies to be $2\pi \times 3$ MHz for the transition at 1126 nm and $2\pi \times 6$ MHz for the transition at 1006 nm [Dan08]. After a variable hold time τ_h, we reverse the pulse sequence to transfer the molecules back to $|s>$. For short τ_h below 40 μs we typically leave L_1 on between the two STIRAP pulse sequences. For longer τ_h we switch L_1 off to avoid any residual optical excitation of molecules in $|v=73, J=2>$ and possible effects of dipole forces generated by the tightly focused laser beam L_1.

The result of double STIRAP transfer in the optical lattice is shown in Figure 4.9 A. Here, $\tau_p = 10$ μs and $\tau_h = 15$ μs. As in our previous work [Dan08], we interrupt the transfer after a given STIRAP time τ_S and record the number of molecules in the initial state $|s>$. The molecules first disappear, and then a sizable fraction of about 65% returns after the reverse STIRAP transfer. Thus, as in our previous work [Dan08], the single pass efficiency is about 80% when both lasers are on resonance. Figure 4.9 B shows the double STIRAP transfer efficiency as a function of the detuning Δ_2 of laser L_2 from the excited intermediate level while laser L_1 is held on resonance (detuning $\Delta_1 \approx 0$). A Gaussian fit yields a full width at half maximum of 830 kHz. With τ_p so short, we do not resolve molecular hyperfine structure in $|v=73, J=2>$.

We find that the molecules transferred to $|v=73, J=2>$ are trapped at the individual wells of the lattice. The $1/e$-lifetime is about 19 ms for a lattice depth of 15 E_R. This is much shorter than the lifetime of Feshbach molecules as shown above, but sufficiently long to allow future implementation of a second lattice-based STIRAP step to the rovibronic ground state $|v=0, J=0>$, for which the lifetime is expected to be much longer as discussed below. We determine the lifetime by repeating the double STIRAP transfer while increasing the hold time τ_h in steps of 3.5 ms. The result is shown in Figure 4.8 D. The number of molecules can be well fit by an exponentially decaying function as a function of τ_h. For a higher lattice depth of 25 E_R, the lifetime is reduced to 15 ms. We thus attribute the reduced molecular lifetime to off-resonant scattering of lattice light, exciting the molecules to levels of the $(A^1\Sigma_u^+ - b^3\Pi_u)$ 0_u^+ states, which then in turn leads to loss into other ground state rovibrational levels that we do not detect. Note that in the wavelength region of our trapping laser, the lifetime is expected to show strong variations as a function of trapping laser wavelength due to the presence of excited state levels. Hence, also the polarizability as discussed in the next section should strongly depend on the wavelength of the laser generating the lattice light.

4.3.4. Determination of molecule trapping parameters

We determine the molecular trapping frequency $\omega_{|v=73>}$ for molecules in $|v=73, J=2>$ by modulating the lattice phase and, alternatively, by modulating the lattice amplitude. In the first case, we primarily excite transitions from the lowest band in the lattice to the first excited band and then to higher bands. In the second case, we primarily excite into the second excited band and then

to higher bands. For sufficiently strong modulation, molecules are lost from the lattice, as tunneling to neighboring sites and hence inelastic collisions with neighboring molecules become more probable. We thus expect to detect increased molecular loss if the modulation frequency is tuned into resonance with the inter-band transitions. The results are shown in Figure 4.10. At a lattice depth of 15 E_R, we observe resonant loss at 5.2 kHz in the case of phase modulation and at 10.1 kHz in the case of amplitude modulation of the lattice. Phase modulation at 22 E_R and amplitude modulation at 20 E_R yield resonances at 6.5 kHz and 12.2 kHz, respectively. These values for different trap depths are consistent with each other when compared with a calculation of the band structure. For comparison, to determine the trapping frequency ω_F of the Feshbach molecules in level $|g>$, we measure that phase modulation (amplitude modulation) of a 15 E_R deep lattice leads to loss at a modulation frequency of 9.4 kHz (18.4 kHz). Relating the dynamical polarizability $\alpha_{|v=73>}$ of the deeply bound molecules in $|v=73>$ to the dynamical polarizability α_F of the Feshbach molecules via $\alpha_{|v=73>}/\alpha_F = \omega^2_{|v=73>}/\omega^2_F$, we obtain that the molecular polarizability in $|v=73, J=2>$ is $\sim 30\%$ of the polarizability of the Feshbach molecules at the wavelength of our trapping light.

4.3.5. Conclusion

We have transferred an ultracold sample of Cs_2 molecules to the deeply bound rovibrational level $|v=73, J=2>$ of the singlet $X^1\Sigma_g^+$ potential in the presence of an optical lattice. We essentially find the same transfer efficiency as in our previous work [Dan08] where no lattice was used. The transferred molecules are trapped, and we have determined their polarizability in this particular level. The trapping time is sufficiently long to allow for subsequent lattice-based STIRAP transfer to the rovibronic ground state $|v=0, J=0>$ by means of a second two-photon transition [Mar09]. A lower bound for the STIRAP pulse time and hence for the minimal required trapping time is set by the time needed to resolve the molecular hyperfine structure. This minimal time is the inverse of three times the ground state hyperfine coupling constant $c_4 \approx 14$ kHz [Ald09], giving 24 μs. Hence a compromise can easily be found between Fourier-resolving the molecular hyperfine structure and keeping the STIRAP pulse time sufficiently short in view of finite laser coherence time and finite trapping time. Note that for optimum transfer efficiency also the hyperfine structure of the intermediate state needs to be resolved, which requires longer STIRAP times also for the first transfer step.

For Cs_2 molecules in the rovibronic ground state $|v=0, J=0>$ we expect much longer trapping times in the lattice as optical excitation at 1064.5 nm into excited molecular states can only occur in a far off-resonant process. At this wavelength transitions to the $(A^1\Sigma_u^+ - b^3\Pi_u)$ 0_u^+ states are relevant. These are possible only to levels that have a sizable singlet contribution stemming from the $A^1\Sigma_u^+$ state. 0_u^+ levels below the minimum of the $A^1\Sigma_u^+$ state, corresponding to a wavelength of ~ 1041 nm as measured from the rovibronic ground state [Ver87], have little singlet component and hence these transitions are strongly

suppressed. We thus expect the formation of a stable molecular quantum gas in $|v=0, J=0>$ when the lattice depth is lowered and the molecules are released into a larger-volume optical dipole trap, possibly allowing the observation of Bose-Einstein condensation of ground state molecules.

Our technique can readily be applied to other molecular systems, e.g. heteronuclear dimers such as RbCs [Pil09] and KRb [Ni08]. These dimers carry a sizable electric dipole moment. In the presence of the lattice, one should thus be able to exploit the long range nature of the dipole-dipole interaction and be able to prepare interesting novel quantum phases with nearest-neighbor interaction [Gór02, Wal09].

We are indebted to R. Grimm for generous support and we thank S. Knoop, N. Boloufa, and O. Dulieu for valuable discussions. We gratefully acknowledge funding by the Austrian Ministry of Science and Research (BMWF) and the Austrian Science Fund (FWF) in form of a START prize grant. R.H. acknowledges support by the European Union in form of a Marie-Curie International Incoming Fellowship (IIF).

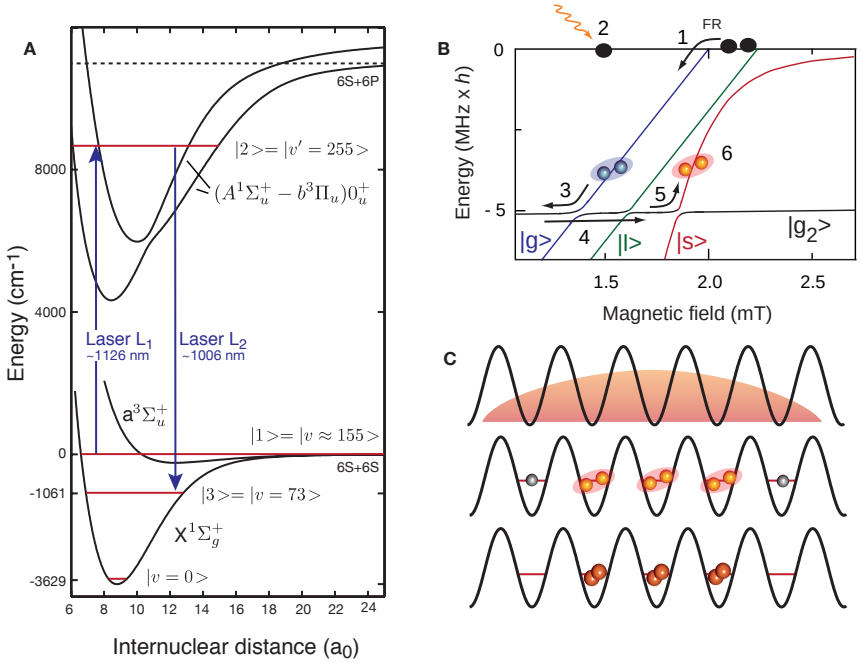

Fig. 4.7.: **A** Molecular level scheme for Cs_2. Molecules in a weakly bound Feshbach level |1> are transferred to rovibrational level $|3\rangle = |v=73, J=2\rangle$ of the singlet $X^1\Sigma_g^+$ potential in the presence of an optical lattice. Level |3> with a binding energy of 1061 cm^{-1} is reached in a two-photon STIRAP process with wavelengths near 1126 nm and 1006 nm via the 225th level of the electronically excited $(A^1\Sigma_u^+ - b^3\Pi_u)\ 0_u^+$ potentials. The $X^1\Sigma_g^+$ potential has about 155 vibrational levels. **B** Zeeman diagram showing the energy of all relevant weakly bound molecular levels for initial Feshbach molecular state preparation [Mar07a]. The binding energy is given with respect to the $F=3, m_F=3$ two-atom asymptote. The molecules are first produced on a g-wave Feshbach resonance at 1.98 mT in state |g> (1). Residual atoms are removed by a combined microwave and resonant light pulse (2). The molecules are then transferred to the weakly bound s-wave state $|1\rangle = |s\rangle$ (6), the starting state for the STIRAP transfer, via three avoided state crossings involving state $|g_2\rangle$ by slow (3,5) and fast magnetic field ramps (4). **C** Lattice based ground state transfer. Top: The BEC is adiabatically loaded into the three-dimensional optical lattice, creating a Mott-insulator state. Middle: Atoms at doubly occupied sites are converted to Feshbach molecules. Atoms at singly occupied sites are removed thereafter. Bottom: The molecules are subsequently transferred to the deeply bound rovibrational level $|3\rangle = |v=73, J=2\rangle$ while shielded from collisions by the lattice potential.

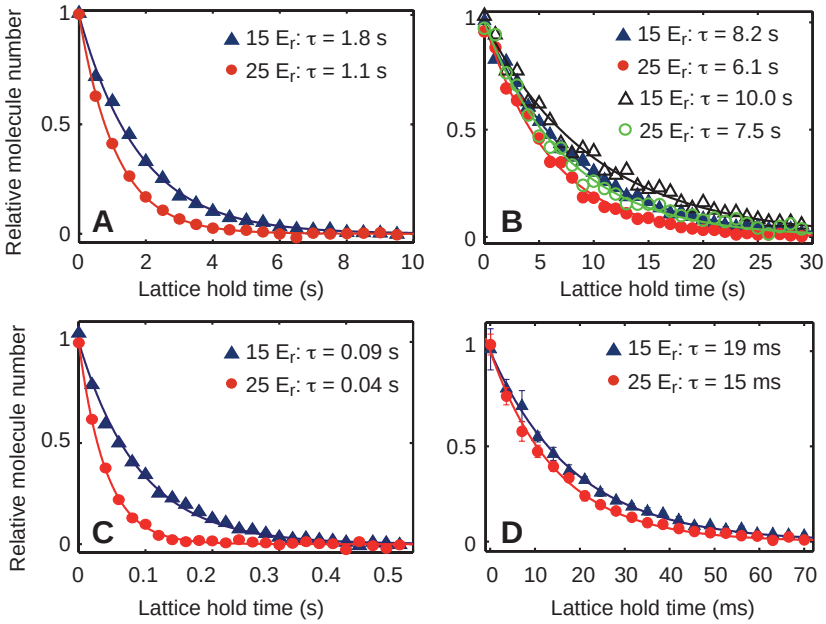

Fig. 4.8.: Lifetime measurements of ultracold molecules trapped in the optical lattice. **A**, **B**, and **C** show the decay of trapped Feshbach molecules, while **D** shows the decay for molecules in $|3>= |v = 73, J = 2>$ of the $X^1\Sigma_g^+$ ground state potential. In all cases, the triangles (circles) correspond to a lattice depth of 15 E_R (25 E_R). All lifetimes τ are determined from exponential fits to the data as shown by the the solid lines. **A** Lifetime of state $|g>$. **B** Lifetime of state $|g_2>$ (filled symbols) and of state $|s>$ at $B = 2.9$ mT (open symbols). **C** Lifetime of state $|s>$ at $B = 1.9$ mT, from where we drive the STIRAP transfer. **D** Lifetime of molecules in the rovibrational level $|3>= |v = 73, J = 2>$. The STIRAP lasers are switched off during the hold time in $|3>$. In **D**, each data point is the average of 4 experimental runs, error bars correspond to the 1σ statistical uncertainty. The typical uncertainty for the lifetimes is one unit of the last digit given.

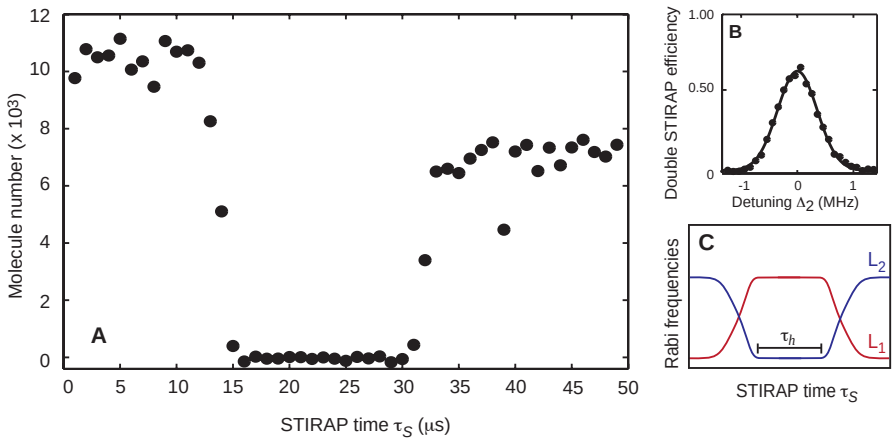

Fig. 4.9.: STIRAP transfer from the weakly bound state $|1>=|s>$ to the deeply bound rovibrational level $|3>=|v=73, J=2>$ and back to $|1>$ in the optical lattice. **A** shows the number of molecules in state $|1>$ as a function of STIRAP time τ_S for both lasers on resonance (laser detunings $\Delta_1 \approx 0 \approx \Delta_2$). The measured pulse overlap begins at about 5 μs and ends at about 15 μs. The second pulse overlap starts at 30 μs and ends at about 38 μs. The lattice depth is 15 E_R. Data points represent a single experimental realization, not an average over several runs. The data point at 39 μs represents a "bad shot", which occasionally occurs. **B** Double STIRAP efficiency as a function of the detuning Δ_2 of laser L_2 for $\Delta_1 \approx 0$. The solid line is a Gaussian fit with a full width at half maximum of 830 kHz. **C** schematically shows the timing for the Rabi frequencies, Ω_i, $i = 1, 2$, for lasers L_1 and L_2 during the double STIRAP sequence. For short hold times $\tau_h < 40$ μs laser L_1 is left on after the first STIRAP sequence as shown here. For longer hold times $\tau_h > 40$ μs we shut off L_1 to avoid possible optical excitation.

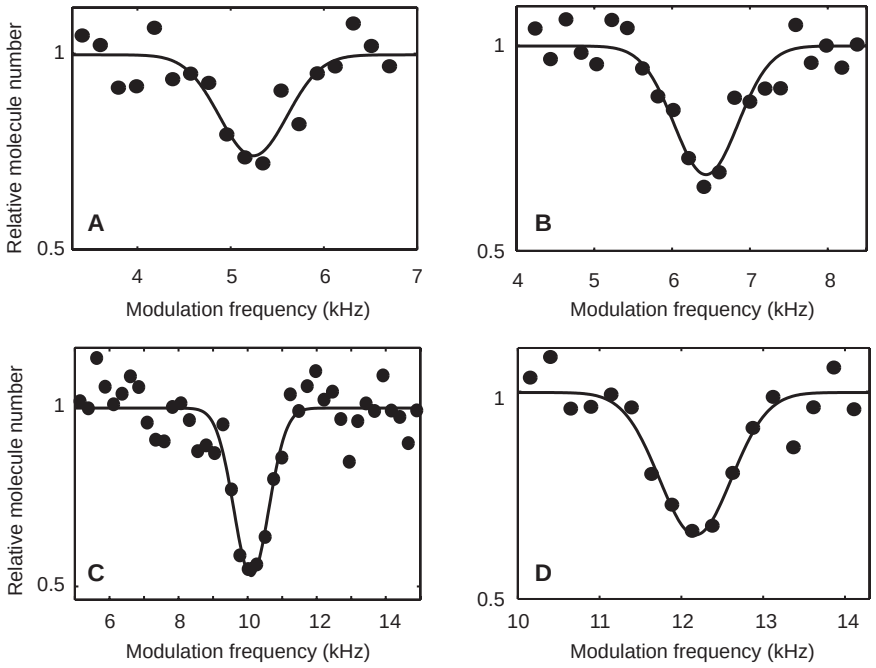

Fig. 4.10.: Trapping of deeply bound molecules in the wells of the optical lattice. While the molecules reside in level $|3\rangle = |v=73, J=2\rangle$, one of the lattice beams of the 3 dimensional optical lattice is either phase modulated (**A** and **B**) or amplitude modulated (**C** and **D**). As the frequency of the phase or amplitude modulation is scanned, a series of resonances due to transfer to higher bands arise, reflected in a decrease in molecule number. The respective resonances at the lowest modulation frequency are shown here. For phase modulation ("shaking" of the lattice), this corresponds to the first lattice band, for amplitude modulation to the second band. To determine the center frequency, the resonances are fit by a Gaussian. The lattice depth is 15 E_R, 22 E_R, 15 E_R, and 20 E_R in **A**, **B**, **C**, and **D**, respectively.

4.4. Publication: An ultracold, high-density sample of rovibronic ground-state molecules in an optical lattice

Nature Physics **6**, 265 (2010)†

Johann G. Danzl[1], Manfred J. Mark[1], Elmar Haller[1], Mattias Gustavsson[1], Russell Hart[1], Jesus Aldegunde[2], Jeremy M. Hutson[2], and Hanns-Christoph Nägerl[1]

[1] *Institut für Experimentalphysik und Zentrum für Quantenphysik, Universität Innsbruck, Technikerstraße 25, A–6020 Innsbruck, Austria*

[2] *Department of Chemistry, University of Durham, South Road, Durham, DH1 3LE, England*

Control over all internal and external degrees of freedom of molecules at the level of single quantum states will enable a series of fundamental studies in physics and chemistry [Car09, Kre08]. In particular, samples of ground-state molecules at ultralow temperatures and high number densities will allow novel quantum-gas studies [Gór02] and future applications in quantum information science [DeM02]. However, high phase-space densities for molecular samples are not readily attainable as efficient cooling techniques such as laser cooling are lacking. Here we produce an ultracold and dense sample of molecules in a single hyperfine level of the rovibronic ground state with each molecule individually trapped in the motional ground state of an optical lattice well. Starting from a zero-temperature atomic Mott-insulator state [Blo08] with optimized double-site occupancy [Vol06], weakly-bound dimer molecules are efficiently associated on a Feshbach resonance [Chi10] and subsequently transferred to the rovibronic ground state by a stimulated four-photon process with >50% efficiency. The molecules are trapped in the lattice and have a lifetime of 8 s. Our results present a crucial step towards Bose-Einstein condensation of ground-state molecules and, when suitably generalized to polar heteronuclear molecules, the realization of dipolar quantum-gas phases in optical lattices [Bar08, Lah09, Pup09].

†The author of the present thesis contributed to this work by assisting the experimental measurements and optimizing the molecule production and cleaning in the lattice. He also maintained and improved the experimental setup and contributed to the paper writing.

4.4.1. Introduction

Recent years have seen spectacular advances in the field of atomic quantum gases. Ultracold atomic samples have been loaded into optical lattice potentials, allowing the realization of strongly-correlated many-body systems and enabling the direct observation of quantum phase transitions with full control over the entire parameter space [Blo08]. Molecules with their increased complexity are expected to play a crucial role in future generation quantum gas studies. For example, the long-range dipole-dipole force between polar molecules gives rise to nearest-neighbour and next-nearest-neighbour interaction terms in the extended Bose-Hubbard Hamiltonian and should thus lead to novel many-body states in optical lattices in the form of striped, checkerboard, and supersolid phases [Bar08, Lah09, Pup09].

An important prerequisite for all proposed molecular quantum gas experiments is the capability to fully control all internal and external quantum degrees of freedom of the molecules. For radiative and collisional stability, the molecules need to be prepared in their rovibronic ground state, i.e. the lowest vibrational and rotational level of the lowest electronic state, and preferably in its energetically lowest hyperfine sublevel. As a starting point for the realization of novel quantum phases, the molecular ensemble should be in the ground state of the many-body system. Such state control is only possible at ultralow temperatures and sufficiently high particle densities. While versatile non-optical cooling and slowing techniques have recently been developed for molecular ensembles [Fri09] and photo-association experiments with atoms in magneto-optical traps have reached the rovibrational ground state [Car09], the achievable molecular phase-space densities are still far away from the point of quantum degeneracy. Here, we exploit the fact that high phase-space densities can readily be achieved for atoms and that atoms can efficiently be associated on Feshbach resonances to form molecules [Chi10] with minimal loss of phase-space density when an optical lattice is present. Subsequent state transfer to a specific hyperfine sublevel of the rovibronic ground state by means of a stimulated multi-photon process then preserves phase-space density and hence the quantum-gas character of the molecular ensemble. This approach is expected to allow the preparation of a molecular ground-state BEC [Jak02]. Note that some loss of phase-space density can be tolerated if the collisional properties of the ground-state molecules, a priori unknown, turn out to be sufficiently favorable to allow for a final stage of evaporative cooling or, alternatively, sympathetic cooling with atoms.

A crucial ingredient for our experiments is the presence of an optical lattice. It provides full control over the motional wave function and prevents collisional loss. It allows us in particular to maximize the efficiency for initial molecule production and the efficiency for ground-state transfer. For sufficiently high efficiency, a molecular Mott-insulator state is approximated by this preparation procedure [Jak02], providing an excellent starting point for the precision measurements [DeM08, Zel08] and many-body and quantum information experiments [Bar08, Lah09, Pup09] envisioned with ground-state molecules. In the quantum gas regime without the use of an optical lattice, molecular state trans-

fer to deeply-bound rovibrational levels of the singlet $^1\Sigma$ ground-state potential has recently been implemented for Cs_2 [Dan08] and KRb [Ni08]. For KRb, the rovibronic ground state was reached, resulting in a near-quantum-degenerate gas of fermionic ground-state molecules [Ni08]. Transfer of molecules in the presence of an optical lattice has been implemented for Rb_2 molecules [Win07], and the lowest rovibrational level of the shallow triplet $a^3\Sigma_u^+$ potential was reached [Lan08b].

4.4.2. Preparation of Feshbach molecules

Our molecular quantum-gas preparation procedure is summarized in Fig. 4.11. We load a BEC of Cs atoms [Kra04] into a three-dimensional optical lattice and drive the superfluid-to-Mott-insulator phase transition [Blo08]. The atomic number distribution in the Mott-insulator state is inhomogeneous as a result of the external harmonic confinement. Shells with a constant number of precisely n atoms per lattice site, where $n = 1, 2, 3 \ldots$, are separated by narrow superfluid regions [Blo08]. We aim to maximize the size of the two-atom Mott shell in the central region of the lattice in order to obtain the highest number of lattice sites at which there are precisely two atoms (see the Methods section). With up to 45(2)% of the atoms at doubly-occupied lattice sites we come close to the theoretical limit of 53% given the parabolic density profile of the BEC [Vol06]. The atom pairs reside in the motional ground state at each well and are then associated [Tha06] with 94(1)% probability to Cs_2 Feshbach molecules, which are subsequently transferred to the weakly-bound level $|1>$, the starting level for the optical transfer (see the Methods section) [Mar07a, Dan08, Dan09a]. Atoms at singly-occupied sites are removed by a combination of microwave and optical excitation [Tha06]. We now have a pure molecular sample with a high occupation of about 85(3)% in the central region of the lattice (see the Methods section). Each molecule is in the motional ground state of its respective well and perfectly shielded from collisional loss.

4.4.3. STIRAP transfer

We employ stimulated Raman adiabatic passage (STIRAP) [Ber98] involving four laser transitions to coherently transfer the molecules into the lowest rovibrational level $|5>= |v=0, J=0>$ of the ground state singlet $X^1\Sigma_g^+$ potential as shown in Fig. 4.12a, bridging a binding energy of $hc\times$ 3628.7 cm^{-1} $\approx h \times 109$ THz [Dan08]. Here, v and J are the vibrational and rotational quantum numbers, respectively, h is Planck's constant and c is the speed of light. For Cs_2, a homonuclear molecule, the four-photon process is preferred to a direct two-photon process because it allows us to overcome small Franck-Condon overlap. Lasers L_1 through L_4 couple $|1>$ and $|5>$ via three intermediate levels $|2>$,$|3>$, and $|4>$ (see the Methods section). For STIRAP in the presence of the lattice, the lattice light must not impede the transfer through optical excitation or by creating unwanted coherences. Also, the lattice wavelength has to be chosen

such that the dynamical polarizabilities for $|1>$ and $|5>$ are closely matched in order to avoid excitation into higher motional states of the lattice as a result of motional wave-function mismatch [Lan08b]. We typically set the lattice depth to a value of 20 E_R for atoms, corresponding to 80 $\tilde{E}_R$ for Feshbach molecules with twice the polarizability and double the mass and 83 $\tilde{E}_R$ for molecules in $|v=0>$ at a lattice wavelength of 1064.5 nm, as determined below. Here, E_R ($\tilde{E}_R$) is the atomic (molecular) recoil energy.

Our experimental configuration ensures that only one particular molecular hyperfine sublevel is populated. The atomic BEC is prepared in the lowest hyperfine sublevel $|F_a=3, m_{Fa}=3>$, where F_a and m_{Fa} are the total atomic angular momentum and its projection on the magnetic field. Feshbach association and transfer between Feshbach levels via avoided crossings, as illustrated in Fig. 4.12b (see the Methods section), conserve [Chi10] the total angular momentum projection $M_F = m_{Fa_1} + m_{Fa_2} = 6$. Fig. 4.12c shows the hyperfine structure of the target state, i.e. the rovibronic ground state $X^1\Sigma_g^+$ $|v=0, J=0>$. It splits into 28 hyperfine sublevels in the presence of a weak magnetic field, corresponding to the allowed values of the total nuclear spin $I = 0$, 2, 4, 6 and its $2I+1$ projections M_I for each value of I. The total energy splitting is $\sim h \times 270$ kHz at zero field [Ald09] (see the Methods section). Importantly, there is only a single $M_I = M_F = 6$ sublevel of $|v=0, J=0>$, namely the $|I=6, M_I=6>$ level. This level we selectively populate by exploiting the dipole selection rule $\Delta M_F = 0$ for linear polarization along the axis of quantization. It is the lowest-energy hyperfine sublevel and hence the absolute energy ground state of the Cs dimer for magnetic fields above ~ 13 mT.

There are two possibilities for optical transfer from $|1>$ to $|5>$. Sequential STIRAP (s-STIRAP) uses two consecutive two-photon STIRAP processes, first from $|1>$ to $|3>$ and then from $|3>$ to $|5>$. The second scheme generalizes STIRAP [Ber98, Win07] to the five-level system [Mal97]: Four-photon STIRAP (4p-STIRAP) relies on the existence of a dark state of the form $|D> = (\Omega_2\Omega_4|1> - \Omega_1\Omega_4|3> + \Omega_1\Omega_3|5>)/A$ with time-dependent Rabi frequencies $\Omega_i = \Omega_i(t)$ for lasers L_i, $i=1,2,3,4$, and the appropriate normalization function $A = A(t)$. Similar to standard two-photon STIRAP, a counter-intuitive pulse sequence rotates the initial state $|1>$ adiabatically into the final state, here $|5>$. For this, L_2 and L_3 couple the three intermediate levels while L_4 and L_1 deliver time-dependent overlapping pulses with L_4 preceding L_1. Fig. 4.13b and e show the timings for both schemes including the reverse sequence used for detecting the ground-state molecules after a certain hold time τ_h.

We investigate 4p-STIRAP to $|v=0, J=0>$ by interrupting the transfer sequence after a given 4p-STIRAP time τ and measuring the number of Feshbach molecules, as shown in Fig. 4.13a. The molecules are transferred to $|5>$ in a single step. No molecules in $|1>$ are detected during τ_h as the remaining Feshbach molecules are cleared by L_1 at the end of the transfer. When the pulse sequence is reversed, a large fraction of the molecules returns to $|1>$. Typically, 30% of the molecules are recovered after the full double 4p-STIRAP sequence. Almost all reside in the lowest band of the lattice as evidenced by

band-mapping experiments [Blo08]. The rectangular shape of the first Brillouin zone can be clearly seen in the momentum-space image shown in the lower inset of Fig. 4.13a. 92(3)% of the molecules can be found in the first Brillouin zone and hence had resided in the lowest lattice vibrational level. Assuming equal efficiencies for both transfers, the single-pass efficiency is 55%. The upper inset of Fig. 4.13a shows the double 4p-STIRAP efficiency versus detuning Δ_4 of L_4 from the ($|4> \rightarrow |5>$)-transition with all other lasers on resonance. With ground-state transfer efficiencies between 55% and 60%, about half of the lattice sites are occupied by a ground-state molecule. The solid lines in Fig. 4.13a represent a simulation of 4p-STIRAP that takes into account excited-state spontaneous decay and laser linewidth. Transfer times are typically 4 μs to 10 μs. The simulation yields that the transfer efficiency is currently limited by a combination of laser linewidth, which is about 10 kHz when averaged over 1 s, and imperfect adiabaticity due to finite available laser power to drive the extremely weak transitions of the 5-level scheme [Dan08, Mar09]. Molecules not transferred to $|5>$ as a result of insufficient phase coherence or limited adiabaticity are excited to either $|2>$ or $|4>$ by one of the lasers and are hence pumped into a multitude of rovibrational levels, which do not couple to the rovibrational ground state. For comparison, the double s-STIRAP efficiency from $|3>$ to $|v = 0, J = 0>$ and $|v = 0, J = 2>$ is shown in Fig. 4.13c and d, respectively. The solid lines represent a calculation matched to the data for standard 3-level STIRAP. With 55%-60%, the total ($|1> \rightarrow |5>$)-transfer efficiency for s-STIRAP is comparable to 4p-STIRAP.

4.4.4. Polarizability and lifetime

A crucial prerequisite for efficient ground-state transfer without heating is good matching of the motional wave functions for the initial weakly-bound state and the final ground state. A mismatch leads to unwanted excitation of higher lattice vibrational levels or bands and hence to loss of state control. The lattice thus has to be operated at the magic wavelength condition [Ye08], i.e. at a wavelength that gives equal light shifts for the initial and the final molecular states. Our experiment in fact shows, as discussed above, that hardly any population is transferred to higher lattice bands. We now measure the lattice band structure and determine the molecular polarizability of the ground-state molecules (see the Methods section). Molecules residing in the lowest band of the lattice are excited to the first (second) band by phase (amplitude) modulation of the light generating the lattice. Fig. 4.14 shows the measured band energies together with a calculation of the band structure as a function of lattice depth. On resonance, excitation to higher bands can readily be observed in momentum space as shown in inset **a**. For comparison, off-resonant modulation transfers hardly any population into higher bands (see inset **b**). We determine the band energies by taking modulation spectra as shown in inset **c**. We then use the band structure calculation to fit all measured resonance positions with the molecular dynamical polarizability $P_{|v=0>}$ as the single free parameter. These measurements are done

for $|v = 0, J = 2>$. We obtain $P_{|v=0>} = 2.1(1) \times P_a$, where P_a is the atomic polarizability. For the initial, weakly-bound Feshbach molecules in level $|g>$ we obtain $P_{|g>} = 2.0(1) \times P_a$. Hence the magic wavelength condition is well fulfilled.

We measure the lifetime τ_e of the molecules in the lattice by varying the hold time τ_h for up to 20 s and recording the number of remaining molecules as shown in Fig. 4.15. To reduce inelastic light scattering, the lattice depth was adiabatically reduced to about 41.5 $\tilde{E}_R$ after the 4p-STIRAP transfer. An exponential fit gives a $1/e$-lifetime of $\tau_e = 8.1(6)$ s. We attribute this long lifetime to the large detuning $\Delta_L \approx 6.9$ THz from the lowest 0_u^+ level with predominant $A^1\Sigma_u^+$ singlet contribution as shown in the inset to Fig. 4.15. Levels of the 0_u^+ system that lie below this are almost purely of $b^3\Pi_u$ character and thus make negligible contributions to the optical excitation rate.

4.4.5. Conclusion

We are now in a position to determine collisional properties of ultracold ground-state molecules in a fully state-selective way. At magnetic fields beyond 13 mT, where the level $|I = 6, M_I = 6>$ becomes the absolute ground state, the sample should show collisional stability and thus allow the formation of a BEC of ground-state molecules when the lattice is adiabatically removed [Jak02]. For Cs_2, formation of a trimer and an atom in a dimer-dimer collision is predicted to be energetically forbidden (R. Guérout and O. Dulieu, private communication, 2009). The long coherence times and the perfect decoupling from the environment in an optical lattice as demonstrated here will enable a new generation of precision measurements [DeM08, Zel08]. Furthermore, our results can readily be generalized to heteronuclear systems such as KRb [Ni08] and RbCs [Pil09], opening up the possibility to study dipolar quantum phases in optical lattices.

4.4.6. Methods

Lattice loading

We first follow the procedure detailed in Ref. [Dan09a]. In brief, we produce an atomic BEC with typically 1×10^5 Cs atoms in the lowest hyperfine sublevel $|F_a = 3,\ m_{Fa} = 3>$ in a crossed optical dipole trap. We then drive the superfluid-to-Mott-insulator phase transition [Blo08] by exponentially ramping up the power in a three-dimensional optical lattice within about 300 ms. The lattice is generated by three mutually-orthogonal, retro-reflected laser beams at a wavelength of $\lambda = 1064.5$ nm, each with a $1/e^2$-waist of about 350 μm. While ramping up the lattice potential, the power in the two dipole-trap beams is increased to ensure that the central density in the trap is sufficiently high to allow formation of atom pairs at the central wells of the lattice, but not too high to lead to triply occupied sites. Atoms at triply occupied sites would rapidly be cleared out by inelastic three-body collisions. We ramp the lattice to a depth of about 20 E_R before Feshbach association. Here, $E_R = h^2/(2m_a\lambda^2) = k_B \times 64\,\mathrm{nK}$

is the atomic photon-recoil energy with the mass m_a of the Cs atom and Boltzmann's constant k_B. Up to 45(2)% of the atoms reside at doubly occupied lattice sites. We estimate this number from the number of molecules that we obtain and the molecule production efficiency.

For the molecules, the recoil energy is $\tilde{E}_R = h^2/(2\times 2m_a\lambda^2)$. The polarizability of Feshbach molecules is twice the atomic polarizability. The same lattice that has a depth of 20 E_R for the atoms has thus a depth of 80 $\tilde{E}_R$ for the Feshbach molecules.

Feshbach association and Feshbach state transfer

We efficiently produce weakly bound Cs_2 Feshbach molecules in the presence of the optical lattice by a magnetic field sweep [Chi10] across a narrow g-wave Feshbach resonance with its pole at a magnetic field value of $B = 1.98$ mT [Her03, Mar07a]. The molecules are initially in level $|g>$, for which $\ell = 4$. Here, ℓ is the quantum number associated with the mechanical rotation of the nuclei [Chi10]. We subsequently transfer the molecules via level $|g_2>$ with 95(3)% efficiency into level $|s> \equiv |1>$ with $\ell = 0$ by magnetic field ramping [Mar07a, Dan09a] as shown in Fig. 4.12b. For this level, the transitions to excited molecular levels are stronger than for the initial level $|g>$ [Dan09b]. We obtain up to 2.5 $\times 10^4$ Feshbach molecules in the lattice in the desired starting state. Assuming a perfect filling of the two-atom Mott-shell at the center of the trap, taking into account the efficiencies for molecule production and state transfer, and factoring in weak additional loss during sample purification, 85(3)% of the central lattice sites are occupied. We detect the molecules in $|1>$ by reversing the Feshbach state transfer sequence, dissociating the molecules at the Feshbach resonance and detecting the resulting atoms by standard absorption imaging [Her03].

Molecular states for ground state transfer

The relevant molecular states for Cs_2 are shown in Fig. 4.12a. Levels $|2>$ and $|4>$ belong to the coupled $(A^1\Sigma_u^+ - b^3\Pi_u)0_u^+$ potentials [Dan08]. We have recently identified suitable transitions linking $|1>$ to $|5>$, where levels $|2>$, $|3>$, and $|4>$ were chosen to give balanced transition strengths on the four optical transitions [Dan09b, Mar09]. For $|3>$ we choose either $|v=73, J=2>$ or $|v=73, J=0>$ of the $X^1\Sigma_g^+$ ground state with a binding energy of $\sim hc \times 1061$ cm^{-1}.

Hyperfine structure of the rovibronic ground state

The hyperfine levels are calculated using the molecular constants from Ref. [Ald09] by constructing and diagonalizing a Hamiltonian matrix in an uncoupled basis set of functions representing the molecular rotation and the spins of the two nuclei, using the matrix elements given in the Appendix of Ref. [Ald09]. For $J = 0$ states the hyperfine structure is dominated by the scalar spin-spin

coupling and the nuclear Zeeman effect, but for $J > 0$ additional terms are important.

STIRAP laser setup

STIRAP lasers L_i with $i = 1, 2, 3, 4$ are continuous-wave grating-stabilized tunable diode lasers, which are stabilized to optical resonators for short-term stability and referenced to an optical frequency comb for long-term stability and reproducibility. We estimate the linewidth of the lasers to be about 10 kHz. In order to ensure minimum momentum recoil imparted on the molecules, the beams for lasers L_1 and L_2 are co-propagating. The beams for L_3 and L_4 are also co-propagating but run antiparallel to the beams of L_1 and L_2. All beams run horizontally and are linearly polarized with the polarization axis in the vertical direction, parallel to the direction of the magnetic field, which defines the axis of quantization. We operate at Rabi frequencies in the range of $2\pi\times$ (1 to 4) MHz.

Polarizability measurement

For determining the ground state molecular polarizability, transfer to $|v = 0>$ is performed at a fixed lattice depth of 83 $\tilde{E}_R$ for $|v = 0>$ molecules. The lattice depth is then ramped to the desired value within 50 ms. For phase modulation of the lattice, the frequency of one lattice beam is usually modulated with a modulation depth of 2 MHz at the desired frequency for about 10 ms. For amplitude modulation, the intensity is typically modulated by 20% for about 10 ms.

Acknowledgements We thank H. Ritsch, S. Dürr, N. Bouloufa, and O. Dulieu for valuable discussions. We are indebted to R. Grimm for generous support and to H. Häffner for the loan of a charge-coupled camera. We gratefully acknowledge funding by the Austrian Ministry of Science and Research (Bundesministerium für Wissenschaft und Forschung) and the Austrian Science Fund (Fonds zur Förderung der wissenschaftlichen Forschung) in form of a START prize grant and by the European Science Foundation within the framework of the EuroQUASAR collective research project QuDeGPM and within the framework of the EuroQUAM collective research project QuDipMol. R.H. is supported by a Marie Curie International Incoming Fellowship within the 7th European Community Framework Programme.

Author Contributions All authors contributed extensively to the work presented in this paper.

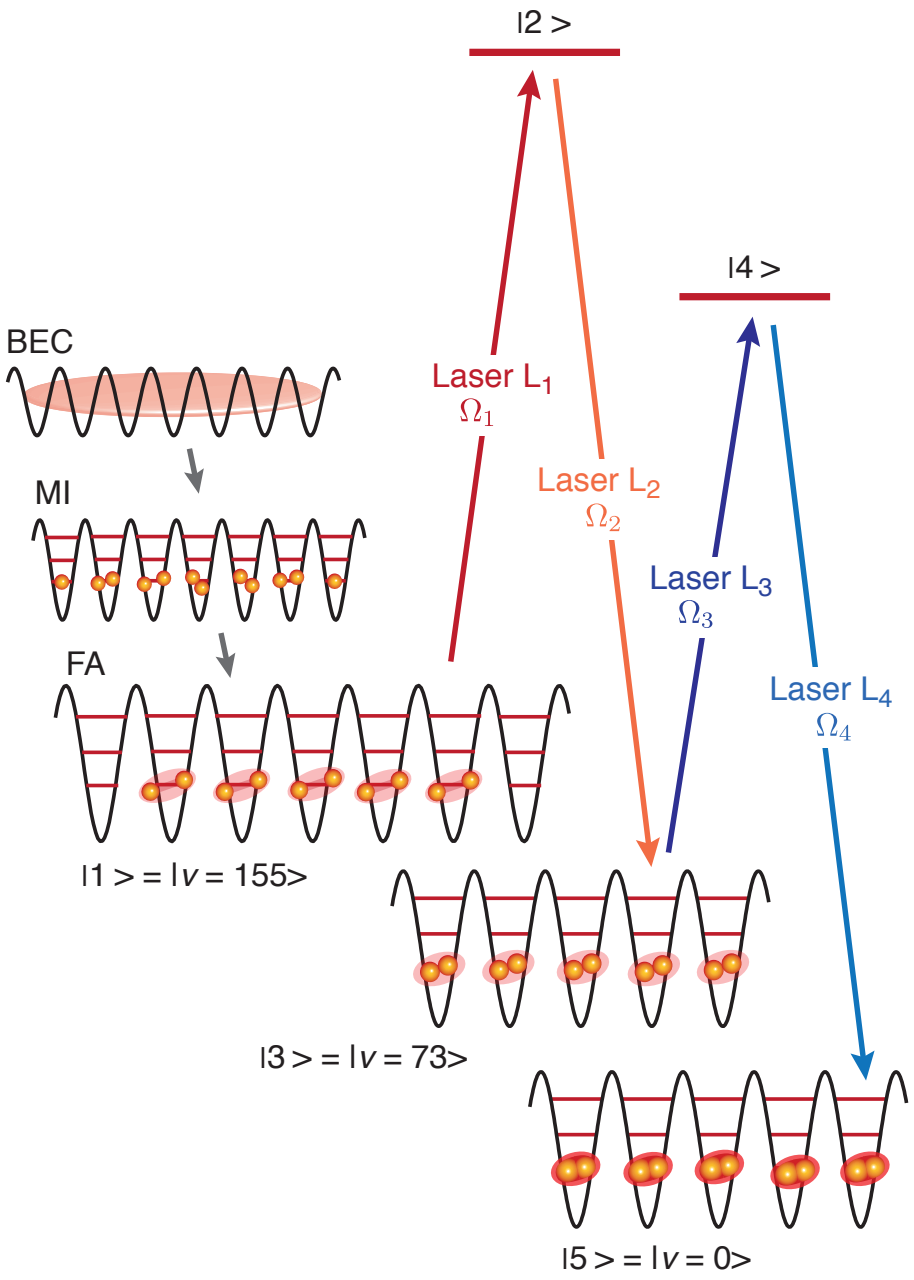

Fig. 4.11.: Molecular quantum gas preparation procedure. A BEC of Cs atoms is loaded into an optical lattice. By increasing the lattice depth, a Mott-insulator state (MI) with preferentially two atoms per site is created. Feshbach association (FA) subsequently converts atom pairs into weakly-bound molecules in state $|1>$. These are then transferred in the presence of the lattice to a specific hyperfine level $|I=6, M_I=6>$ of the rovibronic ground state $|5> = X^1\Sigma_g^+ \; |v=0, J=0>$ by a stimulated four-photon process (STIRAP) involving lasers L_i with Rabi frequencies Ω_i $i = 1, 2, 3, 4$, and three intermediate levels $|2>$, $|3>$, and $|4>$.

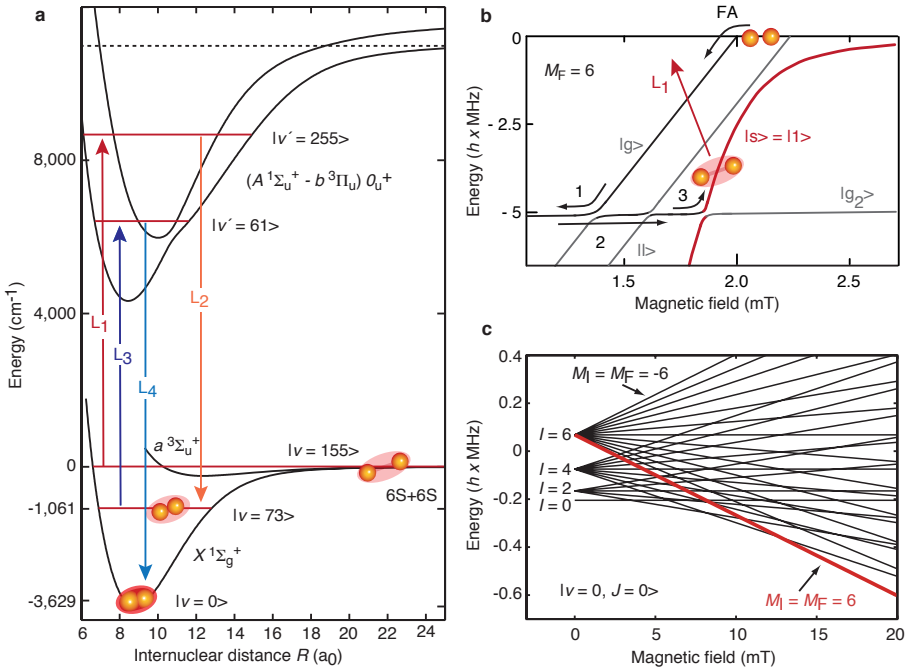

Fig. 4.12.: Molecular potentials and level schemes for ground-state transfer. **a**, The four-photon transfer from the weakly-bound Feshbach level $|1\rangle = |\nu \approx 155\rangle$ (not resolved near the 6S+6S asymptote) to the rovibrational ground state $|5\rangle = |\nu = 0, J = 0\rangle$ of the singlet $X^1\Sigma_g^+$ potential involves the deeply bound level $|3\rangle = |\nu = 73\rangle$ of the $X^1\Sigma_g^+$ potential [Dan08] and the levels $|2\rangle = |\nu' = 225, J = 1\rangle$ and $|4\rangle = |\nu' = 61, J = 1\rangle$ of the electronically excited $(A^1\Sigma_u^+ - b^3\Pi_u)\ 0_u^+$ potentials [Dan09b, Mar09]. The laser wavelengths for L_1, L_2, L_3, and L_4 are near 1126 nm, 1006 nm, 1351 nm, and 1003 nm, respectively. **b**, Zeeman diagram for weakly bound molecules near the 6S+6S asymptote. Molecules are associated at a g-wave Feshbach resonance [Her03] at 1.98 mT (FA) and then transferred to the desired starting level $|1\rangle = |s\rangle$ for optical transfer via three avoided level crossings by slow (arrows 1,3) and fast (arrow 2) magnetic field ramps [Mar07a]. The binding energy is given with respect to the $(F_{a_1} = 3, m_{Fa_1} = 3) \times (F_{a_2} = 3, m_{Fa_2} = 3)$ two-atom lowest hyperfine asymptote. All Feshbach levels are characterized by $M_F = 6$. **c**, Calculated Zeeman diagram for the hyperfine manifold of the rovibronic ground state $|5\rangle = |\nu = 0, J = 0\rangle$. The optical transfer goes selectively to level $|I = 6, M_I = 6\rangle$, indicated in red. This level becomes the lowest-energy absolute ground state for magnetic-field values above ~ 13 mT. There are no avoided crossings between different hyperfine sublevels [Ald09].

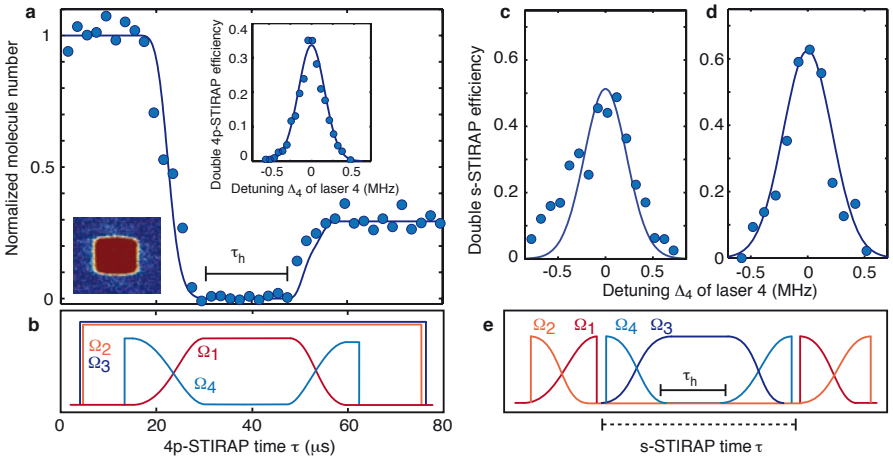

Fig. 4.13.: STIRAP transfer to the rovibronic ground state $|5>=|\nu=0, J=0>$ **and back.** **a**, 4p-STIRAP transfer and **b**, schematic timing for the Rabi frequencies Ω_i, $i = 1, 2, 3, 4$: Number of molecules in state $|1>$ as a function of 4p-STIRAP time τ for all 4 lasers on resonance. The lattice depth is 80 $\tilde{E}_R$ and 83 $\tilde{E}_R$ for molecules in levels $|1>$ and $|5>$, respectively. Data points represent a single experimental realization, not an average over several runs. The solid line is a 4p-STIRAP model calculation. τ_h is the hold time in $|5>=|\nu=0, J=0>$. Upper inset: double 4p-STIRAP efficiency as a function of the detuning Δ_4 of laser L_4 and corresponding model calculation. The peak corresponds to a single-pass efficiency of 57%. Lower inset: Band mapping of molecules after the double STIRAP sequence. The absorption images corresponding to data points beyond $\tau = 60$ μs are averaged and smoothed with a Gaussian filter. The colour scale is chosen to emphasize any small population in higher bands. **c**, and **d**, s-STIRAP: Double STIRAP efficiency for the inner two-photon STIRAP from $|3>$ to $|v=0, J=0>$ (**c**) and to $|v=0, J=2>$ (**d**) and back, corresponding to the dotted bar in the timing sequence in **e**, as a function of the detuning Δ_4 of laser L_4. The number of molecules is normalized to the initial number in $|3>$. All measurements are performed at an offset magnetic field of 1.9 mT.

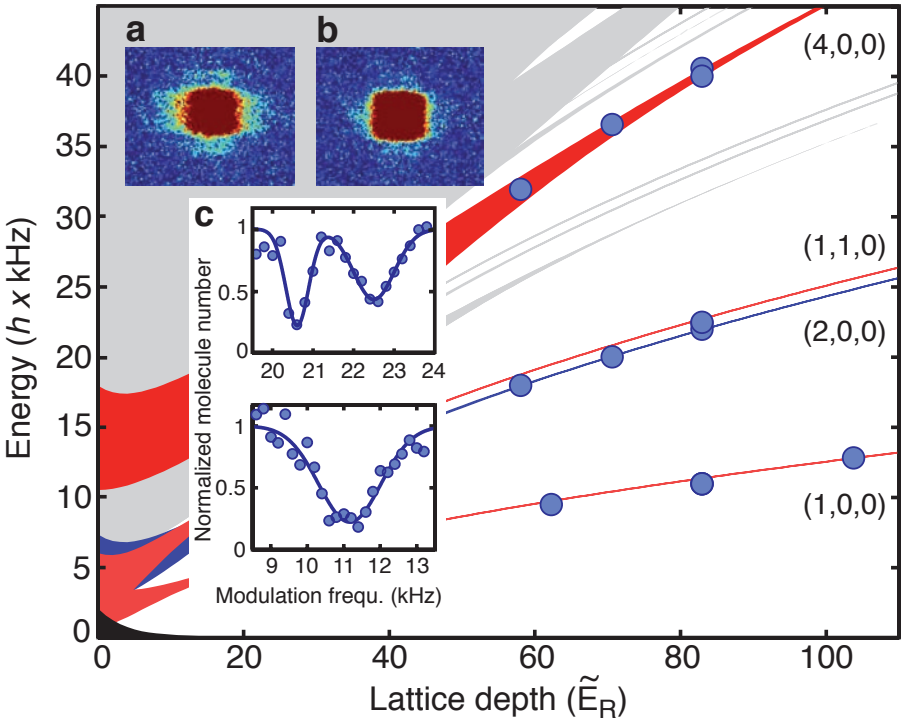

Fig. 4.14.: Lattice band structure for $|v = 0>$ molecules. Band energies as a function of lattice depth in units of the molecular recoil energy $\tilde{E}_R$ as measured by phase and amplitude modulation of the lattice. The lattice bands are labeled by (k, l, m), where k, l, and m give the number of vibrational quanta along the three spatial directions in the limit of a deep lattice. The horizontal position of the data points (filled circles, representing the position of excitation resonances as shown in inset **c**) is given by the molecular polarizability, which is determined by a fit of the data to the band structure. Inset **a** shows the molecular momentum distribution after transfer to higher lattice bands by resonant lattice amplitude modulation. The distribution represents an average of 5 experimental runs, smoothed with a Gaussian filter. For comparison, inset **b** shows that hardly any population is transferred to higher bands for off-resonant modulation. Inset **c** shows typical excitation spectra for amplitude (top) and phase (bottom) modulation at 83 $\tilde{E}_R$. For these, we determine the number of molecules in the first Brillouin zone as a function of the excitation frequency. The solid lines are Gaussian fits. The resonance at 22.5 kHz corresponds to excitation to the nearly-degenerate bands (2,0,0) and (1,1,0) (not resolved). The resonance at 20.6 kHz is a two-phonon excitation to (4,0,0).

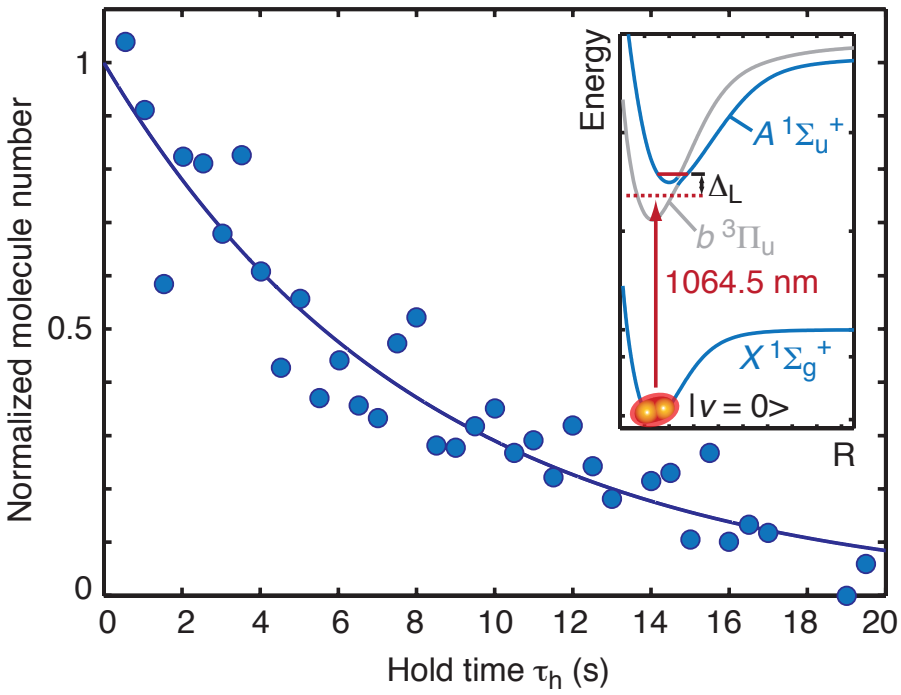

Fig. 4.15.: Lifetime of trapped ground-state molecules in the optical lattice. Normalized number of molecules in $|5\rangle = |\nu = 0, J = 0\rangle$ as a function of hold time τ_h. The solid line is an exponential fit, yielding a lifetime of 8.1(6)s. The inset schematically shows the excited-state potentials to which off-resonant optical excitation is possible (cf. Fig. 4.12a). Δ_L is the detuning of the lattice light at 1064.5 nm with respect to the lowest 0_u^+ level with $A^1\Sigma_u^+$ character. During the hold time, all STIRAP laser fields are turned off.

4.5. Publication: Precision molecular spectroscopy for ground state transfer of molecular quantum gases

Faraday Discuss. **142**, 283 (2009)†

Johann G. Danzl[1], Manfred J. Mark[1], Elmar Haller[1], Mattias Gustavsson[1], Nadia Bouloufa[2], Olivier Dulieu[2], Helmut Ritsch[3], Russell Hart[1], and Hanns-Christoph Nägerl[1]

[1] *Institut für Experimentalphysik und Zentrum für Quantenphysik, Universität Innsbruck, Technikerstraße 25, A–6020 Innsbruck, Austria.*
[2] *Laboratoire Aimé Cotton, CNRS, Université Paris-Sud, Bât. 505, 91405 Orsay Cedex, France.*
[3] *Institut für Theoretische Physik und Zentrum für Quantenphysik, Universität Innsbruck, Technikerstraße 25, A–6020 Innsbruck, Austria.*

One possibility for the creation of ultracold, high-phase-space-density quantum gases of molecules in the rovibrational ground state relies on first associating weakly-bound molecules from quantum-degenerate atomic gases on a Feshbach resonance and then transfering the molecules via several steps of coherent two-photon stimulated Raman adiabatic passage (STIRAP) into the rovibronic ground state. Here, in ultracold samples of Cs_2 Feshbach molecules produced out of ultracold samples of Cs atoms, we observe several optical transitions to deeply bound rovibrational levels of the excited 0_u^+ molecular potentials with high resolution. At least one of these transitions, although rather weak, allows efficient STIRAP transfer into the deeply bound vibrational level $|v=73>$ of the singlet $X^1\Sigma_g^+$ ground state potential, as recently demonstrated [Dan08]. From this level, the rovibrational ground state level $|v=0, J=0>$ can be reached with one more transfer step. In total, our results show that coherent ground state transfer for Cs_2 is possible using a maximum of two successive two-photon processes or one single four-photon STIRAP process.

†The author of the present thesis contributed to this work by assisting the experimental measurements. He also maintained and improved the experimental setup and contributed to the paper writing.

4.5.1. Introduction

Ultracold and dense molecular samples in specific deeply bound rovibrational levels are of high interest for fundamental studies in physics and chemistry. They are expected to find applications in high resolution spectroscopy and fundamental tests [Zel08, DeM08], few-body collisional physics [Sta06, Zah06], ultracold chemistry [Kre05], quantum processing [DeM02], and in the field of dipolar quantum gases and dipolar Bose-Einstein condensation [Gór02, Bar02]. Ideally, full control over the molecular wave function is desired, i.e. full (quantum) control over the internal and external degrees of freedom of the molecules. High phase space densities are needed for molecular quantum gas studies. For many of the envisaged studies and applications, initial preparation of the molecular sample in the rovibronic ground state, i.e. the lowest energy level of the electronic ground state, is desired. Only in this state one can expect sufficient collisional stability.

But how is it possible to produce dense samples of ultracold molecules in the rovibrational ground state? Laser cooling of atoms, which has lead to the production of quantum degenerate atomic Bose and Fermi gases [Sou02], can so far not be adapted to the case of molecular systems as suitable cycling transitions are not available. Versatile non-optical cooling and slowing techniques such as buffer gas cooling and Zeeman slowing in combination with molecule trapping [Doy04, Kre08, van08] have been developed, but high molecular densities and in particular high phase space densities are yet to be reached. An alternative route to producing ultracold molecular samples is given by first producing ultracold atomic samples and then associating molecules out of the atomic sample. While this technique is so far limited to the production of selected species of dimer molecules, it has the advantage that ultra-low temperatures and high particle densities are easily inherited from the atomic precursor sample. There are essentially two association techniques, photoassociation [Jon06] and magnetically induced Feshbach association [Köh06, Fer08]. In photoassociation experiments [Nik00, Sag05, Vit08, Dei08], ultracold samples of deeply bound molecules have been created. Additional techniques such as vibrational cooling [Vit08] should allow selective pumping into the rovibrational ground state and open up the prospect for high molecular phase space densities. In Feshbach association experiments [Reg03, Her03], high-density samples of weakly bound molecules are produced. For dimer molecules composed of Fermions, collisional stability of the highly excited molecules is assured as a result of a Pauli blocking effect, and molecular Bose-Einstein condensation could be achieved in the limit of extremely weak binding [Ing08].

Here, we are interested in combining the techniques of Feshbach association and coherent molecular state transfer to produce quantum gases of molecules in the rovibrational ground state $|v = 0, J = 0>$ of the lowest electronic state. As usual, v and J are the vibrational and rotational quantum numbers, respectively. The molecules, produced on a Feshbach resonance and hence initially very loosely bound, are to be transferred in a few successive steps of coherent two-photon laser transfer to the rovibrational ground state, acquiring more and more binding energy in each step. The general idea is sketched in Fig. 4.16A for

the case of Cs_2. Each two-photon step involves an excited state level. Population transfer into this level needs to be avoided to prevent loss due to spontaneous emission. One possibility is to use the technique of stimulated Raman adiabatic passage (STIRAP) [Ber98], which is very robust and largely insensitive to laser intensity fluctuations. The scheme has several advantages. First, production of Feshbach molecules out of a quantum degenerate atomic sample can be very efficient [Mar05]. Second, the optical transition rate on the first transition starting from the Feshbach molecules is greatly enhanced in comparison to the free atom case. Further, the scheme is fully coherent, not relying on spontaneous processes, allowing high state selectivity, and involving only a comparatively small number of intermediate levels. A ground state binding energy of typically 0.5 eV for an alkali dimer can be removed essentially without heating the molecular sample, as the differential photon recoil using pairwise co-propagating laser beams driving the two-photon transitions is very small. If losses and off-resonant excitations can be avoided, the scheme essentially preserves phase space density and coherence of the initial particle wave function, allowing the molecular sample to inherit the high initial phase space density from the atomic precursor sample.

Certainly, several challenges have to be met: Going from weakly bound Feshbach to tightly bound ground state molecules corresponds to a large reduction in internuclear distance. Consequently, the radial wave function overlap between successive levels is small, and a compromise has to be found between the number of transitions and the minimum tolerable wave function overlap. To keep the complexity of the scheme low, one or at most two two-photon transitions are desirable. Accordingly, suitable intermediate levels have to be identified that allow a balanced division of wave function overlap, as given by the Franck-Condon factors, between the different transitions. For example, for a four-photon transition scheme with Cs_2 as shown in Fig. 4.16A the Franck-Condon factors are all on the order of 10^{-6}. We emphasize that the identification of the first excited level and hence of the first transition starting from the Feshbach molecules is of crucial importance. Detailed calculations determining the wave function overlap are generally missing, and estimates on the Franck-Condon factors using hypothetical last bound states of either the singlet or triplet potentials of an alkali dimer molecule do not necessarily reflect the transition dipole moments adequately. In addition, for electronic molecular states or energy regions where spectroscopic data is missing, the precise energy of the excited state levels above the atomic threshold is known only with a large uncertainty which can approach the vibrational spacing of a few nanometers. Hence, considerable time has to be spent on searching for weak transitions starting from the initial Feshbach molecules.

In a pioneering experiment, Winkler *et al.* [Win07] demonstrated that the STIRAP technique can efficiently be implemented with quantum gases of weakly bound Feshbach molecules. In this work, the transferred molecules, in this case Rb_2, were still weakly bound with a binding energy of less than 10^{-4} of the binding energy of the rovibronic ground state, and the intermediate excited state level was close to the excited-atom asymptote. Here, we observe several

optical transitions starting from a weakly bound Feshbach level to deeply bound rovibrational levels of the mixed excited $(A^1\Sigma_u^+ - b^3\Pi_u)$ 0_u^+ molecular potentials of the Cs_2 molecule in a wavelength range from 1118 to 1134 nm, far to the red of the atomic D_1 and D_2 transitions. The Cs_2 molecular potentials are shown in Fig. 4.16A. We observe the levels as loss from an ultracold sample of Cs_2 Feshbach molecules as shown in Fig. 4.16B. We observe two progressions, one that we attribute to the $(A^1\Sigma_u^+ - b^3\Pi_u)$ 0_u^+ potentials and one that we associate to the triplet $(1)^3\Sigma_g^+$ potential. From the loss measurements, we determine the transition strengths and find that the stronger transitions should be suitable for STIRAP to an intermediate, deeply bound rovibrational level of the singlet $X^1\Sigma_g^+$ potential with $v = 73$. Recently, we could implement STIRAP into $|v = 73, J = 2>$ [Dan08]. For the case of the dimer molecule KRb, Ni *et al.* [Ni08] could demonstrate quantum gas transfer all the way into the rovibrational ground state $|v = 0, J = 0>$ of the singlet $X^1\Sigma^+$ molecular potential. Here, the transfer could be achieved in only a single step as a result of the favorable run of the excited state potentials, which is generally the case for heteronuclear molecules composed of alkali atoms [Stw04]. Also recently, transfer to the rovibrational ground state of the lowest triplet state $a^3\Sigma_u^+$ of Rb_2 could be achieved [Lan08b].

4.5.2. Preparation of a sample of weakly bound Feshbach molecules

We produce ultracold samples of molecules on two different Feshbach resonances, one near 1.98 mT and one near 4.79 mT [Mar07a]. In both cases, essentially following the procedure detailed in Ref.[Web03a], we first produce an ultracold sample of typically 2×10^5 Cs atoms in the lowest hyperfine sublevel $F = 3,\ m_F = 3$ in a crossed optical dipole trap. As usual, F is the atomic angular momentum quantum number, and m_F its projection on the magnetic field axis. The trapping light at 1064.5 nm is derived from a single-frequency, highly-stable Nd:YAG laser. The offset magnetic field value for evaporative cooling is 2.1 mT. We support optical trapping by magnetic levitation with a magnetic field gradient of 3.1 mT/cm. We then produce weakly bound Feshbach molecules out of the atomic sample [Her03]. We produce a sample every 8 s, i.e. our spectroscopic measurements are performed at a rate of one data point every 8 s. In order to be able to search for optical transitions over large frequency ranges it is advantageous to work with the shortest possible sample preparation times. For this reason we stop evaporative cooling slightly before the onset of Bose-Einstein condensation (BEC), which also makes sample preparation somewhat less critical. The temperature of the initial atomic sample is then typically about 100 nK. At higher temperatures and hence lower phase space densities the molecule production efficiency is reduced, so that there is a trade off between ease of operation and molecule number. We note that for our ground state transfer experiments reported in Ref.[Dan08] we produce a pure atomic BEC at the expense of longer sample preparation times.

The spectrum of weakly-bound Feshbach levels near the two-free-atom asymp-

tote is shown in Fig. 4.17 [Mar07a]. For molecule production at the Feshbach resonance at 4.79 mT, we first ramp the magnetic field from the BEC production value to 4.9 mT, about 0.1 mT above the Feshbach resonance. We produce the molecular sample on a downward sweep at a typical sweep rate of 0.025 mT/ms. The resulting ultracold sample contains up to 11000 molecules, immersed in the bath of the remaining ultracold atoms. The resonance at 4.79 mT is a d-wave resonance [Mar07a], and hence the molecules are initially of d-wave character, i.e. $\ell = 2$, where ℓ is the quantum number associated with the mechanical rotation of the nuclei. However, there is a weakly bound s-wave Feshbach state ($|s>=|\ell = 0>$) belonging to the open scattering channel right below threshold. This state couples quite strongly to the initial d-wave state, resulting in an avoided state crossing (as shown in the inset to Fig. 4.17), on which the molecules are transferred to the s-wave state $|s>$ upon lowering the magnetic field [Mar07a, Dan08]. Upon further lowering the magnetic field to less than 2.0 mT, the molecules acquire more and more character of a closed channel s-wave state on a second, very broad avoided crossing. Here, we perform spectroscopy in this transition range from open channel to closed channel s-wave character. At a magnetic field value of 2.0 mT, the binding energy of the molecules is near 5 MHz$\times h$ with respect to the $F = 3, m_F = 3$ two-atom asymptote, where h is Planck's constant.

For molecule production at the Feshbach resonance at 1.98 mT, we simply ramp the magnetic field down from the initial BEC production value. Again, we produce an ultracold molecular sample with about 11000 molecules. The molecules in $|g>$ have g-wave character, i.e. $\ell = 4$. When we lower the magnetic field to 1.6 mT, the binding energy of the molecules is also near 5 MHz$\times h$ with respect to the $F = 3, m_F = 3$ two-atom asymptote.

For spectroscopy, we release the molecules from the trap after magnetic field ramping is completed and perform all subsequent experiments in free flight without any other light fields on except for the spectroscopy laser.

For molecule detection in both cases, we reverse the magnetic field ramps [Her03]. The g-wave molecules are dissociated on the g-wave Feshbach resonance at 1.98 mT, and the s-wave molecules are dissociated on the d-wave Feshbach resonance at 4.79 mT. Prior to the reverse magnetic field ramp, we apply a magnetic field gradient of 3.1 mT/cm for about 5 ms to separate the molecular from the atomic sample in a Stern-Gerlach-type experiment. Finally, we detect atoms by standard absorption imaging. The minimum number of molecules that we can detect is on the order of 200 molecules.

4.5.3. Spectroscopy

We perform optical spectroscopy on Feshbach molecules in the wavelength region around 1125 nm. Based on symmetry considerations, there are two sets of electronically excited states that we address in the spectroscopic measurements presented here, namely the
$(\mathrm{A}^1\Sigma_u^+ - \mathrm{b}^3\Pi_u)$ 0_u^+ coupled state system and the $(1)^3\Sigma_g^+$ electronically excited

states. We first discuss transitions to the 0_u^+ coupled state system. Transitions to the latter state are discussed in Sec. 4.5.3.

Transitions to the $(\mathbf{A}^1\Sigma_u^+ - \mathbf{b}^3\Pi_u)$ 0_u^+ coupled electronically excited states

We are primarily interested in transitions from Feshbach levels to rovibrational levels of the $(\mathrm{A}^1\Sigma_u^+ - \mathrm{b}^3\Pi_u)$ 0_u^+ electronically excited states. In the heavy alkali dimers, most notably in Cs_2, the $\mathrm{A}^1\Sigma_u^+$ state and the $\mathrm{b}^3\Pi_u$ state are strongly coupled by resonant spin-orbit interaction [Dul95, Ami99], yielding the 0_u^+ coupled states in Hund's case (c) notation. The singlet component of the 0_u^+ states allows us to efficiently couple to deeply bound $\mathrm{X}^1\Sigma_g^+$ state levels, specifically to the $|v=73, J=2>$ level of the ground state potential, as has recently been shown in a coherent transfer experiment [Dan08]. We have chosen to do spectroscopy in the wavelength range of 1118 nm to 1134 nm above the $6S_{\frac{1}{2}}+6S_{\frac{1}{2}}$ dissociation threshold of the Cs_2 dimer. This corresponds to a detuning of roughly 2300 cm^{-1} from the cesium D_1 line and to an energy range of approximately 12572 cm^{-1} to 12450 cm^{-1} above the rovibronic ground state $\mathrm{X}^1\Sigma_g^+$ $|v=0, J=0>$. This region was chosen in order to give a balanced distribution of transition dipole moments in a 4-photon transfer scheme to the rovibronic ground state. In addition, the wavelengths of the four lasers used in the transfer experiments were chosen such that they lie within the energy range covered by the infrared fiber-based frequency comb that we use as a frequency reference in the state transfer experiments.

The transitions of interest here lie outside the energy regions for which Fourier transform spectroscopic data was obtained at Laboratoire Aimé Cotton from transitions to the $\mathrm{X}^1\Sigma_g^+$ state [Sal08b]. The vibrational progression of the 0_u^+ states is highly perturbed by the resonant spin-orbit coupling and exhibits an irregular vibrational spacing. Molecular structure calculations are complicated by the spin-orbit coupling and calculated term values are highly sensitive to the coupling. Prior to the experiments discussed here the absolute energies of the vibrational levels of the $(\mathrm{A}^1\Sigma_u^+ - \mathrm{b}^3\Pi_u)$ 0_u^+ excited state levels were poorly known in the region of interest from 1118 nm to 1134 nm. We therefore perform a broad range search by irradiating the weakly-bound Feshbach molecules at a fixed wavelength for a certain irradiation time τ of up to $\tau = 6$ ms and by recording the number of remaining molecules as a function of laser frequency. In one run of the experiment one particular laser frequency is queried. We thus take data points at the repetition rate of our experiment, which is given by the sample preparation time of 8 seconds. Based on the available laser intensity from L_1 and an estimate of the dipole transition moments for the strongest expected lines, we chose a frequency step size of about 100 MHz to 150 MHz for initial line searching. We obtain the laser light at 1118 nm - 1134 nm from a grating-stabilized external cavity diode laser. For coarse frequency scanning, the laser is free running and tuned via a piezoelectric element on the grating of the laser. For more precise measurements, we lock the laser to a narrow-band optical resonator that can be tuned via a piezoelectric element. Fig. 4.18A shows a typical loss spectrum starting from Feshbach state $|s>$ for excitation

near 1126 nm, measured at a magnetic field of 1.98 mT. In this particular case we find three resonances, which we associate with the rotational splitting of the excited state level, $J = 5, 3, 1$, where J is the rotational quantum number. Based on molecular structure calculations we identify this level as the 225th one of the 0_u^+ progression with an uncertainty of about two in the absolute numbering. We zoom in on these three transitions in Fig. 4.18B, C, and D and record loss resonances at reduced laser intensity in order to avoid saturation of the lines. For these measurements, the laser is locked to the narrow-band optical resonator and the resonator in turn is stabilized to the optical frequency comb to assure reproducibility and long term frequency stability. As one can expect, the loss is strongest on the transition to the $|J = 1>$ level, and it is weakest on the transition to $|J=5>$. All lines have an excited state spontaneous decay rate of around $2\pi \times 2$ MHz, in agreement with the typical expected lifetimes of excited molecular levels. The transition to $|J=1>$ shown in Fig. 4.18D is of special interest to the current work. It has been used as intermediate excited state level for coherent transfer to $X^1\Sigma_g^+$ $|v=73, J=2>$ in our recent experiments [Dan08].

By fitting a two level model that takes into account decay from the upper level to a series of such measurements obtained with different laser intensities, we determine the transition strength as given by the normalized Rabi frequency. As the Feshbach molecules scatter photons and spontaneously decay to other molecular levels, the number of Feshbach molecules N decays as a function of laser detuning Δ_1 according to

$$N(\Delta_1) = N_0 \exp\left(-\tau\Omega_1^2/(\Gamma(1 + 4\pi^2\Delta_1^2/\Gamma^2))\right),$$

where N_0 is the molecule number without laser irradiation and τ is the irradiation time. From the fit we obtain the Rabi frequency on resonance Ω_1 and the excited state spontaneous decay rate Γ. We determine the normalized Rabi frequency to $\Omega_1 = 2\pi \times 2$ kHz $\sqrt{I/(\mathrm{mW/cm^2})}$ for $|J=1>$, where I is the laser intensity. This value is sufficient to perform STIRAP given the available laser power [Dan08]. The corresponding transition strengths for $|J=3>$ and $|J=5>$ are $\Omega_1 = 2\pi\times 0.3$ kHz $\sqrt{I/(\mathrm{mW/cm^2})}$ and $\Omega_1 = 2\pi\times 0.1$ kHz $\sqrt{I/(\mathrm{mW/cm^2})}$, respectively. The absolute values of these transition strengths bear an estimated uncertainty of 20 % because the laser beam parameters for the spectroscopy laser are not well determined.

We also record the time dependence of the molecular loss on some of the stronger lines. For this, we step the laser irradiation time τ from 0 to 150 μs, while laser L_1 is kept on resonance. The result is shown in Fig. 4.19A for the transition at 1126.173 nm for two different values of the excitation laser intensity.

We note that the transition strength for a particular line starting from Feshbach level $|s>$ strongly depends on the value of the magnetic field, as evidenced in Fig. 4.19B. Loss resonances for the transition at 1126.173 nm at 1.9 mT and 2.2 mT are shown. For ground state transfer [Dan08], we choose a magnetic field of around 1.9 mT, which is somewhat below the magnetic field region where state $|s>$ is strongly curved, but above the avoided state crossing with state $|g_2>$,

as seen in Fig. 4.17. The pronounced bending of $|s>$ is the result of a strong avoided crossing between two s-wave Feshbach levels [Mar07a]. For magnetic field values beyond 3.0 mT the level $|s>$ can be associated to the $F_1=3, F_2=3$ asymptote, where $F_i, i=1,2$, is the atomic angular momentum quantum number of the i-th atom, respectively. Below 2.0 mT the level $|s>$ can be associated to the $F_1=4, F_2=4$ asymptote. It is hence of closed channel character and much more deeply bound with respect to its potential asymptote, effectively by twice the atomic hyperfine splitting, improving the radial wave function overlap with the excited state levels. This increases the transition strength. Trivially, the resonance frequency is shifted as the binding energy is reduced for larger magnetic field values. Coupling to the excited state level is reduced from $\Omega_1=2\pi\times 2$ kHz $\sqrt{I/(\mathrm{mW/cm^2})}$ to $\Omega_1=2\pi\times 1$ kHz $\sqrt{I/(\mathrm{mW/cm^2})}$ when the magnetic field is changed from 1.9 mT to 2.2 mT.

As will be discussed in Sec.4.5.4 it is advantageous to be able to choose different Feshbach states as a starting state for ground state transfer experiments. Therefore, we probe transitions from Feshbach level $|g>$ to $(\mathrm{A}^1\Sigma_u^+ - \mathrm{b}3\Pi_u)\ 0_u^+$ levels. Fig. 4.20 shows loss resonances to the same excited state levels as shown in Fig. 4.18, only that now the initial Feshbach level is $|g>$ instead of $|s>$. In this case, the transition to $|J=3>$ is the strongest, while the transition to $|J=1>$ is very weak, but can be detected. A comparison of the transition strengths from $|g>$ to the excited state level $|J=3>$, giving $\Omega_1=2\pi\times 1$ kHz $\sqrt{I/(\mathrm{mW/cm^2})}$ versus $|s>$ to $|J=1>$ giving $\Omega_1=2\pi\times 2$ kHz $\sqrt{I/(\mathrm{mW/cm^2})}$ shows that level $|g>$ could also be potentially used as a starting level for coherent population transfer to deeply bound levels of the ground state but requires longer STIRAP times in order to assure sufficient adiabaticity [Ber98]. The $|J=3>$ excited state level in turn couples to $|J=2>$ in the ground state, as in previous work [Dan08].

In addition to the transition near 1126 nm we find a series of other excited state levels that we assign to the $(\mathrm{A}^1\Sigma_u^+ - \mathrm{b}^3\Pi_u)\ 0_u^+$ coupled state system. These are listed in Table 4.1. The assignment to either the $(\mathrm{A}^1\Sigma_u^+ - \mathrm{b}^3\Pi_u)\ 0_u^+$ system or to the $(1)^3\Sigma_g^+$ electronically excited state discussed below is primarily based on the spacing between neighboring vibrational levels and in addition on the pattern of loss resonances associated with each particular vibrational level. Resonant spin-orbit coupling in the case of the 0_u^+ states leads to an irregular vibrational spacing. In contrast, the $(1)^3\Sigma_g^+$ state is not perturbed by spin-orbit interaction and therefore has a regular vibrational progression. The levels near 1126 nm and near 1123 nm have been used to detect dark resonances with deeply bound levels of the $\mathrm{X}^1\Sigma_g^+$ state [Dan08]. The ability to couple to these essentially purely singlet ground state levels unambiguously assigns the corresponding excited state levels to the 0_u^+ system. The data given in Table 4.1 does not represent a fully exhaustive study of the $(\mathrm{A}^1\Sigma_u^+ - \mathrm{b}^3\Pi_u)\ 0_u^+$ coupled states in the wavelength range of interest. In fact, for the most part we observe those levels of the 0_u^+ system that have a dominant $\mathrm{A}^1\Sigma_u^+$ state contribution, as determined from molecular structure calculations.

Transitions to the $(1)^3\Sigma_g^+$ electronically excited state

The Feshbach levels that serve as starting levels for the spectroscopy are of mixed $X^1\Sigma_g^+$ and $a^3\Sigma_u^+$ character. In the wavelength range explored here, excitation to the $(1)^3\Sigma_g^+$ electronically excited triplet state is possible from the $a^3\Sigma_u^+$ component of the Feshbach molecules. In fact, for a heavy molecule as Cs_2, the $(1)^3\Sigma_g^+$ state is better described by the two separate electronic states 0_g^- and 1_g, denoted by the Hund's case (c) notation. The $(1)^3\Sigma_g^+$ has been previously studied by Fourier transform spectroscopy [Ami85]. This state is not of prime interest for the present work as transitions from this state down to the $X^1\Sigma_g^+$ ground state are expected to be strongly suppressed, but would be important for STIRAP transfer into the rovibrational ground state level of the shallow triplet $a^3\Sigma_u^+$ potential [Lan08b]. Certainly, it is important to be able to distinguish rovibrational levels belonging to the $(1)^3\Sigma_g^+$ state from the ones belonging to the 0_u^+ system, because otherwise time would be wasted in searching for ground state dark resonances that are very weak or even do not exist. Fig. 4.21A shows a typical loss spectrum for one of the lines that we detected near 1127.37 nm. Due to hyperfine splitting, levels of triplet character exhibit a much richer substructure than the 0_u^+ levels used for ground state transfer. Several components can be identified as a result of rotational and excited state hyperfine splitting. Zoomed-in regions are shown in Fig. 4.21B, C, D, and E. We have observed a regularly spaced series of optical transitions which we attribute to the $(1)^3\Sigma_g^+$ excited state as listed in Table 4.1. The levels are well reproduced by molecular structure calculations using the Dunham coefficients from Ref.[Ami85]. The vibrational numbering used here is the same as in that work. However, it relies on the absolute energy position of the potential, T_e, which was not determined precisely in Ref. [Ami85].

4.5.4. Conclusion

We have performed optical spectroscopy starting from weakly bound Cs_2 Feshbach molecules into deeply bound rovibrational levels of the mixed excited state 0_u^+ system and the excited triplet $(1)^3\Sigma_g^+$ state. At least one of the observed transitions, namely the one at 1126.173 nm starting from the Feshbach level $|s>$ at an offset magnetic field value of 1.9 mT to the excited level $|v'=225, J=1>$ of the 0_u^+ system, is strong enough to allow efficient STIRAP transfer into deeply bound rovibrational levels of the singlet $X^1\Sigma_g^+$ ground state potential. The use of this transition for STIRAP has recently been demonstrated in Ref.[Dan08]. In that work, the deeply bound rovibrational level $|v=73, J=2>$ of the $X^1\Sigma_g^+$ ground state potential was populated in the molecular quantum gas regime with 80% efficiency. The rovibrational ground state $|v=0, J=0>$ of the $X^1\Sigma_g^+$ ground state potential can thus be reached from the atomic threshold with a maximum of two two-photon STIRAP transfers. Dark resonances connecting $|v=73, J=2>$ to $|v=0, J=0>$ have recently been observed [Mar09], and two-step STIRAP into $|v=0, J=0>$ has recently been implemented [Dan10b]. For future experiments, the use of Feshbach level $|g>$ as the initial state might

be advantageous. Level $|g>$ can be more easily populated, as the Feshbach resonance connected to this level is at a low magnetic field value of 1.98 mT [Mar07a], where the atomic background scattering length has a moderate value of 155 a_0, where a_0 is Bohr's radius. The use of this resonance avoids excitation of collective motion of the atomic BEC as a result of a large mean field interaction near the Feshbach resonance at 4.79 mT [Dan08], where the atomic background scattering length is about 935 a_0. The transition starting from level $|g>$ appears to be strong enough to allow STIRAP, this time via the excited state level $|v' = 225, J = 3>$ of the 0_u^+ system. An attractive strategy for the production of a BEC of ground state molecules relies on the addition of a three-dimensional optical lattice. Starting from the atomic BEC, pairs of atoms at individual lattice sites can be produced in a superfluid-to-Mott-insulator transition [Gre02a] with high efficiencies of up to 50% [Dür08]. These pairs can then be very efficiently associated on a Feshbach resonance [Tha06] and subsequently transferred to the rovibronic ground state with STIRAP. The lattice has the advantage of shielding the molecules against inelastic collisions during the association process and subsequent state transfer. In particular, it should allow long STIRAP pulse durations, allowing us to resolve the weak hyperfine structure of ground state molecules [Ald09]. As proposed by Jaksch *et al.* [Jak02], dynamical melting of the lattice should ideally result in the formation of a BEC of molecules in the rovibronic ground state in a Mott-insulator-to-superfluid-type transition.

We are indebted to R. Grimm for generous support and we thank T. Bergeman, H. Salami, J. Hutson, J. Aldegunde, and E. Tiemann for valuable discussions. We gratefully acknowledge funding by the Austrian Ministry of Science and Research (BMWF) and the Austrian Science Fund (FWF) in form of a START prize grant and by the European Science Foundation (ESF) in the framework of the EuroQUAM collective research project QuDipMol. R.H. acknowledges support by the European Union in form of a Marie-Curie International Incoming Fellowship (IIF).

Table 4.1.: Observed excited state levels in the wavelength range from 1118 nm to 1134 nm. Transitions were measured from Feshbach state $|s>$ to the first electronically excited state, addressing both $(A^1\Sigma_u^+ - b^3\Pi_u)0_u^+$ levels and $(1)^3\Sigma_g^+$ levels. Levels are given according to the excitation wavelength (WL) from $|s>$, which essentially corresponds to the $F=3, m_F=3$ two-atom asymptote. The data is taken at a magnetic field of 1.98 mT. Wavemeter accuracy is about 0.001 nm. The energy of these levels above the rovibronic ground state $X^1\Sigma_g^+$ $|v=0, J=0>$ is given in the second column, where the binding energy of the rovibronic ground state is taken from Ref.[Dan08]. The assignment to either the coupled $(A^1\Sigma_u^+ - b^3\Pi_u)0_u^+$ system or to the $(1)^3\Sigma_g^+$ is based on the vibrational spacing and similarities in the substructure of the levels. The levels marked with $*$ have been used for dark resonance spectroscopy coupling to deeply bound levels of the $X^1\Sigma_g^+$ state [Dan08]. The ability to couple to such levels unambiguously reflects an important singlet component stemming from the $A^1\Sigma_u^+$ state and therefore clearly assigns these levels to the 0_u^+ system. The quantum numbers given for the 0_u^+ levels are coupled channels quantum numbers derived from molecular structure calculations and bear an uncertainty of two in the absolute numbering. The calculations show that these levels have about 70% $A^1\Sigma_u^+$ state contribution. Two further levels observed near 1120.17 nm and 1117.16 nm that belong to the 0_u^+ progression are not given in the table since no further measurements have been done on these levels. The level near 1129.5 nm exhibits a somewhat richer structure than the other levels assigned to 0_u^+ and than exemplified in Fig. 4.18. Levels assigned to the $(1)^3\Sigma_g^+$ state form a regular vibrational progression and show a more complex substructure than the levels attributed to the 0_u^+ system, as exemplified in Fig. 4.21. For these levels, the transition wavelength to one of the most prominent features is given, since an in depth analysis of the rotational and hyperfine structure remains to be done. The vibrational numbering for the $(1)^3\Sigma_g^+$ levels is the same as in Ref [Ami85].

WL [nm]	Energy above $X^1\Sigma_g^+$ $\|v=0>$ [cm^{-1}]	Assignment
1132.481	12458.875	0_u^+ $\|v'=221, J=1>$
1129.492	12482.245	0_u^+
1126.173$*$	12508.332	0_u^+ $\|v'=225, J=1>$
1123.104$*$	12532.598	0_u^+ $\|v'=226, J=1>$
1133.680	12449.536	$(1)^3\Sigma_g^+$ $\|v'=32>$
1130.510	12474.274	$(1)^3\Sigma_g^+$ $\|v'=33>$
1127.379	12498.838	$(1)^3\Sigma_g^+$ $\|v'=34>$
1124.274	12523.334	$(1)^3\Sigma_g^+$ $\|v'=35>$
1121.196	12547.756	$(1)^3\Sigma_g^+$ $\|v'=36>$
1118.155	12572.013	$(1)^3\Sigma_g^+$ $\|v'=37>$

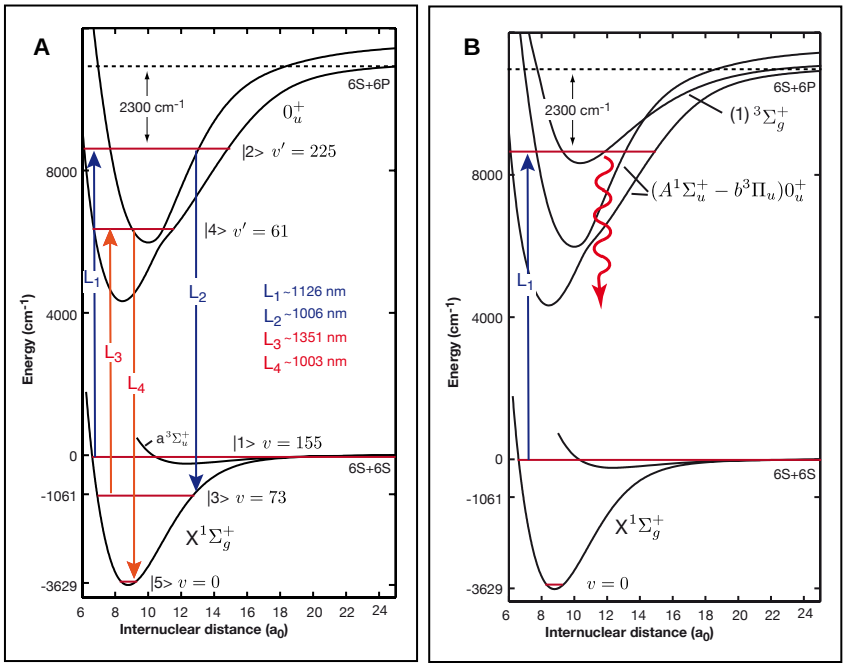

Fig. 4.16.: (**A**) Simplified molecular level scheme for Cs_2 showing the relevant ground state and excited state potentials involved in rovibrational ground state transfer. Molecules in a weakly bound Feshbach level $|1\rangle = |v \approx 155\rangle$ (not resolved near the $6S_{\frac{1}{2}} + 6S_{\frac{1}{2}}$ two-atom asymptote, but shown in Fig. 4.17) are to be transferred to the rovibrational ground state level $|5\rangle = |v = 0, J = 0\rangle$ of the singlet $X^1\Sigma_g^+$ potential with a binding energy of 3629 cm^{-1} by two sequential two-photon STIRAP processes involving lasers L_1 and L_2 near 1126 nm and 1006 nm and lasers L_3 and L_4 near 1351 nm and 1003 nm. The intermediate ground state level $|3\rangle = |v = 73, J = 2\rangle$ has a binding energy of 1061 cm^{-1}. (**B**) Probing candidate levels for $|2\rangle$ belonging to the electronically excited coupled $(A^1\Sigma_u^+ - b^3\Pi_u)\ 0_u^+$ potentials. Here, we search for $|2\rangle$ in loss spectroscopy with laser L_1 in a region near 8890 cm^{-1} above the $6S_{\frac{1}{2}} + 6S_{\frac{1}{2}}$ asymptote, corresponding an excitation wavelength range of 1118 to 1134 nm. The wiggly arrow indicates loss from the excited levels due to spontaneous emission. Also shown is the excited $(1)^3\Sigma_g^+$ potential, for which we find several levels.

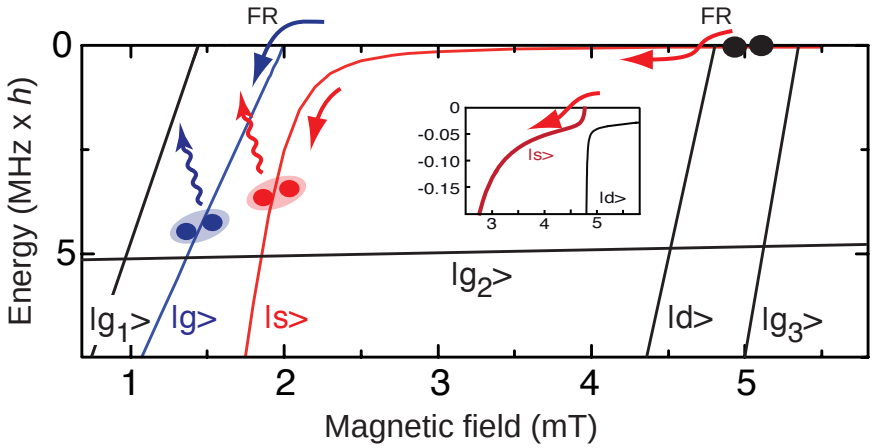

Fig. 4.17.: Initial Feshbach molecule production: Zeeman diagram showing the energy of weakly bound Feshbach levels [Mar07a] and the Feshbach resonances (FR) used in the present work. The binding energy is given with respect to the $F = 3, m_F = 3$ two-atom asymptote. The molecules are produced either on a d-wave Feshbach resonance at 4.79 mT (see inset) and then transferred to the weakly bound s-wave state $|s>$ on an avoided state crossing, or on a g-wave Feshbach resonance at 1.98 mT, resulting in molecules in level $|g>$. In the first case, further lowering of the magnetic offset field to below 2.0 mT changes the character of the $|s>$ level from open-channel to closed-channel dominated [Mar07a]. The levels $|s>$ and $|g>$ are both candidate levels for the initial level $|1>$ shown in Fig. 4.16. For completeness, further g-wave Feshbach levels, $|g_1>$, $|g_2>$, and $|g_3>$ are shown. Level $|g_2>$ connects $|g>$ to $|s>$ and can be used for Feshbach state transfer [Mar07a]. Level $|g_3>$ is a further interesting candidate level for $|1>$ with low nuclear spin contribution [Mar07a].

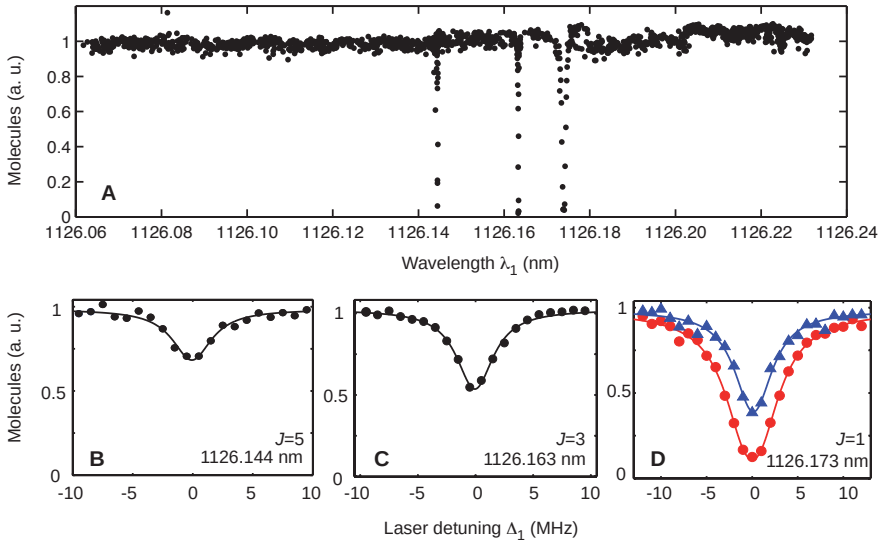

Fig. 4.18.: Loss resonances for excitation from the initial Feshbach level $|s>$ to the 0_u^+ system. (**A**) Typical scan showing the number of molecules in $|s>$ as a function of laser wavelength λ_1 near 1126 nm. Three resonances can be identified, corresponding to $|J=5>$, $|J=3>$, and $|J=1>$, from left to right. The sample is irradiated with laser light at an intensity of 1×10^6 mW/cm^2 for $\tau = 200$ μs. The laser is locked to a narrow band optical resonator that is tuned via a piezoelectric element with a step size of approximately 40 MHz. Wavelength is measured on a home-built wavemeter. The molecule number is normalized to the atom number measured in the same individual realization of the experiment to cancel out fluctuations that stem from shot-to-shot atom number fluctuations and the baseline is set to 1. (**B**), (**C**), and (**D**) represent measurements of the three individual lines with $|J=5>$, $|J=3>$, and $|J=1>$ at reduced intensity in order to avoid saturation. The solid lines represent fits as described in the text. The spectroscopy laser is stabilized to an optical resonator and the resonator is in turn referenced to an optical frequency comb, which allows precise and reproducible tuning of the frequency. The transition to $|J=1>$ in panel (**D**) is recorded at an intensity of 1.5×10^4 mW/cm^2 (circles) and 6×10^3 mW/cm^2 (triangles), (**B**) and (**C**) are recorded at 1×10^6 mW/cm^2 and 2×10^5 mW/cm^2, respectively. Pulse duration is $\tau = 10$ μs.

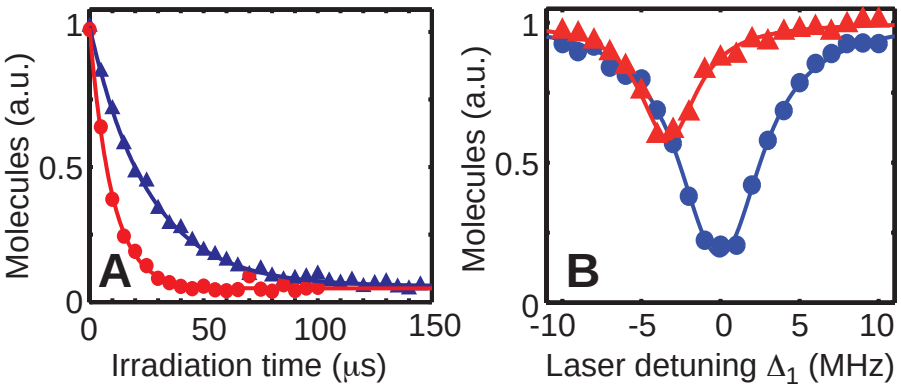

Fig. 4.19.: Loss of molecules for excitation near 1126.173 nm from Feshbach level $|s>$. (**A**) Time dependence of molecular loss on resonance at 1126.173 nm for two different laser intensities, 5.7×10^5 mW/cm^2 (circles) and 2.1×10^5 mW/cm^2 (triangles). The magnetic offset field is 1.9 mT. The fitted exponential decay gives the decay constants $\tau = 9.7 \pm 0.6$ μs (circles) and $\tau = 25.5 \pm 1$ μs (triangles). (**B**) Loss of molecules in $|s>$ as a function of laser detuning Δ_1 near 1126 nm with an irradiation time of $\tau = 10\,\mu$s for two values of the magnetic field, 1.9 mT (dots) and 2.2 mT (triangles). In both cases, the excited state spontaneous decay rate was determined to $\approx 2\pi \times 2$ MHz. At higher magnetic fields, Feshbach level $|s>$ acquires more open-channel character, reducing radial wave function overlap with the excited rovibrational levels. The shift in transition frequency is the result of a differential magnetic field shift of the Feshbach level $|s>$ and the excited state level.

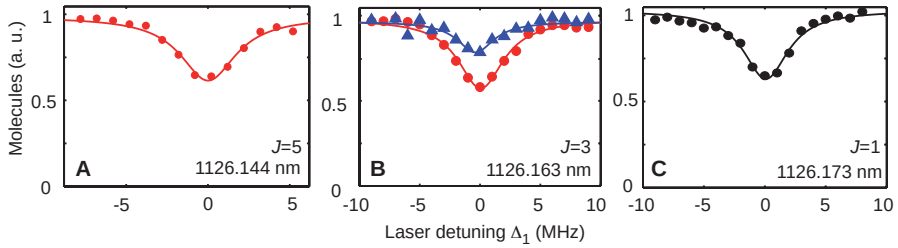

Fig. 4.20.: Loss resonances for excitation from the initial Feshbach level $|g>$. **(A)**,**(B)**, and **(C)** show the loss for excitation to $|J=5>$, $|J=3>$, and $|J=1>$, corresponding to the resonances shown in Fig. 4.18. The laser intensities are 1.5×10^4 mW/cm^2 for panel **(A)** and for the circles in panel **(B)**. The second resonance in **(B)** (triangles) is measured with 5.6×10^3 mW/cm^2. **(C)** The line at 1126.173 nm is measured at 1×10^6 mW/cm^2. All measurements are done with an irradiation time of $\tau = 10$ μs. From a series of such measurements at different intensities we determine the line strengths for $|J=5>$, $|J=3>$, and $|J=1>$ to $\Omega_1 = 2\pi\times1$ kHz $\sqrt{I/(\mathrm{mW/cm^2})}$, $\Omega_1 = 2\pi\times1$ kHz $\sqrt{I/(\mathrm{mW/cm^2})}$, and $\Omega_1 = 2\pi\times0.1$ kHz $\sqrt{I/(\mathrm{mW/cm^2})}$, respectively.

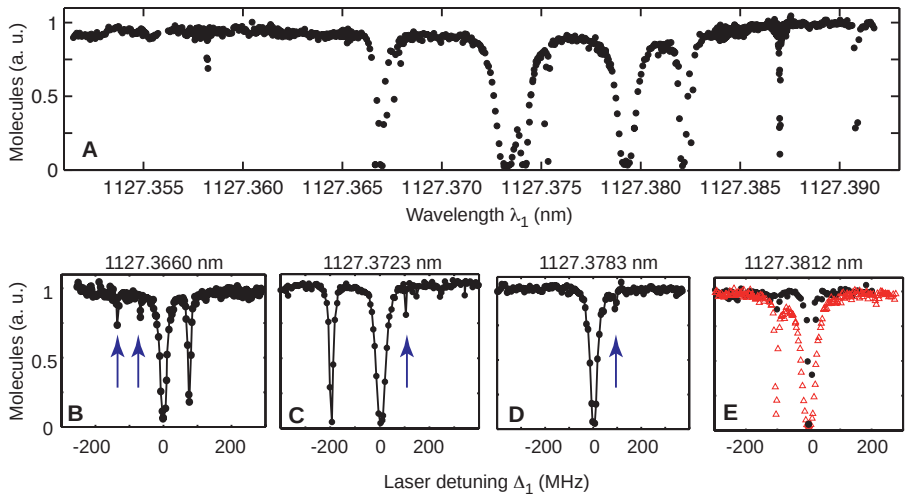

Fig. 4.21.: Loss of molecules for excitation near 1127.17 nm from Feshbach level $|s>$ to the triplet $(1)^3\Sigma_g^+$ state. (**A**) represents a broad scan with laser irradiation at an intensity of 5×10^5 mW/cm^2 for $\tau = 100$ μs at a step size of 20 MHz. A rich structure due to rotation and excited state hyperfine splitting can be seen which is qualitatively different from the spectrum shown in Fig. 4.18. The lines are greatly broadened by the high intensity and long irradiation time. The spectroscopy laser is locked to a narrow band optical resonator that is stepped via a piezoelectric element. Scans of about 750 MHz were recorded as a function of piezo voltage on the resonator. Voltage was converted to wavelength for each scan by a linear interpolation. (**B**)-(**E**) represent scans over some of the observed features at a reduced intensity of 8×10^4 mW/cm^2 and an irradiation time of $\tau = 10$ μs in order to reduce broadening of the lines. The step size is about 7 MHz. Resonator piezo voltage is converted to frequency with an estimated error of 10 %. The vertical arrows indicate weak lines that have been verified in additional scans with higher power. In panel (**E**) the power was somewhat increased for an additional measurement (triangles) that emphasizes such a weak line. The wavelengths given to identify the zero point on the frequency axis for each subpanel are not meant to imply this level of accuracy which is limited to 0.001 nm by wavemeter calibration. Nevertheless, they give a measure of the energy of the sublines relative to each other.

4.6. Publication:Dark resonances for ground-state transfer of molecular quantum gases

Appl. Phys. B **95** 219-225 (2009)†

Manfred J. Mark[1], Johann G. Danzl[1], Elmar Haller[1], Mattias Gustavsson[1], Nadia Bouloufa[2], Olivier Dulieu[2], Houssam Salami[3], Tom Bergeman[3], Helmut Ritsch[4], Russell Hart[1], and Hanns-Christoph Nägerl[1]

[1]*Institut für Experimentalphysik und Zentrum für Quantenphysik, Universität Innsbruck, Technikerstraße 25, A–6020 Innsbruck, Austria*
[2]*Laboratoire Aimé Cotton, CNRS, Université Paris-Sud, Bât. 505, 91405 Orsay Cedex, France*
[3]*Department of Physics and Astronomy, SUNY Stony Brook, NY 11794-3800, USA*
[4]*Institut für Theoretische Physik und Zentrum für Quantenphysik, Universität Innsbruck, Technikerstraße 25, A–6020 Innsbruck, Austria*

One possible way to produce ultracold, high-phase-space-density quantum gases of molecules in the rovibronic ground state is given by molecule association from quantum-degenerate atomic gases on a Feshbach resonance and subsequent coherent optical multi-photon transfer into the rovibronic ground state. In ultracold samples of Cs_2 molecules, we observe two-photon dark resonances that connect the intermediate rovibrational level $|v=73, J=2>$ with the rovibrational ground state $|v=0, J=0>$ of the singlet $X^1\Sigma_g^+$ ground state potential. For precise dark resonance spectroscopy we exploit the fact that it is possible to efficiently populate the level $|v=73, J=2>$ by two-photon transfer from the dissociation threshold with the stimulated Raman adiabatic passage (STIRAP) technique. We find that at least one of the two-photon resonances is sufficiently strong to allow future implementation of coherent STIRAP transfer of a molecular quantum gas to the rovibrational ground state $|v=0, J=0>$.

†The author of the present thesis contributed to this work by performing the measurements and the data analysis together with JGD. He also maintained and improved the experimental setup and contributed to the paper writing.

4.6.1. Introduction

Laser cooling of atoms and the production of quantum degenerate atomic Bose and Fermi gases have revolutionized the field of atomic physics [Sou02]. For molecular systems, ultralow temperatures and high phase space densities are much more difficult to achieve. Laser cooling of molecules has not yet been demonstrated, and with alternative cooling and slowing techniques such as buffer gas cooling and Zeeman slowing high phase space densities are yet out of reach [Doy04, Kre08, van08]. In photoassociation experiments from magneto-optical traps, [Jon06, Nik00, Sag05, Vit08, Dei08], cold samples of deeply bound molecules in the lowest vibrational levels have been created. Yet, the phase space densities are far away from the quantum degenerate regime. In the limit of extremely weak binding, molecular Bose-Einstein condensation could be achieved [Ing08] by using the trick of first cooling an atomic Fermi gas to high phase space densities and subsequently associating pairs of atoms to molecules. For molecules composed of Fermions, collisional stability of the highly excited molecules is assured as a result of a Pauli blocking effect. Here, we are interested in ultracold and dense molecular systems in specific deeply bound rovibrational levels. Such samples are of high interest for fundamental studies in physics and chemistry, ranging from ultracold chemistry [Kre05] and few-body collisional physics [Sta06, Zah06] to high resolution spectroscopy [Zel08, DeM08], to applications in quantum processing [DeM02], and to the formation of dipolar quantum gases and dipolar Bose-Einstein condensates [Gór02, Bar02]. For these experiments full control over the molecular wave function is desired. In addition, high densities are required for molecular quantum gas studies. Only in the rovibronic ground state, i.e. the lowest energy level of the electronic ground state, is collisional stability assured.

For the production of molecular quantum gases in the absolute ground state, we follow a scheme in which the technique of stimulated two-photon transfer is repeatedly applied to molecules associated on a Feshbach resonance from a high-density sample of ultracold atoms such as a Bose-Einstein condensate (BEC). The initially very loosely bound molecules are to be transferred in a few successive steps to the rovibrational ground state, acquiring more and more binding energy. The scheme has several advantages. It is fully coherent, not relying on spontaneous processes, allowing high state selectivity, and it involves only a comparatively small number of intermediate levels. The scheme is expected to allow the removal of a ground state binding energy of typically 0.5 eV for an alkali dimer without appreciably heating the molecular sample. It essentially preserves phase space density and coherence of the particle wave function, allowing the molecular sample to inherit the high initial phase space density from the atomic sample. Ideally, the scheme will ultimately result in the formation of a molecular BEC. A major challenge is given by the low radial wave function overlap between successive molecular levels, potentially leading to prohibitively low transition rates for the two-photon transitions that could only be compensated by the use of further (smaller) transfer steps.

In a crucial experiment, Winkler *et al.* [Win07] demonstrated that coherent

two-photon transfer by means of the stimulated Raman adiabatic passage (STIRAP) technique [Ber98] can efficiently be implemented with quantum gases of weakly bound Feshbach molecules. In this work, the transferred molecules, in this case Rb_2, were still weakly bound with a binding energy of much less than 10^{-4} of the binding energy of the rovibrational ground state. In particular, wave function overlap of the final level with the rovibrational ground state is negligible. Nevertheless, an important result of this experiment was the demonstration that, even with excitation near the excited S+P asymptote, parasitic excitation of unwanted molecular transitions by the STIRAP laser beams could largely be avoided. Recently, Danzl *et al.* [Dan08] showed efficient coherent STIRAP transfer into deeply bound rovibrational levels in the quantum gas regime. More specifically, transfer into the rovibrational level $|v = 73, J = 2>$ of the singlet $X^1\Sigma_g^+$ molecular potential of the Cs dimer was demonstrated. This level is bound by 1061 wavenumbers, more than one-fourth of the binding energy of the rovibrational ground state. Here, as usual, v and J denote the vibrational and rotational quantum numbers, respectively. This intermediate level was chosen as to give a balanced distribution for the wave function overlap in a four-photon transfer scheme to the ground state, i.e. to assure that all four dipole transition moments are of comparable magnitude. This level could thus serve as a transfer state towards the rovibrational ground state $|v = 0, J = 0>$, allowing coherent ground state transfer with two two-photon transitions. Also recently, Ni *et al.* [Ni08] could demonstrate transfer all the way into the rovibrational ground state $|v=0, J=0>$ of the singlet $X^1\Sigma^+$ molecular potential in a quantum gas of KRb molecules. The transfer could be achieved in a single step as a result of the favorable run of the excited state potentials in the case of heteronuclear alkali dimers [Stw04]. Also, the lowest rovibrational level of the Rb_2 triplet $a^3\Sigma_u^+$ potential could recently be populated in the quantum gas regime using the STIRAP technique [Lan08b].

Here, in an ultracold and dense sample of Cs molecules, we present two-photon dark resonances connecting the rovibrational level $|v = 73, J = 2>$ of the Cs dimer singlet $X^1\Sigma_g^+$ molecular potential with the rovibrational ground state $|v=0, J=0>$. Starting from $|v=73, J=2>$, we first perform molecular loss spectroscopy by laser excitation in the wavelength range from 1329 nm to 1365 nm to search for and identify suitable excited state levels of the mixed $(A^1\Sigma_u^+ - b^3\Pi_{0u})$ 0_u^+ excited molecular potentials. These levels are 9893 to 10091 wavenumbers above the rovibronic ground state, corresponding to a wavelength range from 1011 nm to 991 nm for the transition to the rovibronic ground state. We then perform dark state spectroscopy by simultaneous laser irradiation near 1350 nm and 1000 nm. We find several dark resonances, from which we derive normalized transition strengths and find that at least one of the two-photon transitions is favorable for ground state transfer.

4.6.2. Molecular energy levels and laser transitions

Fig.4.22 shows the energy of the relevant Cs_2 molecular states and the optical transitions for our transfer scheme. State |1> is the initial weakly bound Feshbach state that we populate out of an atomic BEC of Cs atoms via Feshbach association [Her03]. For the transfer from |1> to the ro-vibrational ground state $|5\rangle = |v=0, J=0\rangle$, three intermediate levels |2>, |3>, and |4> are needed. All five molecular levels are coupled by two two-photon transitions in a distorted M-shaped configuration as shown in Fig.4.23. Levels |2> and |4> belong to the excited mixed $(A^1\Sigma_u^+ - b^3\Pi_{0u})\ 0_u^+$ potentials. We have identified level |2> as the 225th one of the coupled 0_u^+ system, with an uncertainty of 2 in the absolute numbering, and |3> is the level with $v=73$ and $J=2$ of the $X^1\Sigma_g^+$ ground state potential [Dan08]. A two-photon laser transition with laser L_1 at 1126 nm and laser L_2 at 1006 nm couples |1> to |3> via |2>. There are now several possibilities for coupling |3> to |5>, differing in the choice of the excited state |4>. The aim of this work is to identify a suitable state |4> from the $(A^1\Sigma_u^+ - b^3\Pi_{0u})\ 0_u^+$ potentials with sufficient wave function overlap with both |3> and |5>. We search for state |4> in the energy range of 9893 to 10091 wavenumbers above the rovibrational ground state |5>. Molecular structure calculations as outlined in Sec. 4.6.4 show that in this range there are candidate states for |4> that have dipole transition matrix elements with both |3> and |5> of comparable magnitude, allowing optimum STIRAP performance. The wavelengths for the lasers L_3 and L_4 driving the associated two-photon transition are near 1350 nm and 1000 nm, respectively. We derive all laser light for driving the molecular transitions from highly stable, widely tunable diode laser systems with kHz linewidths. For short term stability, the lasers are all locked to narrow-band optical resonators. For long term stability, the optical resonators are referenced to an infrared, fiber-laser-based frequency comb, covering the wavelength range from about 980 nm to about 2000 nm.

4.6.3. Preparation of a molecular quantum gas in $v=73, J=2$

Our sample preparation procedure follows Ref. [Dan08]. In summary, we first produce a cigar-shaped BEC of typically 1.5×10^5 cesium atoms in the lowest hyperfine sublevel $F = 3,\ m_F = 3$ in a crossed optical dipole trap. As usual, F is the atomic angular momentum quantum number, and m_F its projection. The trapping light at 1064.5 nm is derived from a single-frequency, highly-stable Nd:YAG laser. Using a *d*-wave Feshbach resonance at 4.8 mT [Mar07a] we then produce a quantum gas of weakly bound Feshbach molecules out of the BEC [Her03]. For this, we first ramp the magnetic field from the BEC production value of 2.0 mT to 4.9 mT, slightly above the Feshbach resonance. The molecules are produced on a downward sweep at a typical sweep rate of 0.025 mT/ms. The resulting ultracold sample contains up to 11000 molecules, immersed in the bath of the remaining BEC atoms. For the present experiments we shut off the trap and perform all subsequent measurements in free flight. This reduces the particle density, in particular during the later detection stage of the experiment, and

hence reduces atom-molecule collisional loss, thus increasing the molecular signal. Following two avoided state crossings while further sweeping the magnetic field to lower values, we transfer the molecules via a weakly bound, open channel s-wave molecular state into the still weakly bound, closed channel s-wave molecular state $|1\rangle$ by magnetic field ramping [Dan08]. This is the starting state for the subsequent optical transfer. As with all other weakly bound Feshbach states, it belongs to both the $X^1\Sigma_g^+$ ground state potential and the lowest triplet $a^3\Sigma_u^+$ potential and is hence of mixed character. It has zero rotational angular momentum. At a field of 1.9 mT, it has a binding energy of 5 MHz$\times h$, where h is Planck's constant, with respect to the $F=3, m_F=3$ two-atom asymptote [Mar07a]. We detect molecules in $|1\rangle$ by reverse magnetic field ramping, leading to dissociation on the Feshbach resonance at 4.8 mT, and by subsequent imaging of the resulting atoms [Her03].

We transfer the molecules from $|1\rangle$ to the rovibrational level $|3\rangle = |v=73, J=2\rangle$ with the STIRAP technique [Dan08]. For this, about 3 ms after molecule production, with the magnetic field ramping completed, laser L_2 at 1006 nm is pulsed on first and then laser L_1 at 1126 nm. Both lasers are on resonance within a few kHz. The pulse overlap time is about 10 μs. With peak Rabi frequencies of $\Omega_1 \approx 2\pi\times 3$ MHz and $\Omega_2 \approx 2\pi\times 6$ MHz we transfer about 80 % of the molecules to $|3\rangle$. We find that the molecular sample is not heated as a result of the STIRAP transfer. A residual kinetic energy on the order of $k_B \times 10$ nK comes from the expansion energy of the initial atomic sample. Our current procedure allows us to produce a sample of up to 8000 molecules in state $|3\rangle$ every 12 s. For the loss spectroscopy as detailed below, we irradiate the molecules in $|3\rangle$ with light near 1350 nm for a certain waiting time. We then measure the fraction of molecules that have remained in $|3\rangle$. For this, we transfer the remaining molecules back to $|1\rangle$ using the reverse STIRAP process and determine the number of molecules in $|1\rangle$. Without irradiation with light near 1350 nm we transfer more than 65% of the molecules from $|1\rangle$ to $|3\rangle$ and back to $|1\rangle$ [Dan08].

4.6.4. Loss spectroscopy

Prior to the present experiments, the energies of the levels with predominant $A^1\Sigma_u^+$ character in the region of interest were established to about $\pm$ 0.06 cm^{-1} by fits [Sal08b] to data obtained by Fourier transform spectroscopy (FTS) at Laboratoire Aimé Cotton (LAC) using transitions to the $X^1\Sigma_g^+$ state. However, the predominantly $b^3\Pi_{0u}$ levels were only known to about $\pm$ 2 cm^{-1} because this region was above that for which data was obtained from $2^3\Delta_{1g} \rightarrow b^3\Pi_{0u}$ emission [Xie08], but lower than the regime where $b^3\Pi_{0u}$ levels acquire sufficient singlet character (by spin-orbit mixing) to be observed in the FTS work. Paradoxically, the predominantly $b^3\Pi_{0u}$ levels are of special interest here because they happen to have significant singlet character over regions of the internuclear distance that are most important for transitions of interest in this work.

The coupled channel calculations used to characterize the level structure of the strongly interacting $A^1\Sigma_u^+$ and $b^3\Pi_{0u}$ states employed methods developed

from previous work on A and b states of K_2 [Lis01, Man02], RbCs [Ber03a], Na_2 [Qi07], and Rb_2 [Sal08a]. The DVR approach [Col92] was used to calculate eigenvalues primarily for two coupled channels, although some information on $b^3\Pi_{1u}$ was found in the FTS data from LAC. Similar computational approaches, differing in the detailed numerical methods, have been applied recently also to the A and b states of NaRb [Doc07].

Because of the initial $\pm$ 2 cm^{-1} uncertainty in the positions of $b^3\Pi_{0u}$ levels of interest, we decided to perform a systematic, broad-range search around expected transition energies in the wavelength range from 1329 nm to 1365 nm. For this, we perform double STIRAP from |1> to |3> and back with a waiting time of typically $\tau = 1$ ms. During the waiting time, we irradiate the sample with laser L_3 at an estimated intensity of $5 \cdot 10^4$ mW/cm^2. Laser L_3 is a diode laser with grating feedback. On the timescale of our experiment, the resonator of the laser is sufficiently stable, allowing systematic tuning of the laser without locking the laser to its external resonator. We step the laser frequency in units of typically 20 MHz by tuning the piezo element on the grating. We monitor the laser wavelength with a home-built wavemeter at approximately 300 MHz accuracy. For the initial broad range line search we increased the repetition rate of the experiment by stopping evaporative cooling slightly before condensation sets in. While stepping the laser, taking data points essentially at the cycle rate corresponding to the sample production time, we look for a dip in the molecule number. Once such a dip is found, typically consisting of a few data points, we perform a more precise scan by locking the laser to the external, highly-stable resonator and then the external resonator to the infrared frequency comb. This allows us to detune the laser with kHz precision. Fig.4.24 (A) shows a typical loss resonance near 1351 nm. We reduce the laser intensity such that on resonance at most 80% of the molecules are lost within 20 μs. From such measurements the transition strength as given by the normalized Rabi frequency and the natural linewidth of the excited state can be deduced. The typical width of the excited state molecular levels that we have identified is $2\pi \times 2$ MHz, in agreement with typical expected lifetimes. Fig.4.24 (B) shows a measurement of the time dependence of the molecular loss. Here, we step the waiting time τ from 0 to 50 μs, while the laser is kept on resonance. In total, we have found 7 excited levels belonging to the $(A^1\Sigma_u^+ - b^3\Pi_{0u})$ 0_u^+ coupled state system. They are listed in Table 4.2 along with the dominant overall character (either $A^1\Sigma_u^+$ state or $b^3\Pi_{0u}$ state) of the vibrational wave function as determined from the coupled state calculations. Within the wavelength range from 1329 nm to 1365 nm, theory predicts the existence of 5 more states of the 0_u^+ coupled state system, whose energies are also displayed in Table 4.2. For most of them, the wave function overlap is not expected to be favorable for STIRAP transfer to X $^1\Sigma_g^+$ $|v=0>$. However, an improved model of the energy level structure, based on all the data except one FTS point with a large residual, fits the observed transitions to a rms residual error of 0.02 cm^{-1}, indicating that additional resonances can be found with searches over very limited ranges of laser frequency.

4.6.5. Dark resonances with $|v=0, J=0>$ and $|v=0, J=2>$

In our recent work [Dan08] we could greatly improve the value for the binding energy of the rovibrational ground state $|5>= |v=0, J=0>$ by determining the binding energy of $|v=73>$ and using well-known data from conventional molecular spectroscopy [Wei85, Ami02]. Our measurement was limited by the calibration of our wavemeter, not allowing us to determine the number of the teeth of the frequency comb, and by the precision of the spectroscopy data. Searching for $|5>$ in dark state spectroscopy is now a straightforward task as only a range of about 0.002 wavenumbers needs to be scanned. We do this by exciting the transitions from $|3>$ to $|4>$ with laser L_3 and from $|4>$ to $|5>$ with laser L_4 simultaneously. The intensity for L_4 is typically $5 \cdot 10^4$ mW/cm^2. As is well known, the two light fields create a molecule-molecule dark state. The molecules initially in $|3>$ are lost unless laser L_4 is on two-photon resonance, provided that the Rabi frequency Ω_4 on the fourth transition is equal to or greater than Ω_3, the Rabi frequency on the third transition. We look for the resonance condition with the rovibrational ground state $|v=0, J=0>$ for some of the excited levels that we found above. Table 4.2 lists the observed transition wavelengths. We check that we can identify the level with rotational quantum number $J=2$ as the rotational energy splitting is well known. Fig.4.25 shows typical molecular dark resonances when we set L_4 on resonance and step the detuning Δ_3 of L_3 near 1350 nm. From a three-level model matched to the data for the dark resonances, taking into account off-resonant excitations and laser line widths, we determine the molecular transition strengths as given by the normalized Rabi frequencies. One of the two-photon transitions appears to be a particularly good candidate for STIRAP ground state transfer. It involves the excited state level $|4>$ with vibrational number $v' = 61$ of the $(A^1\Sigma_u^+ - b^3\Pi_{0u})\ 0_u^+$ coupled state system. For the transition from $|3>$ to $|4>$ and from $|4>$ to $|5>$ the normalized Rabi frequencies are $\Omega_3 = 2\pi \times 6$ kHz $\sqrt{I/(\mathrm{mW/cm^2})}$ and $\Omega_4 = 2\pi \times 5$ kHz $\sqrt{I/(\mathrm{mW/cm^2})}$, respectively. These values carry an estimated error of 50% as the laser beam parameters for L_3 and L_4 are not well determined. A comparison with a typical atomic transition strength of $\Omega_a = 2\pi \times 5$ MHz $\sqrt{I/(\mathrm{mW/cm^2})}$ giving $|\Omega_3/\Omega_a|^2 \approx 10^{-6}$ and $|\Omega_4/\Omega_a|^2 \approx 10^{-6}$ reflects the minuteness of the wave function overlap. Nevertheless, their value is sufficient for STIRAP as seen in our recent work [Dan08]. Also, they are of similar magnitude. This facilitates STIRAP, for which the peak Rabi frequencies should be approximately equal for optimum performance.

4.6.6. Conclusion

We observe several two-photon dark resonances that connect the intermediate rovibrational level $|v=73, J=2>$ of the $X^1\Sigma_g^+$ ground state potential with the rovibrational ground state level $|v=0, J=0>$. At least one of the two-photon transitions is sufficiently strong for implementing STIRAP to $|v=0, J=$

$0 >$ in the quantum gas regime, paving the way for the realization of a BEC of ground state molecules. STIRAP can in principle be implemented in two ways, either in the form of two sequential two-photon STIRAP steps, or in the form of four-photon STIRAP [Sho91, Kuz08]. An attractive strategy for the production of a BEC of ground state molecules relies on the addition of an optical lattice. Starting from an atomic BEC, pairs of atoms at individual lattice sites are produced in a superfluid-to-Mott-insulator transition [Gre02a]. These pairs can then be very efficiently associated on a Feshbach resonance and subsequently transfered to the rovibronic ground state with STIRAP. The lattice has the advantage of shielding the molecules against inelastic collisions during the association process and subsequent state transfer. As proposed by Jaksch *et al.* [Jak02], dynamical melting of the lattice should ideally result in the formation of a BEC of molecules in the rovibronic ground state in a Mott-insulator-to-superfluid-type transition.

We are indebted to R. Grimm for generous support and we thank E. Tiemann for valuable discussions and C. Amiot for providing the FTS data of LAC on Cs_2. We gratefully acknowledge funding by the Austrian Ministry of Science and Research (BMWF) and the Austrian Science Fund (FWF) in form of a START prize grant and by the European Science Foundation (ESF) in the framework of the EuroQUAM collective research project QuDipMol. R.H. acknowledges support by the European Union in form of a Marie-Curie International Incoming Fellowship (IIF). The work at Stony Brook was supported by the US NSF, under grant PHY0652459.

Table 4.2.: Levels of the excited 0_u^+ coupled state system in the region 9893 cm^{-1} to 10091 cm^{-1} above $X^1\Sigma_g^+$ $|v=0, J=0>$. The first column gives the coupled channel vibrational numbers of the individual levels. Levels marked with * have not been searched for and the level energies given are those determined from the coupled channels calculations. The column labeled 'C' gives the predominant contribution to the overall vibrational wave function, which is either predominantly $A^1\Sigma_u^+$ or predominantly $b^3\Pi_{0u}$, indicated by A and b, respectively. The number in brackets gives the order within the two progressions of levels with either predominantly $A^1\Sigma_u^+$ or predominantly $b^3\Pi_{0u}$ character. Both the $|J=1>$ and the $|J=3>$ rotational levels were identified for all oberved excited state levels. The wavemeter accuracy gives a typical uncertainty in wavelength of ± 0.002 nm, which translates into $\pm 0.011\,cm^{-1}$ uncertainty in the value for the energy above $|v=0, J=0>$. The energy relative to $X^1\Sigma_g^+$ $|v=0, J=0>$ of experimentally determined levels is based on the measured excitation wavelength from $X^1\Sigma_g^+$ $|v=73, J=2>$ and the $X^1\Sigma_g^+$ $|v=73>$ level energy from Ref. [Ami02], which introduces an additional uncertainty of 0.001 cm^{-1}. Deexcitation wavelengths are obtained from dark resonance spectroscopy involving the respective intermediate excited state level and the rovibronic ground state $X^1\Sigma_g^+$ $|v=0, J=0>$. n. m.: not measured

v'	C	J	Excitation wavelength from $X^1\Sigma_g^+$ $\|v=73, J=2>$ [nm]	Energy above $X^1\Sigma_g^+$ $\|v=0, J=0>$ [cm^{-1}]	De-excitation wavelength to $X^1\Sigma_g^+$ $\|v=0, J=0>$ [nm]
57	A (7)	1	1365.148	9893.002	n. m.
57	A (7)	3	1365.131	9893.094	n. m.
*58	b (50)	0	1362.893	9905.126	n. m.
*59	A (8)	0	1357.748	9932.927	n. m.
60	b (51)	1	1357.091	9936.497	n. m.
60	b (51)	3	1357.071	9936.606	n. m.
61	b (52)	1	1351.367	9967.707	1003.240
61	b (52)	3	1351.347	9967.816	n. m.
*62	A (9)	0	1350.388	9973.068	n. m.
63	b (53)	1	1345.725	9998.729	1000.128
63	b (53)	3	1345.705	9998.839	n. m.
*64	A (10)	0	1343.082	10013.351	n. m.
65	b (54)	1	1340.162	10029.576	997.052
65	b (54)	3	1340.143	10029.682	n. m.
66	A (11)	1	1335.833	10053.759	994.653
66	A (11)	3	1335.816	10053.853	n. m.
*67	b (55)	0	1334.675	10060.249	n. m.
68	b (56)	1	1329.257	10090.794	991.003
68	b (56)	3	1329.238	10090.902	n. m.

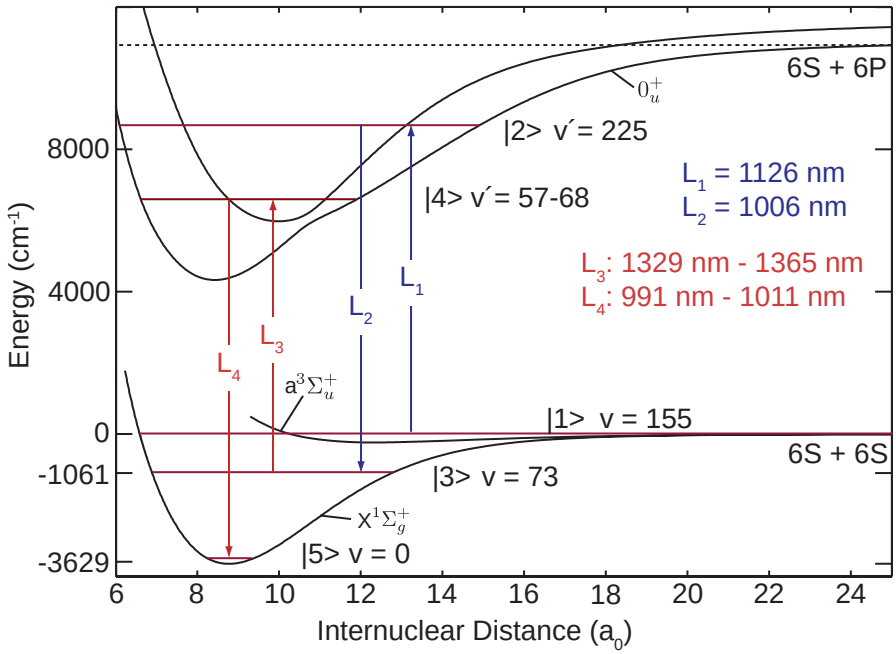

Fig. 4.22.: Molecular level scheme for Cs_2. Molecules in a weakly bound Feshbach level $|1\rangle = |v \approx 155\rangle$ (not resolved near the 6S+6S asymptote) are transferred to the rovibrational level $|3\rangle = |v = 73, J = 2\rangle$ of the singlet $X^1\Sigma_g^+$ ground state potential with a binding energy of 1061 cm^{-1} by a two-photon STIRAP process [Dan08] involving lasers L_1 and L_2 near 1126 nm and 1006 nm. The following two-photon transition from $|3\rangle$ to $|5\rangle = |v = 0, J = 0\rangle$ and also to $|v = 0, J = 2\rangle$ is then probed by lasers L_3 and L_4 near 1350 nm and 1000 nm, respectively. Level $|2\rangle$ is the 225th level of the electronically excited coupled $(A^1\Sigma_u^+ - b^3\Pi_{0u})$ 0_u^+ potentials. Here, we probe suitable candidate levels for $|4\rangle$, connecting $|3\rangle$ to $|5\rangle$. These candidate levels also belong to the 0_u^+ coupled state system and include levels with coupled channel vibrational numbers $v' = 57$ to 68. The position of the vertical arrows is not meant to reflect the internuclear distance at which the transition takes place.

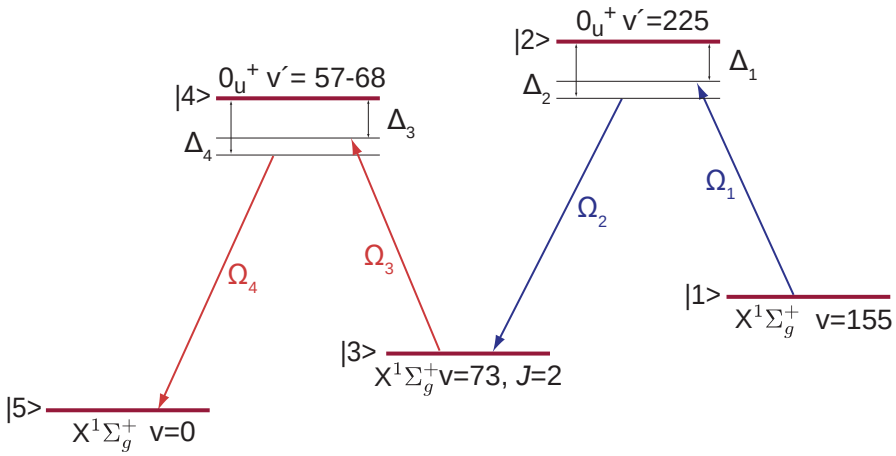

Fig. 4.23.: 5-level distorted M-scheme. The one-photon-detunings and Rabi frequencies of L_i are Δ_i and Ω_i, $i = 1, 2, 3, 4$. For STIRAP to $|v=73, J=2>$ the detunings for L_1 and L_2 are $\Delta_1 \approx 0 \approx \Delta_2$.

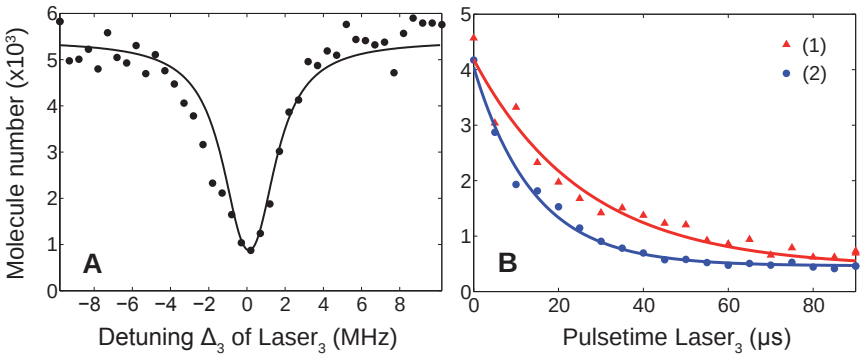

Fig. 4.24.: Loss resonances for excitation near 1351 nm from $|3>= |v=73, J=2>$ of the $X^1\Sigma_g^+$ ground state potential. **(A)** Loss of molecules in $|3>$ as a function of laser detuning Δ_3 near 1351 nm after a waiting time of 20 μs. The solid line represents a model calculation matched to the data yielding an excited state natural linewidth of $2\pi \times 2$ MHz. **(B)** Time dependence of molecular loss on resonance at 1351 nm for two different laser intensities. (1) 270 $\pm$ 80 mW/cm^2, (2) 570 $\pm$ 80 mW/cm^2. The fitted exponential decay gives the decay constants $\tau = 26 \pm 4$ μs for 270 mW/cm^2 and $\tau = 14 \pm 2$ μs for 570 mW/cm^2.

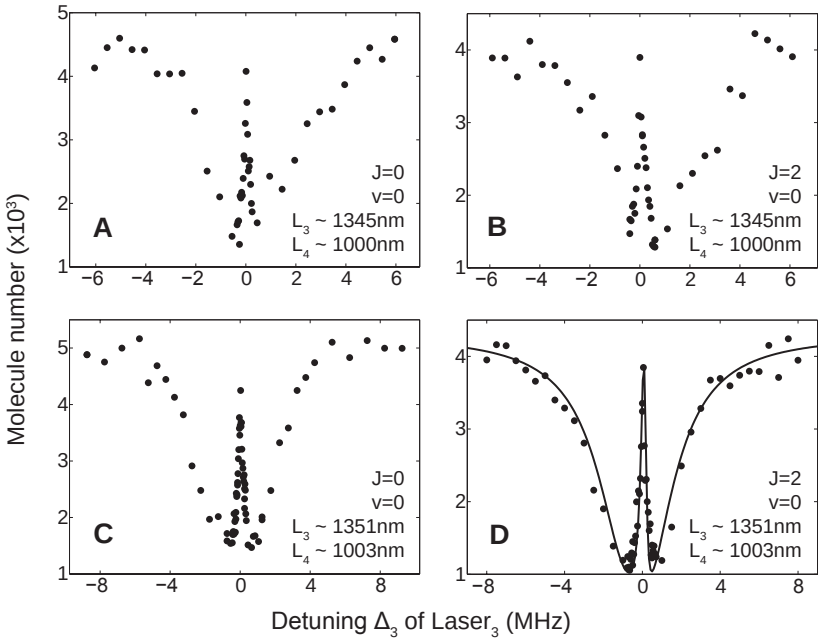

Fig. 4.25.: Dark resonances involving $X^1\Sigma_g^+$ state levels $|v=73, J=2>$ and $|v=0>$ for two different intermediate levels. **(A** and **B)** Dark resonances with $X^1\Sigma_g^+$ $|v=0, J=0>$ and $|v=0, J=2>$ involving the 0_u^+ excited state level $|v'=63, J=1>$ at an excitation wavelength near 1345 nm. **(C** and **D)** Dark resonances with $X^1\Sigma_g^+$ $|v=0, J=0>$ and $|v=0, J=2>$ involving the excited state level $|v'=61, J=1>$ at an excitation wavelength near 1351 nm. The solid line in **(D)** is the result of a model calculation, solving the three-level master equation including laser bandwidth and loss, matched to the data giving $\Omega_3 = 2\pi\times 6$ kHz $\sqrt{I/(\mathrm{mW/cm^2})}$ and $\Omega_4 = 2\pi\times 4$ kHz $\sqrt{I/(\mathrm{mW/cm^2})}$ for $X^1\Sigma_g^+$ $|v=0, J=2>$. The corresponding calculation for $X^1\Sigma_g^+$ $|v=0, J=0>$ yields $2\pi\times 5$ kHz $\sqrt{I/(\mathrm{mW/cm^2})}$.

CHAPTER 5

LOW-DIMENSIONAL SYSTEMS

5.1. Introduction

In this chapter, we investigate the properties of tunable Bose gases in an one-dimensional geometry. This geometry is especially interesting, since many theoretical models are analytically solvable and allow a direct comparison without the need of approximations [Gia03]. As a mathematical one-dimensional model cannot be realized directly, the best way to simulate them is to strongly confine the particles along two directions, either by creating potential tubes within a two-dimensional lattice structure [Gre01] or by single magnetic traps with a high aspect ratio [Det01, Hof07]. For very low temperatures and strong transversal confinement, particles in such a tube are only allowed to move along the tube, the motion perpendicular is frozen out. From a quantum mechanical point of view, the atoms are in the transversal groundstate of the tube, and the energy gap to the first excited state in this directions is much larger than any other energy scale in the system, especially temperature [Ols98]. A more detailed introduction and description of the experiments in this chapter is given in the PhD thesis of Elmar Haller [Hal10a].

Tunability of interactions is realized by means of a Feshbach resonance as described in chapter 1.6. In 1D, the relevant parameter describing the interaction strength is the coupling constant g_{1D}, which is directly proportional to the 3D scattering length a_{3D} as long as a_{3D} is much smaller than the harmonic confinement length $a_\perp$ perpendicular to the tube axis [Ols98]. For strong interactions one has to take the effect of the confinement into account, which leads to a so-called confinement induced resonance (CIR) at the point where $a_{3D} \sim a_\perp$ [Ber03b]. The physical origin of this resonance relies on the fact that the confinement provides excited states. The CIR appear when the binding energy of a molecular state from a excited trap state crosses the energy threshold of two scattering particles in the lowest harmonic oscillator state, in a way similar to the appearance of a Feshbach resonance in free space. The interaction strength g_{1D} diverges at this point, whereas the divergence of a_{3D} at the original Fesh-

bach resonance disappears in g_{1D}. Figure 5.1 shows the behavior of a_{3D} and g_{1D} as a function of the magnetic field around the free-space Feshbach resonance in cesium at $\sim 47.8\,\mathrm{G}$.

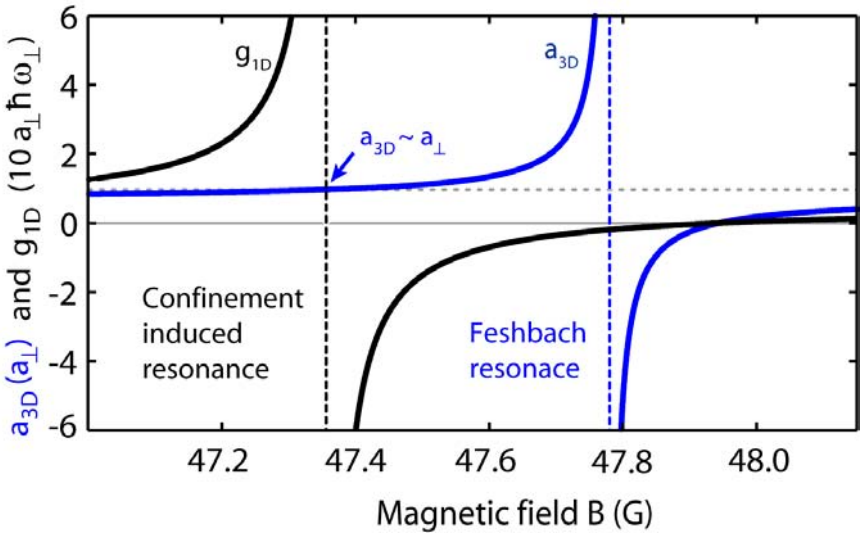

Fig. 5.1.: Interaction strengths as a function of the magnetic field in our one-dimensional geometry. The 3D scattering length a_{3D} diverges at the Feshbach resonance at $\sim 47.8\,\mathrm{G}$, while the 1D interaction strength g_{1D} shows resonant behavior at the point where $a_{3D} \sim a_\perp$. The figure is adapted from [Hal09]

Using two retroreflected laser beams, we are able to create an array of tubes as shown in figure 5.2, which provide an tight confinement perpendicular to the long tube axis. A weak harmonic confinement along the tubes is given by the lattice beams itself, and it can be increased by our initial dipole trap when needed. As tunneling between individual tubes can be neglected for the duration of our typical experiments, they can be treated as independent traps, realizing up to 6000 1D systems in parallel. To load atoms into the tubes, we either adiabatically ramp up the two-dimensional lattice directly or we first drive the Mott insulator transition with a three-dimensional lattice and subsequently ramp down one lattice direction adiabatically. The density shape of our initial BEC results in a spatial number variance across the tubes, slightly different between the two preparation methods, which has to be taken into account for the analysis of the experiments.

In section 5.2 we observe the appearance of an atom loss resonance connected to the CIR by varying the interaction strength across the calculated resonance position. We investigate the properties of this loss resonance in more detail by determining its position in a_{3D} as a function of $a_\perp$, where we find good agreement with the expected dependence on $a_\perp$. By introducing an asymmetry in the perpendicular confinement, we observe a splitting of the loss feature into two resonances. The two resonances shift according to the harmonic confinement length in each perpendicular direction of the asymmetric tube, and in the limiting case of vanishing confinement in one perpendicular direction - the 2D

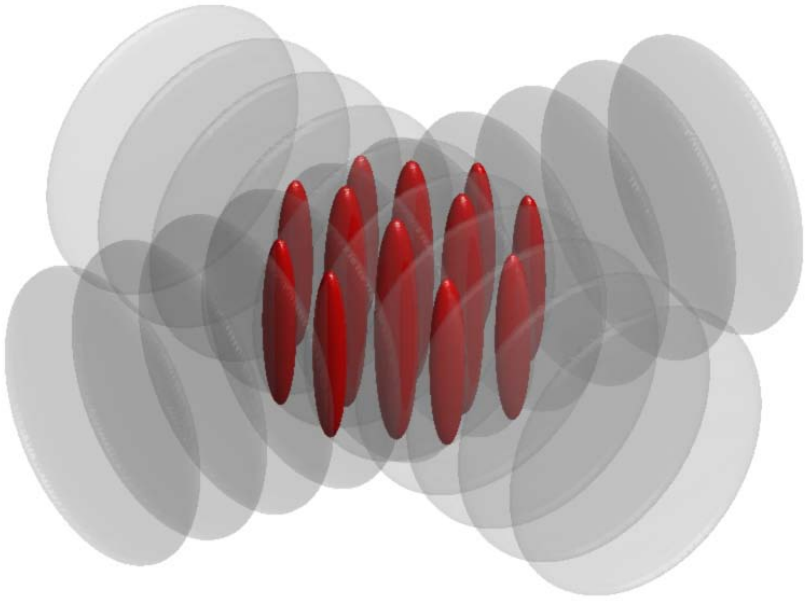

Fig. 5.2.: Experimental realization of 1D systems. An array of tube-shaped traps is created by two standing light waves. For typical experimental parameters tunneling between tubes can be neglected, and the aspect ratio of the tubes reach up to ~ 1000. The tubes can be loaded with up to ~ 60 atoms each.

limit - one of the resonances survives. In contrast to theoretical predictions [Pet01, Nai07] it is located in the repulsive interaction region.

Going back to the configuration with symmetric tubes, we investigate in section 5.3 the properties of the system as a function of the interaction strength, showing that we can prepare the noninteracting, weakly-interacting and strongly-interacting regime. For very strong interactions the bosonic atoms tend to avoid each other, forming the so-called Tonks-Girardeau gas [Gir60, Lie63]. The atoms behave like impenetrable particles, and their density distribution gets similar to the one from non-interacting fermions. By ramping over the CIR, we instantly switch interactions from strong repulsion to strong attraction, thus entering a highly excited metastable many-body state, the so-called Super-Tonks-Girardeau gas [Ast05]. It preserves and even enhances the particle correlations from the Tonks-Girardeau gas and can be mapped to fermions with long-range interactions. We show that this state exhibits a long lifetime and an increased stiffness.

In Section 5.4 we modify the system by adding a lattice potential along the tubes and investigate the superfluid to Mott insulator phase transition in 1D geometry in various interaction regimes. In the Tonks-Girardeau regime, where the particles are already ordered due to increased correlations, we observe a novel type of phase transition, the so-called pinning transition. For interactions beyond a critical value an already infinitesimal weak lattice induces this quantum

phase transition from a superfluid to the Mott insulator, presumed that the density of the superfluid is commensurate with the lattice [Gia03, Büc03]. We map out the phase boundary for all interaction strengths and see good agreement with the theoretical expectations.

To investigate in more detail the strong modification of particle correlations due to reduced dimensionality, we perform a measurement of the local three-body correlation function $g^{(3)}$ in section 5.5. To deduce $g^{(3)}$ we use the fact that three-body recombination processes, which lead to particle loss, are directly connected to the local three-body correlation function. Compared to the 3D situation, we observe a reduction of $g^{(3)}$ by 3 orders of magnitude when increasing the interactions such that we enter the strongly correlated Tonks-Girardeau regime, in good agreement with theory [Gan03, Che06b].

5.2. Publication: Confinement-induced resonances in low-dimensional quantum systems

Phys. Rev. Lett. **104**, 153203 (2010)†

Elmar Haller[1], Manfred J. Mark[1], Russell Hart[1], Johann G. Danzl[1], Lukas Reichsöllner[1], Vladimir Melezhik[2], Peter Schmelcher[3], and Hanns-Christoph Nägerl[1]

[1] *Institut für Experimentalphysik und Zentrum für Quantenphysik, Universität Innsbruck, Technikerstraße 25, A–6020 Innsbruck, Austria*
[2] *Bogoliubov Laboratory of Theoretical Physics, Joliot-Curie 6, 141980 Dubna, Russia*
[3] *Theoretische Chemie, Physikalisch-Chemisches Institut, Universität Heidelberg, Im Neuenheimer Feld 229, 69120 Heidelberg, Germany*

We report on the observation of confinement-induced resonances in strongly interacting quantum-gas systems with tunable interactions for one- and two-dimensional geometry. Atom-atom scattering is substantially modified when the s-wave scattering length approaches the length scale associated with the tight transversal confinement, leading to characteristic loss and heating signatures. Upon introducing an anisotropy for the transversal confinement we observe a splitting of the confinement-induced resonance. With increasing anisotropy additional resonances appear. In the limit of a two-dimensional system we find that one resonance persists.

† The author of the present thesis contributed to this work by maintaining and improving the experimental setup and paper writing.

5.2.1. Introduction

Low-dimensional systems have recently become experimentally accessible in the context of ultracold quantum gases. For a two-dimensional (2D) geometry, the Berezinskii-Kosterlitz-Thouless (BKT) transition has been observed [Had06], and in one dimension the strongly-correlated Tonks-Girardeau (TG) [Gir60, Kin04, Par04, Sya08, Hal09] and super-Tonks-Girardeau (sTG) gases [Hal09] have been realized. In these experiments steep optical potentials freeze out particle motion along one or two directions and restrict the dynamics to a plane or to a line. Such quasi-2D or quasi-1D systems can be realized with ultracold gases when the kinetic and the interaction energy of the particles are insufficient to transfer the particles to transversally excited energy levels. Whereas the confinement removes motional degrees of freedom, it also provides an additional structure of discrete energy levels that can be used to modify scattering along the unconfined direction and by this to effectively control the interaction properties of the low-dimensional system [Ols98, Pet00b, Ber03b]. In this Letter, we investigate the few-body scattering processes that give rise to the capability to tune interactions and hence to drastically alter the properties of low-dimensional many-body quantum systems [Hal09].

In three-dimensional (3D) geometry magnetically-induced Feshbach resonances (FBRs) [Chi10] allow tuning of the inter-particle interaction strength. A FBR occurs when the scattering state of two atoms is allowed to couple to a bound molecular state. Typically, scattering state and bound state are brought into degeneracy by means of the magnetically tunable Zeeman interactions. For particles in 1D and 2D geometry a novel type of scattering resonance occurs. Coupling between the incident channel of two incoming particles and a transversally excited molecular bound state generates a so-called confinement-induced resonance (CIR) [Ols98, Pet00b, Ber03b, Tie00, Yur05, Mel07, Sae08, Kim05, Nai07]. A CIR occurs when the 3D scattering length $a_{3\mathrm{D}}$ approaches the length scale that characterizes the transversal confinement, i.e. the harmonic oscillator length $a_\perp = \sqrt{\hbar/(m\omega_\perp)}$ for a particle with mass m and transversal trapping frequency $\omega_\perp$. This causes the 1D coupling parameter $g_{1\mathrm{D}} = \frac{2\hbar^2 a_{3\mathrm{D}}}{m a_\perp^2} \frac{1}{1 - C a_{3\mathrm{D}}/a_\perp}$ to diverge at $a_\perp = C a_{3\mathrm{D}}$, where $C = 1.0326$ is a constant [Ols98, Ber03b]. The CIR allows tuning of interactions from strongly repulsive to strongly attractive and thus represents a crucial ingredient for the control of interactions in a low-dimensional system. Modification of scattering properties due to confinement has been measured near a FBR for fermions [Gün05], and, recently, a CIR has been observed for a strongly-interacting 1D quantum gas of bosonic Cs atoms and was used to drive the crossover from a TG gas with strongly repulsive interactions to an sTG gas with strongly attractive interactions [Hal09]. Here, for an ultracold quantum gas of Cs atoms with tunable interactions, we study the properties of CIRs by measuring particle loss and heating rate and, in particular, confirm the resonance condition $a_\perp = C a_{3\mathrm{D}}$ for symmetric 1D confinement. For the case of transversally anisotropic confinement we find that the CIR splits and, to our surprise, persists for positive $a_{3\mathrm{D}}$ even when the anisotropy reaches the limit of

a 2D system.

5.2.2. Confinement induced resonances

Figure 5.3(a) reviews the basic mechanism that causes a CIR for zero collisional energy in 1D [Ber03b]. It is assumed that in 3D the scattering potential supports a single universal bound state for strong repulsive interactions (dotted line) [Chi10]. The point where the incoming channel of two colliding atoms and the universal dimer state are degenerate marks the position of a 3D FBR (triangle). In 1D, strong transversal confinement shifts the zero-energy of the incoming channel (middle dashed line) and introduces a transversally excited state (upper dashed line). As a result of the strong confinement, the universal dimer state with binding energy E_{B} (lower solid line) exists also for attractive interactions [Mor03a] whereas the original 3D FBR has disappeared. Instead, there is a CIR (star) when the incoming scattering channel becomes degenerate with the transversally excited molecular bound state (upper solid line). It is assumed that the binding energy of this state is also E_{B}, shifted by $2\hbar\omega_{\perp}$[Ols98]. In more detail, as depicted in Fig. 5.3(b), we assume that the energy levels of non-interacting atoms, as a result of cylindrically symmetric transversal confinement, can be approximated by those of a 2D harmonic oscillator with $E_{n_1,n_2} = \hbar\omega_{\perp}(n_1+n_2+1)$ and quantum numbers n_1 and n_2 belonging to the two Cartesian directions. Scattering atoms [1] in the transversal ground state $(0,0)$ can couple to the excited states (n_1,n_2) if the parity of the total wave function is preserved [Kim05]. The energetically lowest allowed excited states are threefold degenerate with an energy $E = 3\hbar\omega_{\perp}$ and with quantum numbers $(1,1)$, $(2,0)$ and $(0,2)$. For the transversally symmetric confinement, they contribute towards a single CIR [Ber03b]. However, the contribution of the state (1,1) is negligible due to the zero contact probability of the atoms and the short-range character of the interatomic interaction. Unequal transversal trapping frequencies ω_1 and $\omega_2 = \omega_1 + \Delta\omega$ lift this degeneracy and shift the energy levels according to $E_{n_1,n_2} = \hbar\omega_1(n_1+n_2+1) + \hbar\Delta\omega(n_2+1/2)$. One thus expects a splitting of the CIR.

5.2.3. Experimental procedure

We start from a tunable Bose-Einstein condensate (BEC) of 1.0 to 1.4×10^5 Cs atoms in the energetically lowest hyperfine sublevel [Kra04] confined in a crossed-beam optical dipole trap and levitated against gravity by a magnetic field gradient of $|\nabla B| \approx 31.1$ G/cm. Tunability of $a_{3\mathrm{D}}$ is given by a FBR as shown in Fig. 5.3(d) with its pole at $B_0 = 47.78(1)$ G and a width of 164 mG [Kra04, Lan09]. The BEC is produced at $a_{3\mathrm{D}} \approx 290\ a_0$. We load the atoms within 300 ms into an optical lattice, which is formed by two retro-reflected laser beams at a wavelength of $\lambda = 1064.49(1)$ nm, one propagating vertically and one propagating horizontally as illustrated in Fig. 5.3(c). These lattice beams confine

[1] Center-of-mass and relative motion separate for identical particles in a harmonic trap

the atoms to an array of approximately 3000 horizontally oriented, elongated 1D tubes with a maximum occupation of 60 atoms at a linear peak density of approximately $n_{1D} \approx 2/\mu$m. Weak longitudinal confinement results from the Gaussian-shaped intensity distribution of the beams. We raise the lattice to a depth of typically $V = 30\ E_R$, where $E_R = h^2/(2m\lambda^2)$ is the photon recoil energy. At this depth, the resulting transversal and longitudinal trap frequencies are $\omega_\perp = 2\pi \times 14.5$ kHz and $\omega_\parallel = 2\pi \times 16$ Hz and we then have $a_\perp \approx 1370\ a_0$. After loading we slowly ramp down $|\nabla B|$ in 50 ms and adiabatically increase a_{3D} to 915 a_0 in 100 ms to create a TG gas with well-defined starting conditions near the CIR [Hal09]. To detect the CIR as a function of B, manifested by a loss resonance, we quickly set B in less than 200 μs to the desired value, wait for a hold time of typically $\tau = 200$ ms, and then measure the number N of remaining atoms by absorption imaging. For this, we re-levitate the atoms, ramp down the lattice beams adiabatically with respect to the lattice band structure, and allow for 50 ms of levitated expansion and 2 ms time-of-flight. Note that τ is chosen to be much longer than the lifetime of the sTG phase [Hal09].

5.2.4. Transversally symmetric confinement

We observe the CIR in the form of an atomic loss signature as shown in Fig. 5.4. We attribute the loss near the resonance to inelastic three-body collisions [Web03a], which lead to molecule formation and convert binding energy into kinetic energy, causing trap loss and heating, similar to the processes observed near a FBR [Chi10]. In Fig. 5.4(a) the CIR can be identified as a distinct "edge" for the atom number N. Initially, in the TG regime losses are greatly suppressed, but increase rapidly on the attractive side of the CIR. N drops to a minimum when B is increased and then recovers somewhat. A clear shift of the loss signature to lower values for B and hence lower values for a_{3D} can be discerned when the confinement is stiffened. When we identify the position of the edge with the position of the CIR, we find good agreement with the analytical result $Ca_{3D} = a_\perp$ as shown in Fig. 5.4(b). As we have no theoretical description of the detailed shape of the loss resonance, we also plot, for comparison, the position of the minimum, which is shifted accordingly.

In Fig. 5.4(c) we juxtapose the loss and the heating rate that we measure in the vicinity of the CIR. For this, we measure the increase of the release energy within the first 100 ms. After holding the atoms for time τ at a given value of B, we decrease a_{3D} back to 250 a_0 in 20 ms, switch off the lattice potential and determine the release energy in the direction of the tubes from the momentum distribution in free space expansion. We observe an increase for the heating rate when the CIR is crossed. From a low value of 10 nK/s in the TG regime it rises to a maximum of approximately 150 nK/s and then drops to settle at some intermediate value. The position of the maximum agrees well with the maximum for atom loss. We check that the system's increase in energy is sufficiently small so that its 1D character is not lost. The release energy, even at maximal heating, remains below $k_B \times 30$ nK, which is far below the energy spacing of the harmonic

oscillator levels, $\hbar\omega_\perp \approx k_B \times 600$ nK.

5.2.5. Transversally asymmetric confinement

We now examine 1D systems with transversally anisotropic confinement. Starting from a lattice depth of $V = 25\ E_R$ along both transversal directions, yielding $\omega_\perp = \omega_1 = \omega_2 = 2\pi \times 13.2(2)$ kHz, we increase the horizontal confinement to frequencies up to $\omega_2 = 2\pi \times 16.5(2)$ kHz, corresponding to a lattice depth of $39\ E_R$, while keeping the depth of the vertical confinement constant. Fig. 5.5(a) shows a distinct splitting of the original CIR into two loss resonances, CIR_1 and CIR_2. The splitting increases as the anisotropy is raised. In Fig. 5.5(b) we plot the 3D scattering length values $a_{3\mathrm{D},1}$ and $a_{3\mathrm{D},2}$ that we associate with the positions of CIR_1 and CIR_2 as a function of the frequency ratio ω_2/ω_1. For this, as it becomes difficult to assign an edge to both of them, we simply determine the associated atom number minima and subtract a constant offset of 88(7) a_0 as determined from the measurement shown in Fig. 5.4(b). One of the resonances, CIR_2, exhibits a pronounced shift to smaller values for $a_{3\mathrm{D}}$ as the horizontal confinement is stiffened. The second resonance, CIR_1, shows a slight shift towards higher values for $a_{3\mathrm{D}}$. We now use the lifting of the degeneracy for the energy levels as indicated in Fig. 5.3(b) to model the observed splitting of the CIR. We assume that the implicit equation $\zeta(1/2, -E_\mathrm{B}/(2\hbar\omega_\perp) + 1/2) = -a_\perp/a_{3D}$ for the binding energy E_B [Ber03b] remains approximately valid for sufficiently small $\Delta\omega$, taking $\omega_\perp = \omega_1$. Here, ζ is the Hurwitz zeta function. We translate the scattering length values $a_{3\mathrm{D},1}$ and $a_{3\mathrm{D},2}$ into binding energies and calculate the energy difference $\Delta E_\mathrm{B} = E_\mathrm{B}(a_{3\mathrm{D},1}) - E_\mathrm{B}(a_{3\mathrm{D},2})$, shown in Fig. 5.5(c). While this model does not explain the upward deviation seen for CIR_1, the difference ΔE_B is in reasonable agreement with the expected energy shift caused by the shifts of the excited harmonic oscillator states $(E_{0,2} - E_{2,0}) = 2\hbar\Delta\omega$ (solid line in Fig. 5.5(c)). We thus attribute CIR_2 to the stiffened confinement along the horizontal direction and hence to state $(0, 2)$, while CIR_1 corresponds to the unchanged confinement along the vertical direction and hence to state $(2, 0)$.

5.2.6. Limit of a 2D-system

We observe the appearance of additional structure in the measured loss curves when we increase the transversal anisotropy by weakening the confinement along one axis, here along the vertical direction. Fig. 5.6(a) shows the atom number after $\tau = 300$ ms for trapping frequency ratios ω_1/ω_2 from 0.67 to 0.45. Multiple loss resonances appear close to the position of CIR_1. The number of resonances increases and the positions shift continuously as the confinement is weakened. We speculate that those resonances are a result of a coupling to additional excited states, resulting in a multi-channel scattering situation. Also the weakening of the confinement could induce sufficient anharmonicity to allow for violation of the parity rule [Pea05].

Surprisingly, we find that one of the CIRs persists in the limit of a 2D system.

Previous theoretical studies on 2D systems have predicted the appearance of a CIR for negative a_{3D}, but not for positive a_{3D} [Pet01, Nai07]. In the experiment, we reduce the horizontal confinement while keeping the vertical confinement constant to probe the transition from the array of tubes to a stack of pancake-shaped, horizontally-oriented 2D systems. Trapping in the horizontal direction is still assured, now by the Gaussian profile of the vertically propagating laser beam, for which $\omega_2 = 2\pi \times 11$ Hz. Fig. 5.6(b) shows that the CIR associated with the tight confinement shifts to lower values for B and hence for a_{3D} as the horizontal confinement is weakened. In the limit of 2D confinement, one of the CIRs, and in fact all the additional structure observed above, have disappeared, but one resonance persists. To check that the observed resonance is indeed the result of the 2D confinement, we vary the confinement along the tight vertical direction. Fig. 5.6(c) plots the positions of edge and minimum of the loss signature as a function of $a_{\perp,2D}$, the confinement length associated with this direction. When we again associate the edge with the pole of the resonance, we obtain $C_{2D}a_{3D} = a_{\perp,2D}$ with $C_{2D} = 1.19(3)$, where C_{2D} is a scaling factor similar to C for the 1D case. Further scattering experiments are needed to elucidate the energy dependence of this 2D scattering resonance.

In summary, we have investigated the properties of CIRs, which appear in low-dimensional quantum systems as a result of tight confinement and which replace "conventional" 3D Feshbach resonances to tune the effective atomic interaction strength. We observed a splitting of the CIR for anisotropic transversal confinement, the appearance of multiple resonances for strongly anisotropic confinement, and the survival of one resonance for positive a_{3D} in the limit of 2D confinement. We expect that CIRs will not only be used in 1D geometry to tune the effective interaction strength as recently demonstrated [Hal09], but also in 2D geometry and mixed dimensions [Lam10] for the study of strongly-interacting quantum systems.

We thank W. Zwerger for discussions and R. Grimm for generous support. We acknowledge funding by the Austrian Science Fund and by the European Union within the framework of the EuroQUASAR collective research project QuDeGPM. R.H. is supported by a Marie Curie Fellowship within FP7. P.S. acknowledges financial support by the DFG. Financial support by the Heisenberg-Landau Program is appreciated by P.S. and V.M.

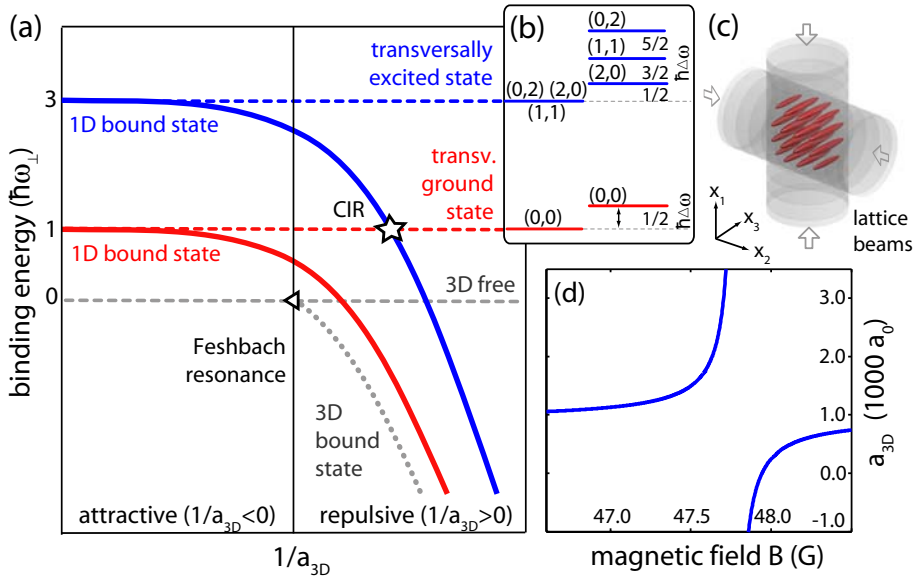

Fig. 5.3.: (color online) (a) Illustration of the mechanism responsible for a CIR, see Ref.[Ber03b] and text for details. The energy levels near a scattering resonance are plotted as a function of $1/a_{3D}$. The CIR occurs for $Ca_{3D} = a_\perp$ when scattering atoms are allowed to couple to transversally excited bound states. (b) indicates the shift and splitting for anisotropic confinement characterized by $\Delta\omega$. (c) Experimental configuration. Two laser beams create an optical lattice that confines the atoms to an array of approximately 3000 independent, horizontally-oriented elongated 1D tubes. (d) Tuning of a_{3D} is achieved by means of a FBR with a pole at $B = 47.78(1)$ G [Lan09].

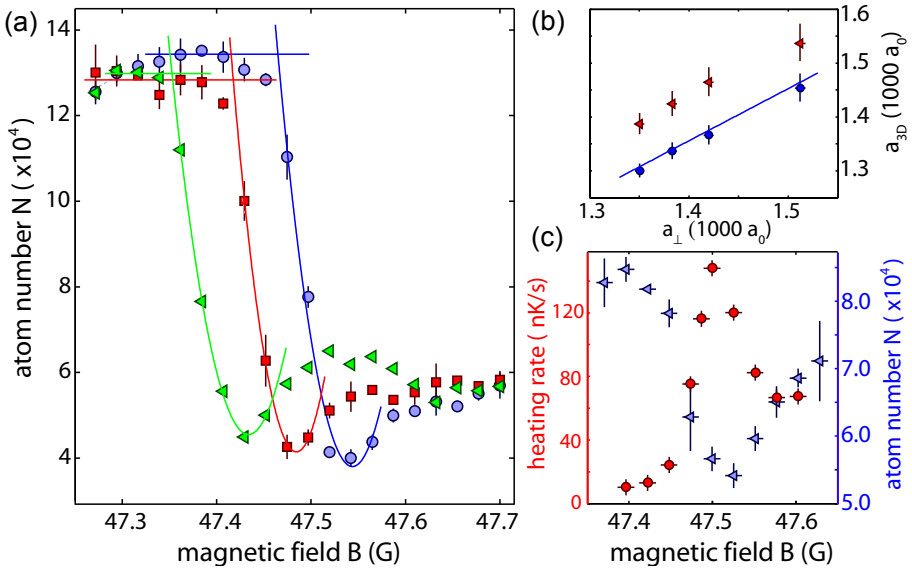

Fig. 5.4.: (color online) Particle loss and heating rates in the vicinity of a CIR. (a) The number N of remaining atoms after $\tau = 200$ ms shows a distinct drop ("edge") when B is scanned across the CIR. A clear shift of the position of the edge to lower values for B can be observed when the transversal confinement is stiffened, $\omega_\perp = 2\pi \times (0.84, 0.95, 1.05) \times 14.2(2)$ kHz (circles, squares, triangles). (b) Position of the edge (circles) as determined from the intersection point of a second-order polynomial fit to the minimum for N and the initial horizontal baseline as shown in (a), converted into values for a_{3D}. For comparison, the position of the minimum (triangles) is also shown. The solid line is given by $Ca_{3D} = a_\perp$. (c) Heating rates near the CIR (circles). For comparison, N is also shown (triangles). Here, $\omega_\perp = 2\pi \times 12.0(2)$ kHz. All error bars reflect 1σ statistical uncertainty.

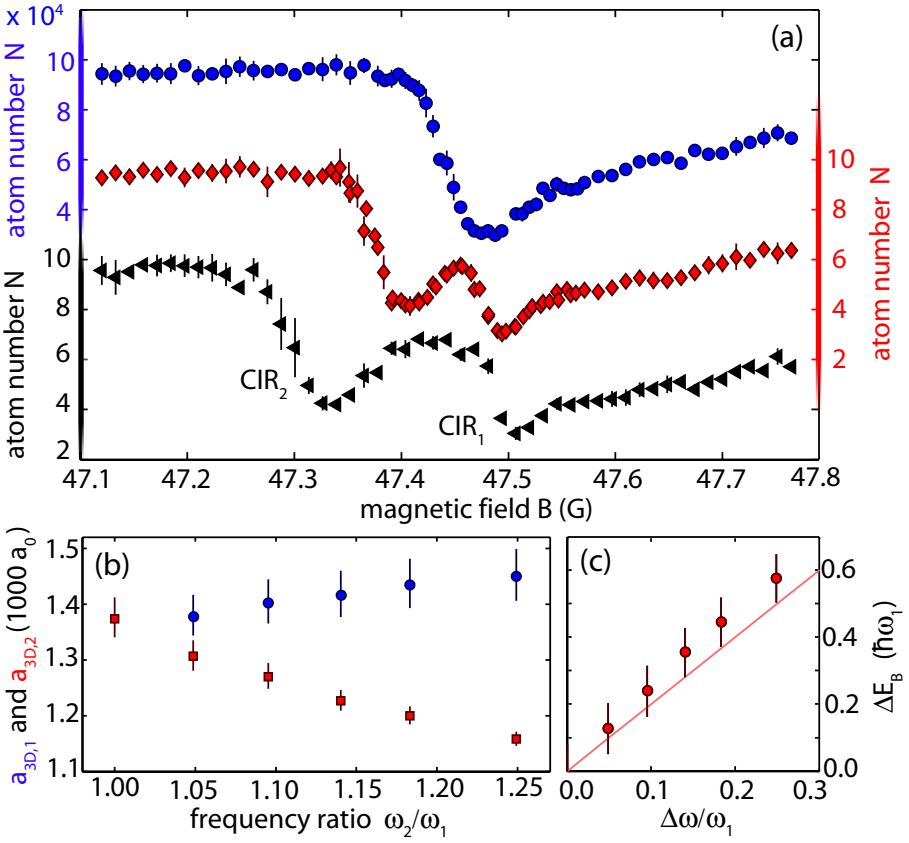

Fig. 5.5.: (color online) Splitting of a CIR for a 1D system with transversally anisotropic confinement. (a) As the horizontal confinement is stiffened, $\omega_2/\omega_1 = 1.00, 1.10, 1.18$ (circles, diamonds, triangles) for $\omega_1 = 2\pi \times 13.2(2)$ kHz, the CIR splits into CIR_1 and CIR_2. (b) Position of CIR_1 ($a_{3\mathrm{D},1}$, circles) and CIR_2 ($a_{3\mathrm{D},2}$, squares) as a function of the frequency ratio ω_2/ω_1. (c) Binding energy difference ΔE_B as determined from the implicit equation (see text) in comparison to the expectation from the simple harmonic oscillator model (solid line).

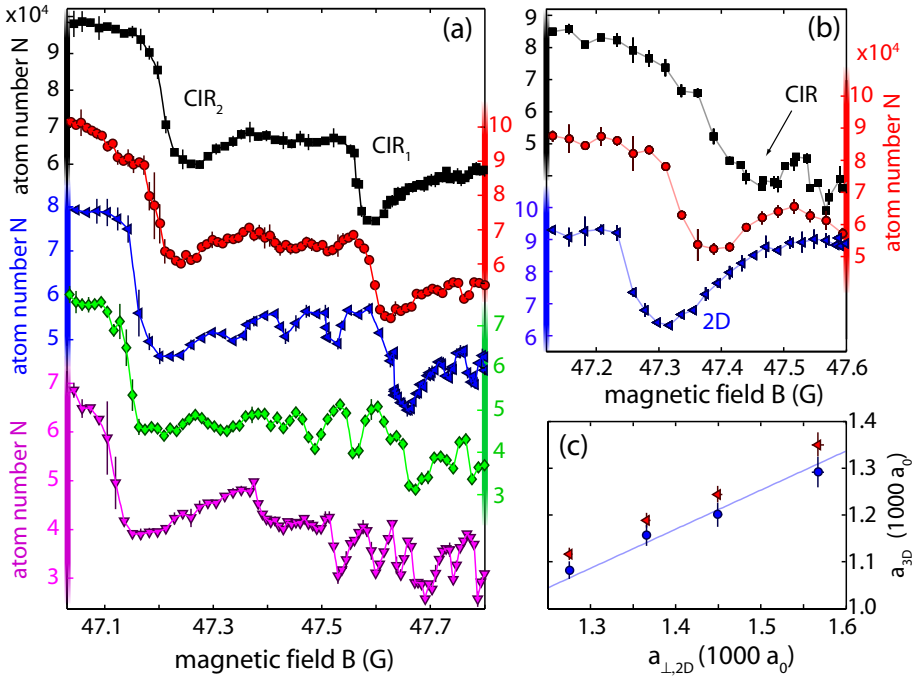

Fig. 5.6.: (color online) (a) Appearance of additional structure in the vicinity of CIRs for strongly anisotropic transversal confinement. The trap frequencies are $\omega_2 = 2\pi \times 16.6(2)$ kHz and $\omega_1/\omega_2 = 0.67, 0.60, 0.53, 0.49, 0.45$ from top to bottom. (b) Transition from 1D to 2D confinement. As the horizontal lattice is ramped down, CIR_2 shifts and persists, while CIR_1 disappears ($\omega_1 = 2\pi \times 13.0(2)$ kHz and $\omega_2/\omega_1 = 0.58, 0.42, 0.00$ for squares, circles, and triangles). (c) Scaling of the CIR's position in 2D, in analogy to the 1D case shown in Fig. 5.4(b). The position of the CIR as determined from the edge (circles) and, alternatively, from the minimum in atom number (triangles) shifts to lower values for $a_{3\mathrm{D}}$ as the confinement is stiffened and $a_{\perp,2\mathrm{D}}$ is reduced. The solid line is a linear fit according to $C_{2\mathrm{D}} a_{3\mathrm{D}} = a_{\perp,2\mathrm{D}}$ with $C_{2\mathrm{D}} = 1.19(3)$.

5.3. Publication: Realization of an Excited, Strongly-Correlated Quantum Gas Phase

Science **325**, 1224 (2009)†

Elmar Haller [1], Mattias Gustavsson[1], Manfred J. Mark[1], Johann G. Danzl[1], Russell Hart[1], Guido Pupillo[2,3], and Hanns-Christoph Nägerl[1]

[1] *Institut für Experimentalphysik und Zentrum für Quantenphysik, Universität Innsbruck, Technikerstraße 25, A–6020 Innsbruck, Austria*

[2] *Institut für Theoretische Physik, Universität Innsbruck, Technikerstraße 25, A–6020 Innsbruck, Austria*

[3] *Institut für Quantenoptik und Quanteninformation der Österreichischen Akademie der Wissenschaften, Technikerstraße 21a, A–6020 Innsbruck, Austria*

Ultracold atomic physics offers myriad possibilities to study strongly correlated many-body systems in lower dimensions. Typically, only ground state phases are accessible. Using a tunable quantum gas of bosonic cesium atoms, we realize and control in one dimensional geometry a highly excited quantum phase that is stabilized in the presence of attractive interactions by maintaining and strengthening quantum correlations across a confinement-induced resonance. We diagnose the crossover from repulsive to attractive interactions in terms of the stiffness and the energy of the system. Our results open up the experimental study of metastable excited many-body phases with strong correlations and their dynamical properties.

† The author of the present thesis contributed to this work by maintaining and improving the experimental setup and paper writing.

5.3.1. Introduction

In many-body quantum physics the interplay between strong interactions and confinement to a low-dimensional geometry amplifies the effects of quantum fluctuations and correlations. A remarkable example in one dimension is the Tonks-Girardeau (TG) gas, where bosons with strong repulsive interactions minimize their interaction energy by avoiding spatial overlap and acquire fermionic properties [Gir60, Lie63]. Evidence for this ground state phase was found using Bose-Einstein condensates (BEC) loaded into optical lattices [Par04, Kin04]. While many-body quantum systems are usually found in their ground state phases, long-lived excited state phases are responsible for some of the most striking physical effects, examples ranging from vortex lattices in superfluids to subtle topological excitations in spin liquids [Ale06]. However, the experimental realization of excited phases is difficult, as these usually quickly decay by intrinsic effects or by coupling to the environment. In this context, cold atoms [Pet00b, Mor03a, Par04, Kin04, O'H04, Pet07, Hof07, Sya08, Blo08] may provide unique opportunities for the realization of long-lived, strongly interacting, excited many-body phases due to the excellent decoupling from the environment and the tunability of interactions via, for example, Feshbach resonances.

For an ultracold one-dimensional (1D) system of bosons, we prepare a highly-excited many-body phase known as the super-Tonks-Girardeau (sTG) gas [Ast05]. In this highly-correlated quantum phase, interactions are attractive, and rapid decay into a cluster-type ground state is in principle possible. However, a surprising property of this many-body phase is its metastability. Attractive interactions strengthen correlations between particle positions and ensure, similar to an effective long-range repulsive interaction, that particles rarely come together. To realize this exotic phase, we observe and exploit a 1D confinement-induced resonance (CIR) [Ber03b, Ols98]. This resonance allows us to first enter deeply into the repulsive TG regime to establish strong particle correlations and then to switch interactions from strongly repulsive to strongly attractive. The frequency ratio of the two lowest-energy collective modes [Men02] provides accurate diagnostics for the crossover from the TG to the sTG regime. In particle loss and expansion measurements we study the time evolution of the system through the crossover.

5.3.2. Scattering in 1D systems

We tune the strength of the interaction as characterized by the three-dimensional (3D) scattering length a_{3D} by means of a magnetically-induced Feshbach resonance [Ino98]. For a 1D system, a CIR arises and strongly modifies the 1D scattering properties when a_{3D} approaches the harmonic oscillator length $a_\perp = \sqrt{\hbar/(m\omega_\perp)}$ of the transversal confinement with trap frequency $\omega_\perp$ [Ols98, Ber03b]. Here, m is the mass of the particles and $\hbar$ is Planck's constant divided by 2π. More precisely, the coupling constant g_{1D} of the 1D δ-function contact

potential $U_{1D}(z) = g_{1D}\delta(z)$ behaves as [Ber03b]

$$g_{1D} = -\frac{2\hbar^2}{ma_{1D}} = \frac{2\hbar^2 a_{3D}}{ma_\perp^2}\frac{1}{1 - C\ a_{3D}/a_\perp}, \tag{5.1}$$

where a_{1D} is the 1D scattering length defined by this equation and $C = 1.0326$ is a constant. Thus, the CIR allows tuning of g_{1D}. For values of a_{3D} less but close to $a_\perp/C$ ($a_{3D} \lesssim a_\perp/C$) the coupling parameter g_{1D} is large and positive, and for $a_{3D} \gtrsim a_\perp/C$ it is large and negative, leading to an effectively attractive interaction. For homogenous systems with $g_{1D} > 0$, it is customary to characterize the strength of interactions by the Lieb-Liniger parameter $\gamma = g_{1D}m/(\hbar^2 n_{1D})$, where n_{1D} is the linear 1D density of the system [Lie63, Pet00b]. The TG gas corresponds to the limit $\gamma \gg 1$ or $g_{1D} \to \infty$. As interactions are increased, the system becomes strongly correlated and is fully dominated by its kinetic energy. In previous experiments, without the capability to tune a_{3D}, a maximum of $\gamma \approx 5.5$ was achieved [Kin04], while an effective strength $\gamma_{\text{eff}} \approx 200$ was reached with an additional shallow lattice potential along the longitudinal direction [Par04]. In the former experiment, a saturation for the size and energy of the 1D system was observed, and in the latter experiment the momentum distribution was studied.

But what happens in the case of strong attractive interactions $g_{1D} \to -\infty$, i.e. $a_{1D} \gtrsim 0$? The ground state for a system of N attractively interacting bosons in 1D is a cluster state [McG65, Tem08], which one would expect, in a cold atom system, to decay quickly via molecular channels. However, by crossing the CIR from the TG side, i.e. switching interactions from $g_{1D} = +\infty$ to $g_{1D} = -\infty$, an excited gas-like phase, the sTG gas, should be accessible [Ast05]. Is this excited phase stable, i.e. does it exist at all? The expectation is that the large kinetic energy inherited from the TG gas, in a Fermi-pressure like manner, prevents the gas from collapsing [Bat05]. This stability can most simply be inferred from a Bethe-ansatz solution to the Lieb-Liniger model with attractive interactions [Ast04, Bat05]. This ansatz yields for the energy per particle $E/N \approx \hbar^2\pi^2 n_{1D}^2/[6m(1 - n_{1D}a_{1D})^2]$, corresponding to the energy of a gas of hard rods [Gir60], for which a_{1D} represents the excluded volume. This results in a positive inverse compressibility and also in an increased stiffness of the systems as long as $n_{1D}a_{1D}$ is sufficiently small. Interestingly, in this phase the density correlations are even stronger than in the TG gas, as they show a power-law decay that is slower than for a TG gas [Ast05], indicating an effective long-range interaction.

We realize the crossover all the way from a non-interacting gas via the 1D mean-field Thomas-Fermi (TF) regime to a TG gas and then to a sTG gas. We exploit the fact that our 1D systems possess weak harmonic confinement along the axial direction characterized by the confinement length $a_\parallel$. Whereas the frequency ω_D of the lowest dipole mode depends only on the confinement, the frequency ω_C of the lowest axial compressional mode is sensitive to the various regimes of interaction [Men02]. For the non-interacting system one expects $R \equiv \omega_C^2/\omega_D^2 = 4$. This value then changes to $R = 3$ for weakly repulsive interactions

in a 1D TF regime [Mor03a]. For increasing positive interaction strength, R is expected to change smoothly to 4 when entering the TG regime as the system becomes fermionized and hence effectively non-interacting. A rise beyond the value of 4, after crossing the CIR, would then constitute clear evidence for the sTG regime [Ast05]. As a_{1D} is further increased, the system will finally become unstable and R is expected to turn over and drop towards zero. For a harmonically confined system, the point of instability is reached when the overall length of the system of hard rods, Na_{1D}, becomes of the order of the size $\sqrt{N}a_{\|}$ for the wave function of N non-interacting fermions, i.e. $A \equiv Na_{1D}/(\sqrt{N}a_{\|}) \approx 1$. We use A^2 as an alternative parameter to γ to characterize the strength of the interaction as it accounts for the harmonic confinement.

5.3.3. Experimental procedure

We start from a 3D Bose-Einstein condensate (BEC) with up to 2×10^5 Cs atoms with no detectable thermal fraction in a crossed-beam dipole trap with magnetic levitation [Web03a]. Depending on the interaction regime to be studied, we then set the number of atoms in the BEC to values in the range of $(1-4)\times10^4$ by means of forced radio-frequency evaporation. To confine the atoms in 1D, i.e. to freeze out transversal motion, we use a two-dimensional optical lattice [Blo08], which forms an array of vertically oriented elongated tubes with an aspect ratio that we set to values between 100 and 1000 (Fig. 5.7A). We occupy between $3000-6000$ independent tubes with 8-25 atoms in the center tube. The interaction strength g_{1D} is controlled by magnetic tuning of a_{3D} by means of a combination of a broad and a narrow Feshbach resonance (Fig. 5.7C) with poles at $B = -11.1(6)$ G and $B = 47.78(1)$ G and widths of about 29.2 G and 164 mG, respectively [Lan09]. The broad resonance provides a slow variation of a_{3D}, allowing us to gently tune a_{3D} from 0 a_0 near 17.119 G to about 1240 a_0 near 76 G, while the narrow resonance allows us to tune a_{3D} to absolute values beyond 4000 a_0 given our magnetic field control. We convert the applied magnetic field B into a_{3D} using the fit formula of Ref. 23. A magnetic field gradient, used to levitate the atomic sample (see Sec. 5.3.7), introduces a small spread in the value of a_{3D} across the sample.

To determine the oscillation frequencies ω_C and ω_D of the fundamental modes (Fig. 5.7 B), we excite each mode separately at a given value of the magnetic field B (see Sec. 5.3.7) and let the atoms evolve for a varying amount of hold time. The distribution is then imaged in momentum space by taking an absorption picture after release and expansion. To avoid possible broadening effects due to interaction during the initial expansion, a_{3D} is set to zero near $B = 17.119$ G at the moment of release. To extract the frequency, we determine for each hold time the axial $1/e$-width of the distribution and then fit a damped sinusoid with linear offset to this data. Typical measurements of ω_C are shown in Fig. 5.7 D and E. Whereas the atom number remains constant for $g_{1D} > 0$, we observe some atom loss and a slight broadening of the distribution for attractive 1D interactions. In all parameter regimes, the 1D system is sufficiently stable

to allow a reliable measurement of ω_C.

5.3.4. Transitions between the mean field, TG and STG regimes

First, we show that we can tune the system from the non-interacting regime deeply into the repulsive TG regime (Fig. 5.8). In agreement with expectations, the value for $R = \omega_C^2/\omega_D^2$ first drops from 4 to 3 and then increases back to 4 as γ is tuned by means of the gently-varying background scattering length. We find that the TG regime is fully reached for $\gamma > 50$. A further increase to values up to $\gamma \approx 500$ does not lead to changes for R. Note that, as a_{3D} approaches $a_\perp$, the divergence of g_{1D} according to Eq. 1 has to be taken into account when determining γ (see Sec. 5.3.7). Heating of the system can be excluded as we can return to a 3D BEC without significant thermal background when ramping down the lattice potential.

The attractive regime is entered by crossing the CIR on the low-field wing of the 47.78 G Feshbach resonance. a_{1D} is now small and positive. The central results of this work are summarized in Fig. 5.9A and compared to the theoretical work of Ref. 13. We plot $R = \omega_C^2/\omega_D^2$ as a function of the interaction parameter A^2. For reference, Fig. 5.9B plots a_{3D}, a_{1D}, and g_{1D} in the vicinity of the Feshbach resonance as a function of the magnetic field B. As the CIR is crossed and A^2 is increased, R rises beyond the value of 4. This provides clear evidence for the sTG regime as $R = 4$ is the maximal value for bosons with repulsive contact interaction. This increase is expected from the model of a gas of hard rods, and our data initially follows the prediction from this model. However, as A^2 is increased, R reaches a maximum and then starts to drop. The maximum of about 4.5 is reached for $A^2 \approx 3 \times 10^{-2}$. The existence of the maximum is in qualitative agreement with the results obtained from Monte-Carlo simulations [Ast05]. The theoretical prediction, however, underestimates the measured R. This is probably due to the local density approximation, which may not be applicable to our system with low particle numbers. For comparison, the results from Fig. 5.8 for $\gamma \geq 1$ are shown. Note that $\gamma \approx 500$ corresponds to small values of $A^2 \approx 10^{-4}$. For this data, at higher particle numbers, there is excellent agreement with the theoretical prediction (solid line) in the entire crossover from the mean-field regime to the TG regime[Men02].

5.3.5. Losses and heating

We study the stability of the system in the crossover from the TG to the sTG regime and find further evidence for the existence of the CIR by recording particle loss and measuring the axial width of the atomic cloud after release from the tubes. The axial width is a measure for the kinetic energy of the system as interactions are instantly switched off upon release. Similar conditions are used as for the measurements on the sTG regime presented in Fig. 5.9. The TG regime is entered adiabatically to avoid the excitation of collective modes. The system is prepared at $a_{3D} = 887(1)$ a_0 at a magnetic field of $B = 42.77(2)$ G

with about 11 atoms in the central tube. The magnetic field is then ramped to a specific value within 0.2 ms and the sample is held at this value for a variable hold time τ from 10 to 200 ms. $a_\perp$ is set to 1523(6) a_0. The results (Fig. 5.10) for different hold times τ in the tubes show that, for $\tau = 10$ ms, corresponding to the timescale of the measurements in the sTG regime shown in Fig. 5.9, the transition from the TG to the sTG regime appears very smooth. There is essentially no particle loss when the system is deep in the TG regime and close to the CIR. The loss gradually increases in the attractive regime as one moves to larger values of B and towards the pole for a_{1D}. Correspondingly, the width of the sample exhibits a smooth behavior across the CIR, showing a slight increase for larger B. This behavior is consistent with the expectation of an increased energy in the sTG regime [Ast05].

For longer hold times, the data for the atom number and the sample width develop distinct features at the calculated position of the CIR. Evidently, the system is in a transient state. For $\tau = 50$ ms, the number of remaining atoms shows a dip that correlates with a peak in the kinetic energy of the sample. Both features become more prominent and asymmetric for longer hold times ($\tau = 100$ and 200 ms). Note that, in comparison, no pronounced effects are visible at the pole of the Feshbach resonance for a_{3D}. Our results must be connected to the fact that the energy spectrum of the system changes dramatically across the CIR, from the TG to the sTG regime [Tem08]. The system acquires a deeply lying ground state together with a family of lower lying many-body excited states, potentially opening up new decay channels. Also, the CIR strongly modifies the two-body scattering problem, making formation of confinement-induced molecules in transversally excited trap states [Ber03b] possible.

5.3.6. Summary

The non-trivial time evolution observed in this system raises intriguing questions on possible coupling and decay mechanisms for strongly interacting excited many-body systems, in particular in the context of integrability of 1D systems [Kin06]. Our results offer an example of the counter-intuitive effects that occur in many-body systems, and open up the possibility to study the dynamical properties of strongly-correlated systems with effective long-range interactions [Boc99, Ste08] under conditions where all parameters are tunable and, in fact, can be changed dynamically. Similar to magnetic Feshbach resonances in atomic scattering, we expect the confinement-induced resonance demonstrated here to serve as a general tool to tailor interactions in 1D and possibly also in 2D systems [Pet00a], allowing for the further investigation of strongly correlated phases in the context of cold atomic gases.

We thank S. Giorgini and C. Menotti for helpful discussions and for providing the theory curves shown in Fig. 5.9A. We are indebted to R. Grimm for generous support and to H. Häffner and his group for the loan of a CCD camera.

We gratefully acknowledge funding by the Austrian Ministry of Science and Research (Bundesministerium für Wissenschaft und Forschung) and the Austrian Science Fund (Fonds zur Förderung der wissenschaftlichen Forschung) in form of a START prize grant and by the European Union through the STREP FP7-ICT-2007-C project NAME-QUAM (Nanodesigning of Atomic and MolEcular QUAntum Matter) and within the framework of the EuroQUASAR collective research project QuDeGPM. R.H. is supported by a Marie Curie International Incoming Fellowship within the 7th European Community Framework Programme.

5.3.7. Materials and Methods

Lattice loading

We produce a BEC of Cs atoms in the lowest hyperfine sublevel with hyperfine quantum numbers $F = 3$ and $m_F = 3$ in a crossed beam dipole trap with trap frequencies $\omega_{x,y,z} = 2\pi \times (15, 20, 13)$ Hz, where z denotes the vertical direction. The BEC is adiabatically transferred from the dipole trap to the array of tubes by exponentially ramping up the power in the lattice laser beams with waists ~ 350 μm within 500 ms. The repulsive interaction causes the atoms to move radially outwards during the initial phase of the lattice loading in response to the strong local compression. We use this effect to vary the total number of tubes loaded and hence the atom number per tube by setting a_{3D} for the loading process to values between 40 a_0 and 350 a_0. For the data set in the repulsive regime (Fig. 5.9A, circles), we exponentially ramp down the crossed beam dipole trap during the loading process and reach longitudinal and transversal trap frequencies of $\omega_D = 2\pi \times 15.4(1)$ Hz and $\omega_\perp = 2\pi \times 13.1(1)$ kHz with a transversal confinement length $a_\perp = 1440(6)$ a_0. Here, depending on the regime of interaction to be studied, the number of atoms in the central tube is set to values between 8 and 25. For the data set in the sTG regime (Fig. 5.9A, squares) we increase ω_D to $2\pi \times 115.6(3)$ Hz to reduce the vertical extent of the sample and hence the variation of the magnetic field across the atom cloud, see below. For this, we keep the depth of the crossed beam dipole trap constant during the loading process and then ramp up the power in one of the beams within 100 ms. In this regime we choose $\omega_\perp = 2\pi \times 15.0(1)$ kHz, corresponding to $a_\perp = 1346(5)$ a_0. The number of atoms in the central tube is set to values between 8 and 11.

Array of 1D tubes

The atom number per tube becomes fixed once tunneling is suppressed during the loading process and can be determined by integrating a Thomas-Fermi profile along the tubes (1). The number of atoms in tube (i, j) is given by

$$N_{i,j} = N_{0,0} \left[1 - \left(i \frac{d_{\mathrm{lat}}}{R_x} \right)^2 - \left(j \frac{d_{\mathrm{lat}}}{R_y} \right)^2 \right]^{3/2} \qquad \text{with} \quad N_{0,0} = \frac{5 N_{\mathrm{tot}} d_{\mathrm{lat}}^2}{2\pi R_x R_y},$$

where N_{tot} is the total atom number, $N_{0,0}$ is the occupation of the central tube, $d_{\mathrm{lat}} = \lambda/2$ is the lattice spacing at a wavelength $\lambda = 1064.5$ nm, and $R_{x,y}$ are the Thomas-Fermi radii in the horizontal directions. To calculate the effective atom number per tube N, we average over the tubes, weighting each tube by its atom number. This procedure accounts for the fact that we measure an averaged frequency ω_C, as ω_C is expected to slightly vary from tube to tube. The result for ω_C should be dominated by the more heavily occupied tubes close to the center of the array.

Magnetic levitation

To hold the $(F = 3,\ m_F = 3)$ atoms in the vertically oriented tubes, magnetic levitation by means of a magnetic field gradient of 31.1 G/cm is applied. The gradient introduces a small field spread over the atomic sample. This sets our precision to tune the interaction strength. For the measurements in the sTG regime the distribution has a full width at half maximum (FWHM) of 30 mG. We measure the atom distribution in the magnetic field by driving a magnetic-field-dependent microwave transition. A typical distribution is shown in the bottom left corner of Fig. 5.9B.

Excitation of collective modes

We use two different methods to excite the lowest compressional mode. For a measurement in the mean-field regime, we use a rapid change of the interaction strength to excite the oscillation. For this, we ramp the scattering length adiabatically in 100 ms to a value that is approximately 50 a_0 from the desired final value and then perform the last part of the ramp non-adiabatically. For a measurement in the sTG regime, we use an analogous method. We simply ramp sufficiently quickly, within about 5 ms, all the way from the mean-field across the TG into the sTG regime. For the TG regime, we chose to excite the mode by compressing the cloud adiabatically with an additional dipole trap laser beam, starting the motion by rapidly ramping down the power of this beam. In all cases, we adjust the ramp speeds so that the measured oscillation amplitude is within 10-20% of the initial cloud size. To excite the dipole mode at frequency ω_D, we adiabatically lower the levitating magnetic field gradient and hence displace the cloud along the vertical direction. Quickly readjusting the gradient back to full levitation leads to excitation of the dipole oscillation.

Determination of γ

We make a conservative estimate to determine the Lieb-Liniger interaction parameter γ

$$\gamma = \frac{m\, g_{1\mathrm{D}}}{\hbar^2\, n_{1\mathrm{D}}} = \frac{2}{n_{1\mathrm{D}}\, |a_{1\mathrm{D}}|}.$$

To take into account that the atom number varies according to $N_{i,j}$, we first calculate $\gamma_{i,j}$ for every tube separately. We calculate the center density for each

tube both in the mean-field and in the TG regime and use the larger value to determine $\gamma_{i,j}$. We then take γ as the weighted average over $\gamma_{i,j}$. The error in determining γ largely comes from the determination of $a_{1\mathrm{D}}$, reflecting the magnetic field distribution across the sample.

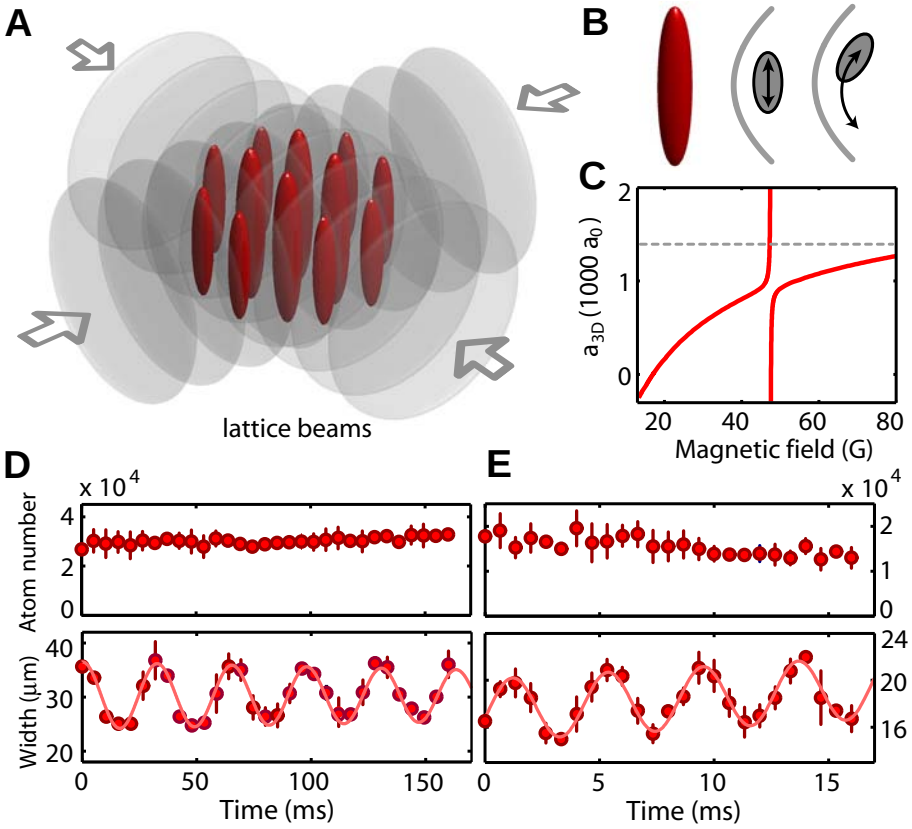

Fig. 5.7.: (color online) **A**, Experimental setup. The lattice potential is created by two retro-reflected laser beams confining the atoms to an array of one-dimensional tubes with equipotential surfaces shown in red. **B**, Along each tube (left) we excite the lowest compressional mode (center) and compare its frequency to the dipole mode (right). **C**, The strength of the interatomic interaction is adjusted by tuning the s-wave scattering length a_{3D}. The background scattering length rises gently from 0 to 1240 a_0 when the magnetic field B is tuned from 17 to 76 G. Further tuning is possible near a Feshbach resonance at 47.78(1) G to absolute values beyond 4000 a_0. The dashed line indicates $a_\perp/C$ for a transversal trap frequency of $\omega_\perp = 2\pi \times 13.1$ kHz. **D** and **E** present typical data sets for the compressional mode in the TG and sTG regime at $a_{3D} = 875(1)$ a_0 and $a_{3D} = 2300(200)$ a_0, respectively. The upper panels show the atom number, the lower panels show the $1/e$-cloud-width after time-of-flight. The solid lines in the lower panels are sinusoidal fits (see online material), yielding the oscillation frequencies $\omega_C = 2\pi \times 30.6(3)$ Hz and $\omega_C = 2\pi \times 241(1)$ Hz, respectively.

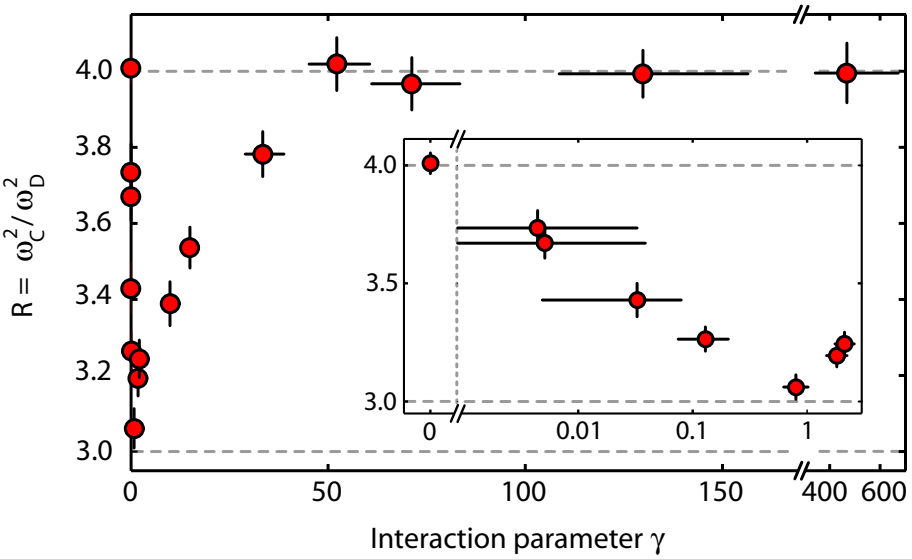

Fig. 5.8.: (color online) Transition from the non-interacting regime via the mean-field TF regime into the TG regime. The squared frequency ratio $R = \omega_C^2/\omega_D^2$ of the lowest compressional mode with frequency ω_C and the dipole mode with frequency ω_D serves as an indicator for the different regimes of interaction. For increasing interactions from $\gamma = 0$ to $\gamma \approx 500$ the system passes from the ideal gas regime ($R = 4$) to the 1D TF regime ($R \approx 3$) and then deeply into the TG regime ($R = 4$). The inset shows the transition from the non-interacting regime to the mean-field regime in more detail. The vertical error bars refer to standard error and the horizontal error bars reflect the uncertainty in determining a_{1D} and n_{1D} (see online material). The horizontal error bar on the data point at $\gamma = 0$ (not shown in the inset) is ± 0.03 a_0 .

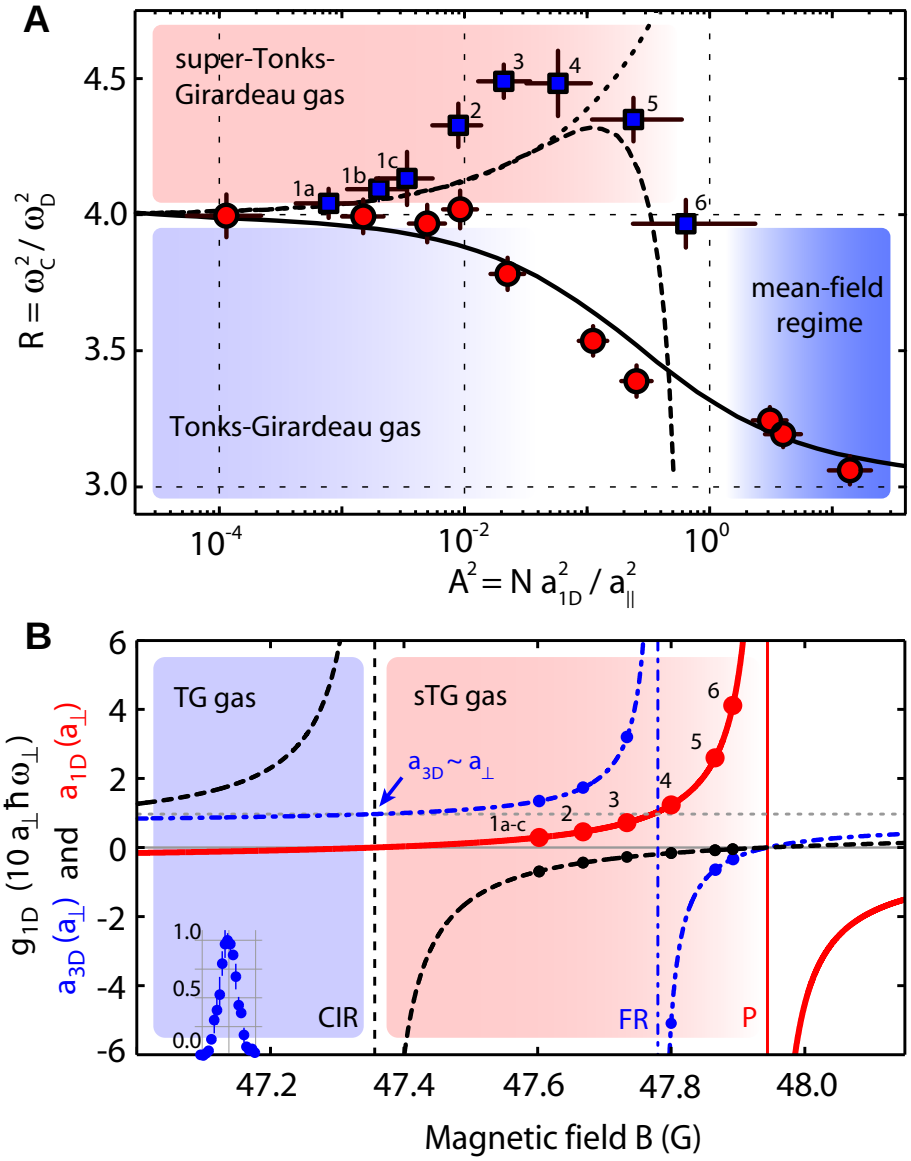

Fig. 5.9.: (color online) **A**, The ratio $R = \omega_C^2/\omega_D^2$ is plotted as a function of the interaction parameter $A^2 = Na_{1D}^2/a_\parallel^2$. The squares show the measurements in the attractive regime ($g_{1D} < 0$), providing evidence for the super-Tonks-Girardeau gas. The circles show the transition from the TF to the TG regime ($g_{1D} > 0$, same data as in Fig. 5.8 for $\gamma > 1$). The solid (dashed) line presents the theoretical data for $g_{1D} > 0$ ($g_{1D} < 0$) by Astrakharchik et al.[Ast05]. The dotted line corresponds to the model of hard rods. For reference, the measurements for $g_{1D} < 0$ are numbered. Data points 1c to 6 are taken at $\omega_D = 2\pi \times 115.6(3)$ Hz. For data points 1a and 1b the trap frequency is $\omega_D = 2\pi \times 22.4(1)$ Hz and $\omega_D = 2\pi \times 52.3(1)$ Hz, respectively. For all measurements in the sTG regime $a_\perp = 1346(5)$ a_0. **B**, The parameters a_{3D} (dashed-dotted), a_{1D} (solid), and g_{1D} (dashed) are plotted in the vicinity of the Feshbach resonance (FR) at 47.78(1) G. The horizontal dotted line indicates the value of $a_\perp/C$. The pole of the CIR is at 47.36(2) G. a_{1D} has a pole (P) at 47.96(2) G. The bell-shaped curve at the bottom left indicates the atomic distribution as a function of the magnetic field determined from high-resolution microwave spectroscopy.

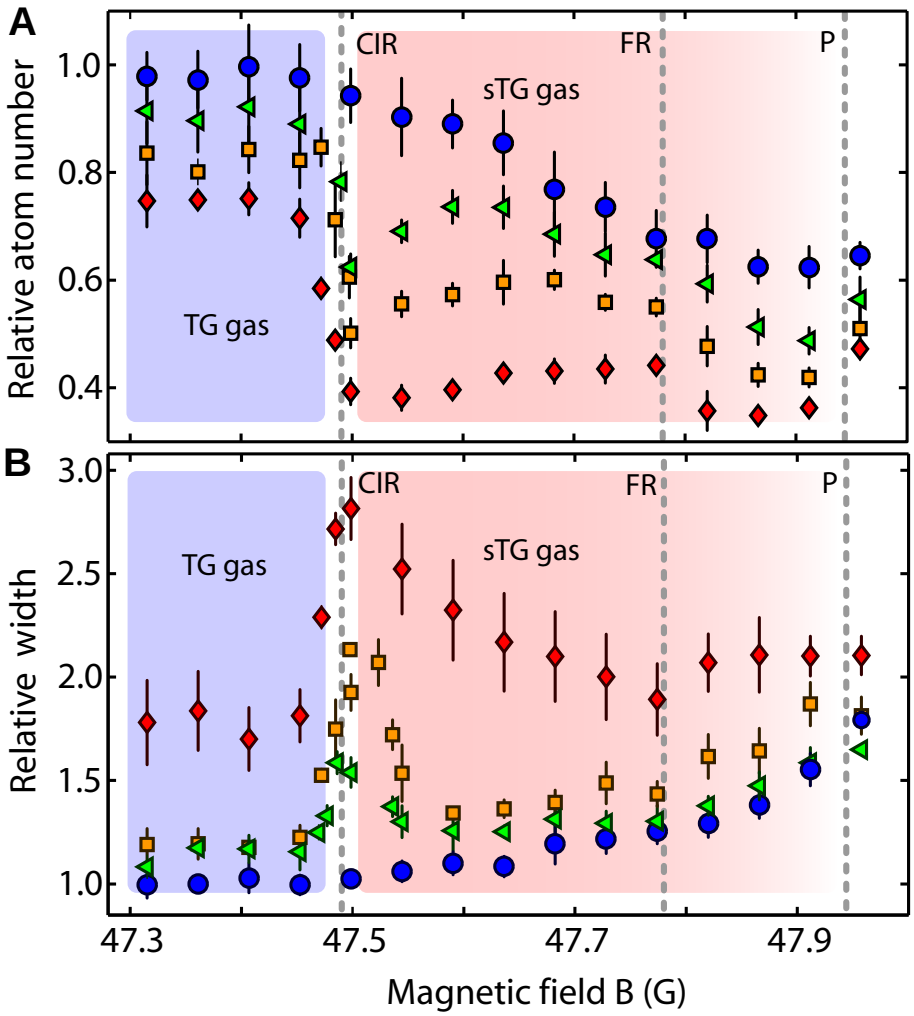

Fig. 5.10.: (color online) Stability and kinetic energy in the TG and sTG regimes. **A**, relative number of atoms remaining and **B**, relative $1/e$-width along the axial direction after 10 ms expansion, after a hold time τ = 10, 50, 100, and 200 ms (circles, triangles, squares, and diamonds, respectively) at a given magnetic field B. The position of the CIR, the pole of the Feshbach resonance (FR), and the pole for a_{1D} (P) are as indicated. For these measurements $a_\perp = 1523(6)$ a_0 and $\omega_D = 2\pi \times 115.6(3)$ Hz. The atom number is normalized to the initial value of $1.7(1) \times 10^4$ and the width is normalized to the initial value in the TG regime.

5.4. Publication: Pinning quantum phase transition for a Luttinger liquid of strongly interacting bosons

Nature **466**, 597 (2010)†

Elmar Haller[1], Russell Hart[1], Manfred J. Mark[1], Johann G. Danzl[1], Lukas Reichsöllner[1], Mattias Gustavsson[1], Marcello Dalmonte[2,3,4,5], Guido Pupillo[2,3], and Hanns-Christoph Nägerl[1]

[1] *Institut für Experimentalphysik und Zentrum für Quantenphysik, Universität Innsbruck, Technikerstraße 25, A-6020 Innsbruck, Austria*
[2] *Institut für Theoretische Physik, Universität Innsbruck, Technikerstraße 25, A-6020 Innsbruck, Austria*
[3] *Institut für Quantenoptik und Quanteninformation der Österreichischen Akademie der Wissenschaften, Technikerstraße 21a, A–6020 Innsbruck, Austria*
[4] *Dipartimento di Fisica dell'Università di Bologna, via Irnerio 46, 40127 Bologna, Italy*
[5] *Istituto Nazionale di Fisica Nucleare, via Irnerio 46, 40127 Bologna, Italy*

One of the most remarkable results of quantum mechanics is the fact that many-body quantum systems may exhibit phase transitions even at zero temperature [Sac00]. Quantum fluctuations, deeply rooted in Heisenberg's uncertainty principle, and not thermal fluctuations, drive the system from one phase to another. Typically, the relative strength of two competing terms in the system's Hamiltonian is changed across a finite critical value. A well-known example is the Mott-Hubbard quantum phase transition from a superfluid to an insulating phase [Jak98, Gre02a], which has been observed for weakly interacting bosonic atomic gases. However, for strongly interacting quantum systems confined to lower-dimensional geometry a novel type of quantum phase transition may be induced for which an arbitrarily weak perturbation to the Hamiltonian is sufficient to drive the transition [Gia03, Gog98]. Here, for a one-dimensional (1D) quantum gas of bosonic caesium atoms with tunable interactions, we observe the sine-Gordon quantum phase transition from a superfluid Luttinger liquid to a Mott-insulator [Büc03, Pok79]. For sufficiently strong interactions, the transition is induced by adding an arbitrarily weak optical lattice commensurate with the atomic granularity, which leads to immediate pinning of the atoms. We map out the phase diagram and find that our measurements in the strongly interacting regime agree well with a quantum field description based on the exactly solvable sine-Gordon model [Col75]. We trace the phase boundary all the way to the weakly interacting regime where we find good agreement with the predictions of the 1D Bose-Hubbard model. Our results open up the experimental study of quantum phase transitions, criticality, and transport phenomena beyond Hubbard-type models in the context of ultracold gases.

†The author of the present thesis contributed to this work by maintaining and improving the experimental setup and paper writing.

5.4.1. Introduction

Ultracold atomic gases are a versatile tunable laboratory system for the investigation of complex many-body quantum phenomena [Blo08]. The study of quantum phases and quantum phase transitions is greatly enriched by the possibility to independently control the kinetic energy and the interactions. In deep optical lattice potentials the many-body dynamics for a weakly interacting gas is, to a very good approximation, governed microscopically by a Hubbard Hamiltonian [Jak98] with a local onsite interaction energy U and kinetic energy J, which corresponds to tunneling of atoms from one lattice site to the next. Experiments with Bose-Einstein condensates (BEC) of Rb atoms have demonstrated the quantum phase transition from a superfluid phase for large J to an insulating Mott-Hubbard (MH) phase [Gre02a]. The transition between these two phases was obtained by quenching J in a lattice of finite depth. Recent experiments with fermionic atoms have demonstrated the presence of a fermionic MH insulating state [Jör08, Sch08], potentially opening the way to the study of high-temperature superconductivity in proximity of the MH phase in 2D.

While the focus in the study of quantum phase transitions in the context of ultracold atoms has so far been on Hubbard-type physics in the weakly interacting regime, novel quantum phenomena occur in lower dimensions, where the effects of quantum fluctuations and correlations are enhanced. In a 1D bosonic gas, strong repulsive interactions lead to the formation of a Tonks-Girardeau (TG) gas, where bosons minimize their interaction energy by avoiding spatial overlap and acquire fermionic properties [Gir60, Kin04, Par04, Hal09]. The addition of an arbitrarily weak lattice potential commensurate with the atomic density, i.e. $n \sim 2/\lambda$, where n is the linear 1D density and $\lambda/2$ is the lattice periodicity, is expected to lead to a novel kind of quantum phase transition [Gia03, Büc03]: the strongly correlated 1D gas is immediately pinned by the lattice and the superfluid TG phase is turned into an insulating, gapped phase. Figure 5.11 contrasts the Hubbard-type superfluid-to-Mott-insulator transition to this pinning transition. Given the universality of 1D quantum physics, the pinning transition will occur for interacting bosons as well as for fermions in 1D and has been discussed with respect to a variety of quantum models in low dimensions [Gia03].

5.4.2. The pinning transition

The pinning transition is described by the (1+1) quantum sine-Gordon (sG) model, which is an exactly solvable quantum field theory, extensively studied in high energy, condensed matter, and mathematical physics [Gog98]. The sG Hamiltonian reads

$$\mathcal{H} = \frac{\hbar v_s}{2\pi} \int dx[(\partial_x\theta)^2 + (\partial_x\phi)^2 + \mathcal{V}\cos(\sqrt{4K}\theta)]. \tag{5.2}$$

Here, $\partial_x\theta$ and $\partial_x\phi$ are the fluctuations of the long-wavelength density and phase fields θ and ϕ, respectively, of the hydrodynamic description of the 1D liquid

with commutation relation $[\partial_x\theta(x), \phi(y)] = i\pi\delta(x-y)$, v_s is the velocity of the soundlike excitations of the 1D gas, $\mathcal{V} = Vn\pi/(\hbar v_\mathrm{s})$ is proportional to the depth V of a weak lattice [Gia03, Büc03], and $\hbar$ is Planck's constant h divided by 2π. For vanishing lattice $\mathcal{V} = 0$, Eq. (5.2) describes a Luttinger liquid, where the strength of interactions is parameterized by the dimensionless parameter $K = \hbar\pi n/(mv_\mathrm{s})$, which determines the long-distance power-law decay of the correlation functions, e.g. $\langle n(x)n(x')\rangle \sim n^2 + cK/(x-x')^2 + c'\cos(2\pi n * (x - x'))/(x-x')^{2K} + \ldots$, with c and c' constants and m the atomic mass. The sG model with a weak but finite lattice predicts a quantum phase transition of the Berezinskii-Kosterlitz-Thouless (BKT) type between a superfluid state for $K > K_\mathrm{c} = 2$, where the shallow lattice is an irrelevant perturbation, to an insulating Mott phase for $K < K_\mathrm{c}$, for which the spectrum is gapped for any value of $\mathcal{V}$.

While in general K is a phenomenological parameter, in the case of a 1D bosonic gas it can be microscopically related to the Lieb-Liniger parameter $\gamma = mg/(\hbar^2 n)$, which characterizes interactions in a homogenous 1D system [Lie63] (see Methods). Here, $g \simeq 2\hbar\omega_\perp a_\mathrm{3D}$ is the coupling constant of the 1D δ-function interaction potential $U(x) = g\delta(x)$, where $\omega_\perp$ is the frequency of transverse confinement and a_3D is the 3D scattering length. The strength of interactions, and thus K, can be tuned by varying a_3D near a Feshbach resonance [Chi10]. The TG regime corresponds to $\gamma \gg 1$. Using the relation between K and γ, Büchler and coworkers [Büc03] have shown that particles are pinned for experimentally accessible values of $\gamma > \gamma_\mathrm{c} \simeq 3.5$ in the limit of a vanishingly weak lattice. The pinning transition is expected to continuously transform into the MH-type quantum phase transition, which occurs for the weakly interacting gas when the lattice depth becomes sufficiently large. Here, using a quantum gas of caesium (Cs) atoms with tunable interactions confined to an array of independent 1D tubes (see Methods), we drive the superfluid-to-Mott-insulator phase transition by varying γ and determine the phase boundary all the way from the strongly to the weakly interacting regime using modulation spectroscopy and measurement of transport. For shallow lattices under conditions of commensurability, we observe immediate pinning of the particles for strong interactions when $\gamma > \gamma_\mathrm{c}$.

5.4.3. Experimental procedure

We first discuss our experiments in the strongly interacting regime. We start with a 3D Bose-Einstein condensate (BEC) of typically 1.3×10^5 Cs atoms without detectable thermal fraction in a crossed-beam dipole trap with magnetic levitation [Kra04] and initialize our system by creating a conventional 3D MH-state in a deep 3D lattice at $U/(6J) \approx 75$ with precisely one atom per lattice site [Gre02a]. We find, by reversing the loading, that the procedure does not lead to heating of the sample. The array of 1D tubes is obtained by reducing the lattice depth V along one direction. Our procedure ensures that a majority of tubes has a near-commensurate number density (see Methods). A Feshbach resonance allows us to control a_3D with a precision of 3 a_0 limited

by the presence of the magnetic field gradient. Here, a_0 is Bohr's radius. For the case of the shallow lattice, we probe the state of the system by amplitude modulation spectroscopy [Stö04, Iuc06]. We determine the presence of an excitation gap E_g by testing whether energy can be deposited into the 1D system at a given excitation frequency f. The lattice depth V is modulated at f by 25% to 45% for $40-60$ ms. After ramping down the lattice beams adiabatically with respect to the lattice band structure and after a levitated expansion time of $40-60$ ms [Kra04], we detect the atoms by time-of-flight absorption imaging. We determine the spatial width of the atomic sample from a gaussian fit to the absorption profile and obtain the change δ of the spatial width compared to the unmodulated case as a function of f. Two typical measurements are shown in Fig. 5.12(a), one in the superfluid phase and one deep in the 1D Mott phase at the same value for the lattice depth, $V = 1.5(1)E_R$, where $E_R = h^2/(2m\lambda^2)$ is the photon recoil energy. For weak interactions the system exhibits a linear increase for δ as a function of f, which we attribute to the superfluid character of the gas. For strong interactions, the increase, after a slow rise, shows a clear kink. We attribute the initial slow rise to excitation of residual superfluid portions of our inhomogeneous system and the sudden change in slope to the presence of an excitation gap. We associate the axis intercept f_g obtained from a linear fit to the steep part of the spectrum with the frequency of the gap. To determine the phase transition from the 1D Mott state to the superfluid state, we repeat this measurement for a given depth V as we scan γ by changing a_{3D}. A typical result is shown in Fig. 5.12(c). The gap closes as γ is reduced. For values $V \leq 2.0E_R$, the transition point is identified with the abrupt step, i.e. we determine the critical value $\gamma_{c,V}$ at which the transition happens by an error-function fit to the data. Note that we always observe some small residual value for f_g of about 120 Hz for weak interactions. In general, we find that the measured value for the frequency of the gap is robust against variations of modulation amplitude, while the slope increases with stronger modulation.

For comparison, we present in Fig. 5.12(b) and (d) excitation spectra for an intermediate value of the lattice depth and for the case of a deep lattice, respectively. For $V = 3.0(2)E_R$ the spectrum shows additional structure for high frequencies as band structure comes into play. We find that for $V > 2.0E_R$ the gap opens up approximately linearly as a function of γ beyond a critical $\gamma_{c,V}$, see inset to Fig. 5.12(c). For deep lattices and for comparatively weak interactions the spectrum exhibits a broad distribution characteristic of a superfluid. For stronger interactions we recover the discrete excitation spectrum of the Mott phase in the Hubbard regime [Gre02a, Stö04] with a pronounced peak at $f = 1.0\ U/h$. Additional peaks [Cla06b] can be found at $f = 0.5\ U/h$ and above $f = 1.5\ U/h$.

For the case of a deep lattice, we find that the state of the system is very sensitively probed by transport measurements [Fer05, Mun07]. A characteristic property of the Mott state is the inhibition of particle motion. In our experiment with the capability to tune interactions we expect the phase transition to manifests itself, at fixed V, through a strong suppression of transport when the

strength of the interaction is raised above a certain critical value. Essentially, we test whether momentum can be imparted to the 1D system as a function of interaction strength. For a given V we apply a weak axial magnetic force for a brief time to the interacting system, chosen such that the imparted momentum would be approximately $0.2\hbar k$ if the system were non-interacting. Then, as a function of a_{3D}, we determine the center-of-mass displacement x_0 of the sample after a fixed time of flight. Fig. 5.13 shows that x_0 decreases monotonically with a_{3D}. For the case of a deep lattice with $V = 9.0(5)E_R$ the quenching of transport is abrupt. At a certain critical value for a_{3D} transport is fully inhibited [Alt05, Sch10]. We find the critical a_{3D} by a linear fit to the decreasing data and by determining the axis intercept and derive from this a critical $\gamma_{c,V}$. Reducing the lattice depth to $V = 5.0(3)E_R$ and $V = 2.0(1)E_R$ leads to a less abrupt quenching of transport. For stronger interactions, the decrease starts to level off. Nevertheless, the initial decrease is still linear, allowing us to determine the critical $\gamma_{c,V}$ by an extrapolation of the initially linear decrease to zero. The inset to Fig. 5.13 shows the measured critical ratio $(U/J)_c$ determined by our transport method as a function of lattice depth V. When we compare our results with the predicted value [Rap99] of $(U/J)_c \approx 3.85$ for the transition in 1D, we find a slight systematic overestimation of the transition point. This, however, is expected in view of e.g. the spatial inhomogeneity of the sample and the BKT-type nature of the transition in a finite size system.

5.4.4. Phase diagram

We summarize our results in Fig. 5.14, where we present the phase diagram as a function of $1/\gamma$ and V. The set $\{\gamma_{c,V}\}$ defines the phase boundary between the 1D Mott insulator and the 1D superfluid. The measurements based on modulation spectroscopy cover a range from $V = 4E_R$ down to $0.5E_R$ (circles), while the transport measurements extend from $V = 2E_R$ to $10E_R$ (squares). In the weakly interacting regime, $1/\gamma > 2$, our data are in good agreement with the prediction of the MH model (dashed line). In the strongly interacting regime, $1/\gamma < 1$, the measured phase boundary extrapolates to a finite critical value $1/\gamma_c$ for the Lieb-Liniger parameter as the lattice depth V is reduced to zero. Our results are in excellent quantitative agreement with the theory for a commensurate system based on the sine-Gordon model (solid line, see Methods), for which $\gamma_c = 3.5$. We also find good agreement between our two types of measurement techniques in the intermediate regime ($V = 2E_R$ to $4E_R$). Our results demonstrate the striking consequence of strong interactions in 1D geometry in the presence of a lattice: Beyond a critical value γ_c, an insulating Mott state exists for vanishingly small lattice depth V. The particles are immediately pinned by the lattice.

We measure a finite gap energy E_g for $\gamma > \gamma_c$ in the regime of a shallow lattice. In the limit of $\gamma \to \infty$ and $V \to 0$ one would expect the simple relation $E_g = V/2$ as the bosonic system has become fully fermionized and the lattice effectively induces a band insulator of fermions [Büc03]. In the inset to Fig. 5.14 we plot the measured E_g as a function of V at fixed $\gamma = 11(1)$. For $V < 1E_R$

our data is in good agreement with the analytical result for the gap energy at finite γ (see Methods). Note that, for $V \geq 1E_{\mathrm{R}}$, we observe a deviation for E_{g} away from the predicted values. This deviation occurs at rather shallow lattices. However, one does expect the curve to have a reduced slope for deeper lattices, for which E_{g} becomes of order U and is only weakly dependent on V.

Our results are a benchmark realization of quantum field theory models with tunable parameters in cold atomic systems. These results open up the experimental study of the out-of-equilibrium properties of sine-Gordon-type models. In particular, thermalization in integrable models beyond the Luttinger liquid model, quenches across quantum phase transitions, and their relations to the breakdown of the adiabatic theorem in low dimensions can now be investigated with full tunability of system parameters.

5.4.5. Methods Summary

Sample preparation.

We begin with a BEC with no detectable thermal fraction of typically 1.3×10^5 Cs atoms in the $|F=3, m_F=3>$ hyperfine ground state in a crossed-beam dipole trap with magnetic levitation. Details of the BEC preparation are presented elsewhere [Kra04]. The BEC is adiabatically transferred to the 3D lattice by exponentially ramping up the power in the lattice laser beams within 300 ms. We create a 3D Hubbard-type Mott insulator with precisely one atom per site in the central region of the trap by adjusting the external dipole trap confinement prior to loading into the lattice. The array of vertically oriented tubes is created by ramping down the power in the vertically propagating beam pair. Typical trapping frequencies for the tubes are $\omega_{r,z} = 2\pi \times (12300(200), 21.9(3))$ Hz along the transversal and longitudinal directions, respectively.

It is not necessary to strictly adhere to the commensurate density condition to observe the pinning transition at very weak lattices [Büc03]. However, we prepare our sample such that the commensurability condition is on average best fulfilled over the inhomogeneously populated array of tubes. We find this optimal configuration when the total atom number is chosen such that the peak density of the center tube is approximately 1.2 n_{c}, where $n_{\mathrm{c}} = 2/\lambda$ is the commensurate 1D density. Typically there are about 60 atoms in the center tube.

Phase transition line.

For the case of a 1D Bose gas in a weak optical lattice the effective sine-Gordon Hamiltonian Eq. (5.2) is realized. In this regime, the BKT transition line between the superfluid and the Mott-insulating phases can be derived in terms of V and $\gamma = \gamma_{\mathrm{c},V}$ as

$$\frac{V}{E_{\mathrm{R}}} = 2\left(\frac{\pi}{\sqrt{\gamma - \gamma^{3/2}/(2\pi)}} - 2\right).$$

When the system is weakly interacting, $\gamma \ll 1$, and for deeper lattices, $V \gg 1E_{\mathrm{R}}$, the system can be described by the Bose-Hubbard Hamiltonian [Jak98]. In this

regime, the quantum phase transition between a superfluid and a MH state occurs at [Rap99] $(U/J)_{\mathrm{c}} \approx 3.85$, which determines a transition line in the (V, γ) - plane via

$$\frac{4V}{E_{\mathrm{R}}} = \ln^2 \left[\frac{2\sqrt{2}\pi}{\gamma} \left(\frac{U}{J} \right)_{\mathrm{c}} \sqrt{\frac{V}{E_{\mathrm{R}}}} \right].$$

Here, J is the hopping energy, and U is onsite interaction energy of the Bose-Hubbard model.

We thank W. Zwerger for discussions. We are indebted to R. Grimm for generous support. We gratefully acknowledge funding by the Austrian Ministry of Science and Research (Bundesministerium für Wissenschaft und Forschung, BMWF) and the Austrian Science Fund (Fonds zur Förderung der wissenschaftlichen Forschung, FWF) in form of a START prize grant and by the European Union through the STREP FP7-ICT-2007-C project NAME-QUAM (Nanodesigning of Atomic and MolEcular QUAntum Matter) and within the framework of the EuroQUASAR collective research project QuDeGPM. R.H. is supported by a Marie Curie International Incoming Fellowship within the 7th European Community Framework Programme.

5.4.6. Methods

1D Bose gas in a weak optical lattice

In the absence of the optical lattice, $V = 0$, the Luttinger liquid parameter K can be expressed in terms of the Lieb-Liniger parameter $\gamma = gm/(\hbar^2 n)$ for all strengths of interactions [Lie63, Caz04]. For $\gamma \leq 10$ and $\gamma \gg 10$ one gets $K \simeq \pi/\sqrt{\gamma - \gamma^{3/2}/(2\pi)}$ and $K \simeq (1 + 2/\gamma)^2$, respectively. The addition of a weak but finite commensurate optical lattice with $V \leq 1E_{\mathrm{R}}$ realizes the effective sine-Gordon Hamiltonian Eq. (5.2). Using a perturbative renormalization group approach, the BKT transition line between the superfluid and the Mott-insulating phases can be derived in terms of V and $\gamma = \gamma_{\mathrm{c},V}$ as

$$\frac{V}{E_{\mathrm{R}}} = 2\left(\frac{\pi}{\sqrt{\gamma - \gamma^{3/2}/(2\pi)}} - 2\right).$$

For small lattice depths, the integrable structure of the sine-Gordon model [Zam79, Zam95] allows one to derive the following analytical expression for the dependence of the spectral gap E_{g} on V and K

$$\frac{E_{\mathrm{g}}}{E_{\mathrm{R}}} = \frac{8\Gamma[\frac{\pi K}{2(2-K)}]}{\sqrt{\pi}\Gamma[\frac{1}{2}\frac{2+K(\pi-1)}{2-K}]}\left[\left(\frac{K^2 V}{16E_{\mathrm{R}}}\right)\frac{\Gamma[1-\frac{K}{2}]}{\Gamma[1+\frac{K}{2}]}\right]^{\frac{1}{2-K}}.$$

Here, Γ is the gamma function. For strong interactions $K \simeq 1$, the dependence of the gap on V is linear, and E_{g} approaches the free fermion value $E_{\mathrm{g}} = V/2$. In the vicinity of $K = 2$, the gap closes exponentially approaching the BKT transition line.

Deep lattice: the Bose-Hubbard model

In the weakly interacting regime $\gamma \ll 1$, for $V \gg 1E_{\mathrm{R}}$, when all atoms occupy the lowest vibrational state in each potential well of the lattice, the system can be described by the following Bose-Hubbard model [Jak98]

$$H = -J\sum_i (b_i^\dagger b_{i+1} + h.c.) + \frac{U}{2}\sum_i b_i^\dagger b_i^\dagger b_i b_i.$$

Here, b_i ($b_i^\dagger$) is the operator destroying (creating) a bosonic particle at the position of the i^{th}-well, $J = 4E_{\mathrm{R}}(V/E_{\mathrm{R}})^{\frac{3}{4}}\exp[-2\sqrt{V/E_{\mathrm{R}}}]/\sqrt{\pi}$ is the hopping energy, and $U = \sqrt{2\pi}g(V/E_{\mathrm{R}})^{1/4}/\lambda$ is onsite interaction energy. The quantum phase transition between a superfluid and a MH state occurs at [Rap99] $(U/J)_{\mathrm{c}} \approx 3.85$, which determines a transition line in the (V, γ) - plane via

$$\frac{4V}{E_{\mathrm{R}}} = \ln^2\left[\frac{2\sqrt{2}\pi}{\gamma}\left(\frac{U}{J}\right)_{\mathrm{c}}\sqrt{\frac{V}{E_{\mathrm{R}}}}\right].$$

Magnetic Feshbach resonance

The strength of interaction can be tuned by means of a broad magnetic Feshbach resonance with a pole at -11.7 G and with a zero crossing for the scattering length near 17 G [Kra04]. To hold the atoms in the vertically oriented tubes, magnetic levitation by means of a magnetic field gradient is applied. For a cesium atom in the hyperfine state $|F = 3, m_F = 3 >$ a magnetic field gradient of 31.1 G/cm cancels the gravitational force.

Lattice loading and array of 1D tubes

We create a 3D optical lattice by interference of 3 pairs of counterpropagating dipole trap laser beams at wavelength $\lambda = 1064.5$ nm with $1/e^2$ beam waists of ~ 350 μm. The atomic BEC, initially trapped in a crossed-beam dipole trap, is adiabatically transferred to the 3D lattice by exponentially ramping up the power in the lattice laser beams within 300 ms. At the same time we increase the interaction strength by linearly raising the magnetic field strength and finally reach a 3D Hubbard-type Mott insulator with precisely one atom per site in the central region. The array of vertically oriented tubes is created by linearly ramping down the power in the vertically propagating beam pair in 100 ms reaching lattice depths from 10 to 0.5 E_R. At the same time we linearly reduce the magnetic field strength to set $a_{3\mathrm{D}}$. Typical trapping frequencies for the tubes are $\omega_{r,z} = 2\pi \times (12300(200), 21.9(3))$ Hz along the transversal and longitudinal directions, respectively. The depth of the lattice along the tubes is calibrated by the pulsed Raman-Nath technique [Gou86]. The transversal trapping frequencies of the tubes are determined by parametric heating measurements. The distribution of the atom number per tube can be directly determined from the density distribution in the Mott-insulating phase and shows an occupation of about 60 atoms in the center tube. Here, we assume a constant filling factor of one atom and no thermal or superfluid components. In view of our inhomogeneous system we calculate γ, for a given tube, by assuming a 1D Thomas-Fermi distribution and taking the center density. The reported γ is a weighted average over all tubes.

Commensurability

To observe the pinning transition it is not necessary to fulfill the condition of commensurability precisely [Büc03]. A finite commensurability parameter $Q = 2\pi(n - n_{\mathrm{c}})$ corresponds to a shift $\delta\mu$ of the chemical potential. Here, $n_{\mathrm{c}} = 2/\lambda$ is the commensurate 1D density. The system stays locked to the Mott insulating phase as long as $\delta\mu$ remains smaller than the energy necessary to add another atom. When Q rises beyond a critical value $Q_{\mathrm{c}}(\gamma, V)$, the system develops finite density excitations, which destroy the long range order of the Mott insulator. We find that, for the array of 1D tubes, the commensurability condition in the superfluid regime is fulfilled best when the total atom number is chosen in such a way that the peak density of the center tube is approximately

1.2 n_c.

Modulation parameters and error bars.

For the data in Fig. 5.12 **a, b, d** we chose the following modulation times and amplitudes: **a** 40 ms, 35%, **b** 40 ms, 30%, **d** 30 ms, 35% for the superfluid phase and 25% for the Mott phase. In Fig. 5.12 **a, b, d**, the error bars for δ reflect the 1σ statistical error. In Fig. 5.12 **c**, the error bars for f_g are derived from the 1σ error on the fit parameters. The error for γ results from the 1σ statistical error of the independent input variables and the spread of γ due to the distribution of tubes. For the data in Fig. 5.14 the error in γ is derived from the 1σ error of the fit parameters for the modulation measurements. For the transport measurements, the error in γ results from the 1σ statistical error of the independent input variables and the spread of γ due to the distribution of tubes.

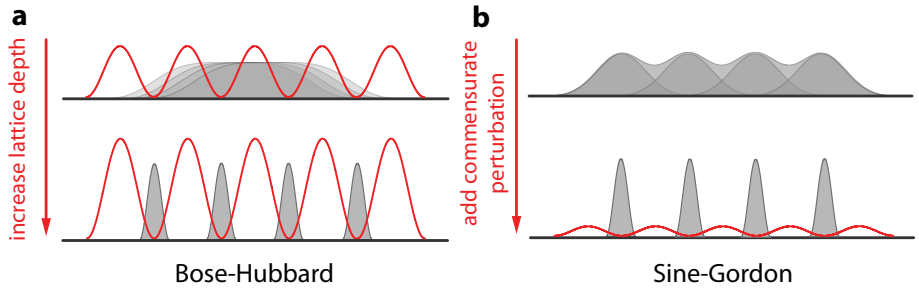

Fig. 5.11.: Comparing two types of superfluid-to-Mott-insulator phase transitions in 1D. Schematic density distributions (grey) in the presence of a periodic potential (red solid line). **a**, Mott-Hubbard type quantum phase transition for weak interactions [Gre02a]. The system is still superfluid at finite lattice depth (top). The transition to the insulating state is induced by raising the lattice depth above a finite critical value (bottom). **b**, Sine-Gordon type quantum phase transition for strong interactions [Büc03]. In the absence of any perturbation, the system is a strongly correlated superfluid (top). For sufficiently strong interactions, not necessarily infinitely strong, an arbitrarily weak perturbation by a lattice potential commensurate with the system's granularity induces the transition to the insulating Mott state (bottom).

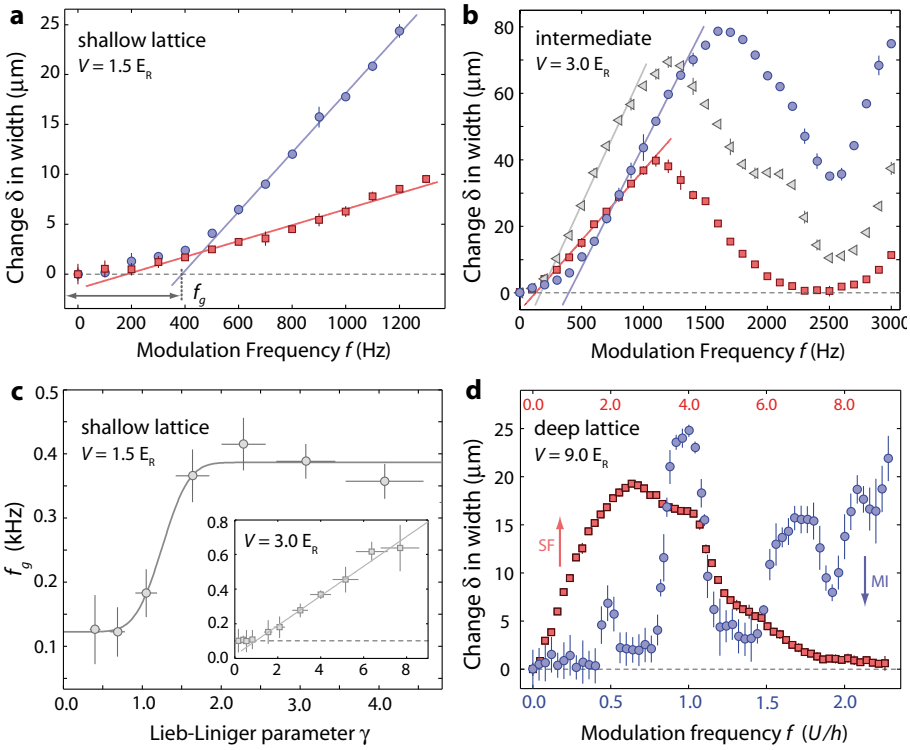

Fig. 5.12.: Modulation spectroscopy on bosons in 1D. a, b, d, Excitation spectra for low, intermediate, and high lattice depth V. The change δ of the spatial width after amplitude modulation is plotted as a function of the modulation frequency f for different values of γ. **a**, Characteristic spectra for $V = 1.5(1)E_{\mathrm{R}}$ in the superfluid (squares, $a_{3\mathrm{D}} = 115(2)\ a_0$, $\gamma = 1.0(1)$) and in the Mott regime (circles, $a_{3\mathrm{D}} = 261(2)\ a_0$, $\gamma = 3.1(2)$). The solid lines are linear fits to the high-frequency part of the spectrum. We determine the axis intercept f_{g} as indicated. **b**, Spectra for $V = 3.0(2)E_{\mathrm{R}}$. The system is superfluid at $\gamma = 0.51(6)$ (squares), while it exhibits a gap for $\gamma = 1.6(1)$ (triangles) and $\gamma = 4.1(3)$ (circles). **c**, Determination of the transition point for the case of the shallow lattice with $V = 1.5(1)E_{\mathrm{R}}$. The frequency f_{g} is plotted as a function of γ. The solid line is an error-function fit to the data. The inset plots f_{g} as a function of γ for $V = 3.0(2)E_{\mathrm{R}}$. **d**, Spectra for $V = 9.0(5)E_{\mathrm{R}}$ for weak (squares, $\gamma = 0.10(3)$) and strong (circles, $\gamma = 8.1(4)$) interactions in the superfluid (SF) and Mott insulator (MI) regimes. Here, f is in units of U. Modulation parameters and errors bars are discussed in the Methods.

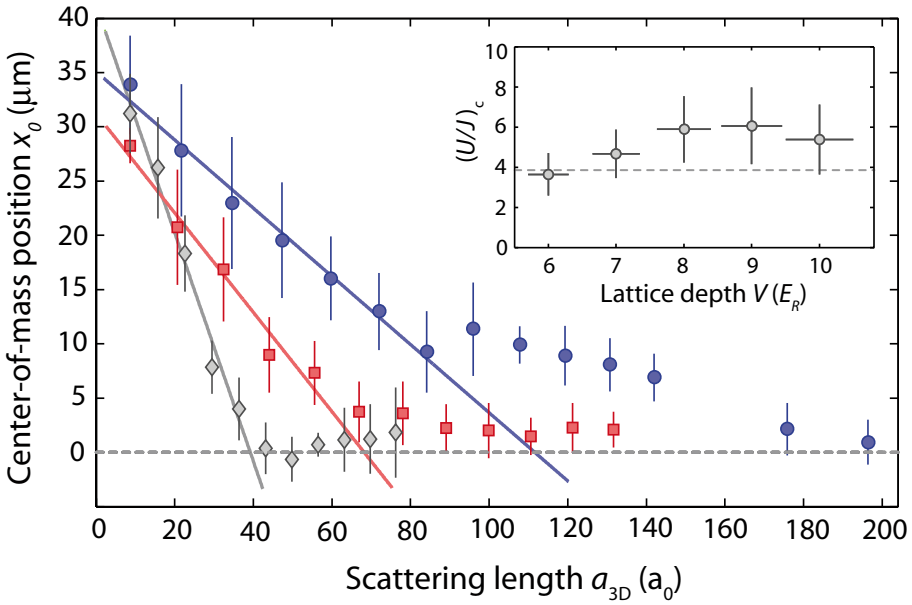

Fig. 5.13.: Transport measurements on the 1D Bose gas. Center-of-mass displacement x_0 as a function of a_{3D} for different values of V ($V = 9.0(5)E_R$ (diamonds), $V = 5.0(3)E_R$ (squares), $V = 2.0(1)E_R$ (circles)). We extrapolate the linear slope at small values for a_{3D} and associate the transition point with the axis intercept. For the data with $V = 2.0(1)E_R$ transport is not fully quenched as the condition of commensurability is not fulfilled for all atoms. All errors are the 1σ statistical error. The inset plots the mesured critical ratio $(U/J)_c$ at the transition point as a function of lattice depth V. The dashed line indicates the theoretical result $(U/J)_c \approx 3.85$ for the 1D Bose-Hubbard regime [Rap99].

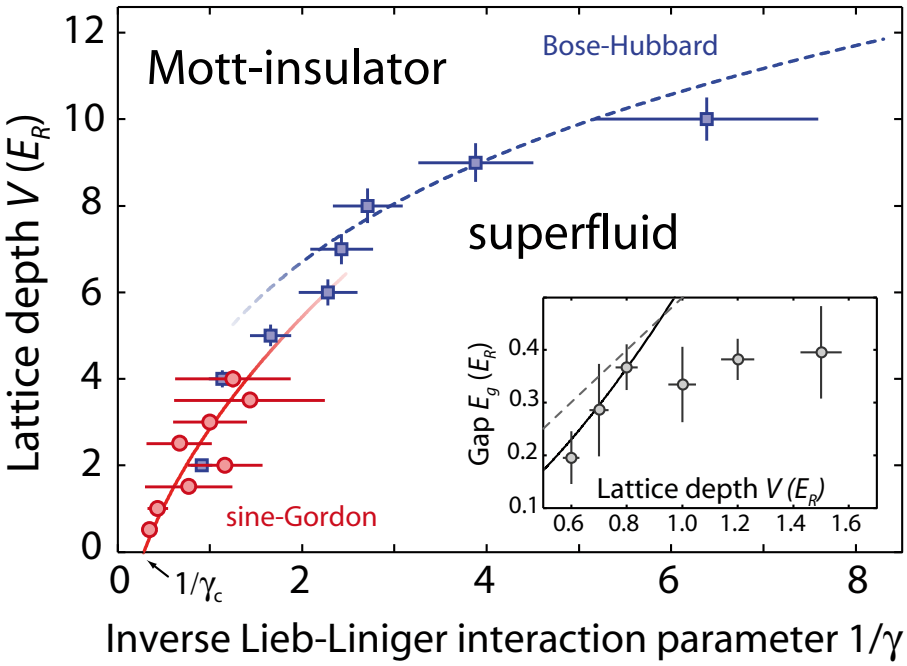

Fig. 5.14.: Phase diagram for the strongly interacting 1D Bose gas. Superfluid and Mott insulating phases in 1D versus inverse Lieb-Liniger interaction parameter $1/\gamma$ and optical lattice depth V in units of the photon recoil energy E_R. The critical interaction parameter is γ_c. For strong interactions and shallow lattices we determine the transition by amplitude modulation spectroscopy (circles). For weak interactions and deep lattices we probe the phase boundary by transport measurements (squares). The solid (dashed) line is the prediction from the sine-Gordon (Bose-Hubbard) model. Error bars are discussed in the Methods. The inset plots the measured gap energy $E_\mathrm{g} = hf_\mathrm{g}$ as a function of V for $\gamma = 11(1)$ and compares our data to the analytical result for finite γ as given by the sine-Gordon model (solid line, see Methods). Also shown is the universal behavior $E_\mathrm{g} = V/2$, which is valid for non-interacting fermions (dashed line).

5.5. Publication: Three-body correlation functions and recombination rates for bosons in three and one dimensions

Physical Review Letters **107**, 230404 (2011)†

Elmar Haller[12], Mohamed Rabie[1], Manfred J. Mark[1], Johann G. Danzl[1], Russel Hart[1], Katharina Lauber[1], Guido Pupillo[23], and Hanns-Christoph Nägerl[1]

[1] *Institut für Experimentalphysik und Zentrum für Quantenphysik, Universität Innsbruck, Technikerstraße 25, A-6020 Innsbruck, Austria*
[2] *Institut für Quantenoptik und Quanteninformation der Österreichischen Akademie der Wissenschaften, Technikerstraße 21a, A–6020 Innsbruck, Austria*
[3] *Institut für Theoretische Physik, Universität Innsbruck, Technikerstraße 25, A-6020 Innsbruck, Austria*

We investigate local three-body correlations for bosonic particles in three and one dimensions as a function of the interaction strength. The three-body correlation function $g^{(3)}$ is determined by measuring the three-body recombination rate in an ultracold gas of Cs atoms. In three dimensions, we measure the dependence of $g^{(3)}$ on the gas parameter in a BEC, finding good agreement with the theoretical prediction accounting for beyond-mean-field effects. In one dimension, we observe a reduction of $g^{(3)}$ by several orders of magnitude upon increasing interactions from the weakly interacting BEC to the strongly interacting Tonks-Girardeau regime, in good agreement with predictions from the Lieb-Liniger model for all strengths of interaction.

†The author of the present thesis contributed to this work by maintaining and improving the experimental setup and paper writing.

5.5.1. Introduction

Correlation functions reflect the non-classical nature of quantum many-body systems. They may be used to characterize the latter when quantities such as temperature, density, dimensionality, and particle statistics are varied in experiments. It is particularly instructive to monitor a system's correlation functions as the strength of particle interactions is tuned from weak to strong. A paradigm is given by an ensemble of bosons in one-dimensional (1D) geometry with contact interactions [Caz11]: For weak repulsive interactions, in the zero-temperature limit, the system is a quasicondensate with essentially flat particle correlation functions in position space to all orders. For strong repulsive interactions, the bosons avoid each other, leading to loss of coherence and strong increase of local correlations. In the context of ultracold atomic gases, with exquisite control over temperature, density, and dimensionality [Blo08], tuning of interactions is enabled by Feshbach resonances [Chi10]. Local two- and three-body correlations in atomic many-body systems can be probed e.g. in measurements of photoassociation rates [Kin05] and of three-body recombination processes [Bur97, O'H04], respectively. Non-local two-body correlations for atomic matter waves have been measured in atom counting [Yas96, Ött05, Sch05, Jel07], noise-correlation [Gre05, Föl05, Rom06], and in-situ imaging [Jac11] experiments. Recently, also non-local three-body correlations have become accessible in experiments [Arm10, Hod11].

Recombination processes are sensitive to the properties of the many-body wave function at short distances. In particular, the process of three-body recombination, in which three particles collide inelastically to form a dimer, is directly connected to the local three-particle correlation function $g^{(3)} \equiv < \hat{\psi}^\dagger(x)^3 \hat{\psi}(x)^3 > /n^3$, which compares the probabilities of having three particles at the same position for a correlated and an uncorrelated system. Here, $\hat{\psi}^\dagger$ and $\hat{\psi}$ are atomic field operators and n is the density. The function $g^{(3)}$ depends strongly on quantum statistics [Bur97, Hod11] and temperature T [Khe03, Kor09, Kor11]. For example, in 3D geometry, statistics change the value of $g^{(3)}$ from zero for identical fermions to one for non-interacting classical particles and to six for thermal (non-condensed) bosons. For non-interacting bosons statistical bunching is suppressed in a Bose-Einstein condensate (BEC), for which $g^{(3)} = 1$. In addition, interactions also have a pronounced effect on $g^{(3)}$: In a 3D BEC, quantum depletion due to quantum fluctuations reduces the condensate fraction by increasing the number of occupied single-particle modes. In this case, beyond-mean-field calculations [Kag85] predict an increase of $g^{(3)}$ proportional to the square root of the gas parameter $(na_{3D}^3)^{1/2}$, where a_{3D} is the 3D s-wave scattering length. This increase of $g^{(3)}$ has never been seen experimentally and is in stark contrast to the behavior of 1D systems. In 1D geometry, bosons with repulsive interactions minimize their interaction energy by avoiding spatial overlap. For very strong repulsive interactions in the Tonks-Girardeau (TG) limit [Gir60, Kin04, Par04, Hal09, Caz11] a strong reduction of $g^{(3)}$ with a γ^{-6} scaling is predicted [Gan03]. Here, γ is the dimensionless Lieb-Liniger parameter, which characterizes interactions in a homogeneous 1D system [Caz11] (see 5.5.5

for suppl. material). Recently, $g^{(3)}$ has been calculated all the way from the weakly to the strongly interacting 1D regime for $T = 0$ [Che06b, Che06a] and also for $T \geq 0$ [Kor09, Kor11]. Experimentally, Laburthe Tolra *et al.* [O'H04] have observed a reduction of $g^{(3)}$ by a factor of about 7(5) for a weakly interacting gas of Rb atoms with $\gamma = 0.45$.

5.5.2. Experimental procedure

In this work we experimentally determine $g^{(3)}$ in 3D and in 1D geometry using a trapped ultracold gas of Cs atoms with tunable (repulsive) interactions. For a BEC in 3D geometry we find clear evidence for an increase of $g^{(3)}$ with increasing interaction strength, in good agreement with the prediction of Ref. [Kag85]. In 1D, for which we can tune γ from zero to above 100 [Hal09], we determine $g^{(3)}$ in the crossover regime from weak (1D BEC regime) to strong interactions (TG regime). Here our data agrees well with the prediction of Ref. [Che06b]. For strong interactions in the TG regime, our measurements show that $g^{(3)}$ is suppressed by at least three orders of magnitude. For high densities and strong interactions, we observe a rather sudden increase of three-body losses after long hold times in the trap. Understanding the behavior of $g^{(3)}$ at short and long times is an important step towards understanding integrability and thermalization in 1D systems [Kin06, Hof08].

A three-body loss process [Fed96, Chi10] consists of the collision of three particles, the formation of a dimer, and the release of the dimer's binding energy typically sufficient to allow both, the dimer and the remaining particle, to escape from the trap. The loss, assuming negligible one- and two-body loss, is modeled by the rate equation $\dot{n} = -\alpha K^{(3)} g^{(3)} n^3$. Here, we have explicitly split the loss rate coefficient $\alpha K^{(3)} g^{(3)}$ into its three contributions. The parameter $\alpha = 3$ describes a situation where exactly three particles are lost in each recombination event. In principle, secondary losses [Zac09] could modify its value. However, in the following we will be interested in *relative* measurements of $\alpha K^{(3)} g^{(3)^{(3)}}$, which are only weakly dependent on the precise value of α (see 5.5.5 for suppl. material), allowing us to neglect a possible deviation of α from the value of 3. The parameter $K^{(3)}$ contains the effect of few-body physics on the loss process [Chi10]. It depends on the probability of dimer formation (a process that can be strongly enhanced near Efimov resonances [Kra06]) and generally varies strongly with a_{3D} [Fed96, Esr99, Nie99, Bed00, Web03b]. For a_{3D} much larger than the range of the scattering potential, $K^{(3)}$ shows a generic a_{3D}^4 scaling. Contributions of many-body physics are contained in the three-particle distribution function $g^{(3)} n^3$. In what follows, we aim to measure $g^{(3)}$ as a function of a_{3D} both in 3D and 1D geometry.

We determine $K^{(3)} g^{(3)}$ from measurements of the decay of the total number of atoms $N(t)$ in our trap [Bur97, Web03b], which obeys the loss equation $\dot{N} = -3K^{(3)} g^{(3)} \int n^3(\mathbf{r}) d^3r$. Figures 5.15(a) and 5.16(c) show typical atom number measurements for 3D and 1D geometry. The data in 3D geometry is well fit by solutions to the loss equation. The determination of $K^{(3)} g^{(3)}$ depends critically

on an exact knowledge of the atomic density profile $n(\mathbf{r})$. In particular, particle loss and loss-induced heating of the sample [Web03b] can modify the density profile in a non-trivial way. Also, on long time scales evaporative losses might start to play a role. To avoid these complications we restrict ourselves to short time intervals, during which not more than 15% of the atoms are lost, and we determine the slope $\dot{N}(0)$ from a linear fit to the data. We determine $\int n^3(\mathbf{r})d^3r$ from a measurement of the total atom number N and the trap frequencies $\omega_{x,y,z}$ using interaction dependent models for $n(\mathbf{r})$ (see 5.5.5 for suppl. material). We find that the linear approximation underestimates $K^{(3)}g^{(3)}$ by approximately 12%, however, the data analysis is greatly simplified, especially in 1D. Finally, a comparative measurement of $K^{(3)}g^{(3)}$ allows us to eliminate $K^{(3)}$, as explained below, and to determine $g^{(3)}$ in 3D and 1D geometry.

5.5.3. Correlation function in 3D:

We measure $K^{(3)}g^{(3)}$ for both a non-condensed thermal sample and a BEC as a function of a_{3D}. For the thermal sample we start with typically 3.5×10^5 Cs atoms at a temperature of $T \approx 200$ nK. The peak density is about $n_0 = 1 \times 10^{14}$ cm^{-3}. In the BEC [Web03b, Kra04] we have about 9×10^4 Cs atoms without any detectable non-condensed fraction at about $n_0 = 5 \times 10^{13}$ cm^{-3}. We tune a_{3D} in the range from 50 a_0 to 800 a_0 by means of a broad magnetic Feshbach resonance [Web03b, Lan09] (a_0 is Bohr's radius). The magnetic field gradient needed to levitate the atoms against gravity [Web03b] introduces a slight (less than 5 a_0) variation of a_{3D} across the samples. We determine N by means of absorption imaging after a variable hold time t and 50 ms of expansion in the presence of the levitation field. We note that we do not observe the appearance of any non-condensed fraction in all measurements using the BEC. Figure 5.15(b) displays the ratio $K^{(3)}_{\rm th}g^{(3)}_{\rm th}/(K^{(3)}_{\rm BEC}g^{(3)}_{\rm BEC}) = g^{(3)}_{\rm th}/g^{(3)}_{\rm BEC}$ determined from the thermal sample and the BEC as a function of a_{3D}. Here we have made the reasonable assumption that $K^{(3)}$ is independent of the system's phase in 3D geometry, i.e. $K^{(3)}_{\rm th} = K^{(3)}_{\rm BEC}$. Our measurement shows that the ratio $g^{(3)}_{\rm th}/g^{(3)}_{\rm BEC}$ attains the expected value of 6 for weak interactions [Bur97], but then exhibits a pronounced decrease as a_{3D} is increased. For comparison, we plot the prediction of Ref. [Kag85]

$$g^{(3)}_{\rm th}/g^{(3)}_{\rm BEC} = 6/\left(1 + \frac{64}{\sqrt{\pi}}\sqrt{n_0 a^3_{3D}}\right). \tag{5.3}$$

We note that the density n_0 enters into this equation as a measured quantity. In general, we find good agreement between the experimental and the theoretical result, establishing our measurement as a clear demonstration of beyond mean-field effects on $g^{(3)}$ in 3D bosonic quantum gases.

5.5.4. Correlation function in 1D:

Figure 5.16 (a) illustrates our experimental setup to generate an array of 1D systems. We load a BEC of typically 8×10^4 atoms within 400 ms into approximately

5000 vertically (z-direction) oriented tubes that are formed by two horizontally propagating, retro-reflected lattice laser beams. Each tube with index (i, j) in the x-y-plane has a transversal trapping frequency of $\omega_\perp = 2\pi \times 12.2(5)$ kHz and an aspect ratio $\omega_\perp/\omega_z$ of approximately 800. The transversal motion of the atoms in the tubes is effectively frozen out as kinetic and interaction energy are much smaller than $\hbar\omega_\perp$. We adjust a_{3D} in 100 ms to its final value. After time t we turn off the lattice potential and determine the total atom number $N(t)$ by absorption imaging in a time-of-flight measurement. In order to determine $g_{1D}^{(3)}$ we calculate the ratio $K_{1D}^{(3)} g_{1D}^{(3)}/(K_{3D}^{(3)} g_{3D}^{(3)}) = g_{1D}^{(3)}/g_{3D}^{(3)}$. Here, it is not obvious that few-body physics is not affected by the confinement and that hence $K_{1D}^{(3)}$ and $K_{3D}^{(3)}$ cancel each other. Nevertheless, it is reasonable to assume that $K^{(3)}$ is not significantly changed by the confinement as long as the confinement length $a_\perp = \sqrt{\hbar/(m\omega_\perp)}$ is larger than the extent of the dimer produced in the recombination event and the range of the scattering process, which are both of order of a_{3D}. Here, m is the atom mass. We choose a moderately deep lattice potential with $a_\perp \approx 1500\ a_0$ and restrict a_{3D} to $a_{3D} \lesssim 800\ a_0$. In particular, we avoid the confinement-induced resonance condition $a_{3D} \approx a_\perp$ [Hal09, Hal10c].

The main difficulty in the determination of $K_{1D}^{(3)} g_{1D}^{(3)}$ comes from the fact that the initial atom number of the tubes varies across the lattice as a result of the harmonic confinement. We choose to always load the lattice in a regime of weak repulsive interactions such that almost all 1D samples are initially in the 1D Thomas-Fermi (TF) regime [Men02]. The local chemical potentials $\mu_{i,j}$, the total atom number N, and the chemical potential μ are then unambiguously related, and we can directly calculate the initial occupation number $N_{i,j}$ for each tube (i, j) (see 5.5.5 for suppl. material and Fig. 5.16(b)). The variation in $N_{i,j}$ results in a considerable variation in the type of density profile for each of the 1D systems after the strength of interactions is increased to the desired value: Some tubes remain in the 1D TF regime, while others are now in the TG regime. For tubes that are in the weakly interacting regime we determine the 1D density n_{1D} numerically by solving the 1D Gross-Pitaevskii equation. For the TG regime the density profiles are determined following Ref. [Men02]. In general, we find good agreement when we compare the numerical results to integrated density distributions from in-situ absorption images. For the interaction parameter γ we take a mean value that is calculated as an average over all local $\gamma_{i,j}$ at the center of each tube (i, j) weighted by $N_{i,j}$ (see 5.5.5 for suppl. material).

As before we determine $K_{1D}^{(3)} g_{1D}^{(3)}$ from the initial slope of the loss curve as shown in Fig. 5.16(c). In Fig. 5.17(a) we compare the data that we obtain in 1D geometry to our data for $K_{3D}^{(3)} g_{3D}^{(3)}$ for a 3D-BEC as we vary a_{3D}. We note that the BEC data is in good agreement with previous three-body loss data on thermal samples when one takes into account the combinatorial factor $3! = 6$ [Web03b, Kra06]. In particular, the 3D data follows the universal scaling law $K^{(3)} \sim {a_{3D}}^4$ for sufficiently large a_{3D} [Fed96, Esr99, Nie99, Bed00, Web03b]. We exclude data points affected by the presence of a narrow Feshbach resonance in the vicinity of $a_{3D} = 150 a_0$ [Mar07a]. Note that in the range from $a_{3D} \approx 10 a_0$ to $a_{3D} \approx 850 a_0$ three-body losses in 3D increase by nearly 3 orders of magnitude.

This behavior is in stark contrast to the measurements in 1D. In 1D, we observe a *reduction* of $K^{(3)}g^{(3)}$ by approximately a factor of 2 upon increasing a_{3D} over the same range of values. In fact, for $a_{3D} \geq 200a_0$ our measurement only gives an upper bound on $K^{(3)}_{1D}g^{(3)}_{1D}$ as losses become so small that we have difficulty in determining $\dot{N}(0)$ in view of shot-to-shot particle number variations. We note that not only the behavior of $g^{(3)}_{1D}$ reduces the atom loss, but also the fact that the density is decreased as repulsive interactions are increased. In addition, on a more technical side, our loading procedure for $a_{3D} \geq 200a_0$, aimed at avoiding the Feshbach resonance near $150a_0$, leads to a lower density. Also note that tunneling between tubes (on a timescale of 1 s for the parameters of our lattice) sets an upper bound for the timescale for which the tubes can be considered to be independent and hence fully in the 1D regime.

In Fig. 5.17(b) we plot $K^{(3)}_{1D}g^{(3)}_{1D}/(K^{(3)}_{3D}g^{(3)}_{3D}) \approx g^{(3)}_{1D}$ as a function of γ. A striking decrease by 3 orders of magnitude from the value 1 at $\gamma \approx 0.03$ to 10^{-3} at $\gamma \approx 50$ can be seen. We compare this result to the predictions based on the Lieb-Liniger model of interacting bosons in 1D: In the weakly interacting Gross-Pitaevskii regime ($\gamma \ll 1$) the Bogoliubov approach yields $g^{(3)}(\gamma) \simeq 1 - 6\sqrt{\gamma}/\pi$, while in the TG regime, $\gamma \gg 1$, $g^{(3)}$ can be expressed through derivatives of the three-body correlation function of free fermions, giving $g^{(3)} = 16\pi^6/(15\gamma^6)$ [Gan03]. Cheianov *et al.* [Che06b] have recently calculated numerically $g^{(3)}$ for all strengths of interactions within the Lieb-Liniger model, providing an interpolation between the weakly and strongly interacting limits (red continuous line in Fig. 5.17(b)). We find very good agreement between the result of our experiment and the theory that is valid for all strengths of interactions. This is the central result of this work.

Finally, for large values of a_{3D} and n_0, and for long hold times in 1D geometry, we find a surprisingly sudden increase of losses as shown in Fig.5.16(d), accompanied by a rapid increase for the expansion energy in the longitudinal direction (data not shown). The onset of increased losses shifts to later times with decreased density in the tubes, i.e. increased γ, and it is rather sensitive to the precise value of γ. We believe that the 1D tubes suffer from a recombination-heating induced breakdown of correlations: For sufficiently large values of a_{3D} the binding energy of the weakly bound dimer produced in the recombination process becomes comparable to the trap depth (here $h \times 45$ kHz). This leads to a positive feedback cycle in the many-body system in which three-body losses lead to an increase of temperature [Web03b] and thus of $g^{(3)}$ [Khe03, Kor09, Kor11], which in turn increases three-body losses.

Summary

In summary, we have measured the local value $g^{(3)}$ for the three-particle correlation function for quantum degenerate gases in 3D and 1D. In 3D, increasing interactions deplete the condensate and increase the value of $g^{(3)}$ in accordance with beyond mean-field calculations. In 1D, we observe a strong suppression for $g^{(3)}$ by 3 orders of magnitude as the TG regime is entered. The accompanying

suppression of three-body losses is crucial to the study of strongly interacting matter in and out of equilibrium in 1D [Kin06, Hof08, Hal09, Hal10d].

We thank R. Grimm for generous support. We gratefully acknowledge funding by the Austrian Science Fund (FWF) within project I153-N16 and within the framework of the European Science Foundation (ESF) EuroQUASAR collective research project QuDeGPM. GP acknowledges funding from the EU through NAME-QUAM and AQUTE.

5.5.5. Supplementary material

Trap parameters

In 3D geometry, we measure the atom loss in a crossed beam dipole trap with one horizontal and one vertical laser beam. The horizontal trap-frequencies $\omega_{x,y}$ and the vertical trap-frequency ω_z vary for the different measurements. The data sets in Fig. 5.15(a) are taken with trap frequencies $\omega_{x,y,z} = 2\pi \times (29(1), 80(2), 74(1))$ Hz for thermal atoms and with $\omega_{x,y,z} = 2\pi \times (11.8(1), 17.9(3), 13.5(1))$ Hz for a BEC. The data sets in Fig. 3(a) are taken at trap frequencies of $\omega_{x,y,z} = 2\pi \times (10.5(8), 17.4(1), 13.9(1))$ Hz for a BEC.

In 1D geometry, we use a crossed dipole trap in addition to the 2D optical lattice potential to adjust the atom number distribution over the tubes. We choose two settings with global trap frequencies $\omega_{x,y,z} = 2\pi \times (9.7(2), 11.4(2), 14.5(1))$ Hz and $2\pi \times (13.1(2), 17.7(2), 17.5(2))$ Hz.

Atom number distribution over the tubes

We calculate the initial occupation number $N_{i,j}$ for tube (i, j) from the global chemical potential μ. For weak repulsive interactions during the loading process almost all tubes are in the 1D Thomas-Fermi (TF) regime with a local chemical potential $\mu_{i,j}$ at the center of each tube

$$\mu_{i,j} = \mu - \frac{1}{2} m(\lambda/2)^2(\omega_x^2 i^2 + \omega_y^2 j^2),$$

where m is the atomic mass and $\lambda = 1064.5$ nm is the wavelength of lattice light. We calculate μ from the condition $N = \sum_{i,j} N_{i,j}(\mu)$ with the $N_{i,j}$ given by [Pet00a]

$$\mu_{i,j} = \left(\frac{3N_{i,j}}{4\sqrt{2}} g_{1\mathrm{D}} \omega_z \sqrt{m} \right)^{2/3},$$

where $g_{1\mathrm{D}}$ is the 1D coupling parameter [Ols98]

$$g_{1\mathrm{D}} = 2\hbar\omega_\perp a_{3\mathrm{D}} \left(1 - 1.0326 \frac{a_{3\mathrm{D}}}{a_\perp} \right)^{-1}.$$

Determination of γ

We determine the mean interaction parameter γ from the local parameters $\gamma_{i,j}$ at the center of each tube (i,j)

$$\gamma_{i,j} = \frac{m g_{1\mathrm{D}}}{\hbar^2 n_{i,j}^{1\mathrm{D}}}, \qquad \gamma = \frac{1}{N}\sum_{i,j} N_{i,j}\gamma_{i,j}.$$

Here, $n_{i,j}^{1\mathrm{D}}$ is the 1D density at the center of the tube (i,j). Note that this gives a lower estimate for γ. Averaging γ over the density profile along each tube gives a slightly larger γ by a factor 1.5 for a 1D TF density profile and a factor 1.27 for a TG density profile.

Density profiles

The density profiles for the individual tubes with index (i,j) depend strongly on the strength of interactions and the occupation number $N_{i,j}$. Figure 5.18 compares the results for the integrated density profiles $\int n_{i,j}^3(\mathbf{r})d^3r$ using the different approximations to calculate the profile (gaussian, TF, TG, numerically solved GP-equation, and Lieb-Liniger solution within the local density approximation [Dun01]) for the specific case of $N_{i,j} = 15$. For our analysis of the experimental data we use the GP result for weak interactions and the TG result [Men02] for strong interactions (continuous red line).

Secondary loss processes

Here we estimate the deviation $\Delta\alpha$ from $\alpha = 3$ in the rate equation $\dot{n} = -\alpha K^{(3)} g^{(3)} n^3$ due to secondary loss processes [Sch01, Zac09]. Within a simple simulation, we determine an upper bound for the correction to the data of the 3D loss experiment of Fig. 5.15(b) and show that secondary loss processes cannot explain our results for $g_{\mathrm{th}}^{(3)}/g_{\mathrm{BEC}}^{(3)}$. In fact for our experimental trap parameters and atom numbers secondary processes would result in an *increase* of $g_{\mathrm{th}}^{(3)}/g_{\mathrm{BEC}}^{(3)}$ with increasing interaction strength, in contradiction with the observed behavior.

A secondary collision is caused by the collision of the dimer and/or free atom from a three-body recombination process with other atoms while leaving the trap, triggering additional losses. We estimate the average number of secondary collisions in our experiment by determining numerically the collisional opacity $< nl > \sigma$ for the products of a three-body recombination event. Here $< nl >$ is the average column density, with l the distance covered by a (randomly chosen) atom leaving the trap, and σ is the scattering cross section. For the atom-atom cross section we use the formula $\sigma = 8\pi a_{3\mathrm{D}}^2/(1 + k^2 {a_{3\mathrm{D}}}^2)$, where $\hbar k$ is the momentum of the free atom gained in the recombination event. For the atom-dimer collision, we use a similar expression for the cross section, with the momentum of the dimer and a scattering length $2a_{3\mathrm{D}}$. For our experimental parameters, we then determine the total number of atoms lost due to secondary processes for a thermal sample, $\Delta\alpha_{\mathrm{th}}$, and a BEC, $\Delta\alpha_{\mathrm{BEC}}$. Figure 5.19 shows

that the ratio $(3 + \Delta\alpha_{\mathrm{th}})/(3 + \Delta\alpha_{\mathrm{BEC}})$ *increases* with increasing $a_{3\mathrm{D}}$ by about 30 percent over the experimentally accessible range of $a_{3\mathrm{D}}$. These results imply that for our experimental parameters secondary loss processes would result in an increase of the ratio $g^{(3)}_{\mathrm{th}}/g^{(3)}_{\mathrm{BEC}}$ in Fig. 5.15(b), in contrast to the measured data. Thus, within the present model, this rules out secondary loss processes as the cause of the effects shown in the present work.

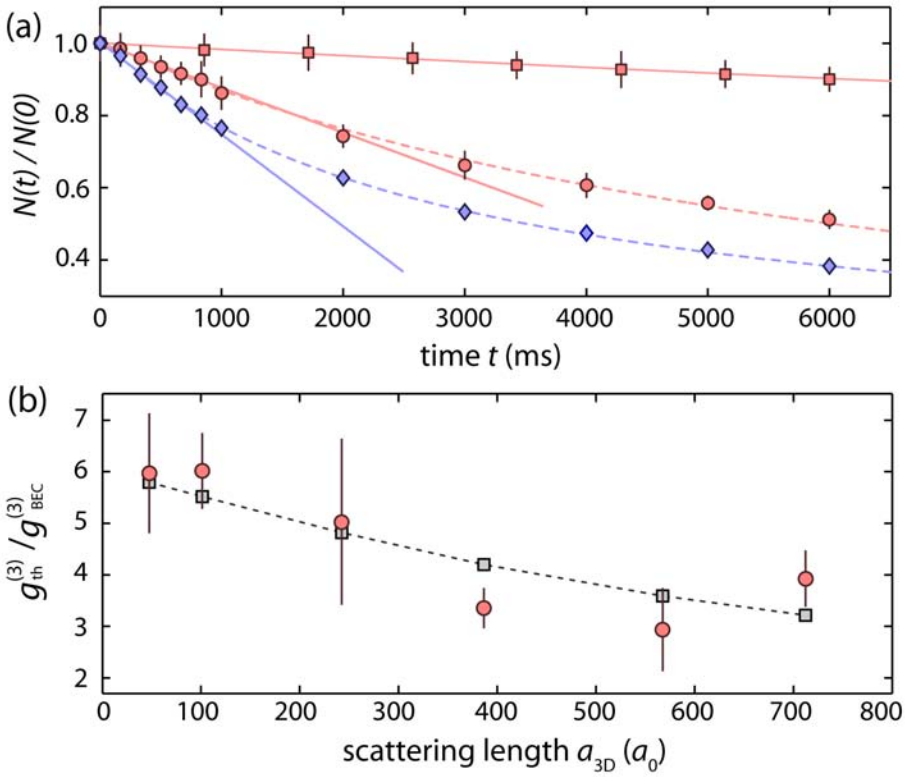

Fig. 5.15.: (color online) (a) Relative atom number $N(t)/N(0)$ vs. hold time t in 3D geometry: BEC (squares and circles) and thermal gas (diamonds) for $a_{3D} = 101(2)\ a_0$, $386(3)\ a_0$, and $386(3)\ a_0$, respectively. The dashed lines are fits to the data based on the loss equation (see text). The solid lines are linear fits that include the data from 100% to 85%. (b) The ratio of correlation functions $g^{(3)}_{\rm th}/g^{(3)}_{\rm BEC}$ as a function of a_{3D} (experimental data: circles; prediction [Kag85]: squares). All error bars reflect the 1σ statistical uncertainty.

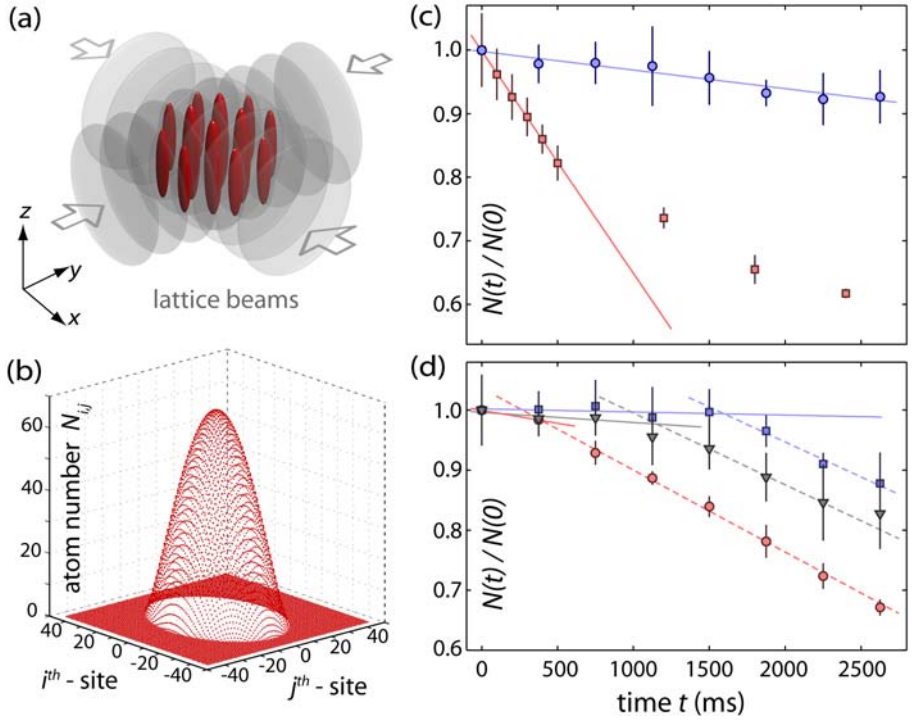

Fig. 5.16.: (color online) (a) Sketch of the experimental setup: A 2D optical lattice traps atoms in an array of 1D tubes. (b) Example of a computed atom number distribution $N_{i,j}$ (see text). (c) The relative atom number $N(t)/N(0)$ as a function of time t in 1D geometry: squares and circles correspond to $a_{3D} = 23(1)\ a_0$ and $568(3)\ a_0$ with initial densities of 4.5 μm^{-1} and 1.7 μm^{-1} at the center of the center tube, respectively. The solid lines are linear fits to the initial slopes. (d) The relative atom number $N(t)/N(0)$ in 1D for fixed $a_{3D} = 568(3)\ a_0$ and for various values of γ as the 1D density is changed: $\gamma = 12$ (circles), $\gamma = 13$ (triangles), and $\gamma = 14$ (squares). The solid (dashed) lines are linear fits to the data points for short (large) times to guide the eye.

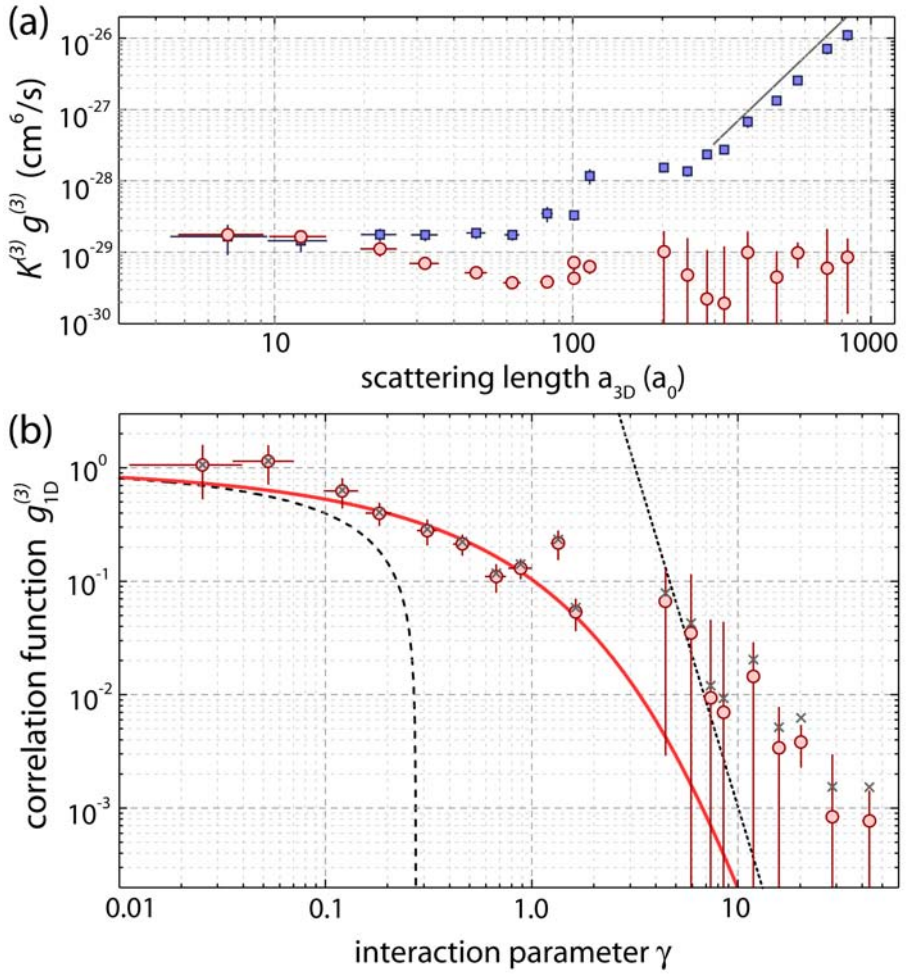

Fig. 5.17.: (color online) (a) Three-body loss coefficient $K^{(3)}g^{(3)}$ vs. a_{3D} for a quantum degenerate gas in 3D (squares) and in 1D (circles). The line gives the $K^{(3)} = C\hbar a_{3D}^4/m$ scaling in the universal regime in 3D with $C = 67.9$ [Fed96, Esr99, Nie99, Bed00, Web03b]. The error bars of $K^{(3)}g^{(3)}$ reflect the 1σ statistical uncertainty of the linear fit. The increased relative error for the larger values of a_{3D} is the result of greatly reduced atom loss, giving smaller slopes for the decay curves at roughly the same shot-to-shot particle variations, primarily due to the behavior of $g^{(3)}$, but also due to a reduction of the density (for details, see text). (b) The measured correlation function $g^{(3)}_{1D}$ vs. γ in 1D geometry (circles). The crosses indicate the values for $g^{(3)}_{1D}$ corrected for the variations of $g^{(3)}_{3D}$ with a_{3D} as in Eq. (5.3) (see text). The dashed and dotted lines are approximate analytical solutions for $\gamma \ll 1$ and $\gamma \gg 1$ from Ref. [Gan03]. The solid line is the prediction from Ref. [Che06b, Che06a].

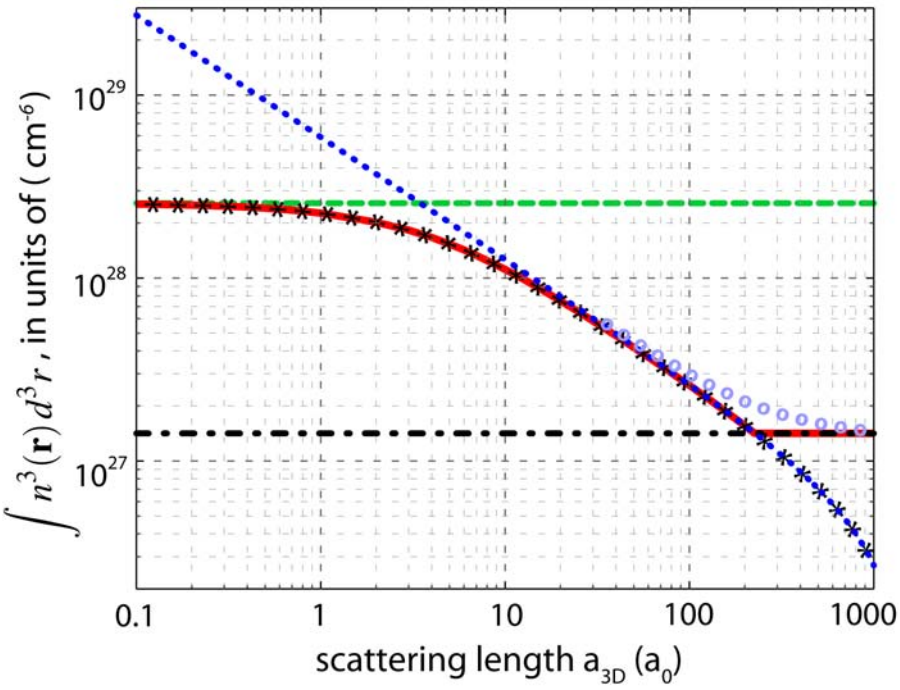

Fig. 5.18.: (color online) The quantity $\int n_{i,j}^3(\mathbf{r})d^3r$ for an occupation number $N_{i,j} = 15$ as a function of the scattering length $a_{3\mathrm{D}}$ for the given trap parameters of our experiment. The various curves correspond to the different approximations: gaussian solution (green dashed line), TF solution (blue dotted line), TG solution (black dash-dotted line), numerically solved GP-equation result (black stars), and Lieb-Liniger solution with local density approximation (blue circles). For the data analysis the continuous red line is used.

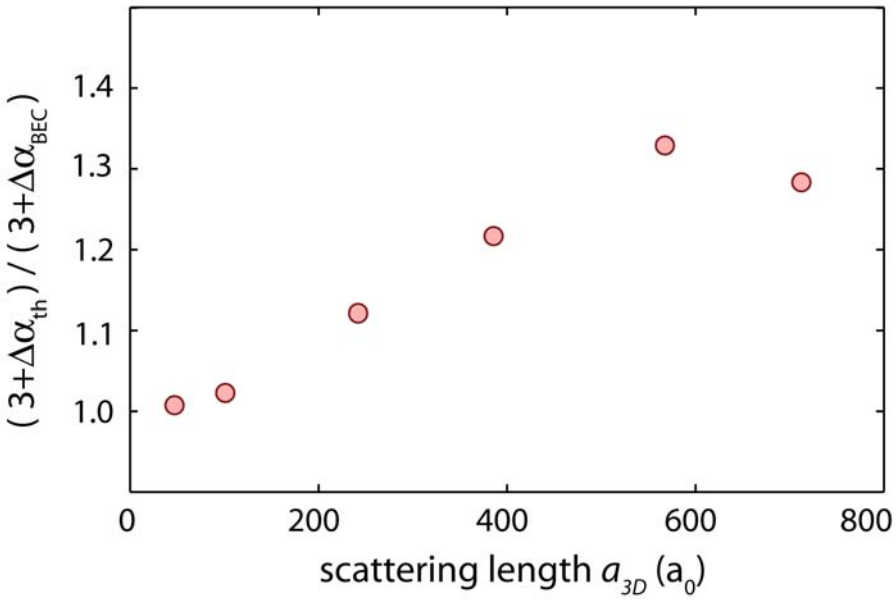

Fig. 5.19.: (color online) Upper estimate for the corrections due to secondary loss. For details see text.

CHAPTER 6

OUTLOOK

Our experimental setup will undergo some mayor changes in the near future. One of these will be the addition of potassium into the setup. To minimize the dead time during which experiments cannot be carried out, this implementation will be accomplished stepwise and the necessary changes are carefully planned in such a way that as many parts as possible are untouched. On the other hand one can take the opportunity and review some old experimental parts to improve them with the knowledge built up in the past years.

The alkali metal potassium naturally occurs in the three isotopes ^{39}K, ^{40}K and ^{41}K, where ^{40}K is a Fermion and slightly radioactive with a lifetime of 1.25 billion years. In the field of ultracold gases, potassium is widely used in combination with other species like lithium [Wil08] and rubidium [Mod01, Roa02, Osp06b, Roa07]. The scattering properties of the potassium isotopes at ultralow temperatures are markedly different. ^{41}K has a small positive scattering length of $\sim 66\,a_0$, which allows to form a stable BEC [Mod01], but there are no broad Feshbach resonances available to tune interactions. In contrast ^{39}K has a small negative scattering length of $\sim 33\,a_0$, but a broad Feshbach resonance at 402 G in its lowest hyperfine state which allows for tuning of the interactions and the creation of the BEC in the vicinity of this resonance [Roa07]. The fermionic ^{40}K, if brought to ultralow temperatures, would not interact at all because its fermionic nature allows only p-wave scattering between identical particles. Mixtures of ^{40}K in different hyperfine states are again allowed to interact via s-wave scattering, and also the tuning via Feshbach resonances is possible [Lof02].

Since the laser frequencies needed for optical cooling of the three different isotopes are very similar, it is possible to use the same laser setup for all of them. This gives the flexibility to investigate Bose-Bose and Fermi-Bose mixtures without the need of major changes to the setup. Interspecies Feshbach resonances between potassium and cesium, where several are predicted to appear below 1000 G [Fer09a], should enable tunability between the two species. Combined with an optical lattice this would enable the study of new exotic phases, for example pairing of fermions with bosons or bosonic holes [Lew04].

An additional strategy is the creation of either bosonic or fermionic heteronuclear KCs molecules and the subsequent transfer into the rovibronic ground state in a similar way as we have shown in chapter 4 for Cs_2. They would exhibit a permanent electric dipole moment [Aym05] and they should be stable against collisions [Żuc10], in contrast to some other heteronuclear combinations like KRb [Osp10]. The electric dipole moment leads to anisotropic long range dipole-dipole interactions, which in combination with an optical lattice, allows for the simulation of quantum magnetism [Bar06] and the implementation of quantum computation schemes [DeM02].

APPENDIX A

ELECTRONIC CIRCUITS

Experiments in the field of ultracold quantum gases would not be realizable without electronic circuits. For example magnetic fields are typically created by a electric current in a coil or wire, and the magnitude of it needs to be controlled dynamically during an experimental cycle to enable magnetic field ramps. In our case, the whole experiment is computer controlled using a bus system, which provides an expandable amount of digital and analog output channels [Gus08a]. The electronic circuits have to interpret these digital or analog signals and control laser intensities and magnetic fields accordingly.

Within this thesis, many new electronic circuits or improvements have been designed, build, tested and implemented into the experiment. The following sections give an introduction into the most important circuits and their functional principle.

A.1. Magnetic field stabilization

The stability of magnetic fields is crucial for every cold atoms experiment, especially when driving atomic radio- or microwave transitions or when interactions are very sensitive to magnetic field changes.

A.1.1. Line trigger

One of the most common magnetic field fluctuations is are generated by stray magnetic field with 50 Hz or higher harmonics of it, since it is related to the frequency of the electric line, powering every laboratory power supply and electric device. To suppress this noise, either a passive filtering with μ-metal around the science chamber or an active counter-regulation by modulating 50 Hz onto the main magnetic field is possible. In our case, we do not want to limit our optical access by shielding, and the active counter-regulation has not been implemented yet.

In most cases we are relying on a reproducible magnetic field value at a specific time during an experimental sequence. This can be realized by either running the experiment fully synchronized to the 50 Hz line frequency via phase lock between the 50 Hz and the clock signal for the experimental control, or by introducing an additional variable wait time during the sequence, waiting until the phase of the 50 Hz is at a specific value before continuing the cycle. Since we need to have a clock frequency, which is synchronized via GPS for long duration time measurements, we have chosen the second implementation scheme. Figure A.1 shows the circuit, which stops the experimental control clock when sending an TTL pulse to it, until the 50 Hz line signal goes through a defined phase point. The maximal wait time introduced is 20 ms. This allowed us to measure the magnetic field fluctuation caused by the 50 Hz line frequency using microwave spectroscopy, which in our case is on the order of 10 mG.

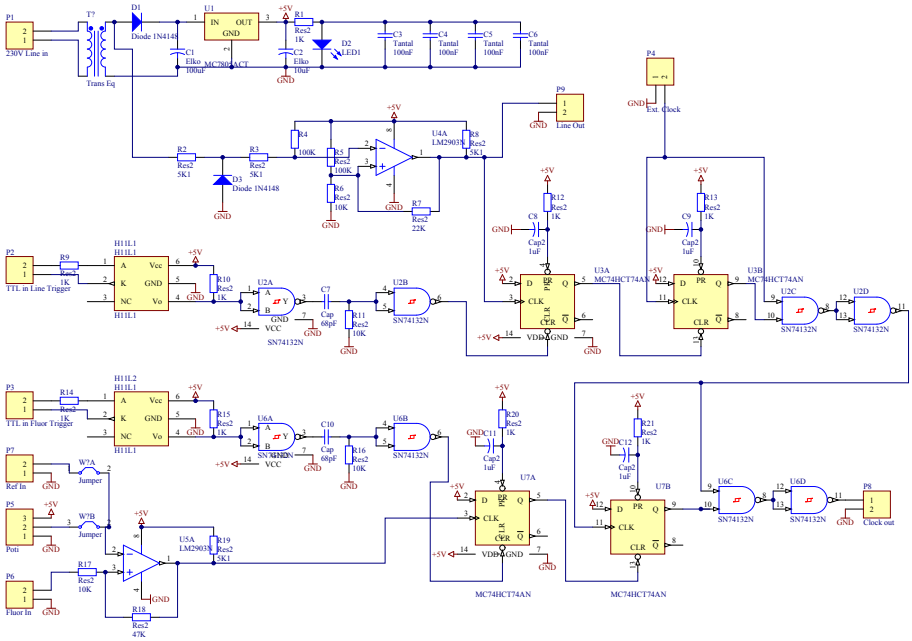

Fig. A.1.: Circuit diagram of the line trigger box.

A.1.2. Current stabilization

Our magnetic offset field is generated with a coil pair and a current in the range of $0 - 50$ A. The current is provided by a Delta Elektronika switching power supply. Such a switching power supply can handle high output powers, but it generates additional noise components at their switching frequency or multiples of it. Even as the coil behaves like a low pass at frequencies on the order of several kHz and the switching frequencies are in the range of 100 kHz or more, the magnetic field noise is noticeable in the experiment. It creates huge shot-to-shot fluctuations for microwave transitions and molecule association efficiencies. A direct low pass filtering of the current is not possible since this would prevent fast magnetic field ramps.

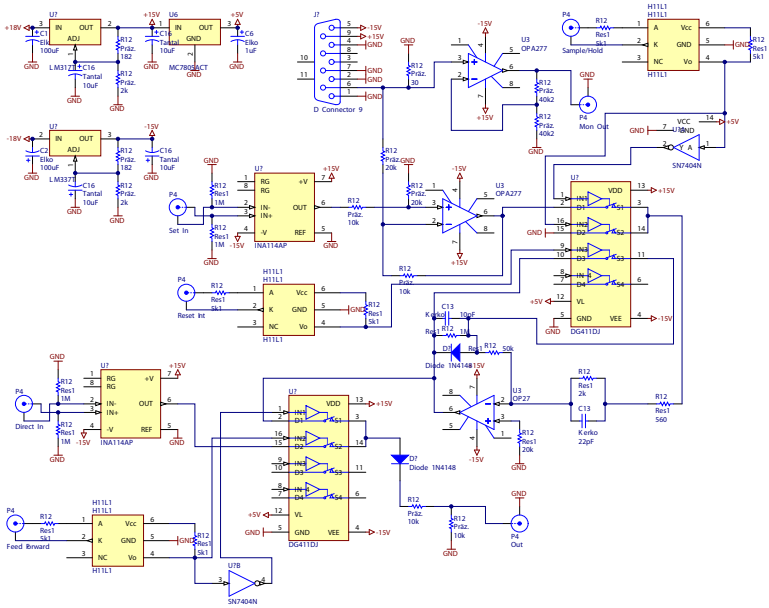

Fig. A.2.: Circuit diagram of the Current PID controller.

Our implemented solution consists of a three-stage feedback, enabling the integration of a car battery as current source for the sensitive parts of the measurement as it provides a very low noise current. By using the car battery only for short times during the experimental cycle, we are able to recharge it in the time between and therefore do not need a huge car battery stack. In the first stage, for the first part of the experimental cycle, where current noise is not that important, the regulation is done with the PID controller in figure A.2 via the feedback input of the Delta power supply. For the second stage we switch to the direct current control of this PID controller, which means that the input voltage of the feedback of the Delta power supply is directly set by the experiment control and not by the feedback provided from the current sensor. At the same time we activate a second PID controller which regulates the current using a power MOSFET stage in series with the coil. By setting the direct output of the Delta power supply slightly higher than needed, the MOSFET stage regulates the current to the desired value. This switching takes about 10 ms and produces some current spikes, therefore we do this during the evaporation ramps where it does not effect the system much. For the third stage we set the Delta power supply output on a higher voltage than the car battery, add the battery via a switch and diodes parallel to the Delta power supply and ramp down the output of the Delta power supply afterwards. This changes the current source from the power supply to the car battery while maintaining a constant current running through the coils. This switching takes again about 10 ms, but it can be done anytime in the experiment cycle, since it does not produce current spikes.

A.2. Laser diode stabilization

Many laser frequencies used in cold atom experiments can be generated with semiconductor laser diodes. Typically the temperature and the supply current of the laser diode needs to be stabilized to ensure a stable single frequency at the wavelength needed for the experiment.

A.2.1. Temperature stabilization

A prerequisite for a stable laser frequency is the temperature stabilization of the laser diode, since temperature shifts change the cavity length of the diode and therefore the frequency. For the latest design of the diode laser housing, we choose a two-stage stabilization scheme, where the laser diode with its metal mounting is temperature stabilized by four peltier elements and the complete housing, consisting of an inner and outer metal shield, is kept on a constant temperature using a heating foil. The temperature of this parts is sensed with NTC resistors, and the circuit which converts the resistance into a temperature signal, shown in figure A.3, is placed within the inner and outer shield to minimize temperature drifts of the electronic components. The circuit also contains connections for monitoring sensors, the laserdiode current and piezo voltages.

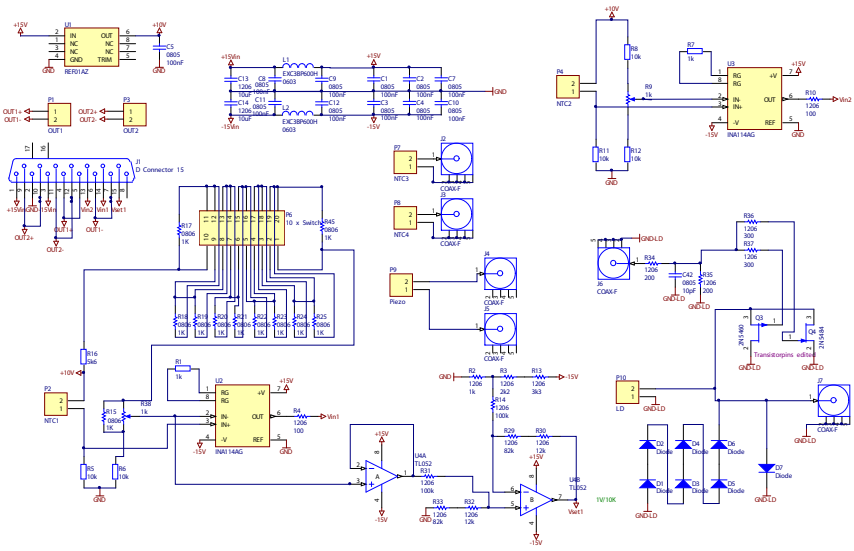

Fig. A.3.: Circuit diagram of the temperature sensing circuit.

It is connected to the actual temperature PID controller shown in figure A.4 via the Sub-D connector, where all signals, power supplies and control currents for the peltier elements and the heating foil are transferred. The temperature PID controller consists of two independent PID circuits, one for the laser diode temperature and one for the housing temperature. After a low pass filtering to remove suspicious high frequency signals, a simple PID circuit drives a high

power bipolar output stage, which provide up to 3 A current for cooling or heating. This circuit, in combination with the careful designed laser diode housing, provides a long term temperature stability of less than 1 mK.

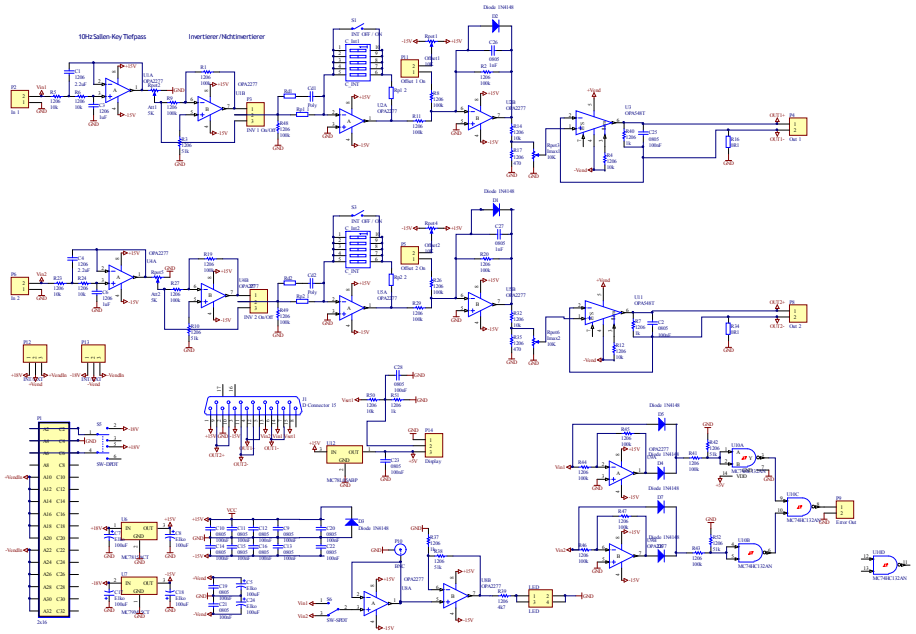

Fig. A.4.: Circuit diagram of the temperature PID controller.

A.2.2. Laser current stabilization

The emitted frequency of a laser diode is very sensitive to the amount of current running through it. For slow current variations, the changing power dissipation in the diode will have the most significant effect, which leads to a change in the temperature and therefore to a changing frequency. For fast current variations, the change of index of refraction inside the diode will be most significant, also leading to a change in frequency. For assuring a most stable and noise-free laser frequency, one needs to provide a stable, low noise current to the laser diode.

Our laser diode current driver shown in figure A.5 is based on a design by Todd P. Meyrath from the group of Prof. Mark Raizen. It should exhibit a temperature stability of the output current on the order of $\sim$ 50 ppm, and a theoretically calculated peak-to-peak noise below one μA integrated from 10 Hz to 100 MHz. Critical to the noise reduction are the components of the Pi-filter after the output stage, the temperature stability is mostly determined by the instrumentation amplifier in the feedback circuit and the stability of the voltage reference. The circuit can provide laser diode currents up to 400 mA for cathode and anode ground laser diodes, switchable via jumper settings. For increased security the switching on and off is rather smooth without generating spikes, and a power failure will switch off the current and keep it off even when the circuit gets its power supply back. A circuit at the output of the current driver enables a fast modulation of the laser diode current for locking purposes.

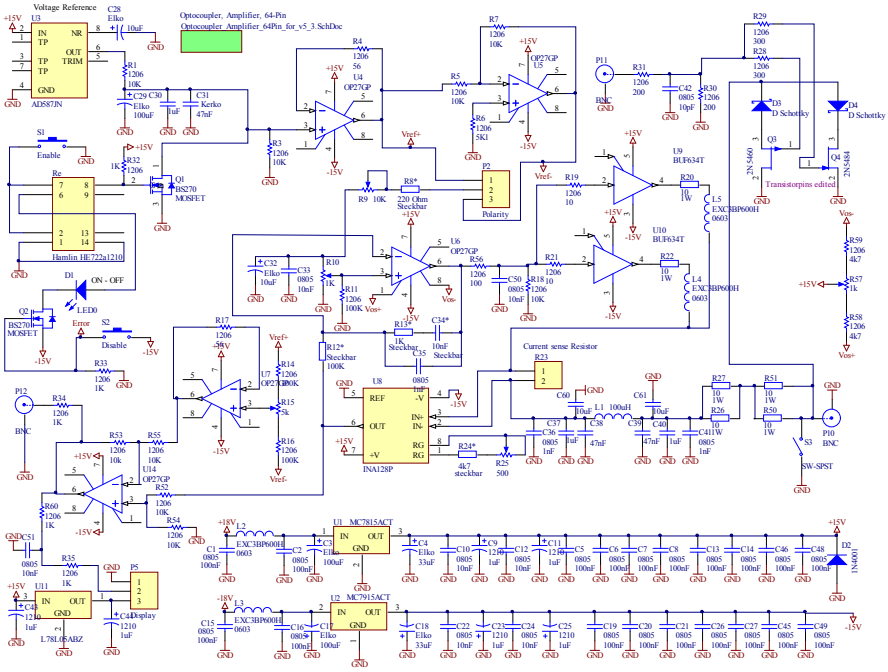

Fig. A.5.: Circuit diagram of the Laser diode current driver.

A.2.3. Laser PID feedback

Typically a laser frequency is locked to a stable reference, for example atoms in a vapor cell or a cavity. After the creation of an error signal via Pound-Drever-Hall for a cavity or Doppler-free modulation transfer spectroscopy for the vapor cell, one needs a circuit which changes the laser frequency accordingly to keep it stable to this reference. We are using grating-stabilized laser diodes in Littrow or Littmann configuration, where the angle of the grating is tunable with a piezoelectric crystal. Therefore the frequency of the laser diode can be tuned by changing the applied voltage to the piezo and by changing the current of the laser diode itself. Alternatively an electro-optical modulator crystal can be placed between the laser diode and the grating, which changes the optical length of the external cavity built up between the laser diode and the grating depending on the voltage applied to the crystal.

We split up the error signal into two paths, on for the piezo control and one for the current control. The usable frequency range of the piezo is limited by its mechanical resonance frequency, typically on the order of kHz. Therefore we use it only to compensate slow drifts or mechanical vibrations. The laser diode current can be modulated up to several MHz, enabling the filtering of acoustic noise or other high frequency laser noise. Our PID feedback circuit is inspired by the homebuilt controller used in the group of T. W. Hänsch and the commercial FALC controller from Toptica and was a joint effort of Johann Danzl and me.

The fast part used for the control of the laser diode current is shown in figure A.6. After a ultra-low noise input amplifier the signal is split into two paths,

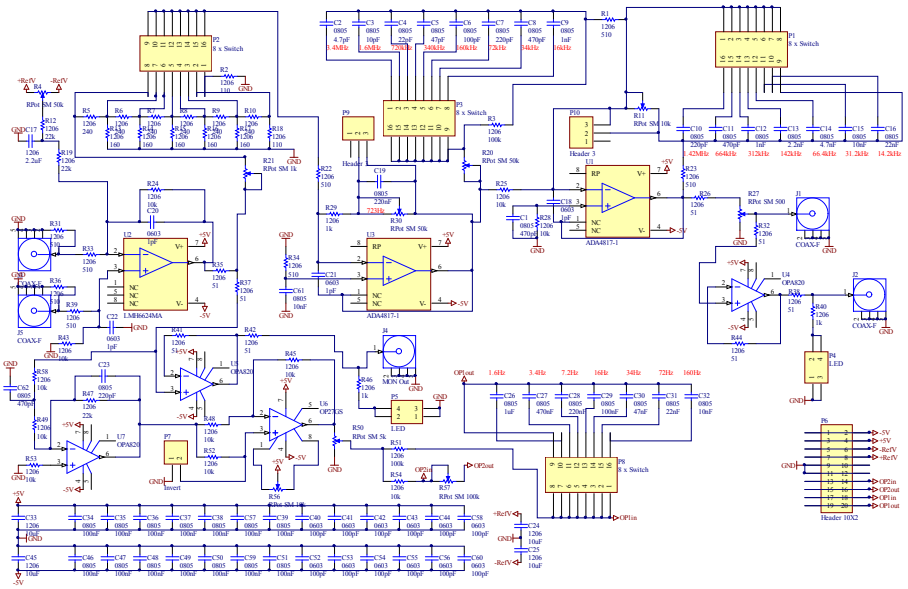

Fig. A.6.: Circuit diagram of the Laser PID frontboard.

where one goes to the slow piezo controller part. An extra filtering stage for this path filters suspicious high frequency components which could lead to a saturation of the following low frequency amplifiers. The fast path consists of a variable attenuator for setting the overall gain, a low frequency integrator stage with fixed corner frequency of 723 Hz and a maximum gain of 40 dB, and a single amplifier PID stage, with a maximum gain of 20 dB and variable corner frequencies of the I and D parts over a range of two decades.

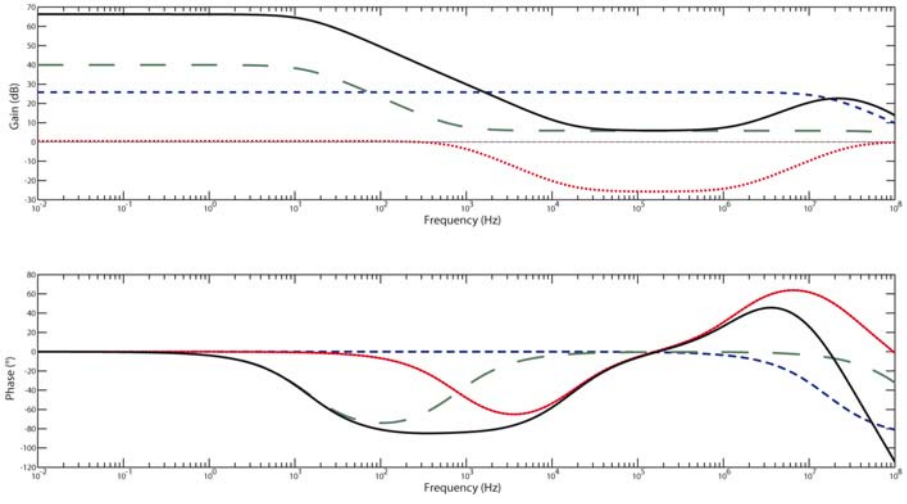

Fig. A.7.: Exemplary Bode diagram for the fast Laser PID circuit.

Through careful SMD board design and specially chosen electronic parts this circuit should be able to reach locking bandwidths of several MHz. A calculated sample Bode diagram of the frequency and phase response of the circuit is shown in figure A.7, where the dotted and dashed lines correspond to the frequency

response of single parts of this circuit and the solid line is the overall transfer function. It does not contain the real frequency behavior of the amplifiers, but shows the general behavior of the circuit.

The circuit for the piezo control is shown in figure A.8. It serves as power supply for the PID frontboard and integrates a sweep generator to scan the laser frequency for spectroscopy purposes.

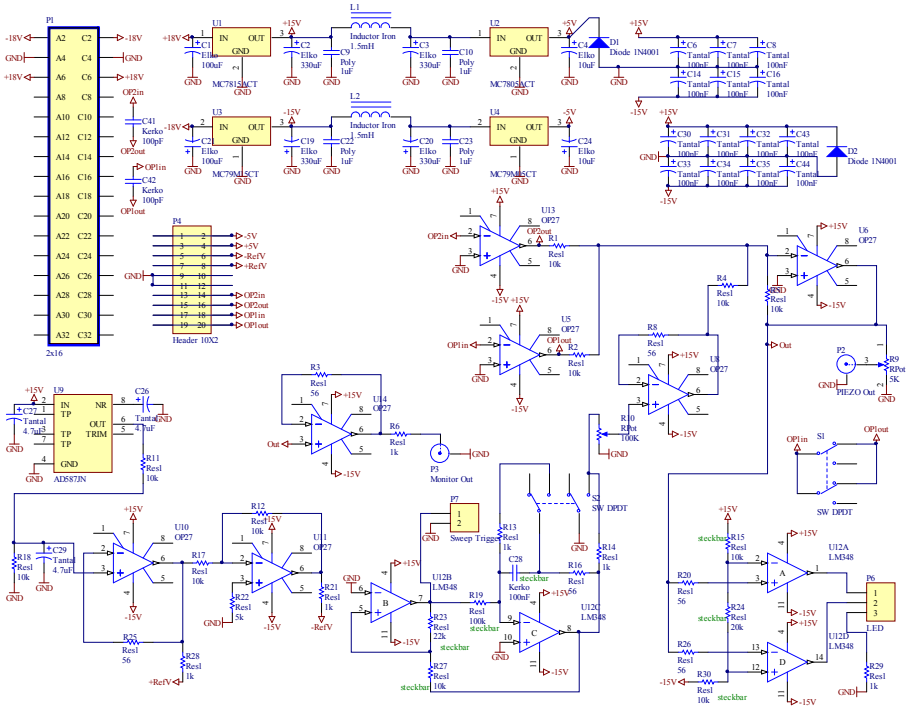

Fig. A.8.: Circuit diagram of the Laser PID mainboard.

BIBLIOGRAPHY

[Alb09] A. Alberti, V. V. Ivanov, G. M. Tino, and G. Ferrari, *Engineering the quantum transport of atomic wavefunctions over macroscopic distances*, Nature Physics **5**, 547 (2009).

[Ald09] J. Aldegunde and J. M. Hutson, *Hyperfine energy levels of alkali-metal dimers: Ground-state homonuclear molecules in magnetic fields*, Phys. Rev. A **79**, 013401 (2009).

[Ale06] F. Alet, A. M. Walczak, and M. P. Fisher, *Exotic quantum phases and phase transitions in correlated matter*, Physica A: Statistical and Theoretical Physics **369**, 122 (2006).

[Alt05] E. Altman, A. Polkovnikov, E. Demler, B. Halperin, and M. Lukin, *Superfluid-Insulator Transition in a Moving System of Interacting Bosons*, Physical Review Letters **95**, 020402 (2005).

[Ami85] C. Amiot and J. Verges, *The (1)* $^3\Sigma_g^+$ *electronic state of* Cs_2, Chemical Physics Letters **116**, 273 (1985).

[Ami99] C. Amiot, O. Dulieu, and J. Vergès, *Resolution of the Apparent Disorder of the* Rb_2 $A^1\Sigma_u^1(0_u^+)$ *and* $b^3\Pi_u(0_u^+)$ *Spectra: A Case of Fully Coupled Electronic States*, Phys. Rev. Lett. **83**, 2316 (1999).

[Ami02] C. Amiot and O. Dulieu, *The* Cs_2 *ground electronic state by Fourier transform spectroscopy: Dispersion coefficients*, The Journal of Chemical Physics **117**, 5155 (2002).

[And81] S. V. Andreev, V. I. Balykin, V. S. Letokhov, and V. G. Minogin, *Radiative slowing and reduction of the energy spread of a beam of sodium atoms to 1.5K in an oppositely directed laser beam*, Pis'ma Zh. Eksp. Teor. Fiz. **34**, 463 (1981).

[And95] M. H. Anderson, J. R. Ensher, M. R. Matthews, C. E. Wieman, and E. A. Cornell, *Observation of Bose-Einstein condensation in dilute atomic vapor*, Science **269**, 198 (1995).

[And97] M. R. Andrews, *Observation of Interference Between Two Bose Condensates*, Science **275**, 637 (1997).

[And98] B. P. Anderson and M. A. Kasevich, *Macroscopic Quantum Interference from Atomic Tunnel Arrays*, Science **282**, 1686 (1998).

[And07] M. Anderlini, P. J. Lee, B. L. Brown, J. Sebby-Strabley, W. D. Phillips, and J. V. Porto, *Controlled exchange interaction between pairs of neutral atoms in an optical lattice*, Nature **448**, 452 (2007).

[And09] R. Anderson, C. Ticknor, A. Sidorov, and B. Hall, *Spatially inhomogeneous phase evolution of a two-component Bose-Einstein condensate*, Physical Review A **80** (2009).

[Arm10] J. Armijo, T. Jacqmin, K. V. Kheruntsyan, and I. Bouchoule, *Probing Three-Body Correlations in a Quantum Gas Using the Measurement of the Third Moment of Density Fluctuations*, Phys. Rev. Lett. **105**, 230402 (2010).

[AS01] J. R. Abo-Shaeer, C. Raman, J. M. Vogels, and W. Ketterle, *Observation of Vortex Lattices in Bose-Einstein Condensates*, Science **292**, 476 (2001).

[Ash76] N. Ashcroft and N. Mermin, *Solid State Physics*, Saunders College, Philadelphia, 1976.

[Ast04] G. Astrakharchik, D. Blume, S. Giorgini, and B. Granger, *Quasi-one-dimensional Bose gases with a large scattering length*, Physical Review Letters **92**, 030402 (2004).

[Ast05] G. E. Astrakharchik, J. Boronat, J. Casulleras, and S. Giorgini, *Beyond the Tonks-Girardeau gas: Strongly correlated regime in quasi-one-dimensional Bose gases*, Phys. Rev. Lett. **95**, 190407 (2005).

[Aym05] M. Aymar and O. Dulieu, *Calculation of accurate permanent dipole moments of the lowest $^{1,3}\Sigma^+$ states of heteronuclear alkali dimers using extended basis sets*, J. Chem. Phys. **122**, 204302 (2005).

[Bah96] J. T. Bahns, W. C. Stwalley, and P. L. Gould, *Laser cooling of molecules: A sequential scheme for rotation, translation, and vibration*, J. Chem. Phys. **104**, 9689 (1996).

[Bai11] J. Bai, E. H. Ahmed, B. Beser, Y. Guan, S. Kotochigova, A. M. Lyyra, S. Ashman, C. M. Wolfe, J. Huennekens, F. Xie, D. Li, L. Li, M. Tamanis, R. Ferber, A. Drozdova, E. Pazyuk, A. V. Stolyarov, J. G. Danzl, H.-C. Nägerl, N. Bouloufa, O. Dulieu, C. Amiot, H. Salami, and T. Bergeman, *Global analysis of data on the spin-orbit-coupled $A\,^1\Sigma_u^+$ and $b\,^3\Pi_u$ states of Cs_2*, Phys. Rev. A **83**, 032514 (2011).

[Bak09] W. S. Bakr, J. I. Gillen, A. Peng, S. Fölling, and M. Greiner, *A quantum gas microscope for detecting single atoms in a Hubbard-regime optical lattice*, Nature **462**, 74 (2009).

[Bak10] W. S. Bakr, A. Peng, M. E. Tai, R. Ma, J. Simon, J. I. Gillen, S. Folling, L. Pollet, and M. Greiner, *Probing the Superfluid-to-Mott Insulator Transition at the Single-Atom Level*, Science **329**, 547 (2010).

[Bar57] J. Bardeen, L. N. Cooper, and J. R. Schrieffer, *Microscopic Theory of Superconductivity*, Phys. Rev. **106**, 162 (1957).

[Bar02] M. Baranov, L. Dobrek, K. Góral, L. Santos, and M. Lewenstein, *Ultracold Dipolar Gases - a Challenge for Experiments and Theory*, Physica Scripta **T102**, 74 (2002).

[Bar04a] M. Bartenstein, A. Altmeyer, S. Riedl, S. Jochim, C. Chin, J. Hecker Denschlag, and R. Grimm, *Collective Excitations of a Degenerate Gas at the BEC-BCS Crossover*, Phys. Rev. Lett. **92**, 203201 (2004).

[Bar04b] M. Bartenstein, A. Altmeyer, S. Riedl, S. Jochim, C. Chin, J. Hecker Denschlag, and R. Grimm, *Crossover from a Molecular Bose-Einstein Condensate to a Degenerate Fermi Gas*, Phys. Rev. Lett. **92**, 120401 (2004).

[Bar06] R. Barnett, D. Petrov, M. Lukin, and E. Demler, *Quantum magnetism with multicomponent dipolar molecules in an optical lattice*, Phys. Rev. Lett. **96**, 190401 (2006).

[Bar08] M. A. Baranov, *Theoretical progress in many-body physics with ultracold dipolar gases*, Physics Reports **464**, 71 (2008).

[Bat04] R. Battesti, P. Cladé, S. Guellati-Khélifa, C. Schwob, B. Grémaud, F. m. c. Nez, L. Julien, and F. m. c. Biraben, *Bloch Oscillations of Ultracold Atoms: A Tool for a Metrological Determination of h/m_{Rb}*, Phys. Rev. Lett. **92**, 253001 (2004).

[Bat05] M. T. Batchelor, M. Bortz, X. W. Guan, and N. Oelkers, *Evidence for the super Tonks-Girardeau gas*, Journal of Statistical Mechanics: Theory and Experiment **2005**, L10001 (2005).

[BD96] M. Ben Dahan, E. Peik, J. Reichel, Y. Castin, and C. Salomon, *Bloch Oscillations of Atoms in an Optical Potential*, Phys. Rev. Lett. **76**, 4508 (1996).

[Bec10] C. Becker, P. Soltan-Panahi, J. Kronjäger, S. Dörscher, K. Bongs, and K. Sengstock, *Ultracold quantum gases in triangular optical lattices*, New Journal of Physics **12**, 065025 (2010).

[Bed00] P. F. Bedaque, E. Braaten, and H.-W. Hammer, *Three-body recombination in Bose gases with large scattering length*, Phys. Rev. Lett. **85**, 908 (2000).

[Ber97] P. Berman, *Atom Interferometry*, New York: Academic, 1997.

[Ber98] K. Bergmann, H. Theuer, and B. W. Shore, *Coherent population transfer among quantum states of atoms and molecules*, Rev. Mod. Phys. **70**, 1003 (1998).

[Ber01] M. Berry, I. Marzoli, and W. P. Schleich, *Quantum carpets, carpets of light*, Phys. World **14**, 39 (2001).

[Ber03a] T. Bergeman, C. E. Fellows, R. F. Gutterres, and C. Amiot, *Analysis of strongly coupled electronic states in diatomic molecules: Low-lying excited states of RbCs*, Phys. Rev. A **67**, 050501 (2003).

[Ber03b] T. Bergeman, M. Moore, and M. Olshanii, *Atom-atom scattering under cylindrical harmonic confinement: Numerical and analytic studies of the confinement induced resonance*, Physical Review Letters **91**, 163201 (2003).

[Ber11] M. Berninger, A. Zenesini, B. Huang, W. Harm, H.-C. Nägerl, F. Ferlaino, R. Grimm, P. S. Julienne, and J. M. Hutson, *Universality of the Three-Body Parameter for Efimov States in Ultracold Cesium*, Phys. Rev. Lett. **107**, 120401 (2011).

[Bes09] T. Best, S. Will, U. Schneider, L. Hackermüller, D. van Oosten, I. Bloch, and D.-S. Lühmann, *Role of Interactions in* ^{87}Rb-^{40}**K** *Bose-Fermi Mixtures in a 3D Optical Lattice*, Phys. Rev. Lett. **102**, 030408 (2009).

[Bis11] U. Bissbort, F. Deuretzbacher, and W. Hofstetter, *Effective multi-body induced tunneling and interactions in the Bose-Hubbard model of the lowest dressed band of an optical lattice* (2011).

[Blo28] F. Bloch, *Über die Quantenmechanik der Elektronen in Kristallgittern*, Zeitschrift für Physik **52**, 555 (1928).

[Blo08] I. Bloch, J. Dalibard, and W. Zwerger, *Many-body physics with ultracold gases*, Rev. Mod. Phys. **80**, 885 (2008).

[Boc99] M. Bockrath, D. Cobden, J. Lu, A. G. Rinzler, R. E. Smalley, L. Balents, and P. McEuen, *Luttinger liquid behavior in carbon nanotubes*, Nature **397**, 598 (1999).

[Bon11] L. Bonnes and S. Wessel, *Pair Superfluidity of Three-Body Constrained Bosons in Two Dimensions*, Phys. Rev. Lett. **106**, 185302 (2011).

[Bou11] R. Bouchendira, P. Cladé, S. Guellati-Khélifa, F. m. c. Nez, and F. m. c. Biraben, *New Determination of the Fine Structure Constant and Test of the Quantum Electrodynamics*, Phys. Rev. Lett. **106**, 080801 (2011).

[Bra95] C. C. Bradley, C. A. Sackett, J. J. Tollett, and R. G. Hulet, *Evidence of Bose-Einstein condensation in an atomic gas with attractive interactions*, Phys. Rev. Lett. **75**, 1687 (1995).

[Bra07] E. Braaten and H. Hammer, *Efimov physics in cold atoms*, Annals of Physics **322**, 120 (2007).

[Bre02] B. Brezger, L. Hackermüller, S. Uttenthaler, J. Petschinka, M. Arndt, and A. Zeilinger, *Matter-Wave Interferometer for Large Molecules*, Phys. Rev. Lett. **88**, 100404 (2002).

[Büc03] H. P. Büchler, G. Blatter, and W. Zwerger, *Commensurate-incommensurate transition of cold atoms in an optical lattice*, Phys. Rev. Lett. **90**, 130401 (2003).

[Büc10] H. P. Büchler, *Microscopic Derivation of Hubbard Parameters for Cold Atomic Gases*, Phys. Rev. Lett. **104**, 090402 (2010).

[Bul09] I. Buluta and F. Nori, *Quantum Simulators*, Science **326**, 108 (2009).

[Bur97] E. A. Burt, R. W. Ghrist, C. J. Myatt, M. J. Holland, E. A. Cornell, and C. E. Wieman, *Coherence, Correlations, and Collisions: What One Learns about Bose-Einstein Condensates from Their Decay*, Phys. Rev. Lett. **79**, 337 (1997).

[Bur99] S. Burger, K. Bongs, S. Dettmer, W. Ertmer, K. Sengstock, A. Sanpera, G. V. Shlyapnikov, and M. Lewenstein, *Dark Solitons in Bose-Einstein Condensates*, Phys. Rev. Lett. **83**, 5198 (1999).

[Bus98] T. Busch, B.-G. Englert, K. Rzążewski, and M. Wilkens, *Two Cold Atoms in a Harmonic Trap*, Foundations of Physics **28**, 549 (1998), 10.1023/A:1018705520999.

[Cad08] M. Cadoret, E. de Mirandes, P. Cladé, S. Guellati-Khélifa, C. Schwob, F. m. c. Nez, L. Julien, and F. m. c. Biraben, *Combination of Bloch Oscillations with a Ramsey-Bordé Interferometer: New Determination of the Fine Structure Constant*, Phys. Rev. Lett. **101**, 230801 (2008).

[Cam06] G. K. Campbell, J. Mun, M. Boyd, P. Medley, A. E. Leanhardt, L. G. Marcassa, D. E. Pritchard, and W. Ketterle, *Imaging the Mott Insulator Shells by Using Atomic Clock Shifts*, Science **313**, 649 (2006).

[Car09] L. D. Carr, D. DeMille, R. V. Krems, and J. Ye, *Cold and ultracold molecules: Science, technology and applications*, New J. Phys. **11**, 055049 (2009).

[Cas48] H. B. G. Casimir and D. Polder, *The Influence of Retardation on the London-van der Waals Forces*, Phys. Rev. **73**, 360 (1948).

[Cas01] Y. Castin, *Coherent atomic matter waves*, Springer, Berlin, 2001.

[Caz04] M. A. Cazalilla, *Bosonizing one-dimensional cold atomic gases*, Journal of Physics B: Atomic, Molecular and Optical Physics **37**, S1 (2004).

[Caz11] M. A. Cazalilla, R. Citro, T. Giamarchi, E. Orignac, and M. Rigol, *One dimensional Bosons: From Condensed Matter Systems to Ultracold Gases* (2011).

[Cha95] M. S. Chapman, C. R. Ekstrom, T. D. Hammond, J. Schmiedmayer, B. E. Tannian, S. Wehinger, and D. E. Pritchard, *Near-field imaging of atom diffraction gratings: The atomic Talbot effect*, Phys. Rev. A **51**, R14 (1995).

[Cha07] J.-C. Charlier, X. Blase, and S. Roche, *Electronic and transport properties of nanotubes*, Rev. Mod. Phys. **79**, 677 (2007).

[Che06a] V. V. Cheianov, H. Smith, and M. B. Zvonarev, *Exact results for three-body correlations in a degenerate one-dimensional Bose gas*, Phys. Rev. A **73**, 051604 (2006).

[Che06b] V. V. Cheianov, H. Smith, and M. B. Zvonarev, *Three-body local correlation function in the Lieb-Liniger model: bosonization approach*, Journal of Statistical Mechanics: Theory and Experiment **8**, P08015 (2006).

[Che11a] D. Chen, M. White, C. Borries, and B. DeMarco, *Quantum Quench of an Atomic Mott Insulator*, Phys. Rev. Lett. **106**, 235304 (2011).

[Che11b] M. Cheneau, P. Barmettler, D. Poletti, M. Endres, P. Schauß, T. Fukuhara, C. Gross, I. Bloch, C. Kollath, and S. Kuhr, *Light-cone-like spreading of correlations in a quantum many-body system* (2011).

[Chi04a] C. Chin, M. Bartenstein, A. Altmeyer, S. Riedl, S. Jochim, J. Hecker Denschlag, and R. Grimm, *Observation of the Pairing Gap in a Strongly Interacting Fermi Gas*, Science **305**, 1128 (2004).

[Chi04b] C. Chin, V. Vuletić, A. J. Kerman, S. Chu, E. Tiesinga, P. J. Leo, and C. J. Williams, *Precision Feshbach spectroscopy of ultracold* Cs_2, Phys. Rev. A **70**, 032701 (2004).

[Chi05] C. Chin, T. Kraemer, M. Mark, J. Herbig, P. Waldburger, H.-C. Nägerl, and R. Grimm, *Observation of Feshbach-like resonances in collisions between ultracold molecules*, Phys. Rev. Lett. **94**, 123201 (2005).

[Chi09] C. Chin, V. V. Flambaum, and M. G. Kozlov, *Ultracold molecules: new probes on the variation of fundamental constants*, New J. Phys. **11**, 055048 (2009).

[Chi10] C. Chin, R. Grimm, P. S. Julienne, and E. Tiesinga, *Feshbach resonances in ultracold gases*, Rev. Mod. Phys. **82**, 1225 (2010).

[Chu85] S. Chu, L. Hollberg, J. E. Bjorkholm, A. Cable, and A. Ashkin, *Three-dimensional viscous confinement and cooling of atoms by resonance radiation pressure*, Phys. Rev. Lett. **55**, 48 (1985).

[Chw10] J. Chwedeńczuk, L. Pezzé, F. Piazza, and A. Smerzi, *Rabi interferometry and sensitive measurement of the Casimir-Polder force with ultracold gases*, Phys. Rev. A **82**, 032104 (2010).

[Cla94] J. F. Clauser and S. Li, *Talbot-vonLau atom interferometry with cold slow potassium*, Phys. Rev. A **49**, R2213 (1994).

[Cla06a] P. Cladé, E. de Mirandes, M. Cadoret, S. Guellati-Khélifa, C. Schwob, F. Nez, L. Julien, and F. Biraben, *Determination of the Fine Structure Constant Based on Bloch Oscillations of Ultracold Atoms in a Vertical Optical Lattice*, Physical Review Letters **96**, 033001 (2006).

[Cla06b] S. R. Clark and D. Jaksch, *Signatures of the superfluid to Mott-insulator transition in the excitation spectrum of ultracold atoms*, New Journal of Physics **8**, 160 (2006).

[Cla09] P. Cladé, S. Guellati-Khélifa, F. m. c. Nez, and F. m. c. Biraben, *Large Momentum Beam Splitter Using Bloch Oscillations*, Phys. Rev. Lett. **102**, 240402 (2009).

[Cle09] D. Clement, N. Fabbri, L. Fallani, C. Fort, and M. Inguscio, *Exploring Correlated 1D Bose Gases from the Superfluid to the Mott-Insulator State by Inelastic Light Scattering*, Phys. Rev. Lett. **102**, 155301 (2009).

[CN09] A. H. Castro Neto, F. Guinea, N. M. R. Peres, K. S. Novoselov, and A. K. Geim, *The electronic properties of graphene*, Rev. Mod. Phys. **81**, 109 (2009).

[Col75] S. Coleman, *Quantum sine-Gordon equation as the massive Thirring model*, Physical Review D **11**, 2088 (1975).

[Col92] D. T. Colbert and W. H. Miller, *A novel discrete variable representation for quantum mechanical reactive scattering via the S-matrix Kohn method*, The Journal of Chemical Physics **96**, 1982 (1992).

[Cor00] S. L. Cornish, N. R. Claussen, J. L. Roberts, E. A. Cornell, and C. E. Wieman, *Stable* ^{85}Rb *Bose-Einstein condensates with widely tunable interactions*, Phys. Rev. Lett. **85**, 1795 (2000).

[Cou98] P. Courteille, R. S. Freeland, D. J. Heinzen, F. A. van Abeelen, and B. J. Verhaar, *Observation of a Feshbach Resonance in Cold Atom Scattering*, Phys. Rev. Lett. **81**, 69 (1998).

[Cri04] M. Cristiani, O. Morsch, N. Malossi, M. Jona-Lasinio, M. Anderlini, E. Courtade, and E. Arimondo, *Instabilities of a Bose-Einstein condensate in a periodic potential: an experimental investigation*, Optics Express **12**, 4 (2004).

[Cro09] A. D. Cronin, J. Schmiedmayer, and D. E. Pritchard, *Optics and interferometry with atoms and molecules*, Rev. Mod. Phys. **81**, 1051 (2009).

[CS07] B. Capogrosso-Sansone, N. V. Prokof'ev, and B. V. Svistunov, *Phase diagram and thermodynamics of the three-dimensional Bose-Hubbard model*, Phys. Rev. B **75**, 134302 (2007).

[Cub03] J. Cubizolles, T. Bourdel, S. J. J. M. F. Kokkelmans, G. V. Shlyapnikov, and C. Salomon, *Production of Long-Lived Ultracold* Li_2 *Molecules from a Fermi Gas*, Phys. Rev. Lett. **91**, 240401 (2003).

[Dal09] A. J. Daley, J. M. Taylor, S. Diehl, M. Baranov, and P. Zoller, *Atomic three-body loss as a dynamical three-body interaction*, Phys. Rev. Lett. **102**, 040402 (2009).

[Dal11] J. Dalibard, F. Gerbier, G. Juzeliunas, and P. Öhberg, *Colloquium : Artificial gauge potentials for neutral atoms*, Rev. Mod. Phys. **83**, 1523 (2011).

[Dan08] J. G. Danzl, E. Haller, M. Gustavsson, M. J. Mark, R. Hart, N. Bouloufa, O. Dulieu, H. Ritsch, and H.-C. Nägerl, *Quantum Gas of Deeply Bound Ground State Molecules*, Science **321**, 1062 (2008).

[Dan09a] J. G. Danzl, M. J. Mark, E. Haller, M. Gustavsson, R. Hart, A. Liem, H. Zellmer, and H.-C. Nägerl, *Deeply bound ultracold molecules in an optical lattice*, New J. Phys. **11**, 055036 (2009).

[Dan09b] J. G. Danzl, M. J. Mark, E. Haller, M. Gustavsson, N. Bouloufa, O. Dulieu, H. Ritsch, R. Hart, and H.-C. Nägerl, *Precision molecular spectroscopy for ground state transfer of molecular quantum gases*, Faraday Discuss. **142**, 283 (2009).

[Dan10a] J. G. Danzl, *Rovibronic Ground-State Molecules near Quantum Degeneracy*, Ph.D. thesis, University of Innsbruck (2010).

[Dan10b] J. G. Danzl, M. J. Mark, E. Haller, M. Gustavsson, R. Hart, J. Aldegunde, J. M. Hutson, and H.-C. Nägerl, *An ultracold high-density sample of rovibronic ground-state molecules in an optical lattice*, Nature Phys. **6**, 265 (2010).

[Dav27] C. Davisson and L. H. Germer, *Diffraction of Electrons by a Crystal of Nickel*, Phys. Rev. **30**, 705 (1927).

[Dav95] K. B. Davis, M. O. Mewes, M. R. Andrews, N. J. van Druten, D. S. Durfee, D. M. Kurn, and W. Ketterle, *Bose-Einstein condensation in a gas of sodium atoms*, Phys. Rev. Lett. **75**, 3969 (1995).

[Deb11] M. Debatin, T. Takekoshi, R. Rameshan, L. Reichsöllner, F. Ferlaino, R. Grimm, R. Vexiau, N. Bouloufa, O. Dulieu, and H.-C. Nägerl, *Molecular spectroscopy for ground-state transfer of ultracold RbCs molecules*, Phys. Chem. Chem. Phys. **13**, 18926 (2011).

[Dei08] J. Deiglmayr, A. Grochola, M. Repp, K. Mörtlbauer, C. Glück, J. Lange, O. Dulieu, R. Wester, and M. Weidemüller, *Formation of Ultracold Polar Molecules in the Rovibrational Ground State*, Physical Review Letters **101**, 133004 (2008).

[DeM99] B. DeMarco and D. S. Jin, *Onset of Fermi Degeneracy in a Trapped Atomic Gas*, Science **285**, 1703 (1999).

[DeM02] D. DeMille, *Quantum Computation with Trapped Polar Molecules*, Phys. Rev. Lett. **88**, 067901 (2002).

[DeM08] D. DeMille, S. Sainis, J. Sage, T. Bergeman, S. Kotochigova, and E. Tiesinga, *Enhanced sensitivity to variation of m_e/m_p in molecular spectra*, Phys. Rev. Lett. **100**, 043202 (2008).

[Den99] L. Deng, E. W. Hagley, J. Denschlag, J. E. Simsarian, M. Edwards, C. W. Clark, K. Helmerson, S. L. Rolston, and W. D. Phillips, *Temporal, Matter-Wave-Dispersion Talbot Effect*, Phys. Rev. Lett. **83**, 5407 (1999).

[Den00] J. Denschlag, J. Simsarian, D. L. Feder, C. W. Clark, L. A. Collins, J. Cubizolles, L. Deng, E. W. Hagley, W. P. Helmerson, K. Reinhardt, S. L. Rolston, B. I. Schneider, and W. D. Phillips, *Generating solitons by phase engineering of a Bose-Einstein condensate*, Science **287**, 97 (2000).

[Det01] S. Dettmer, D. Hellweg, P. Ryytty, J. J. Arlt, W. Ertmer, K. Sengstock, D. S. Petrov, G. V. Shlyapnikov, H. Kreutzmann, L. Santos, and M. Lewenstein, *Observation of Phase Fluctuations in Elongated Bose-Einstein Condensates*, Phys. Rev. Lett. **87**, 160406 (2001).

[Die10] S. Diehl, M. Baranov, A. J. Daley, and P. Zoller, *Observability of Quantum Criticality and a Continuous Supersolid in Atomic Gases*, Phys. Rev. Lett. **104**, 165301 (2010).

[Doc07] O. Docenko, M. Tamanis, R. Ferber, E. A. Pazyuk, A. Zaitsevskii, A. V. Stolyarov, A. Pashov, H. Knöckel, and E. Tiemann, *Deperturbation treatment of the $A^1\Sigma^+$-$b^3\Pi$ complex of NaRb and prospects for ultracold molecule formation in $X^1\Sigma^+(v = 0;J = 0)$*, Physical Review A **75**, 042503 (2007).

[Don02] E. A. Donley, N. R. Clausen, S. T. Thompson, and C. E. Wieman, *Atom-molecule coherence in a Bose-Einstein condensate*, Nature **417**, 529 (2002).

[Doy04] J. Doyle, B. Friedrich, R. Krems, and F. Masnou-Seeuws, *Editorial: Quo vadis, cold molecules?*, Eur. Phys. J. D **31**, 149 (2004).

[Dul95] O. Dulieu and P. S. Julienne, *Coupled channel bound states calculations for alkali dimers using the Fourier grid method*, The Journal of Chemical Physics **103**, 60 (1995).

[Dul06] O. Dulieu, M. Raoult, and E. Tiemann, *Cold molecules: a chemistry kitchen for physicists?*, J. Phys. B **39** (2006).

[Dul09] O. Dulieu and C. Gabbanini, *The formation and interactions of cold and ultracold molecules: new challenges for interdisciplinary physics*, Rep. Prog. Phys. **72**, 086401 (2009).

[Dun01] V. Dunjko, V. Lorent, and M. Olshanii, *Bosons in Cigar-Shaped Traps: Thomas-Fermi Regime, Tonks-Girardeau Regime, and In Between*, Phys. Rev. Lett. **86**, 5413 (2001).

[Dür08] S. Dürr, *private communication* (2008).

[Eck05a] A. Eckardt, T. Jinasundera, C. Weiss, and M. Holthaus, *Analog of Photon-Assisted Tunneling in a Bose-Einstein Condensate*, Physical Review Letters **95**, 200401 (2005).

[Eck05b] A. Eckardt, C. Weiss, and M. Holthaus, *Superfluid-Insulator Transition in a Periodically Driven Optical Lattice*, Phys. Rev. Lett. **95**, 260404 (2005).

[Efi70] V. Efimov, *Energy levels arising from resonant two-body forces in a three-body system*, Phys. Lett. B **33**, 563 (1970).

[End11] M. Endres, M. Cheneau, T. Fukuhara, C. Weitenberg, P. Schauß, C. Gross, L. Mazza, M. C. Banuls, L. Pollet, I. Bloch, and S. Kuhr, *Observation of Correlated Particle-Hole Pairs and String Order in Low-Dimensional Mott Insulators*, Science **334**, 200 (2011).

[Esr99] B. D. Esry, C. H. Greene, and J. P. Burke, *Recombination of Three Atoms in the Ultracold Limit*, Phys. Rev. Lett. **83**, 1751 (1999).

[Est30] I. Estermann and O. Stern, *Beugung von Molekularstrahlen*, Zeitschrift für Physik **61**, 95 (1930).

[Fal04] L. Fallani, L. De Sarlo, J. Lye, M. Modugno, R. Saers, C. Fort, and M. Inguscio, *Observation of Dynamical Instability for a Bose-Einstein Condensate in a Moving 1D Optical Lattice*, Physical Review Letters **93**, 140406 (2004).

[Fat08a] M. Fattori, C. D'Errico, G. Roati, M. Zaccanti, M. Jona-Lasinio, M. Modugno, M. Inguscio, and G. Modugno, *Atom Interferometry with a Weakly Interacting Bose-Einstein Condensate*, Phys. Rev. Lett. **100**, 080405 (2008).

[Fat08b] M. Fattori, G. Roati, B. Deissler, C. D'Errico, M. Zaccanti, M. Jona-Lasinio, L. Santos, M. Inguscio, and G. Modugno, *Magnetic Dipolar Interaction in a Bose-Einstein Condensate Atomic Interferometer*, Phys. Rev. Lett. **101**, 190405 (2008).

[Fed96] P. O. Fedichev, M. W. Reynolds, and G. V. Shlyapnikov, *Three-Body recombination of ultracold atoms to a weakly bound s level*, Phys. Rev. Lett. **77**, 2921 (1996).

[Fer05] C. Fertig, K. O'Hara, J. Huckans, S. Rolston, W. Phillips, and J. Porto, *Strongly Inhibited Transport of a Degenerate 1D Bose Gas in a Lattice*, Physical Review Letters **94**, 3 (2005).

[Fer06] G. Ferrari, N. Poli, F. Sorrentino, and G. M. Tino, *Long-lived Bloch oscillations with bosonic Sr atoms and application to gravity measurement at the micrometer scale*, Phys. Rev. Lett. **97**, 060402 (2006).

[Fer08] F. Ferlaino, S. Knoop, and R. Grimm, *Ultracold Feshbach molecules*, in: R. V. Krems, B. Friedrich, and W. C. Stwalley (Eds.), *Cold Molecules: Theory, Experiment, Applications*, arXiv:0809.3920, 2008.

[Fer09a] R. Ferber, I. Klincare, O. Nikolayeva, M. Tamanis, H. Knöckel, E. Tiemann, and A. Pashov, *$X\,^1\Sigma^+$ and $a\,^3\Sigma^+$ states of the atom pair K+Cs studied by Fourier-transform spectroscopy*, Phys. Rev. A **80**, 062501 (2009).

[Fer09b] F. Ferlaino, S. Knoop, M. Berninger, W. Harm, J. P. D'Incao, H.-C. Nägerl, and R. Grimm, *Evidence for universal four-body states tied to an Efimov trimer*, Phys. Rev. Lett. **102**, 140401 (2009).

[Fer09c] F. Ferlaino, S. Knoop, and R. Grimm, *Cold Molecules: Theory, Experiment, Applications*, chap. Ultracold Feshbach molecules, Taylor & Francis, 2009.

[Fer11] F. Ferlaino, A. Zenesini, M. Berninger, B. Huang, H. Nägerl, H.-C.gerl, and R. Grimm, *Efimov Resonances in Ultracold Quantum Gases*, Few-Body Systems **51**, 113 (2011), 10.1007/s00601-011-0260-7.

[Fis89] M. P. A. Fisher, P. B. Weichman, G. Grinstein, and D. S. Fisher, *Boson localization and the superfluid-insulator transition*, Phys. Rev. B **40**, 546 (1989).

[Fix07] J. B. Fixler, G. T. Foster, J. M. McGuirk, and M. A. Kasevich, *Atom interferometer measurement of the newtonian constant of gravity*, Science **315**, 74 (2007).

[Fli06] A. Flir, *Implementierung und Untersuchung von Raman-Seitenbandkühlung zur Erzeugung eines ultrakalten Cäsiumgases*, Diploma thesis, University of Innsbruck (2006).

[Föl05] S. Fölling, F. Gerbier, A. Widera, O. Mandel, T. Gericke, and I. Bloch, *Spatial quantum noise interferometry in expanding ultracold atom clouds*, Nature **434**, 481 (2005).

[Föl07] S. Fölling, S. Trotzky, P. Cheinet, M. Feld, R. Saers, A. Widera, T. Müller, and I. Bloch, *Direct observation of second-order atom tunnelling*, Nature **448**, 1029 (2007).

[Fri98] D. G. Fried, T. C. Killian, L. Willmann, D. Landhuis, S. C. Moss, D. Kleppner, and T. J. Greytak, *Bose-Einstein Condensation of Atomic Hydrogen*, Phys. Rev. Lett. **81**, 3811 (1998).

[Fri09] B. Friedrich and J. M. Doyle, *Why are cold molecules so hot?*, ChemPhysChem **10**, 604 (2009).

[Fuk09] T. Fukuhara, S. Sugawa, M. Sugimoto, S. Taie, and Y. Takahashi, *Mott insulator of ultracold alkaline-earth-metal-like atoms*, Phys. Rev. A **79**, 041604(R) (2009).

[Gae10] J. P. Gaebler, J. T. Stewart, T. E. Drake, D. S. Jin, A. Perali, P. Pieri, and G. C. Strinati, *Observation of pseudogap behaviour in a strongly interacting Fermi gas*, Nature Physics **6**, 569 (2010).

[Gan03] D. M. Gangardt and G. V. Shlyapnikov, *Stability and Phase Coherence of Trapped 1D Bose Gases*, Phys. Rev. Lett. **90**, 010401 (2003).

[Gem09] N. Gemelke, X. Zhang, C.-L. Hung, and C. Chin, *In situ observation of incompressible Mott-insulating domains in ultracold atomic gases*, Nature **460**, 995 (2009).

[Ger00] J. M. Gerton, D. Strekalov, I. Prodan, and R. G. Hulet, *Direct observation of growth and collapse of a Bose-Einstein condensate with attractive interactions*, Nature **408**, 692 (2000).

[Ger07] S. Gerlich, L. Hackermüller, K. Hornberger, A. Stibor, H. Ulbricht, M. Gring, F. Goldfarb, T. Savas, M. Muri, M. Mayor, and M. Arndt, *A Kapitza-Dirac-Talbot-Lau interferometer for highly polarizable molecules*, Nature Physics **3**, 711 (2007).

[Gia03] T. Giamarchi, *Quantum physics in one dimension*, Clarendon Press, Oxford, 2003.

[Gir60] M. Girardeau, *Relationship between systems of impenetrable bosons and fermions in one dimension*, J. Math. Phys. **1**, 516 (1960).

[Gog98] A. O. Gogolin, A. M. Tsvelik, and A. A. Nersesyan, *Bosonization and strongly correlated systems*, Cambridge University Press, Cambridge UK, 1998.

[Gór02] K. Góral, L. Santos, and M. Lewenstein, *Quantum Phases of Dipolar Bosons in Optical Lattices*, Phys. Rev. Lett. **88**, 170406 (2002).

[Gou86] P. Gould, G. Ruff, and D. Pritchard, *Diffraction of atoms by light: The near-resonant Kapitza-Dirac effect*, Physical Review Letters **56**, 827 (1986).

[Gre01] M. Greiner, I. Bloch, O. Mandel, T. W. Hänsch, and T. Esslinger, *Exploring Phase Coherence in a 2D Lattice of Bose-Einstein Condensates*, Phys. Rev. Lett. **87**, 160405 (2001).

[Gre02a] M. Greiner, O. Mandel, T. Esslinger, T. W. Hänsch, and I. Bloch, *Quantum phase transition from a superfluid to a Mott insulator in a gas of ultracold atoms*, Nature **415**, 39 (2002).

[Gre02b] M. Greiner, O. Mandel, T. W. Hansch, and I. Bloch, *Collapse and revival of the matter wave field of a Bose-Einstein condensate*, Nature **419**, 51 (2002).

[Gre03] M. Greiner, C. A. Regal, and D. S. Jin, *Emergence of a Molecular Bose-Einstein Condensate from a Fermi Gas*, Nature **426**, 537 (2003).

[Gre05] M. Greiner, C. A. Regal, J. T. Stewart, and D. S. Jin, *Probing Pair-Correlated Fermionic Atoms through Correlations in Atom Shot Noise*, Phys. Rev. Lett. **94**, 110401 (2005).

[Gri05] A. Griesmaier, J. Werner, S. Hensler, J. Stuhler, and T. Pfau, *Bose-Einstein condensation of chromium*, Phys. Rev. Lett. **94**, 160401 (2005).

[Gri09] S. Grishkevich and A. Saenz, *Theoretical description of two ultracold atoms in a single site of a three-dimensional optical lattice using realistic interatomic interaction potentials*, Phys. Rev. A **80**, 013403 (2009).

[Gro61] E. Gross, *Structure of a quantized vortex in boson systems*, Il Nuovo Cimento (1955-1965) **20**, 454 (1961), 10.1007/BF02731494.

[Gün05] K. Günter, T. Stöferle, H. Moritz, M. Köhl, and T. Esslinger, *p-wave interactions in low-dimensional fermionic gases*, Physical Review Letters **95**, 1 (2005).

[Gün06] K. Günter, T. Stöferle, H. Moritz, M. Köhl, and T. Esslinger, *Bose-Fermi Mixtures in a Three-Dimensional Optical Lattice*, Phys. Rev. Lett. **96**, 180402 (2006).

[Gup02] S. Gupta, K. Dieckmann, Z. Hadzibabic, and D. E. Pritchard, *Contrast Interferometry using Bose-Einstein Condensates to Measure h/m and α*, Phys. Rev. Lett. **89**, 140401 (2002).

[Gus08a] M. Gustavsson, *A quantum gas with tunable interactions in an optical lattice*, Ph.D. thesis, University of Innsbruck (2008).

[Gus08b] M. Gustavsson, E. Haller, M. J. Mark, J. G. Danzl, G. Rojas-Kopeinig, and H.-C. Nägerl, *Control of interaction-induced dephasing of Bloch oscillations*, Phys. Rev. Lett. **100**, 080404 (2008).

[Gus10] M. Gustavsson, E. Haller, M. J. Mark, J. G. Danzl, R. Hart, A. J. Daley, and H.-C. Nägerl, *Interference of interacting matter waves*, New Journal of Physics **12**, 065029 (2010).

[Hac10] L. Hackermüller, U. Schneider, M. Moreno-Cardoner, T. Kitagawa, T. Best, S. Will, E. Demler, E. Altman, I. Bloch, and B. Paredes, *Anomalous Expansion of Attractively Interacting Fermionic Atoms in an Optical Lattice*, Science **327**, 1621 (2010).

[Had06] Z. Hadzibabic, P. Krüger, M. Cheneau, B. Battelier, and J. Dalibard, *Berezinskii-Kosterlitz-Thouless crossover in a trapped atomic gas*, Nature **441**, 1118 (2006).

[Hal36] H. V. Halbon Jr and P. Preiswerk, *Preuve expérimentale de la diffraction des neutrons*, Comptes Rendus Acad. Sci. Paris **203**, 73 (1936).

[Hal09] E. Haller, M. Gustavsson, M. J. Mark, J. G. Danzl, R. Hart, G. Pupillo, and H. C. Nägerl, *Realization of an excited, strongly correlated quantum gas phase*, Science **325**, 1224 (2009).

[Hal10a] E. Haller, *One dimensional systems with tunable interactions*, Ph.D. thesis, University of Innsbruck (2010).

[Hal10b] E. Haller, R. Hart, M. J. Mark, J. G. Danzl, L. Reichsöllner, and H.-C. Nägerl, *Inducing Transport in a Dissipation-Free Lattice with Super Bloch Oscillations*, Phys. Rev. Lett. **104**, 200403 (2010).

[Hal10c] E. Haller, R. Hart, M. J. Mark, J. G. Danzl, L. Reichsöllner, M. Gustavsson, M. Dalmonte, G. Pupillo, and H.-C. Nägerl, *Pinning quantum phase transition for a Luttinger liquid of strongly interacting bosons*, Nature **466**, 597 (2010).

[Hal10d] E. Haller, M. J. Mark, R. Hart, J. G. Danzl, L. Reichsöllner, V. Melezhik, P. Schmelcher, and H.-C. Nägerl, *Confinement-Induced Resonances in Low-Dimensional Quantum Systems*, Phys. Rev. Lett. **104**, 153203 (2010).

[Hal11] E. Haller, M. Rabie, M. J. Mark, J. G. Danzl, R. Hart, K. Lauber, G. Pupillo, and H.-C. Nägerl, *Three-Body Correlation Functions and Recombination Rates for Bosons in Three Dimensions and One Dimension*, Phys. Rev. Lett. **107**, 230404 (2011).

[Han06] E. Hansis, *diploma thesis* (2006).

[Har04] T. Hartmann, F. Keck, H. J. Korsch, and S. Mossmann, *Dynamics of Bloch oscillations*, New Journal of Physics **6**, 2 (2004).

[Har05] D. M. Harber, J. M. Obrecht, J. M. McGuirk, and E. A. Cornell, *Measurement of the Casimir-Polder force through center-of-mass oscillations of a Bose-Einstein condensate*, Phys. Rev. A **72**, 033610 (2005).

[Har07] R. A. Hart, X. Xu, R. Legere, and K. Gibble, *A quantum scattering interferometer*, Nature **446**, 892 (2007).

[Her03] J. Herbig, T. Kraemer, M. Mark, T. Weber, C. Chin, H.-C. Nägerl, and R. Grimm, *Preparation of a pure molecular quantum gas*, Science **301**, 1510 (2003).

[Hod11] S. S. Hodgman, R. G. Dall, A. G. Manning, K. G. H. Baldwin, and A. G. Truscott, *Direct Measurement of Long-Range Third-Order Coherence in Bose-Einstein Condensates*, Science **331**, 1046 (2011).

[Hof07] S. Hofferberth, I. Lesanovsky, B. Fischer, T. Schumm, and J. Schmiedmayer, *Non-equilibrium coherence dynamics in one-dimensional Bose gases*, Nature **449**, 324 (2007).

[Hof08] S. Hofferberth, I. Lesanovsky, T. Schumm, A. Imambekov, V. Gritsev, E. Demler, and J. Schmiedmayer, *Probing quantum and thermal noise in an interacting many-body system*, Nature Physics **4**, 489 (2008).

[Hub63] J. Hubbard, *Electron Correlations in Narrow Energy Bands*, Proceedings of the Royal Society of London. Series A, Mathematical and Physical Sciences **276**, pp. 238 (1963).

[Hud02] J. J. Hudson, B. E. Sauer, M. R. Tarbutt, and E. A. Hinds, *Measurement of the electron electric dipole moment using YbF molecules*, Phys. Rev. Lett. **89**, 023003 (2002).

[Hun10] C.-L. Hung, X. Zhang, N. Gemelke, and C. Chin, *Slow Mass Transport and Statistical Evolution of an Atomic Gas across the Superfluid–Mott-Insulator Transition*, Phys. Rev. Lett. **104**, 160403 (2010).

[Iij91] S. Iijima, *Helical microtubules of graphitic carbon*, Nature **354**, 56 (1991).

[Ima97] A. Imamoglu, M. Lewenstein, and L. You, *Inhibition of Coherence in Trapped Bose-Einstein Condensates*, Physical Review Letters **78**, 2511 (1997).

[Ing08] M. Inguscio, W. Ketterle, and C. Salomon (Eds.), *Ultracold Fermi gases, Proceedings of the international school of physics "Enrico Fermi", Course CLXIV, Varenna, June 2006*, IOS Press, Amsterdam, 2008.

[Ino98] S. Inouye, M. R. Andrews, J. Stenger, H.-J. Miesner, D. M. Stamper-Kurn, and W. Ketterle, *Observation of Feshbach resonances in a Bose-Einstein condensate*, Nature **392**, 151 (1998).

[Iuc06] A. Iucci, M. Cazalilla, A. Ho, and T. Giamarchi, *Energy absorption of a Bose gas in a periodically modulated optical lattice*, Physical Review A **73**, 1 (2006).

[Iva08] V. V. Ivanov, A. Alberti, M. Schioppo, G. Ferrari, M. Artoni, M. L. Chiofalo, and G. M. Tino, *Coherent Delocalization of Atomic Wave Packets in Driven Lattice Potentials*, Physical Review Letters **100**, 043602 (2008).

[Jac11] T. Jacqmin, J. Armijo, T. Berrada, K. V. Kheruntsyan, and I. Bouchoule, *Sub-Poissonian Fluctuations in a 1D Bose Gas: From the Quantum Quasicondensate to the Strongly Interacting Regime*, Phys. Rev. Lett. **106**, 230405 (2011).

[Jak98] D. Jaksch, C. Bruder, J. I. Cirac, C. W. Gardiner, and P. Zoller, *Cold bosonic atoms in optical lattices*, Phys. Rev. Lett. **81**, 3108 (1998).

[Jak02] D. Jaksch, V. Venturi, J. I. Cirac, C. J. Williams, and P. Zoller, *Creation of a Molecular Condensate by Dynamically Melting a Mott Insulator*, Phys. Rev. Lett. **89**, 040402 (2002).

[Jak05] D. Jaksch and P. Zoller, *The cold atom Hubbard toolbox*, Annals of Physics **315**, 52 (2005).

[Jan03] E. Jané, G. Vidal, W. Dür, P. Zoller, and J. Cirac, *Simulation of quantum dynamics with quantum optical systems*, Quantum Information and Computation **3**, 15 (2003).

[Jel07] T. Jeltes, J. M. McNamara, W. Hogervorst, W. Vassen, V. Krachmalnicoff, M. Schellekens, A. Perrin, H. Chang, D. Boiron, A. Aspect, and C. I. Westbrook, *Comparison of the Hanbury Brown-Twiss effect for bosons and fermions*, Nature **445**, 402 (2007).

[Jön61] C. Jönsson, *Elektroneninterferenzen an mehreren künstlich hergestellten Feinspalten*, Zeitschrift für Physik A Hadrons and Nuclei **161**, 454 (1961), 10.1007/BF01342460.

[Joc03a] S. Jochim, M. Bartenstein, A. Altmeyer, G. Hendl, S. Riedl, C. Chin, J. Hecker Denschlag, and R. Grimm, *Bose-Einstein Condensation of Molecules*, Science **302**, 2101 (2003).

[Joc03b] S. Jochim, M. Bartenstein, A. Altmeyer, G. Hendl, C. Chin, J. Hecker Denschlag, and R. Grimm, *Pure Gas of Optically Trapped Molecules Created from Fermionic Atoms*, Phys. Rev. Lett **91**, 240402 (2003).

[Joh09] P. R. Johnson, E. Tiesinga, J. V. Porto, and C. J. Williams, *Effective three-body interactions of neutral bosons in optical lattices*, New Journal of Physics **11**, 093022 (2009).

[Jon06] K. M. Jones, E. Tiesinga, P. D. Lett, and P. S. Julienne, *Ultracold photoassociation spectroscopy: Long-range molecules and atomic scattering*, Reviews of Modern Physics **78**, 483 (2006).

[Jör08] R. Jördens, N. Strohmaier, K. Günter, H. Moritz, and T. Esslinger, *A Mott insulator of fermionic atoms in an optical lattice*, Nature **455**, 204 (2008).

[Kag85] Y. Kagan, B. Svistunov, and S. G.V., *Effect of Bose condensation on inelastic processes in gases*, Pis'ma Zh. Eksp. Teor. Fiz. **42**, 169 (1985).

[Kan95] Y. Kanemitsu and T. Ogawa, *Optical Properties of Low-Dimensional Materials*, World Scientific, Singapore, 1995.

[Kan09] A. Kantian, M. Dalmonte, S. Diehl, W. Hofstetter, P. Zoller, and A. J. Daley, *Atomic Color Superfluid via Three-Body Loss*, Phys. Rev. Lett. **103**, 240401 (2009).

[Kap00] A. E. Kaplan, I. Marzoli, W. E. Lamb, and W. P. Schleich, *Multimode interference: Highly regular pattern formation in quantum wave-packet evolution*, Phys. Rev. A **61**, 032101 (2000).

[Kas95] A. Kastberg, W. D. Phillips, S. L. Rolston, R. J. C. Spreeuw, and P. S. Jessen, *Adiabatic Cooling of Cesium to 700 nK in an Optical Lattice*, Phys. Rev. Lett. **74**, 1542 (1995).

[Kas06] J. Kasprzak, M. Richard, S. Kundermann, A. Baas, P. Jeambrun, J. M. J. Keeling, F. M. Marchetti, M. H. Szymanska, R. Andre, J. L. Staehli, V. Savona, P. B. Littlewood, B. Deveaud, and L. S. Dang, *Bose-Einstein condensation of exciton polaritons*, Nature **443**, 409 (2006).

[Kha02] L. Khaykovich, F. Schreck, G. Ferrari, T. Bourdel, J. Cubizolles, L. D. Carr, Y. Castin, and C. Salomon, *Formation of a Matter-Wave Bright Soliton*, Science **296**, 1290 (2002).

[Khe03] K. V. Kheruntsyan, D. M. Gangardt, P. D. Drummond, and G. V. Shlyapnikov, *Pair Correlations in a Finite-Temperature 1D Bose Gas*, Phys. Rev. Lett. **91**, 040403 (2003).

[Kim05] J. I. Kim, J. Schmiedmayer, and P. Schmelcher, *Quantum scattering in quasi-one-dimensional cylindrical confinement*, Phys Rev A **72**, 1 (2005).

[Kin04] T. Kinoshita, T. Wenger, and D. S. Weiss, *Observation of a one-dimensional Tonks-Girardeau gas*, Science **305**, 1125 (2004).

[Kin05] T. Kinoshita, T. Wenger, and D. S. Weiss, *Local Pair Correlations in One-Dimensional Bose Gases*, Phys. Rev. Lett. **95**, 190406 (2005).

[Kin06] T. Kinoshita, T. Wenger, and D. S. Weiss, *A quantum Newton's cradle*, Nature **440**, 900 (2006).

[Kla10] J. Klaers, J. Schmitt, F. Vewinger, and M. Weitz, *Bose-Einstein condensation of photons in an optical microcavity*, Nature **468**, 545 (2010).

[Koh59] W. Kohn, *Analytic Properties of Bloch Waves and Wannier Functions*, Phys. Rev. **115**, 809 (1959).

[Köh05] M. Köhl, H. Moritz, T. Stöferle, K. Günter, and T. Esslinger, *Fermionic Atoms in a Three Dimensional Optical Lattice: Observing Fermi Surfaces, Dynamics, and Interactions*, Phys. Rev. Lett. **94** (2005).

[Köh06] T. Köhler, K. Góral, and P. S. Julienne, *Production of cold molecules via magnetically tunable Feshbach resonances*, Rev. Mod. Phys. **78**, 1311 (2006).

[Kol06] C. Kollath, A. Iucci, T. Giamarchi, W. Hofstetter, and U. Schollwöck, *Spectroscopy of Ultracold Atoms by Periodic Lattice Modulations*, Phys. Rev. Lett. **97**, 050402 (2006).

[Kol07] C. Kollath, A. M. Läuchli, and E. Altman, *Quench Dynamics and Nonequilibrium Phase Diagram of the Bose-Hubbard Model*, Phys. Rev. Lett. **98**, 180601 (2007).

[Kol09] A. Kolovsky and H. Korsch, *Dynamics of interacting atoms in driven tilted optical lattices*, Arxiv preprint arXiv:0912.2587 (2009).

[Kor03] H. Korsch, *An algebraic solution of driven single band tight binding dynamics*, Physical Review A **317**, 54 (2003).

[Kor09] M. Kormos, G. Mussardo, and A. Trombettoni, *Expectation Values in the Lieb-Liniger Bose Gas*, Phys. Rev. Lett. **103**, 210404 (2009).

[Kor11] M. Kormos, Y.-Z. Chou, and A. Imambekov, *Exact three-body local correlations for arbitrary excited states of the 1D Bose gas* (2011).

[Kra92] W. Krauth, M. Caffarel, and J.-P. Bouchaud, *Gutzwiller wave function for a model of strongly interacting bosons*, Phys. Rev. B **45**, 3137 (1992).

[Kra04] T. Kraemer, J. Herbig, M. Mark, T. Weber, C. Chin, H.-C. Nägerl, and R. Grimm, *Optimized production of a cesium Bose-Einstein condensate*, Appl. Phys. B **79**, 1013 (2004).

[Kra06] T. Kraemer, M. Mark, P. Waldburger, J. G. Danzl, C. Chin, B. Engeser, A. D. Lange, K. Pilch, A. Jaakkola, H.-C. Nägerl, and R. Grimm, *Evidence for Efimov quantum states in an ultracold gas of caesium atoms*, Nature **440**, 315 (2006).

[Kra09] S. Kraft, F. Vogt, O. Appel, F. Riehle, and U. Sterr, *Bose-Einstein condensation of alkaline earth atoms:* ^{40}Ca, Phys. Rev. Lett. **103**, 130401 (2009).

[Kre05] R. Krems, *Molecules near absolute zero and external field control of atomic and molecular dynamics*, International Reviews in Physical Chemistry **24**, 99 (2005).

[Kre08] R. Krems, *Cold controlled chemistry*, Phys. Chem. Chem. Phys. **10**, 4079 (2008).

[Krz89] Krzysztof and Patorski, *I The Self-Imaging Phenomenon and its Applications*, vol. 27 of *Progress in Optics*, 1 – 108, Elsevier, 1989.

[Kuz08] E. Kuznetsova, P. Pellegrini, R. Côté, M. D. Lukin, and S. F. Yelin, *Formation of deeply bound molecules via chainwise adiabatic passage*, Phys. Rev. A **78**, 021402(R) (2008).

[Lah09] T. Lahaye, C. Menotti, L. Santos, M. Lewenstein, and T. Pfau, *The physics of dipolar bosonic quantum gases*, Rep. Prog. Phys. **72**, 126401 (2009).

[Lam10] G. Lamporesi, J. Catani, G. Barontini, Y. Nishida, M. Inguscio, and F. Minardi, *Scattering in mixed dimensions with ultracold gases*, Physical Review Letters **104**, 5 (2010).

[Lan77] L. D. Landau and E. M. Lifshitz, *Quantum Mechanics, vol. 3 (Course of theoretical physics)*, Butterworth-Heinemann, Oxford, 1977.

[Lan08a] F. Lang, P. van der Straten, B. Brandstätter, G. Thalhammer, K. Winkler, P. S. Julienne, R. Grimm, and J. Hecker Denschlag, *Cruising through molecular bound-state manifolds with radiofrequency*, Nature Phys. **4**, 223 (2008).

[Lan08b] F. Lang, K. Winkler, C. Strauss, R. Grimm, and J. Hecker Denschlag, *Ultracold Triplet Molecules in the Rovibrational Ground State*, Phys. Rev. Lett. **101**, 133005 (2008).

[Lan09] A. D. Lange, K. Pilch, A. Prantner, F. Ferlaino, B. Engeser, H.-C. Nägerl, R. Grimm, and C. Chin, *Determination of atomic scattering lengths from measurements of molecular binding energies near Feshbach resonances*, Phys. Rev. A **79**, 013622 (2009).

[Lau48] E. Lau, *Beugungserscheinungen an Doppelrastern*, Annalen der Physik **437**, 417 (1948).

[Leg06] A. J. Leggett, *What DO we know about high Tc?*, Nature Physics **2**, 134 (2006).

[Leo92] K. Leo, *Observation of Bloch oscillations in a semiconductor superlattice*, Solid State Communications **84**, 943 (1992).

[Lew04] M. Lewenstein, L. Santos, M. A. Baranov, and H. Fehrmann, *Atomic Bose-Fermi Mixtures in an Optical Lattice*, Phys. Rev. Lett. **92**, 050401 (2004).

[Lew07] M. Lewenstein, A. Sanpera, V. Ahufinger, B. Damski, A. Sen, and U. Sen, *Ultracold atomic gases in optical lattices: mimicking condensed matter physics and beyond*, Adv. Phys. **56**, 243 (2007).

[Li07] W. Li, A. K. Tuchman, H.-C. Chien, and M. A. Kasevich, *Extended Coherence Time with Atom-Number Squeezed States*, Phys. Rev. Lett. **98**, 040402 (2007).

[Lie63] E. H. Lieb and W. Liniger, *Exact analysis of an interacting Bose gas. I. The general solution and the ground state*, Phys. Rev. **130**, 1605 (1963).

[Lie03] A. Liem, J. Limpert, H. Zellmer, and A. Tünnermann, *100-W single-frequency master-oscillator fiber power amplifier*, Opt. Lett. **28**, 1537 (2003).

[Lig07] H. Lignier, C. Sias, D. Ciampini, Y. Singh, A. Zenesini, O. Morsch, and E. Arimondo, *Dynamical Control of Matter-Wave Tunneling in Periodic Potentials*, Phys. Rev. Lett. **99**, 220403 (2007).

[Lis01] C. Lisdat, O. Dulieu, H. Knöckel, and E. Tiemann, *Inversion analysis of K_2 coupled electronic states with the Fourier grid method*, The European Physical Journal D **17**, 319 (2001).

[Lof02] T. Loftus, C. A. Regal, C. Ticknor, J. L. Bohn, and D. S. Jin, *Resonant Control of Elastic Collisions in an Optically Trapped Fermi Gas of Atoms*, Phys. Rev. Lett. **88**, 173201 (2002).

[Lu11] M. Lu, N. Q. Burdick, S. H. Youn, and B. L. Lev, *Strongly Dipolar Bose-Einstein Condensate of Dysprosium*, Phys. Rev. Lett. **107**, 190401 (2011).

[Lüh09] D.-S. Lühmann, K. Bongs, and D. Pfannkuche, *Excitation spectrum of Mott shells in optical lattices*, Journal of Physics B: Atomic, Molecular and Optical Physics **42**, 145305 (2009).

[Lüh11] D.-S. Lühmann, O. Jürgensen, and K. Sengstock, *Multi-orbital and density-induced tunneling of bosons in optical lattices* (2011), arXiv:1108.3013v1.

[Mad00] K. W. Madison, F. Chevy, W. Wohlleben, and J. Dalibard, *Vortex Formation in a Stirred Bose-Einstein Condensate*, Phys. Rev. Lett. **84**, 806 (2000).

[Mal97] V. S. Malinovsky and D. J. Tannor, *Simple and robust extension of the stimulated Raman adiabatic passage technique to N-level systems*, Phys. Rev. A **56**, 4929 (1997).

[Man02] M. R. Manaa, A. J. Ross, F. Martin, P. Crozet, A. M. Lyyra, L. Li, C. Amiot, and T. Bergeman, *Spin–orbit interactions, new spectral data, and deperturbation of the coupled $b^3\prod_u$ and $A_1\sum_u^+$ states of K_2*, The Journal of Chemical Physics **117**, 11208 (2002).

[Mar05] M. Mark, T. Kraemer, J. Herbig, C. Chin, H.-C. Nägerl, and R. Grimm, *Efficient creation of molecules from a cesium Bose-Einstein condensate*, Europhys. Lett. **69**, 706 (2005).

[Mar07a] M. Mark, F. Ferlaino, S. Knoop, J. G. Danzl, T. Kraemer, C. Chin, H.-C. Nägerl, and R. Grimm, *Spectroscopy of ultracold trapped cesium Feshbach molecules*, Phys. Rev. A **76**, 042514 (2007).

[Mar07b] M. Mark, T. Kraemer, P. Waldburger, J. Herbig, C. Chin, H.-C. Nägerl, and R. Grimm, *Stückelberg Interferometry with Ultracold Molecules*, Phys. Rev. Lett. **99** (2007).

[Mar09] M. J. Mark, J. G. Danzl, E. Haller, M. Gustavsson, N. Bouloufa, O. Dulieu, H. Salami, T. Bergeman, H. Ritsch, R. Hart, and H.-C. Nägerl, *Dark resonances for ground-state transfer of molecular quantum gases*, Appl. Phys. B **95**, 219 (2009).

[Mar11a] M. J. Mark, E. Haller, J. G. Danzl, K. Lauber, M. Gustavsson, and H.-C. Nägerl, *Demonstration of the temporal matter-wave Talbot effect for trapped matter waves*, New Journal of Physics **13**, 085008 (2011).

[Mar11b] M. J. Mark, E. Haller, K. Lauber, J. G. Danzl, A. J. Daley, and H.-C. Nägerl, *Precision Measurements on a Tunable Mott Insulator of Ultracold Atoms*, Phys. Rev. Lett. **107**, 175301 (2011).

[Mar11c] M. J. Mark, E. Haller, K. Lauber, J. G. Danzl, A. Janisch, H. P. Büchler, A. J. Daley, and H.-C. Nägerl, *Preparation and spectroscopy of a metastable Mott insulator state with attractive interaction* (2011), submitted for publication.

[Mat99] M. R. Matthews, B. P. Anderson, P. C. Haljan, D. S. Hall, C. E. Wieman, and E. A. Cornell, *Vortices in a Bose-Einstein Condensate*, Phys. Rev. Lett. **83**, 2498 (1999).

[McG65] J. B. McGuire, *Interacting fermions in one dimension. I. Repulsive potential*, Journal of Mathematical Physics **6**, 432 (1965).

[Mee09] S. A. Meek, H. Conrad, and G. Meijer, *Trapping molecules on a chip*, Science **324**, 1699 (2009).

[Mel07] V. Melezhik, J. Kim, and P. Schmelcher, *Wave-packet dynamical analysis of ultracold scattering in cylindrical waveguides*, Physical Review A **76**, 053611 (2007).

[Men02] C. Menotti and S. Stringari, *Collective oscillations of a one-dimensional trapped Bose-Einstein gas*, Physical Review A **66**, 043610 (2002).

[Men09] J. Mentink and S. Kokkelmans, *Two interacting atoms in an optical lattice site with anharmonic terms*, Phys. Rev. A **79**, 032709 (2009).

[Mig85] A. L. Migdall, J. V. Prodan, W. D. Phillips, T. H. Bergeman, and H. J. Metcalf, *First Observation of Magnetically Trapped Neutral Atoms*, Phys. Rev. Lett. **54**, 2596 (1985).

[Mis77] B. Misra and E. C. G. Sudarshan, *The Zeno's paradox in quantum theory*, J. Math. Phys. **18**, 756 (1977).

[Mod01] G. Modugno, G. Ferrari, G. Roati, R. J. Brecha, A. Simoni, and M. Inguscio, *Bose-Einstein Condensation of Potassium Atoms by Sympathetic Cooling*, Science **294**, 1320 (2001).

[Mor01] O. Morsch, J. H. Müller, M. Cristiani, D. Ciampini, and E. Arimondo, *Bloch Oscillations and Mean-Field Effects of Bose-Einstein Condensates in 1D Optical Lattices*, Phys. Rev. Lett. **87**, 140402 (2001).

[Mor03a] H. Moritz, T. Stöferle, M. Köhl, and T. Esslinger, *Exciting collective oscillations in a trapped 1D gas*, Physical Review Letters **91**, 250402 (2003).

[Mor03b] O. Morsch, J. Müller, D. Ciampini, M. Cristiani, P. Blakie, C. Williams, P. Julienne, and E. Arimondo, *Decay and revival of phase coherence of a Bose-Einstein condensate in a one-dimensional lattice*, Physical Review A **67** (2003).

[Mot37] N. F. Mott and R. Peierls, *Discussion of the paper by de Boer and Verwey*, Proceedings of the Physical Society **49**, 72 (1937).

[Mot49] N. F. Mott, *The Basis of the Electron Theory of Metals, with Special Reference to the Transition Metals*, Proceedings of the Physical Society. Section A **62**, 416 (1949).

[Mun07] J. Mun, P. Medley, G. Campbell, L. Marcassa, D. Pritchard, and W. Ketterle, *Phase Diagram for a Bose-Einstein Condensate Moving in an Optical Lattice*, Physical Review Letters **99**, 1 (2007).

[Nai07] P. Naidon, E. Tiesinga, W. F. Mitchell, and P. S. Julienne, *Effective-range description of a Bose gas under strong one- or two-dimensional confinement*, New Journal of Physics **9**, 19 (2007).

[Nar98] M. Naraschewski and D. M. Stamper-Kurn, *Analytical description of a trapped semi-ideal Bose gas at finite temperature*, Phys. Rev. A **58**, 2423 (1998).

[Nar08] E. Narevicius, A. Libson, C. G. Parthey, I. Chavez, J. Narevicius, U. Even, and M. G. Raizen, *Stopping supersonic oxygen with a series of pulsed electromagnetic coils: A molecular coilgun*, Phys. Rev. A **77**, 051401 (2008).

[Neu78] W. Neuhauser, M. Hohenstatt, P. Toschek, and H. Dehmelt, *Optical-Sideband Cooling of Visible Atom Cloud Confined in Parabolic Well*, Phys. Rev. Lett. **41**, 233 (1978).

[Ni08] K.-K. Ni, S. Ospelkaus, M. H. G. de Miranda, A. Pe'er, B. Neyenhuis, J. J. Zirbel, S. Kotochigova, P. S. Julienne, D. S. Jin, and J. Ye, *A High Phase-Space-Density Gas of Polar Molecules*, Science **322**, 231 (2008).

[Nie99] E. Nielsen and J. H. Macek, *Low-energy recombination of identical bosons by three-body collisions*, Phys. Rev. Lett. **83**, 1566 (1999).

[Nik00] A. N. Nikolov, J. R. Ensher, E. E. Eyler, H. Wang, W. C. Stwalley, and P. L. Gould, *Efficient Production of Ground-State Potassium Molecules at Sub-mK Temperatures by Two-Step Photoassociation*, Phys. Rev. Lett. **84**, 246 (2000).

[Nov04] K. S. Novoselov, A. K. Geim, S. V. Morozov, D. Jiang, Y. Zhang, S. V. Dubonos, I. V. Grigorieva, and A. A. Firsov, *Electric Field Effect in Atomically Thin Carbon Films*, Science **306**, 666 (2004).

[Now97] S. Nowak, C. Kurtsiefer, T. Pfau, and C. David, *High-order Talbot fringes for atomic matter waves*, Opt. Lett. **22**, 1430 (1997).

[O'H04] K. M. O'Hara, B. Laburthe Tolra, J. H. Huckans, W. D. Phillips, S. L. Rolston, and J. V. Porto, *Observation of Reduced Three-Body Recombination in a Correlated 1D Degenerate Bose Gas*, Physical Review Letters **92**, 190401 (2004).

[Ols98] M. Olshanii, *Atomic scattering in the presence of an external confinement and a gas of impenetrable bosons*, Phys. Rev. Lett. **81**, 938 (1998).

[Osp06a] C. Ospelkaus, S. Ospelkaus, L. Humbert, P. Ernst, K. Sengstock, and K. Bongs, *Ultracold Heteronuclear Molecules in a 3D Optical Lattice*, Phys. Rev. Lett. **97** (2006).

[Osp06b] S. Ospelkaus, C. Ospelkaus, L. Humbert, K. Sengstock, and K. Bongs, *Tuning of Heteronuclear Interactions in a Degenerate Fermi-Bose Mixture*, Phys. Rev. Lett. **97**, 120403 (2006).

[Osp06c] S. Ospelkaus, C. Ospelkaus, O. Wille, M. Succo, P. Ernst, K. Sengstock, and K. Bongs, *Localization of Bosonic Atoms by Fermionic Impurities in a Three-Dimensional Optical Lattice*, Phys. Rev. Lett. **96**, 180403 (2006).

[Osp08] S. Ospelkaus, A. Pe'er, K. K. Ni, J. J. Zirbel, B. Neyenhuis, S. Kotochigova, P. S. Julienne, J. Ye, and D. S. Jin, *Efficient state transfer in an ultracold dense gas of heteronuclear molecules*, Nature Phys. **4**, 622 (2008).

[Osp10] S. Ospelkaus, K.-K. Ni, D. Wang, M. H. G. de Miranda, B. Neyenhuis, G. Quemener, P. S. Julienne, J. L. Bohn, D. S. Jin, and J. Ye, *Quantum-state controlled chemical reactions of ultracold potassium-rubidium molecules*, Science **327**, 853 (2010).

[Ött05] A. Öttl, S. Ritter, M. Köhl, and T. Esslinger, *Correlations and Counting Statistics of an Atom Laser*, Phys. Rev. Lett. **95**, 090404 (2005).

[Par04] B. Paredes, A. Widera, V. Murg, O. Mandel, S. Fölling, I. Cirac, G. V. Shlyapnikov, T. W. Hänsch, and I. Bloch, *Tonks-Girardeau gas of ultracold atoms in an optical lattice*, Nature **429**, 277 (2004).

[Par07] B. Paredes, T. Keilmann, and J. I. Cirac, *Pfaffian-like ground state for three-body hard-core bosons in one-dimensional lattices*, Phys. Rev. A **75**, 053611 (2007).

[Pea05] V. Peano, M. Thorwart, C. Mora, and R. Egger, *Confinement-induced resonances for a two-component ultracold atom gas in arbitrary quasi-one-dimensional traps*, New Journal of Physics **7**, 192 (2005).

[Pet00a] D. Petrov, M. Holzmann, and G. Shlyapnikov, *Bose-Einstein condensation in quasi-2D trapped gases*, Physical Review Letters **84**, 2551 (2000).

[Pet00b] D. Petrov, G. Shlyapnikov, and J. Walraven, *Regimes of Quantum Degeneracy in Trapped 1D Gases*, Physical Review Letters **85**, 3745 (2000).

[Pet01] D. S. Petrov and G. V. Shlyapnikov, *Interatomic collisions in a tightly confined Bose gas*, Physical Review A **64**, 012706 (2001).

[Pet07] D. Petrov, D. Gangardt, and G. V. Shlyapnikov, *Low-dimensional trapped gases*, J. Phys. IV France **1**, 1 (2007).

[Phi82] W. D. Phillips and H. Metcalf, *Laser Deceleration of an Atomic Beam*, Phys. Rev. Lett. **48**, 596 (1982).

[Pil09] K. Pilch, A. D. Lange, A. Prantner, G. Kerner, F. Ferlaino, H.-C. Nägerl, and R. Grimm, *Observation of interspecies Feshbach resonances in an ultracold Rb-Cs mixture*, Phys. Rev. A **79**, 042718 (2009).

[Pit61] L. P. Pitaevskii, *Vortex lines in an imperfect Bose gas*, Sov. Phys. JETP **13**, 451 (1961).

[Pok79] V. Pokrovsky and A. Talapov, *Ground State, Spectrum, and Phase Diagram of Two-Dimensional Incommensurate Crystals*, Physical Review Letters **42**, 65 (1979).

[Por11] J. Portegies and S. Kokkelmans, *Efimov Trimers in a Harmonic Potential*, Few-Body Systems **51**, 219 (2011), 10.1007/s00601-011-0237-6.

[Pup09] G. Pupillo, A. Micheli, H. P. Büchler, and P. Zoller, *Condensed matter physics with cold polar molecules*, in: R. V. Krems, W. C. Stwalley, and B. Friedrich (Eds.), chap. 12 in *Cold molecules: Theory, experiment, applications*, CRC Press, Boca Raton, 2009.

[Qi07] P. Qi, J. Bai, E. Ahmed, A. M. Lyyra, S. Kotochigova, A. J. Ross, C. Effantin, P. Zalicki, J. Vigué, G. Chawla, R. W. Field, T.-J. Whang, W. C. Stwalley, H. Knöckel, E. Tiemann, J. Shang, L. Li, and T. Bergeman, *New spectroscopic data, spin-orbit functions, and*

global analysis of data on the $A_1\Sigma_u^+$ and $b^3\Pi_u$ states of Na_2, The Journal of Chemical Physics **127**, 044301 (2007).

[Rap99] S. Rapsch, U. Schollwöck, and W. Zwerger, *Density matrix renormalization group for disordered bosons in one dimension*, Europhysics Letters **46**, 559 (1999).

[Rap10] A. Rapp, S. Mandt, and A. Rosch, *Equilibration Rates and Negative Absolute Temperatures for Ultracold Atoms in Optical Lattices*, Phys. Rev. Lett. **105**, 220405 (2010).

[Rau74] H. Rauch, W. Treimer, and U. Bonse, *Test of a single crystal neutron interferometer*, Physics Letters A **47**, 369 (1974).

[Ray81] L. Rayleigh, *On copying diffraction-gratings, and on some phenomena connected therewith*, Philos. Mag. **11**, 196 (1881).

[Reg03] C. A. Regal, C. Ticknor, J. L. Bohn, and D. S. Jin, *Creation of Ultracold Molecules from a Fermi Gas of Atoms*, Nature **424**, 47 (2003).

[Rei09] T. Reisinger, A. A. Patel, H. Reingruber, K. Fladischer, W. E. Ernst, G. Bracco, H. I. Smith, and B. Holst, *Poisson's spot with molecules*, Phys. Rev. A **79**, 053823 (2009).

[Rie08] S. Riedl, E. R. Sánchez Guajardo, C. Kohstall, A. Altmeyer, M. J. Wright, J. Hecker Denschlag, R. Grimm, G. M. Bruun, and H. Smith, *Collective oscillations of a Fermi gas in the unitarity limit: Temperature effects and the role of pair correlations*, Phys. Rev. A **78**, 053609 (2008).

[Roa02] G. Roati, F. Riboli, G. Modugno, and M. Inguscio, *Fermi-Bose Quantum Degenerate K-Rb Mixture with Attractive Interaction*, Phys. Rev. Lett. **89**, 150403 (2002).

[Roa04] G. Roati, E. de Mirandes, F. Ferlaino, H. Ott, G. Modugno, and M. Inguscio, *Atom Interferometry with Trapped Fermi Gases*, Phys. Rev. Lett. **92**, 230402 (2004).

[Roa07] G. Roati, M. Zaccanti, C. D'Errico, J. Catani, M. Modugno, A. Simoni, M. Inguscio, and G. Modugno, *^{39}K Bose-Einstein Condensate with Tunable Interactions*, Phys. Rev. Lett. **99** (2007).

[Rob01] A. Robert, O. Sirjean, A. Browaeys, J. Poupard, S. Nowak, D. Boiron, C. I. Westbrook, and A. Aspect, *A Bose-Einstein Condensate of Metastable Atoms*, Science **292**, 461 (2001).

[Roj07] G. Rojas Kopeinig, *A tunable Bose-Einstein condensate in a three-dimensional optical lattice potential*, Diploma thesis, University of Innsbruck (2007).

[Rom06] T. Rom, T. Best, D. van Oosten, U. Schneider, S. Fölling, B. Paredes, and I. Bloch, *Free fermion antibunching in a degenerate atomic Fermi gas released from an optical lattice*, Nature **444**, 733 (2006).

[Ruo01] J. Ruostekoski, B. Kneer, W. P. Schleich, and G. Rempe, *Interference of a Bose-Einstein condensate in a hard-wall trap: From the nonlinear Talbot effect to the formation of vorticity*, Phys. Rev. A **63**, 043613 (2001).

[Sac00] S. Sachdev, *Quantum Phase Transitions*, Cambridge University Press, Cambridge UK, 2000.

[Sae08] S. Saeidian, V. Melezhik, and P. Schmelcher, *Multichannel atomic scattering and confinement-induced resonances in waveguides*, Physical Review A **77**, 042721 (2008).

[Sag05] J. M. Sage, S. Sainis, T. Bergeman, and D. DeMille, *Optical production of ultracold polar molecules*, Phys. Rev. Lett. **94**, 203001 (2005).

[Sal08a] H. Salami, T. Bergeman, B. Beser, J. Bai, E. Ahmed, S. Kotochigova, A. M. Lyyra, J. Huennekens, C. Lisdat, O. Dulieu, P. Crozet, and A. J. Ross, *manuscript in preparation* (2008).

[Sal08b] H. Salami, T. Bergeman, O. Dulieu, D. Li, F. Xie, and L. Li, *manuscript in preparation* (2008).

[Sal09] T. Salger, S. Kling, T. Hecking, C. Geckeler, L. Morales-Molina, and M. Weitz, *Directed transport of atoms in a Hamiltonian quantum ratchet*, Science **326**, 1241 (2009).

[Sch93] J. Schmiedmayer, C. R. Ekstrom, M. S. Chapman, T. D. Hammond, and D. E. Pritchard, *Fundamentals of Quantum Optics III, Proceedings, Kühtai, Austria, edited by F. Ehlotzky (Springer Verlag, Berlin)*, Lecture Notes in Physics **420** (1993).

[Sch01] J. Schuster, A. Marte, S. Amtage, B. Sang, G. Rempe, and H. C. W. Beijerinck, *Avalanches in a Bose-Einstein Condensate*, Phys. Rev. Lett. **87**, 170404 (2001).

[Sch05] M. Schellekens, R. Hoppeler, A. Perrin, J. V. Gomes, D. Boiron, A. Aspect, and C. I. Westbrook, *Hanbury Brown Twiss Effect for Ultracold Quantum Gases*, Science **310**, 648 (2005).

[Sch08] U. Schneider, L. Hackermüller, S. Will, T. Best, I. Bloch, T. A. Costi, R. W. Helmes, D. Rasch, and A. Rosch, *Metallic and Insulating Phases of Repulsively Interacting Fermions in a 3D Optical Lattice*, Science **322**, 204 (2008).

[Sch09a] A. Schirotzek, C.-H. Wu, A. Sommer, and M. W. Zwierlein, *Observation of Fermi polarons in a tunable Fermi liquid of ultracold atoms*, Phys. Rev. Lett. **102**, 230402 (2009).

[Sch09b] P.-I. Schneider, S. Grishkevich, and A. Saenz, *Ab initio determination of Bose-Hubbard parameters for two ultracold atoms in an optical lattice using a three-well potential*, Phys. Rev. A **80**, 013404 (2009).

[Sch09c] M. Schnell and G. Meijer, *Cold Molecules: Preparation, applications, and challenges*, Angew. Chem. Int. Ed. **48**, 6010 (2009).

[Sch10] J. Schachenmayer, G. Pupillo, and A. J. Daley, *Time-dependent currents of one-dimensional bosons in an optical lattice*, New Journal of Physics **12**, 025014 (2010).

[She10] J. F. Sherson, C. Weitenberg, M. Endres, M. Cheneau, I. Bloch, and S. Kuhr, *Single-atom-resolved fluorescence imaging of an atomic Mott insulator*, Nature **467**, 68 (2010).

[Sho91] B. W. Shore, K. Bergmann, J. Oreg, and S. Rosenwaks, *Multilevel adiabatic population transfer*, Phys. Rev. A **44**, 7442 (1991).

[Shu10] E. S. Shuman, J. F. Barry, and D. DeMille, *Laser cooling of a diatomic molecule*, Nature **467**, 820 (2010).

[Sia08] C. Sias, H. Lignier, Y. P. Singh, A. Zenesini, D. Ciampini, O. Morsch, and E. Arimondo, *Observation of Photon-Assisted Tunneling in Optical Lattices*, Physical Review Letters **100**, 040404 (2008).

[Sim11] J. Simon, W. S. Bakr, R. Ma, M. E. Tai, P. M. Preiss, and M. Greiner, *Quantum simulation of antiferromagnetic spin chains in an optical lattice*, Nature **472**, 307 (2011).

[Sme03] A. Smerzi and A. Trombettoni, *Nonlinear tight-binding approximation for Bose-Einstein condensates in a lattice*, Phys. Rev. A **68**, 023613 (2003).

[Sor09] F. Sorrentino, A. Alberti, G. Ferrari, V. V. Ivanov, N. Poli, M. Schioppo, and G. M. Tino, *Quantum sensor for atom-surface interactions below 10 μm*, Phys. Rev. A **79**, 013409 (2009).

[Sou02] K. e. Southwell, *Ultracold matter*, Nature (Insight) **416**, 205 (2002).

[SP11a] P. Soltan-Panahi, D.-S. Lühmann, J. Struck, P. Windpassinger, and K. Sengstock, *Quantum phase transition to unconventional multi-orbital superfluidity in optical lattices*, Nature Physics **8**, 71 (2011).

[SP11b] P. Soltan-Panahi, J. Struck, P. Hauke, A. Bick, W. Plenkers, G. Meineke, C. Becker, P. Windpassinger, M. Lewenstein, and K. Sengstock, *Multi-component quantum gases in spin-dependent hexagonal lattices*, Nature Physics **7**, 434 (2011).

[Spi07] I. B. Spielman, W. D. Phillips, and J. V. Porto, *Mott-Insulator Transition in a Two-Dimensional Atomic Bose Gas*, Phys. Rev. Lett. **98**, 080404 (2007).

[Sta06] P. Staanum, S. D. Kraft, J. Lange, R. Wester, and M. Weidemüller, *Experimental Investigation of Ultracold Atom-Molecule Collisions*, Phys. Rev. Lett. **96**, 023201 (2006).

[Ste08] H. Steinberg, G. Barak, A. Yacoby, L. N. Pfeiffer, K. W. West, B. I. Halperin, and K. Le Hur, *Charge fractionalization in quantum wires*, Nature Physics **4**, 116 (2008).

[Ste09] S. Stellmer, M. K. Tey, B. Huang, R. Grimm, and F. Schreck, *Bose-Einstein condensation of strontium*, Phys. Rev. Lett. **103**, 200401 (2009).

[Stö04] T. Stöferle, H. Moritz, C. Schori, M. Köhl, and T. Esslinger, *Transition from a Strongly Interacting 1D Superfluid to a Mott Insulator*, Physical Review Letters **92**, 1 (2004).

[Str02] K. E. Strecker, G. B. Partridge, A. G. Truscott, and R. G. Hulet, *Formation and Propagation of Matter-Wave Soliton Trains*, Nature **417**, 150 (2002).

[Str03] K. E. Strecker, G. B. Partridge, and R. G. Hulet, *Conversion of an Atomic Fermi Gas to a Long-Lived Molecular Bose Gas*, Phys. Rev. Lett. **91**, 080406 (2003).

[Str10] N. Strohmaier, D. Greif, R. Jördens, L. Tarruell, H. Moritz, T. Esslinger, R. Sensarma, D. Pekker, E. Altman, and E. Demler, *Observation of Elastic Doublon Decay in the Fermi-Hubbard Model*, Phys. Rev. Lett. **104**, 080401 (2010).

[Str11] J. Struck, C. Ölschläger, R. Le Targat, P. Soltan-Panahi, A. Eckardt, M. Lewenstein, P. Windpassinger, and K. Sengstock, *Quantum Simulation of Frustrated Classical Magnetism in Triangular Optical Lattices*, Science **333**, 996 (2011).

[Stw04] W. C. Stwalley, *Efficient conversion of ultracold Feshbach-resonance-related polar molecules into ultracold ground state ($X\,^1\Sigma^+ v = 0, J = 0$) molecules*, Eur. Phys. J. D **31**, 221 (2004).

[Sya08] N. Syassen, D. M. Bauer, M. Lettner, T. Volz, D. Dietze, J. J. Garcia-Ripoll, J. I. Cirac, G. Rempe, and S. Dürr, *Strong dissipation inhibits losses and induces correlations in cold molecular gases*, Science **320**, 1329 (2008).

[Tak03] Y. Takasu, K. Maki, K. Komori, T. Takano, K. Honda, M. Kumakura, T. Yabuzaki, and Y. Takahashi, *Spin-singlet Bose-Einstein condensation of two-electron atoms*, Phys. Rev. Lett. **91**, 040404 (2003).

[Tal36] H. F. Talbot, *Facts relating to optical science. No. IV*, Philos. Mag. **9**, 401 (1836).

[Tem08] E. Tempfli, S. Zöllner, and P. Schmelcher, *Excitations of attractive 1D bosons: binding versus fermionization*, New Journal of Physics **10**, 103021 (2008).

[Tha06] G. Thalhammer, K. Winkler, F. Lang, S. Schmid, R. Grimm, and J. Hecker Denschlag, *Long-lived Feshbach molecules in a three-dimensional optical lattice*, Phys. Rev. Lett. **96**, 050402 (2006).

[Tho02] Q. Thommen, J. Garreau, and V. Zehnlé, *Theoretical analysis of quantum dynamics in one-dimensional lattices: Wannier-Stark description*, Physical Review A **65**, 053406 (2002).

[Tie00] E. Tiesinga, C. Williams, F. Mies, and P. Julienne, *Interacting atoms under strong quantum confinement*, Physical Review A **61**, 063416 (2000).

[Tro08] S. Trotzky, P. Cheinet, S. Fölling, M. Feld, U. Schnorrberger, A. M. Rey, A. Polkovnikov, E. A. Demler, M. D. Lukin, and I. Bloch, *Time-Resolved Observation and Control of Superexchange Interactions with Ultracold Atoms in Optical Lattices*, Science **319**, 295 (2008).

[Tro11] S. Trotzky, Y.-A. Chen, A. Flesch, I. P. McCulloch, U. Schollwöck, J. Eisert, and I. Bloch, *Probing the relaxation towards equilibrium in an isolated strongly correlated 1D Bose gas* (2011).

[Tuc06] A. K. Tuchman, C. Orzel, A. Polkovnikov, and M. A. Kasevich, *Nonequilibrium coherence dynamics of a soft boson lattice*, Phys. Rev. A **74**, 051601 (2006).

[Unt05] P. Unterwaditzer, *Aufbau eines vollständigen Diodenlasersystems zur Laserkühlung und Detektion von gespeicherten Cs-Atomen*, Master's thesis, University of Innsbruck (2005).

[van08] S. van de Meerakker, T. Bethlem, and G. Meijer, *Taming molecular beams*, Nature Physics **4**, 595 (2008).

[Ver87] J. Verges and C. Amiot, *The $Cs_2 A^1 \sum_u^+ \rightarrow X^1 \sum_g^+$ fluorescence excited by the Ar^+ 1.09-μm laser line*, Journal of Molecular Spectroscopy **126**, 393 (1987).

[Vex11] R. Vexiau, N. Bouloufa, M. Aymar, J. Danzl, M. Mark, H. Nägerl, and O. Dulieu, *Optimal trapping wavelengths of Cs_2 molecules in an optical lattice*, The European Physical Journal D - Atomic, Molecular, Optical and Plasma Physics **65**, 243 (2011), 10.1140/epjd/e2011-20085-4.

[Vit08] M. Viteau, A. Chotia, M. Allegrini, N. Bouloufa, O. Dulieu, D. Comparat, and P. Pillet, *Optical Pumping and Vibrational Cooling of Molecules*, Science **321**, 232 (2008).

[Vol06] T. Volz, N. Syassen, D. Bauer, E. Hansis, S. Dürr, and G. Rempe, *Preparation of a quantum state with one molecule at each site of an optical lattice*, Nature Phys. **2**, 692 (2006).

[von09] J. von Stecher, J. P. D'Incao, and C. H. Greene, *Signatures of universal four-body phenomena and their relation to the Efimov effect*, Nature Phys. **5**, 417 (2009).

[Wal09] M. L. Wall and L. D. Carr, *Emergent timescales in entangled quantum dynamics of ultracold molecules in optical lattices*, New J. Phys. **11**, 055027 (2009).

[Was93] C. Waschke, H. G. Roskos, R. Schwedler, K. Leo, H. Kurz, and K. Köhler, *Coherent submillimeter-wave emission from Bloch oscillations in a semiconductor superlattice*, Phys. Rev. Lett. **70**, 3319 (1993).

[Web03a] T. Weber, J. Herbig, M. Mark, H.-C. Nägerl, and R. Grimm, *Bose-Einstein condensation of cesium*, Science **299**, 232 (2003).

[Web03b] T. Weber, J. Herbig, M. Mark, H.-C. Nägerl, and R. Grimm, *Three-body recombination at large scattering lengths in an ultracold atomic gas*, Phys. Rev. Lett. **91**, 123201 (2003).

[Wei85] W. Weickenmeier, U. Diemer, M. Wahl, M. Raab, W. Demtröder, and W. Müller, *Accurate ground state potential of Cs_2 up to the dissociation limit*, The Journal of Chemical Physics **82**, 5354 (1985).

[Wei99] J. Weiner, V. S. Bagnato, S. Zilio, and P. S. Julienne, *Experiments and theory in cold and ultracold collisions*, Rev. Mod. Phys. **71**, 1 (1999).

[Wei11] C. Weitenberg, M. Endres, J. F. Sherson, M. Cheneau, P. Schausz, T. Fukuhara, I. Bloch, and S. Kuhr, *Single-spin addressing in an atomic Mott insulator*, Nature **471**, 319 (2011).

[Wes04] S. Wessel, F. Alet, M. Troyer, and G. G. Batrouni, *Quantum Monte Carlo simulations of confined bosonic atoms in optical lattices*, Phys. Rev. A **70**, 053615 (2004).

[Wic02] A. Wicht, J. M. Hensley, E. Sarajlic, and S. Chu, *A Preliminary Measurement of the Fine Structure Constant Based on Atom Interferometry*, Physica Scripta **T102**, 82 (2002).

[Wil96] S. R. Wilkinson, C. F. Bharucha, K. W. Madison, Q. Niu, and M. G. Raizen, *Observation of atomic Wannier-Stark ladders in an accelerating optical potential.*, Physical Review Letters **76**, 4512 (1996).

[Wil08] E. Wille, F. M. Spiegelhalder, G. Kerner, D. Naik, A. Trenkwalder, G. Hendl, F. Schreck, R. Grimm, T. G. Tiecke, J. T. M. Walraven, S. J. J. M. F. Kokkelmans, E. Tiesinga, and P. S. Julienne, *Exploring an ultracold Fermi-Fermi mixture: Interspecies Feshbach resonances and scattering properties of* ^6Li *and* ^{40}K, Phys. Rev. Lett. **100**, 053201 (2008).

[Wil10] S. Will, T. Best, U. Schneider, L. Hackermüller, D.-S. Lühmann, and I. Bloch, *Time-resolved observation of coherent multi-body interactions in quantum phase revivals*, Nature **465**, 197 (2010).

[Win61] R. G. Winter, *Evolution of a Quasi-Stationary State*, Phys. Rev. **123**, 1503 (1961).

[Win78] D. J. Wineland, R. E. Drullinger, and F. L. Walls, *Radiation-Pressure Cooling of Bound Resonant Absorbers*, Phys. Rev. Lett. **40**, 1639 (1978).

[Win06] K. Winkler, G. Thalhammer, F. Lang, R. Grimm, J. Hecker Denschlag, A. J. Daley, A. Kantian, H. P. Büchler, and P. Zoller, *Repulsively bound atom pairs in an optical lattice*, Nature **441**, 853 (2006).

[Win07] K. Winkler, F. Lang, G. Thalhammer, P. van der Straten, R. Grimm, and J. Hecker Denschlag, *Coherent optical transfer of Feshbach molecules to a lower vibrational state*, Phys. Rev. Lett. **98**, 043201 (2007).

[Wit05] D. Witthaut, M. Werder, S. Mossmann, and H. J. Korsch, *Bloch oscillations of Bose-Einstein condensates: Breakdown and revival*, Phys. Rev. E **71**, 036625 (2005).

[Wyn00] R. Wynar, R. S. Freeland, D. J. Han, C. Ryu, and D. J. Heinzen, *Molecules in a Bose-Einstein Condensate*, Science **287**, 1016 (2000).

[Xie08] F. Xie, D. Li, L. Tyree, L. Li, V. B. Sovkov, V. S. Ivanov, S. Magnier, and A. M. Lyyra, *Observation and calculation of the* Cs_2 $2^3\Delta_{1g}$ *and* $b^3\Pi_{0u}$ *states*, The Journal of Chemical Physics **128**, 204313 (2008).

[Yas96] M. Yasuda and F. Shimizu, *Observation of Two-Atom Correlation of an Ultracold Neon Atomic Beam*, Phys. Rev. Lett. **77**, 3090 (1996).

[Ye08] J. Ye, H. J. Kimble, and H. Katori, *Quantum state engineering and precision metrology using state-insensitive light traps*, Science **320**, 1734 (2008).

[Yur05] V. Yurovsky, *Feshbach resonance scattering under cylindrical harmonic confinement*, Physical Review A **71**, 012709 (2005).

[Zac09] M. Zaccanti, B. Deissler, C. D'Errico, M. Fattori, M. Jona-Lasinio, S. Müller, G. Roati, M. Inguscio, and G. Modugno, *Observation of an Efimov spectrum in an atomic system*, Nature Phys. **5**, 586 (2009).

[Zah06] N. Zahzam, T. Vogt, M. Mudrich, D. Comparat, and P. Pillet, *Atom-Molecule Collisions in an Optically Trapped Gas*, Phys. Rev. Lett. **96** (2006).

[Zam79] A. Zamolodchikov, *Factorized S-matrices in two dimensions as the exact solutions of certain relativistic quantum field theory models*, Annals of Physics **120**, 253 (1979).

[Zam95] A. B. Zamolodchikov, *Mass scale in the sine-Gordon model and its reductions*, Int. J. Mod. Phys. **A10**, 1125 (1995).

[Zel08] T. Zelevinsky, S. Kotochigova, and J. Ye, *Precision test of mass-ratio variations with lattice-confined ultracold molecules*, Phys. Rev. Lett. **100**, 043201 (2008).

[Zen34] C. Zener, *A Theory of the Electrical Breakdown of Solid Dielectrics*, Proceedings of the Royal Society of London. Series A, Containing Papers of a Mathematical and Physical Character (1905-1934) **145**, 523 (1934).

[Zha08] R. Zhang, R. Sapiro, R. Mhaskar, and G. Raithel, *Role of the mean field in Bloch oscillations of a Bose-Einstein condensate in an optical lattice and harmonic trap*, Physical Review A **78** (2008).

[Zhe04] Y. Zheng, E. Let, M. Kostrun, J. Javanainen, and M. Kos, *Low-Acceleration Instability of a Bose-Einstein Condensate in an Optical Lattice*, Physical Review Letters **93**, 230401 (2004).

[Żuc10] P. S. Żuchowski and J. M. Hutson, *Reactions of ultracold alkali-metal dimers*, Phys. Rev. A **81**, 060703(R) (2010).

[Zwi03] M. W. Zwierlein, C. A. Stan, C. H. Schunck, S. M. F. Raupach, S. Gupta, Z. Hadzibabic, and W. Ketterle, *Observation of Bose-Einstein Condensation of Molecules*, Phys. Rev. Lett. **91**, 250401 (2003).

ACKNOWLEDGMENTS

This PhD work would not have been possible without the help and contributions of many people, especially since working on such an experiment is rather a team effort than a one-man show. First I want to thank Hanns-Christoph Nägerl, my supervisor, for giving me the opportunity to continue on this great experiment after my Diploma thesis. Especially his ability to keep the right balance between setting the scientific directions and giving room for the investigation of own ideas impressed me a lot. His scientific and technical knowledge were always very helpful and his paper writing skills are impressive. Rudi Grimm as the overall leader of the ultracold atoms group in Innsbruck constantly takes care of the collaborative environment which makes the running of such experiments possible. His strong commitment pushes the whole group and is one of the reasons that Innsbruck is a very attractive research place in this field.

Mattias Gustavsson built up our experiment from scratch and finished his PhD work already three years ago, and his hard work provided the basis for focusing on the scientific part. Also Elmar Haller as the second PhD student on the project put a lot of effort in the basic construction, especially in the high power laser setup and the camera program, and my understanding of physics always improved after a discussion with him. Johann Danzl was the responsible mastermind behind the experiments concerning the groundstate molecules and I really appreciated our nightly measurement series to find the first dark resonance for the molecules and our joint efforts to improve the electronics used in our lab. Russel Hart, who joined our lab as a post-Doc for two years, has brought a lot of experience from his precision measurements background into our lab, and physical discussions with him were always instructive. Our youngest PhD student Katharina Lauber brought a fresh wind into our lab and provided a lot of help in the last measurement stages.

Not only the CsIII-team but all people in the group of Rudi Grimm and Rainer Blatt provided an helpful and stimulating environment by enabling a lot of discussions at coffee breaks or after group meetings and group seminars. Also the theory support in form of our collaborations with many different theory groups, for example with Andrew Daley regarding the Mott insulator measurements, was very helpful and many experimental results would not have been

possible without it. A big thanks goes to our mechanical workshop, especially Anton Schönherr, Helmuth Jordan and Armin Sailer, and our electronics workshop with Arthur Wander, Gerhard Hendl, Michael Hofer and Wolfgang Kratz. Their great support is heavily appreciated. Also our administrative staff, particularly Christine Götsch-Obmascher, Karin Köhle and Nicole Jorda, were very supportive and facilitated our workload concerning administrative tasks a lot.

My family, all my friends and my family in-law provided a lot of support and encouragement. The biggest "Thank you" is dedicated to my beloved wife Amba. She did a great job in keeping me on track and supporting me since the start of my diploma thesis.